Environmental Science and Engineering

Zeng Yang *Editor*

# Environmental Science and Technology: Sustainable Development

## International Conference on Environmental Science and Technology

Springer

# Environmental Science and Engineering

The ultimate goal of this series is to contribute to the protection of our environment, which calls for both profound research and the ongoing development of solutions and measurements by experts in the field. Accordingly, the series promotes not only a deeper understanding of environmental processes and the evaluation of management strategies, but also design and technology aimed at improving environmental quality. Books focusing on the former are published in the subseries Environmental Science, those focusing on the latter in the subseries Environmental Engineering.

Zeng Yang
Editor

# Environmental Science and Technology: Sustainable Development

International Conference on Environmental Science and Technology

Springer

*Editor*
Zeng Yang
Department of Environmental Engineering
School of Environmental Science
and Engineering
Qingdao, China

ISSN 1863-5520 ISSN 1863-5539 (electronic)
Environmental Science and Engineering
ISBN 978-3-031-27430-5 ISBN 978-3-031-27431-2 (eBook)
https://doi.org/10.1007/978-3-031-27431-2



This Springer imprint is published by the registered company Springer Nature Switzerland AG
The registered company address is: Gewerbestrasse 11, 6330 Cham, Switzerland

# Preface

The 2022 13th International Conference on Environmental Science and Technology (ICEST 2022) was held as virtual conference during October 21–23, 2022. The Conference has emerged as an exclusive opportunity for the participants from all over the globe to present and discuss the reviews and results in their respective environmental science and technology research areas.

The international conference was divided into three major parts, including keynote speeches, invited speeches, and oral presentations. Over 60 leading environmental and energy researchers, engineers and scientists from numerous countries, including Canada, Croatia, Peru, Portugal, Australia, Philippines, China, etc. Topics included Water and Wastewater Treatment, Environmental Pollution Analysis and Environmental Remediation, Green Technology, Carbon Emission Reduction and Sustainable Development, Water Quality Analysis, Hydrology and Water Resources Planning, Environmental Pollution Control and Chemical Engineering, Energy, Water and Environment. All presentations were oral with ample time given for Questions and Answers at the end of the presentation. One presentation per session was selected as "best presentation" for its generally outstanding quality.

All full papers presented at the 2022 13th International Conference on Environmental Science and Technology (ICEST 2022) have been selected for this volume by solely considering their quality, novelty and the relevance to the conference.

We believe that the conference was of a high and fruitful level, while meeting international standards. The conference series will continue in the future and will again provide an effective platform for further exchange of advanced know-how and knowledge, while also fostering potential international research collaborations in the topics of Environmental Sciences and Technology.

We would like to acknowledge all scientists and administrative staff who have supported ICEST 2022. We are grateful to the presenters and the participants for their thought-provoking contributions. Each individual and institutional support was very important for the success of this conference . Especially we would like to thank

the organizing committee for their professional organization and coordination of the peer review of the papers. We hope that it met the expectations. We extend our very best wishes to you wherever you may be around the world.

Zeng Yang
Publication Chair
Shandong University
Jinan, China

# Contents

# Part I
# Water Quality Monitoring and Water Resources Management

# Chapter 1
# Remote Sensing on Water Quality of Lakeside Reservoir Based on Landsat Satellite Images


**Zihan Zhao, Haiyan Fu, Lei Jin, Yuanmao Zheng, Yicheng Wu, Mengnan Yu, and Ke Xu**

**Abstract** For dynamic monitoring of the reservoir eutrophication degree, remote sensing technology was used to invert the core parameters that respond to water body eutrophication–chlorophyll a, suspended sediment content and dissolved oxygen. Using remote sensing images as the data source, combined with the actual measurement data of Lakeside Reservoir in Xiamen, the remote sensing quantitative inversion model of three water quality parameters was selected, and the spatial and temporal distribution maps of water quality parameters were generated using The Environment for Visualizing Images software, and the Carlson's Trophic State Index (TSI) method was used to evaluate the eutrophication degree of reservoir water The results shows that the overall concentration of chlorophyll a in Lakeside Reservoir is more than 20 mg/m$^3$,which belongs to eutrophic state, and the concentration of chlorophyll a in summer is generally higher than that in winter. The content of suspended sediment and dissolved oxygen concentration reached the highest values of 9 mg/m$^3$ and 25 mg/m$^3$ in summer, respectively, which was the same as the distribution law of chlorophyll a. It also shows that the nutritional status of lakeside reservoir has only two grades: eutrophic and extremely eutrophic. There is a certain spatial pattern, the northeast of the reservoir is relatively polluted, and the northeast shore of the reservoir is a residential living area, so the conclusion is basically consistent with the actual situation of the reservoir. The study can provide a theoretical basis for the monitoring and early warning of eutrophication of lake water quality in areas prone to eutrophication.

**Keywords** Remote sensing monitoring · Eutrophication · Chlorophyll a · Suspended sediment content · Dissolved oxygen

Z. Zhao · H. Fu (✉) · L. Jin · Y. Zheng · Y. Wu · M. Yu · K. Xu
Key Laboratory of Environmental Biotechnology (XMUT), Fujian Province University, Xiamen University of Technology, Xiamen 361024, China
e-mail: fuhy@xmut.edu.cn



Z. Yang (ed.), *Environmental Science and Technology: Sustainable Development*, Environmental Science and Engineering, https://doi.org/10.1007/978-3-031-27431-2_1

## 1.1 Introduction

Reservoirs are built to meet various purposes, such as drinking water supply, hydropower production, food control, and irrigation. But they change the downstream ecosystem and have negative environmental effects on it. On the other hand, the entry of excess nutrients into the reservoir causes problems such as eutrophication, and consequently, we see a decline in the quality of water in the reservoirs (Yahyaee et al. 2021). Eutrophication of water body has become one of the main environmental pollution problems. Many studies have shown that the eutrophication of water body is due to the existence of excessive nitrogen, phosphorus and other nutrients, which leads to the proliferation of algae in the water, and the reduction of dissolved oxygen causes the deterioration of water quality and the death of aquatic organisms (Zhang 2011). Therefore, the use of scientific and accurate methods to assess the degree of eutrophication of water bodies is of great significance for reflecting the quality and pollution of water bodies and predicting future development trends.

The spectral characteristics of water are mainly determined by the material composition of the water body itself, and the substances in lake water that affect the light intensity and spectral distribution can be roughly divided into 3 categories: planktonic algae pigments, yellow substances and suspended substances (Duan et al. 2006). The difference in the content of components in the water body will cause significant differences in the reflectivity of a certain wavelength range, which is the theoretical basis for the quantitative inversion of water quality parameters by remote sensing (Zhang et al. 2014). There have been many studies on water quality inversion in different regions, different seasons, different water quality parameters, different inversion methods and algorithms, and different satellite remote sensing data sources. Dekker and Peters (1993) used the correlation between each band value in Landsat TM image data and the concentration of chlorophyll a, and found that the index model inverted the chlorophyll a concentration of the study area more accurately than the linear model; Kloiber et al. (2002) used correlation analysis matrix, effective statistical analysis method, using Landsat's first wave band, the ratio of the first wave band and the third wave band reflectance value to establish a transparency inversion model to predict the transparency of typical lakes in the United States. Pan et al. (Zheng 2017) Using the Gaofen-6 satellite imagery, three models were used to invert the chlorophyll a mass concentration of Taihu Lake, and a model suitable for the inversion of chlorophyll a mass concentration in Taihu Lake in the Gaofen 6 satellite image was obtained. Zheng (Pan et al. 2021) based on OLI images, a mathematical regression model of chlorophyll a mass concentration inversion was established, and the spatio-temporal distribution of chlorophyll a mass concentration in Dongzhang Reservoir was analyzed. Ma et al. (2020) took Miyun reservoir as the research object, used BP neural network algorithm to invert 4 water quality parameters, and obtained more credible research results. Xu et al. (Wang and Qin 2022) established a neural network model to invert the chlorophyll a mass concentration of the clean water body of Qiandao Lake, and used the model to analyze the chlorophyll a mass concentration of Qiandao Lake in spatiotemporal characteristics.

In water quality studies of lakes and reservoirs, eutrophic water bodies have their own unique spectral characteristics that are different from the usual clean water bodies. Therefore, the spectral characteristics of water quality parameters can be obtained by remote sensing and spectrometer, etc., and the eutrophication evaluation model of lakes and reservoirs can be established by combining with water quality analysis data. The eutrophication evaluation model provides a basis for remote sensing monitoring of eutrophication in lakes and reservoirs, the remote sensing technology is more practical in the process of water quality research and application. Based on the actual measurement data, the different degrees of eutrophication of water bodies can be classified, which can provide real-time feedback on the water quality condition of lakes and reservoirs, and provide reference for water environmental protection, and also provide a strong basis for the control and management of water environment pollution. Although remote sensing opens new ideas for lake water quality monitoring, there are still some problems, first of all, the signals received by remote sensing are affected by the atmosphere, and the atmospheric correction algorithm is not mature enough, so more accurate atmospheric correction is needed to control the atmospheric influence and eliminate the influence of the atmosphere and light on the reflection of water. In addition, aquatic plants and external forces will cause the error between the measured data and the model estimation (Wang and Qin 2022).

In view of the above, Landsat 8 satellite images with high spatial resolution and one of the most popular multispectral remote sensing data in recent years were selected for this study. Based on the experience of previous studies, the inverse models of three water quality parameters, namely chlorophyll a, suspended sediment content, and dissolved oxygen concentration, were selected for the water bodies in the study area, and the three water quality parameters were mapped to analyze the spatial and temporal distribution characteristics of the above water quality parameters in the lakeside reservoirs. The correlation between the spectral characteristics of water bodies and eutrophication indicators such as chlorophyll a, suspended sediment, and dissolved oxygen is studied. This quantitative remote sensing monitoring model is expected to provide a reference and basis for regional water quality monitoring and water resources scheduling.

## 1.2 Experimental Materials

### *1.2.1 Survey Area*

The Lakeside Reservoir is located in the east of the east city of Xiamen Island (N: 24°29′ ~ 24°30′, E: 118°09′), as shown in Fig. 1.1. It is a small freshwater reservoir with the largest catchment area on the island of Xiamen, and belongs to the key protection waters, with a total planned land area of 4.05 $km^2$, of which the water surface area is 1.03 $km^2$, which can meet the emergency water supply of one million


**Fig. 1.1** Lakeside reservoir in Xiamen

people for about one month and solve the flood discharge problem. As an emergency backup water source for Xiamen Island, it is important to study how to maintain the water quality of Lakeside Reservoir in good condition, which is one of the reasons why it was chosen as the research object of this paper. As shown in Fig. 1.1, there are 6 water quality monitoring points, and the sampling points are evenly distributed near residential areas and the central area of the reservoir.

### *1.2.2 Research Data*

**Acquisition of Remote Sensing Image Data**. Based on the geographical location of Lakeside Reservoir, the Landsat-8 satellite remote sensing image data of Xiamen City in July and November 2020, January and February 2021 were downloaded from the website of United States Geological Survey (USGS). To improve the accuracy of the experimental results, the remote sensing image data of the Lakeside Reservoir with no cloud interference or high resolution were selected.

The Landsat-8 satellite is the eighth satellite in the U.S. Landsat program and was launched on Feb. 11, 2013 BST. The satellite is loaded with the Land Imager (OLI)

**Table 1.1** Landsat-8 satellite parameters

| Parameter | Indicator |
|---|---|
| Launch time | 1913-2-11 |
| Orbit type | Near polar sun-synchronous orbit |
| Orbital altitude (km) | 705 |
| Orbital inclination (°) | 98.2 |
| Orbital period (min) | 98.9 |
| Descending node local time | 10:00 |
| Orbital repetition period (day) | 16 |

and the Thermal Infrared Sensor (TIRS), in which the OLI covering nine wavelength bands ranging from visible to infrared light, which can sense the thermal radiation emitted from the Earth's surface and the re-reflected solar radiation; the TIRS can monitor the heat loss from the Earth and observe moisture depletion in the study areas. The parameters of the Landsat-8 satellite is shown in Table 1.1.

**Remote Sensing Image Data Pre-processing**. In its imaging process, remote sensing images are easily restricted by factors such as radiation resolution, time and wavelength range, which will produce errors deviating from the actual situation in the process of data acquisition. Therefore, the acquired raw images need to be pre-processed, including processes such as radiation calibration, atmospheric correction and water extraction.

**Radiation Calibration**. Using the radiation calibration parameters of the image data of the OLI sensor loaded by Landsat-8, the The Environment for Visualizing Images software comes with the Landsat Calibration tool for radiation calibration, after calibration, the digital quantization value of image elements (Digital Number) will be converted into the radiation brightness value, using the formula shown in Eq. (1.1):

$$L_\lambda = \frac{DN}{a} + L_0 \tag{1.1}$$

where $L_\lambda$ is the radiation brightness value in the λ-band, a is the gain value and $L_0$ is offset value.

For this step, the Radiometric Calibration tool in The Environment for Visualizing Images software will be used. Using the remote sensing image map of February 2021 as an example, a comparison before and after radiometric calibration is shown in Fig. 1.2.

**Atmospheric correction**. The FLAASH atmospheric correction model in the The Environment for Visualizing Images software was used to perform atmospheric correction on the remote sensing image of the Lakeside Reservoir, converting the radiant brightness value into the actual surface reflectance to eliminate the effects of atmospheric scattering and atmospheric absorption during the imaging process, a comparison before atmospheric correction is shown in Fig. 1.3.


**Fig. 1.2** Comparison chart before and after radiometric calibration (left: before radiation calibration; right: after radiation calibration)


**Fig. 1.3** Comparison chart before and after FLAASH atmospheric correction model (left: before atmospheric correction; right: after atmospheric correction)

### *1.2.3 Model Construction*

At present, there are usually three methods for inverting water quality parameters using spectral data observed by remote sensors, namely empirical model method, semi-empirical-semi-analytical model method and model model analysis method. Empirical methods Based on statistical analysis theory, on the basis of a large number of field measured data, the statistical relationship between remote sensing reflectivity and water quality parameter concentration is established, and then the water quality parameter concentration of water body is extrapolated, and the commonly used models mainly include single-band model, first-order differential model, band ratio model and multi-band combination model (Xu et al. 2021). Semi-empirical/semi-analytical model can basically meet the requirements of chlorophyll a concentration inversion accuracy, for the commonly used single-band or band ratio as a remote sensing quantitative inversion of chlorophyll a concentration method, researchers will use three-band or first classification and then modeling method to improve the accuracy of the results. Pattern model, the core of the model lies in modern intelligent algorithms, such as principal component analysis, nonlinear optimization method, neural network algorithm and algebraic algorithm.

**Remote sensing image preprocessing**. During the imaging process, remote sensing images are easily affected by factors such as radiation resolution, time, and wavelength range, and will deviate from the actual situation during data transmission and cause errors. Therefore, it is necessary to preprocess the acquired original images. After radiometric calibration, atmospheric correction, and water body extraction, the extracted images of lakeside reservoirs are shown in Fig. 1.4.

**Remote sensing image inversion model**. Eutrophication index is an index to evaluate the degree of eutrophication in water area, the main eutrophication index is

**Fig. 1.4** Extract image of research water area

water transparency, chlorophyll a content, total phosphorus and total nitrogen content. According to the Nutrient status Index (TSI) method of Carlson (Jin 1990), water transparency, chlorophyll a content, total phosphorus and total nitrogen in water can well reflect the eutrophication degree of water. Chlorophyll a has the most significant effect on reflecting the degree of eutrophication. According to the corresponding relationship between nutrient status index (TSI) of Carlson and nutrient level of water body, the basic status of water body can be determined by inverting the TSI index of chlorophyll a concentration.

In this study, the landsat-8 remote sensing image data of Xiamen city in July and November 2020 and January and February 2021 without cloud disturbance and with high definition were selected, and the estimation models of chlorophyll a, suspended sediment content and dissolved oxygen were selected for interpretation and analysis referring to previous studies.

### *1.2.4 Inversion of Water Quality Parameters Concentration Based on Remote Sensing Images*

**Chlorophyll a Concentration Inversion Method**. Chlorophyll a, as an essential substance in the process of plant photosynthesis, is an important indicator for monitoring phytoplankton and algae in water bodies. Because the fluorescence characteristics of chlorophyll a are very obvious and its concentration and fluorescence are highly positively correlated, the spectral characteristics of chlorophyll a and remote sensing image maps were used to study its concentration. In this study, remote sensing image data from Landsat-8 satellite without cloud interference and with high resolution in July and November 2020, January and February 2021 in Xiamen were selected for interpretation and analysis.

The band ratio method is currently used for chlorophyll a remote sensing inversion model (Ma and Dai 2005), Hoogenboom (Hoogenboom et al. 1998) analyzed the characteristic band of chlorophyll a in Ljsselneer lake and found that the optimal combination of bands to estimate the chlorophyll a concentration in this lake was R708nm/R676nm; Hunter et al. (2010) used the R670nm/R710nm band combination to construct an inversion model, and remotely inverted the chlorophyll a concentration of lakes, and the results were relatively accurate. Li et al. (2002) took Chaohu Lake as the research object, and established a remote sensing quantitative inversion model using the measured water spectra and chlorophyll a concentration, and the results showed that R705nm/R680nm could estimate the chlorophyll a concentration well. Therefore, band ratio model and chlorophyll a concentration were used for remote sensing quantitative inversion in this paper.

In the study of the inversion of multiple chlorophyll a concentrations, Zhao et al. (2017) used a regression model based on the R language and used the stepwise regression method to obtain the ideal regression model for chlorophyll a concentrations, as shown in Eq. (1.2):

$$\begin{aligned} C_{chla} = & -2.1092 \times b_1 - 1.3332 \times b_2 + 0.7338 \times b_3 + 2.0086 \times b_4 \\ & + 65.7671 \times \left(\frac{b_5}{b_2}\right) - 886.3589 \times \left(\frac{b_4}{b_1}\right) \\ & - 319.1904 + 718.3138 \times \left(\frac{b_2}{b_1}\right) \\ & - 132.7472 \times NDVI + 743.8309 \end{aligned} \tag{1.2}$$

The estimation model of chlorophyll a concentration developed by Juli et al. (Zhu et al. 2015) with reference to the previous studies is shown in Eq. (1.3):

$$C_{Chl-a} = 4.089 \times \left(\frac{b_4}{b_3}\right)^2 - 0.746 \times \left(\frac{b_4}{b_3}\right) + 27.93 \tag{1.3}$$

In the formula, $C_{chl\text{-}a}$ is the concentration of chlorophyll a, mg·m-$^3$, $b_1$, $b_2$, $b_3$, and $b_4$ are the DN values of the first, second, third and fourth bands in the image after radiometric calibration and atmospheric correction, respectively.

Comparing with previous related experiences, Eq. (1.3) was chosen to invert the chlorophyll a concentration in this study. Among the three indicators of chlorophyll a concentration, suspended sediment content and dissolved oxygen concentration, chlorophyll a content is the index that can most intuitively reflect the degree of eutrophication of water bodies, so 6 monitoring points were selected in the reservoir to determine the accuracy of the water quality data verification model. The approximate location of the sample point is shown in the Fig. 1.1 Inversion verification results are given in Table 1.2, due to the large number of data, the limited space table only lists 6 representative sets of data, the average relative error is 4.93%, from the results can be seen that most of the sample points relative error is less than 10%, a set of abnormal data its relative error of 24.33%, after discrete analysis of this set of data is an outlier, may be caused by human error in the measured time, but overall it can be seen that the model accuracy is relatively high, and the results of inversion are better.

**Table 1.2** Accuracy of the model validation

| Monitoring sites | Longitude | Latitude | Measured value (mg/L) | Predicted value (mg/L) | Relative error (%) |
|---|---|---|---|---|---|
| 1 | 118.1698137° | 24.5040591° | 8.30 | 8.32 | 0.24 |
| 2 | 118.1725445° | 24.5029412° | 23.40 | 24.59 | 5.09 |
| 3 | 118.1748083° | 24.5012314° | 19.62 | 20.33 | 3.62 |
| 4 | 118.1620883° | 24.4968910° | 7.32 | 8.04 | 9.83 |
| 5 | 118.1699574° | 24.4945234° | 9.34 | 9.52 | 1.93 |
| 6 | 118.1711072° | 24.5008039° | 21.28 | 22.12 | 3.95 |
| Average relative error | | | | | 4.93 |

**Inversion of suspended sediment content**. Water quality characteristics such as turbidity, water color, and transparency are affected by suspended sediment, and the optical characteristics of suspended sediment are obvious (Pan and Guo 2020). The OLI sensor loaded on Landsat-8 satellite covers near-infrared, red, green, and blue wavelengths and can be used for concentration inversion of suspended sediment content in water bodies. In addition, suspended sediment can be used as a reference for sediment transport and can characterize the strength of the carrying capacity of water bodies, which has significant research value for water quality studies and related engineering construction studies at the coast.

In this study, the suspended sediment content of remote sensing images of four time periods of Xiamen Lakeside Reservoir was investigated, and the inverse equation of suspended sediment concentration was constructed as shown in Eq. (1.4) based on the previous experience (Pan and Guo 2020).

$$y = 27.05 \times exp\left(b_4 \times \frac{8.83}{10000}\right) - 27.02 \tag{1.4}$$

**Dissolved Oxygen Concentration Inversion**. The content of dissolved oxygen in water can be used as a parameter indicator to evaluate the degree of pollution in water bodies, and the concentration of dissolved oxygen is generally lower in waters with high eutrophication. Zhong Weiping et al. (Zhan et al. 2017) studied the spectral characteristics of dissolved oxygen, and constructed a mathematical model with dissolved oxygen concentration as the dependent variable and waveband combination as the independent variable, and used stepwise regression analysis to screen the models with higher significance and accuracy.

In this study, the dissolved oxygen content was investigated in remote sensing images of four time periods of Xiamen Lakeside Reservoir, and the constructed dissolved oxygen inversion equation is shown in Eq. (1.5) based on previous experience (Zhan et al. 2017).

$$\begin{aligned} y =& 771.851x_1 - 1.476x_2 + 6.345 \\ x_1 =& \frac{1}{b_a}, x_2 = \frac{b_3^2}{b_1^2} \end{aligned} \tag{1.5}$$

**Eutrophication Evaluation Methods for Water Bodies**. Experts in ecology and environmental science classify the nutrient status of water bodies into poor, moderate, and eutrophic states based on indicators such as the physical and chemical properties of nutrients and biological categories. Water quality and poor eutrophic status are relative and flexible, and there is no strict boundary of division. Table 1.3 shows the comparison of eutrophic and depleted lake characteristics (Zhong et al. 2020).

The trophic state index method is to convert eutrophication indicators into a trophic state index. These eutrophication indicators include water clarity, chlorophyll a content, and total N/P content. The lakes were classified according to the trophic state index. According to Carlson's trophic state index (TSI) method

**Table 1.3** Characteristics of lake eutrophication

| Category | Oligotrophic lake | Eutrophic lake |
|---|---|---|
| Transparency | Lucid | Thick |
| Water color | Blue or green | Green or yellow |
| Biological Species | Diverse | Single |
| Planktonic algae | Rarely, mainly diatoms | Many, mainly cyanobacteria and green algae |
| Dissolved oxygen | The total aquifer is usually saturated with the surface aquifer | Supersaturation of dissolved oxygen |
| Organic content | Less organic matter | More organic matter |
| Water temperature | The water in the lake is cooler | The water in the lake is warmer |

(Xu et al. 2021), indicators such as water clarity, chlorophyll a content, and total N/P of the water body can well reflect the eutrophication level of the water body. Among them, chlorophyll a can most intuitively reflect the degree of eutrophication of water bodies. According to Carlson's trophic state index (TSI) calculation, the correspondence between chlorophyll a content in the TSI eutrophication index. The nutrient status of the lake is shown in Table 1.4.

Based on data related to chlorophyll a concentration in the water column of the Lakeside Reservoir, the trophic state index (TSI) method constructed by Carlson was used to reflect the eutrophication status of the reservoir using the content of chlorophyll a is shown in Eq. (1.6) (Xu et al. 2021):

$$TSI_{chl-a} = 9.18ln(C_{chl-a}) + 30.6 \tag{1.6}$$

**Table 1.4** Corresponding relationship between TSI chlorophyll a content and nutrient state

| TSI | Chlorophyll a concentration (mg/L) | Nutritional status of lakes |
|---|---|---|
| 30–40 | 0.95–2.6 | Poor nutrition: the homogeneous layer of shallow water lake is deficient in oxygen |
| 40–50 | 2.6–7.3 | Mesotrophic: the water is clear and the homogeneous layer of the lake is anoxic in summer |
| 50–60 | 7.3–20 | Eutrophication: homogenous temperature layer hypoxia, large aquatic plants flourish |
| 60–70 | 20–56 | Rich in cyanobacteria and green algae: bloom problems present |
| 70–80 | 56–155 | Highly nutritious: high concentration of algae and macrophytes |
| >80 | >155 | Highly nutritious: high concentration of algae and macrophytes |

In the formula, $TSI_{chl\text{-}a}$ is the chlorophyll eutrophication index, and *chl-a* is the concentration of chlorophyll a, mg $m^3$.

The data images downloaded from the website cover the whole Xiamen area. In this project, only the eutrophication of the Lakeside Reservoir is studied, so the water body area of the Lakeside Reservoir needs to be extracted separately. Based on the geographical location of Lakeside Reservoir, the Landsat-8 satellite remote sensing image data of Xiamen City in July and November 2020, January and February 2021 were downloaded from the website of United States Geological Survey (USGS). To improve the accuracy of the experimental results, the remote sensing image data of the Lakeside Reservoir with no cloud interference or high resolution were selected.

## 1.3 Discussion and Results

### *1.3.1 Inversion Results of Chlorophyll a Concentration*

Using the above-mentioned data and methods, the chlorophyll a concentration inversion was performed on the selected Landsat-8 remote sensing images for four months, and the inversion results are shown in Fig. 1.5.

It can be seen from the Fig. 1.5 that the concentration of chlorophyll a in the Lakeside Reservoir is generally high, which is above 20 mg/$m^3$ and belongs to the eutrophic state. From the perspective of time scale, the concentration of chlorophyll a in summer was the highest, basically above 32 mg/$m^3$, mainly because the water temperature in winter was lower than that in summer, and the amount of terrigenous nutrient salt was reduced, which led to the slow growth rate of algae and the decrease of chlorophyll a concentration. In the early winter season, the concentration of chlorophyll a in other waters was relatively uniform except for the water near the commercial residential area. The possible reasons for this phenomenon are as follows: Xiamen is located in the coastal area, with sufficient sunshine all year round and mild climate. In early winter, the temperature drop is low, which is conducive to the growth and reproduction of algae. The northeast of the reservoir is close to urban settlements, and human activities also have an impact on water quality. A large amount of sewage and its nutrients are discharged into the water body, which is conducive to the growth of algae. Therefore, the concentration of chlorophyll a will be higher. The results showed that the highest concentration of chlorophyll a was mainly concentrated in the eastern part of the water area in summer, and the concentration distribution showed a decreasing trend from north to south.

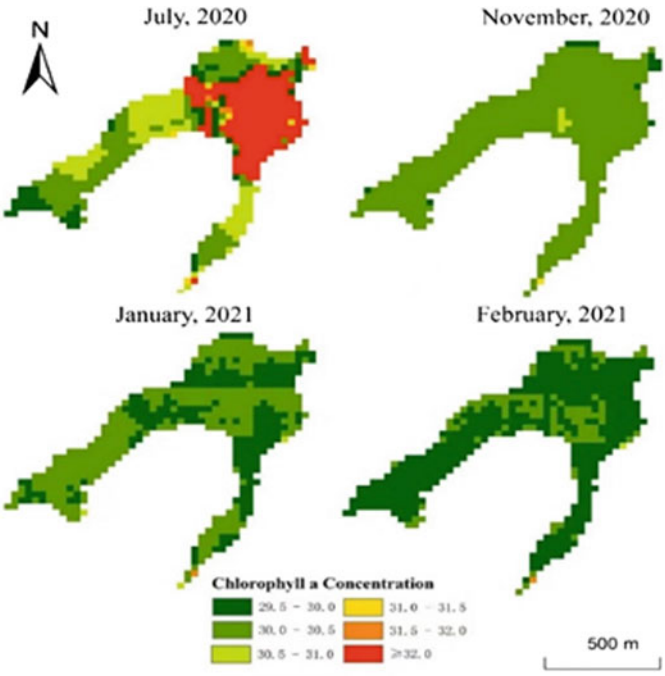


**Fig. 1.5** Plot of inverse changes in chlorophyll a

### *1.3.2 Inversion of Suspended Sediment Content*

Based on the inverse Eq. (1.4), the inverse plot of suspended sediment concentration is obtained as shown in Fig. 1.6. Overall, the suspended sediment concentration shows seasonal and month-to-month variation. The concentration is highest in summer, and the highest value exceeds 9 mg/m$^3$ in July when the temperature in Xiamen is high; the concentration decreases in November and can reach the lowest value, and then rises again in January. Seasonal variations in suspended sediment concentrations depend mainly on runoff flow, temperature and degree of land erosion. Since the general river flood season and dry season runoff are quite different, With the increase of runoff, the concentration of suspended sediment in most sea areas will increase to varying degrees, and the decrease of runoff will reduce the concentration of suspended sediment. Rainfall is also one of the important factors affecting suspended sediment. Summer runoff and rainfall are higher than in winter, so the content of suspended sediment in summer is higher than in winter. Spatially, the spatial distribution of suspended sediment concentration is roughly the same, with higher concentrations in the waters near the pollution source and maximum concentrations in the locations directly connected to the pollution source.

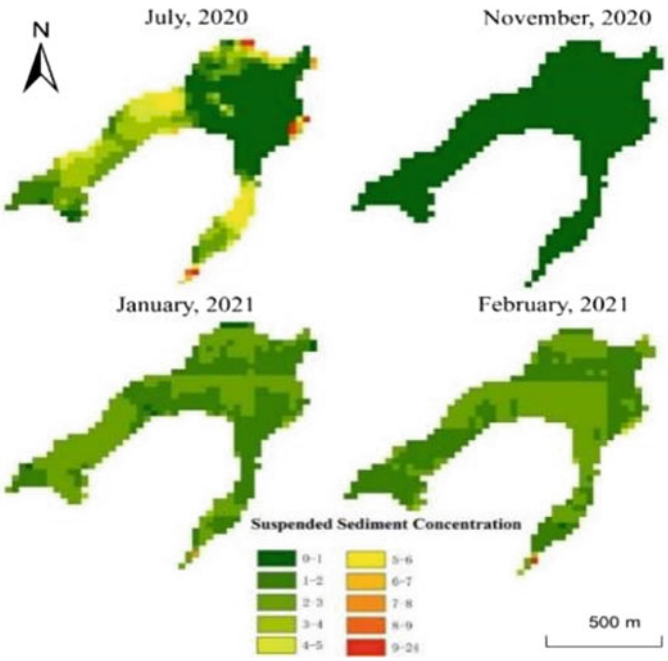


**Fig. 1.6** Plot of inverse changes in suspended sediment content

### *1.3.3 Inversion Results of Dissolved Oxygen Concentration*

Based on the above inversion equation, the inverse plot of dissolved oxygen concentration obtained is shown in Fig. 1.7. From the figure, there is a significant temporal variation in dissolved oxygen concentration in Lakeside Reservoir from 2020 to 2021. According to the four seasons, dissolved oxygen concentrations in the Lakeside Reservoir are generally higher in summer than in autumn and winter. In summer, and the highest value exceeds 25 mg/m$^3$ in July the concentration of dissolved oxygen increases for a short period of time due to algal blooms and the production of large amounts of oxygen by algae photosynthesis during the day. The content of dissolved oxygen in water is related to various factors such as the partial pressure of oxygen in the air, atmospheric pressure, water temperature, depth, content of various salts in water, and light intensity. In the summer, the phosphorus content in the water body is high, and the photosynthesis of aquatic organisms such as algae is strong, a large number of algae occupy the surface of the water body resulting in the inability of gas exchange between the water body and the atmosphere, which can produce more oxygen, so that the dissolved oxygen in the water is fully replenished. At the same time, the growth of zooplankton population increases the consumption of oxygen in water, and the concentration of dissolved oxygen in water decreases. In terms of spatial distribution, the dissolved oxygen concentration in Lakeside Reservoir

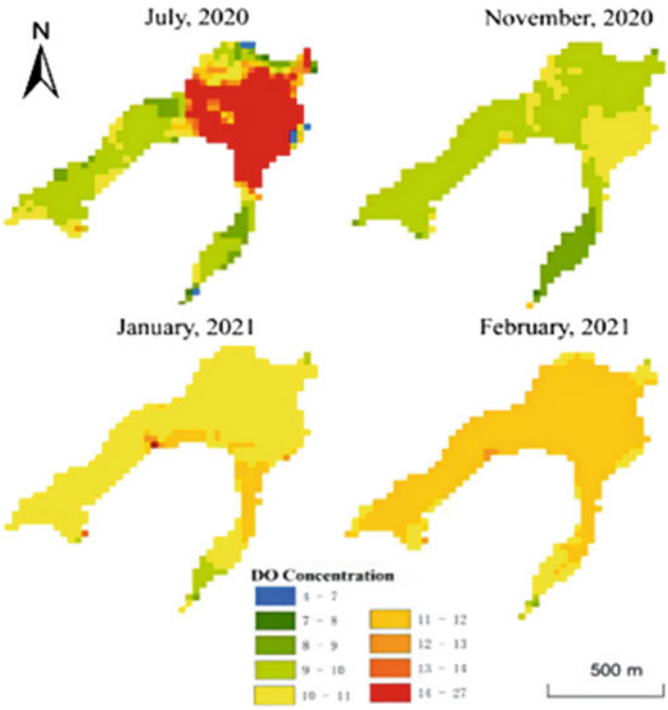


**Fig. 1.7** Plot of inverse changes in dissolved oxygen

from 2020 to 2021 are not uniformly distributed and there are no obvious spatial distribution pattern.

### *1.3.4 Eutrophication Evaluation of Lakeside Reservoir*

Using the TSI index method, the trophic status level of the water bodies in the Lakeside Reservoir was graded with the indicator of chlorophyll a concentration, and Fig. 1.8 shows the evaluation results.

The eutrophication degree distribution of Xiamen Lakeside Reservoir in July 2020 shows that the nutrient index of the water body of Lakeside Reservoir in this month is greater than 50, which means that Lakeside Reservoir is above the eutrophication state. Xiamen is located in a subtropical region, with high temperature and strong light in summer, which is conducive to the growth and reproduction of cyanobacteria and other algae, once the cyanobacteria reproduce wildly in large quantities, they will form water wars, which will consume most of the nutrients in the water body, reduce the dissolved oxygen concentration in the water body, cause the death of fish and shrimp, and then increase the degree of eutrophication in the water body. The

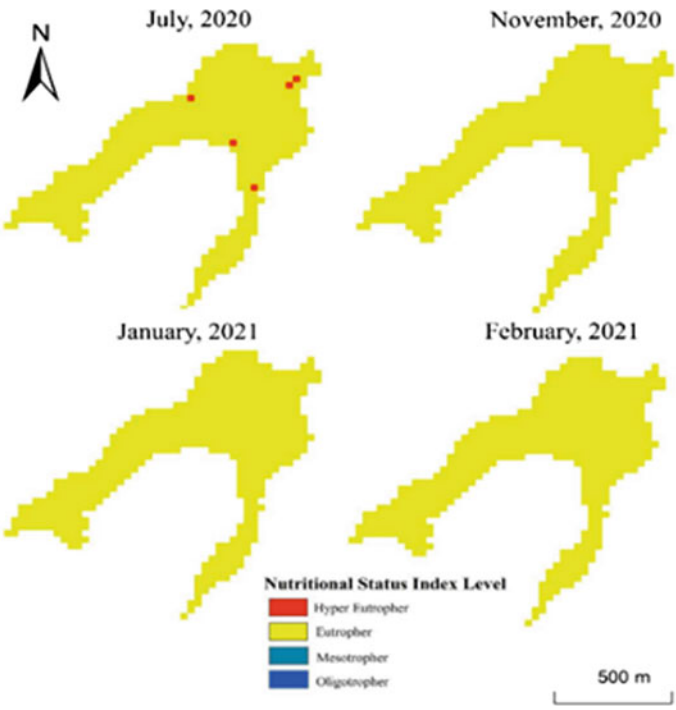


**Fig. 1.8** Distribution of the trophic state of the reservoir

distribution shows that the nutrient index of the Lakeside Reservoir is between 50 and 70 in all three months, which is in the overall eutrophication range, improving relative to the summer season. At the same time, precipitation conditions affect the changes in reservoir levels, and the rise in water level also has a diluting effect on nutrients in the water. A comparison of the two years of data shows that the eutrophic state of the reservoir improves from 2020 to 2021.

Due to the gentle water flow in the reservoir, the flow rate of the discharged water is small and slow. Therefore, except for July 2020, when some areas showed extremely eutrophic state, the eutrophic state of the whole water body was basically the same in the rest of the monitoring months, all of which showed eutrophic state, and the nutrient state level of the water near the pollution source was generally high.

## 1.4 Conclusion

According to the current status of remote sensing monitoring research at home and abroad, this paper uses the Landsat-8 satellite spectral data released by the United States in July and November 2020, January and February 2021 to establish a remote

sensing inversion model about Xiamen Lakeside Reservoir, obtain the inversion results of chlorophyll a, suspended sediment and dissolved oxygen concentration, and finally analyze the spatial and temporal distribution characteristics of these three water quality parameters.

The seasonal distribution of pollutant indicators in Xiamen Lakeside Reservoir has significant spatio-temporal characteristics: in time, it is manifested as higher chlorophyll a concentration in summer, higher content of suspended sediment, super-saturated dissolved oxygen, low concentration of 3 indicators in winter, and not much difference between summer and winter in autumn and winter, spatially manifested as chlorophyll a, suspended sediment, and dissolved oxygen with a higher distribution in the northeast of the reservoir, forming a distribution phenomenon of "high and low values" from northeast to southwest. The northeast of the reservoir is a residential area, which shows that human activities have a greater impact on the changes in water quality of the reservoir.

The use of satellite remote sensing data to invert and monitor lake water quality is the future development trend, but there are fewer cloudless or cloudless images covering the study area, and satellite data is difficult to synchronize with the ground measurement time, and when measuring data in the field, the number and distribution of sampling points will also affect the accuracy of the real data, so that the inversion of the prediction model will be wrong, reducing the accuracy and applicability of the model. Considering the universality of the model, in the future, on the one hand, it is necessary to take more accurate remote sensing images and carry out synchronous lake water quality monitoring, on the other hand, the more universal semi-analytical model can be considered, the inversion algorithm can be improved, or more technical indicators can be introduced to evaluate the eutrophication status of the lake.

**Acknowledgements** This work was funded by Fujian provincial industry-university research collaborative innovation (2021Y4005), Fujian Science and Technology Guiding Project (2020Y0056), Fujian Natural Science Foundation (2021J011176), Fujian Engineering and Research Center of Rural Sewage Treatment and Water Safety.

## References

Dekker AG, Peters SWM (1993) The use of the thematic mapper for the analysis of eutrophic lakes: a case study in the Netherlands. Int J Remote Sens 14(5):799–822

Duan HT, Yu L, Zhang B et al (2006) Hyperspectral data applied in monitoring and evaluating the water trophic state of Lake Chagan. Acta Sci Circum Stantiae 26(7):1219–1226

Hoogenboom HJ, Dekker AG, Althuis IJA (1998) Simulation of AVIRIS sensitivity for detecting chlorophyll-over coastal and inland waters. Remote Sens Environ 65(3):333–340

Hunter PD, Andrew NT, Laurence C et al (2010) Hyperspectral remote sensing of cyanobacteria pigments as indicators for cell pollution and toxins in eutrophic lakes. Remote Sens Environ 114(11):2705–2718

Jin X (1990) Eutrophication of lakes in China. China Environmental Science Press, Beijing

Kloiber SM, Brezonik PL, Bauer ME (2002) Application of Landsat imagery to regional-scale assessments of lake clarity. Water Res 36(17):4330–4340

Li SJ, Wu Q, Wang XJ et al (2002) Relationship between chlorophyll content and reflectance spectral characteristics of phytoplankton in Chaohu Lake. J Lake Sci 14(03):228–234
Ma FK, Jiang QQ, Xu LD et al (2020) Water quality parameters inversion of Miyun Reservoir based on BP neural network algorithm. J Eco-Environ 29(3):569–579
Ma RH, Dai JF (2005) Estimation of chlorophyll and suspended matter contents in Taihu Lake based on Landsat ETM and measured spectra. Lake Sci 17(2):7
Pan X, Yang Z, Yang Y B et al (2021) Retrieval of chlorophyll A concentration in Taihu Lake based on remote sensing image of Gaofen-6 satellite. J Hohai Univ (Nat Sci Edn) 49(1):50–56
Pan LJ, Guo BY (2020) Remote sensing of suspend sediment concentration in Zhoushan islands based on Landsat8 data. Mar Dev Manage 37(09):82–90
Wang SM, Qin BQ (2022) Research progress on remote sensing monitoring of lake water quality parameters. Environ Sci 1–21
Xu PF, Chneg Q, Jin PB (2021) Remote sensing inversion of chlorophyll A in clean water of Qiandao Lake based on neural network model. Resour Environ Yangtze Basin 30(7):1670–1679
Yahyaee AR, Moridi A, Sarang A (2021) A new optimized model to control eutrophication in multi-purpose reservoirs. Int J Environ Sci Technol 18(11):3357–3370
Zhan C, Junbao YU, Wang Q et al (2017) Remote sensing retrieval of surface suspended sediment concentration in the Yellow River Estuary. Chin Geogra Sci 27(006):934–947
Zhang Y (2011) Progress and prospect in lake optics: a review. J Lake Sci 23(4):483–497
Zhang YL, Qin BQ, Chen WM (2014) Research progress of lake optics and its application. Adv Water Sci 33(4):87–89
Zhao WY, Jiang LL, Jiao J et al (2017) Remote sensing inversion and monitoring of chlorophyll a in host sea based on Landsat 8 data. Environ Protect Xinjiang 39(03):28–35
Zheng Z (2017) Retrieval of chlorophyll A mass concentration based on OLI remote sensing image. J Irrig Drainage 36(3):89–93
Zhong WP, Yao HM, Chen HQ (2020) Inversion model of dissolved oxygen in Qinzhou Bay based on automatic monitoring and Sentinel-2 image. J Guangxi Acad Sci 36(4):392–398
Zhu L, Li YM, Zhao SH et al (2015) Remote sensing monitoring of water quality in Taihu lake based on WFV data of GF-1 satellite. Remote Sensing Land Resour 27(01):113–120

# Chapter 2
# Spatio-Seasonal Variation Assessment of Water Quality Based on GIS Techniques to Identify Pollution Sources in Mantaro Basin


**Alejandra Araujo and Steve Camargo**

**Abstract** To generate sustainable management of water resources, it is necessary to know the state of water quality and promote its efficient use. This study was carried out in the Middle Mantaro Sub-basin, an important area in Peru due to its agricultural activity, which provides food to the country's capital. The objective is to explore the spatial-seasonal variation of 10 water quality parameters and analyze their pollution sources. The Geographic Information System (GIS) was used through Inverse Distance Weighted (IDW) interpolation for mapping and obtaining values at the sub-basin level. The results indicate that the high concentrations of physical–chemical, microbiological and heavy metal parameters affect 10, 33, and 27 subcatchments, respectively, out of the 39 that exist. The wet season presents higher concentrations in all parameters except for Mn, $NO^{3-}$ and TP and the primary polluting sources are municipal, domestic wastewater, and mining passives.

**Keywords** Water quality · Spatio-seasonal distribution · Mantaro basin

## 2.1 Introduction

Peru is the eighth country with the largest amount of water in the world, a reality that puts it in a privileged position; the main uses of this resource are agriculture, energy, population, mining, fishing and industrial activities (National Water Authority 2012); however, there is no adequate management of its quality. Among all its hydrographic units, less than 62% have monitoring stations and among these, more than 40% are classified as areas with poor water quality (National Water Authority 2015).

Within these hydrographic units there is the Mantaro Basin, located in the center of the country and subdivided into the Upper Sub-basin, where mining is the main activity; Middle Sub-basin with great importance due to the presence of the Mantaro Valley, which is the main food supplier of the country's capital (Correa et al. 2016);

A. Araujo (✉) · S. Camargo
School of Environmental Engineering, Faculty of Engineering, Universidad Continental, Huancayo, Junin 12000, Peru
e-mail: 72963122@continental.edu.pe



Z. Yang (ed.), *Environmental Science and Technology: Sustainable Development*, Environmental Science and Engineering, https://doi.org/10.1007/978-3-031-27431-2_2

and the Lower Sub-basin. The Basin's water sources are used for consumptive and non-consumptive purposes, with agriculture (47%), population (30%) and mining (14%) in the first category; and in the second, energy use (98%) and aquaculture (2%) (National Water Authority 2020). This very diverse classification of water use has led to conflicts, especially between mining, population and agricultural activities, since there is not enough control in the treatment of the effluents generated, causing the concentrations of many control parameters in the water to increase.

Water quality studies in the wet season in the 7 main rivers of the Mantaro Basin show values of Cu, Pb, Zn, Fe and As below the Peruvian environmental quality standards (PEQS) for irrigation, except in the Upper Sub-basin (Custodio et al. 2020). Custodio et al. (2021a) evaluated the water quality after the cessation of activities caused by the pandemic worldwide, concluding that the mean values of Cu, As, Fe, Pb and Zn did not exceed the PEQS for human consumption, with the exception of Pb, Fe and As in the Mantaro River of the Upper Sub-basin, and As in the Middle Sub-basin. In 2014, the National Water Authority (NWA) identified 436 sources of water contamination in the Basin, including domestic, municipal, mining wastewater, mining passives, hot springs, fish farming, hydroelectric plants and slaughterhouses (National Water Authority 2015), and despite the years and strategies that have been carried out to control the problem, there are no reports on the change in water quality as a result of these projects at the hydrographic region level.

Due to this, the present study aimed to explore the spatial-seasonal variation of 10 physical–chemical, inorganic and biological parameters of surface water quality in the Middle Mantaro Sub-basin between the period 2015 and 2021 using GIS, and to analyze their pollution sources. The Middle Sub-basin was selected as our study area due to its importance in agriculture and the absence of adequate awareness and regulations for sustainable management.

This study is the first to analyze NWA's annual monitoring data in the Mantaro Valley and would serve as input to improve existing water management policies.

## 2.2 Materials and Methods

### *2.2.1 Study Site*

The study area corresponds to the Middle Sub-basin that includes 3 Hydrographic Units: Cunas, Middle Alto Mantaro and Hydrographic Unit 499,691, presented in Fig. 2.1.

It is located between 11°30′ and 12° 30′S latitude and 75°00′ and 75° 50′W longitude. The altitude varies from 2,963 to 5,501 m above sea level, the total area is 4,723 km2, and the provinces of Jauja, Chupaca, Concepcion and Huancayo belonging to the Junin region are located in this sector. The climate is characterized by two quite marked seasons: wet and dry, the first from September to April and the second from May to August (Silva and Takahashi 2008), with average annual precipitation and

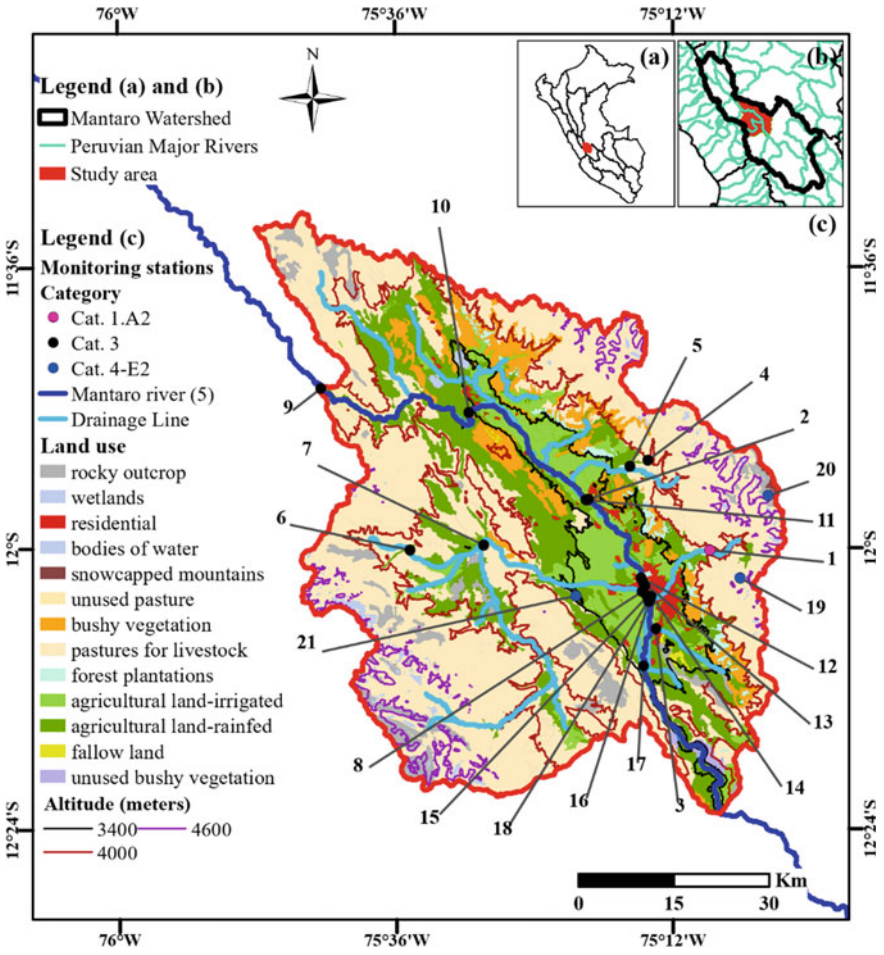


**Fig. 2.1** Location of the monitoring stations, land use and hypsometry in the study area

temperature of 700 to 800 mm and 8 to 12 °C, respectively. The area is occupied by pastures for livestock (56%), mainly in the higher areas, and by agricultural land-rainfed (18%) and irrigated (9%) in the lower areas near the Mantaro River. There are metallic and non-metallic mineral deposits that have fostered mining activities in the area; especially in the sectors closest to the main river.

### *2.2.2 Water Quality Monitoring Data*

Water quality data were obtained from the Portal of the NWA of Peru (National Water Authority 2022). The time series included 13 seasonal monitoring campaigns

between 2015 and 2021, 21 points were analyzed, located at the mouth of 3 lagoons and 8 rivers, with 3 stations in Jauja, 14 in Huancayo, 3 in Concepcion and 1 in Chupaca (Table 2.1).

The parameters that were taken into account include dissolved oxygen (DO), total phosphorus (TP), nitrates (NO3-), biochemical oxygen demand (BOD5), chemical oxygen demand (COD), thermotolerant coliforms (TC), manganese (Mn), iron (Fe), cadmium (Cd) and lead (Pb).

The bodies of water considered in the study have been defined by the NWA in 3 categories according to their main use: Cat. 1-A2 Human consumption after conventional treatment, Cat. 3 Vegetable irrigation and animal drinking, and Cat. 4 Lakes and Lagoons (Fig. 2.1). More than 80% is classified as Cat. 3, so this category was taken for comparison with the PEQS and the FAO.

**Table 2.1** Description and location of the monitoring stations

| N° | Code | Description | Coordinates | |
|---|---|---|---|---|
| | | | Lat (N) | Long (W) |
| 1** | RShul1 | Shullcas R before DWTP | 12° 0.20′ | 75° 8.75′ |
| 2*** | RAcha1 | Achamayo R before confluence with MR | 11° 55.85′ | 75° 19.32’ |
| 3** | RChan1 | Chanchas R | 12° 6.90′ | 75° 13.46’ |
| 4** | RChia1 | Chia R before intake for aquaculture activities | 11° 52.51′ | 75° 14.14’ |
| 5** | RChia2 | Chia R before confluence with Achamayo R | 11° 53.05′ | 75° 15.72’ |
| 6*** | RCons1 | Consac R after confluence with Huasiviejo R | 12° 0.16′ | 75° 34.77’ |
| 7* | RCuna1 | Cunas R | 11° 59.73′ | 75° 28.37’ |
| 8** | RCuna2 | Cunas R before confluence with Mantaro R | 12° 3.76′ | 75° 14.66’ |
| 9* | RMant11 | MR after confluence with Pachacayo R | 11° 46.37′ | 75° 42.50’ |
| 10* | RMant12 | MR before intake for irrigation activities | 11° 48.46′ | 75° 29.67’ |
| 11*** | RMant13 | MR before confluence with Achamayo R | 11° 55.93′ | 75° 19.53’ |
| 12** | RMant14 | MR before dump | 12° 2.57′ | 75° 14.73’ |
| 13** | RMant15 | MR after and before dumps | 12° 2.90′ | 75° 14.59’ |
| 14** | RMant16 | MR | 12° 3.24′ | 75° 14.40’ |
| 15** | RMant17 | MR after and before dumps | 12° 4.17′ | 75° 14.18’ |
| 16** | RMant18 | MR after confluence with Shullcas R | 12° 4.60′ | 75° 14.04’ |
| 17** | RMant19 | MR after WWTP discharge | 12° 10.10′ | 75° 14.52’ |
| 18** | RShul2 | Shullcas R before dump and after WWTP | 12° 4.19′ | 75° 13.87’ |
| 19** | LHuah1S | Exit of Huacracocha L(flows into Shullcas R) | 12° 2.58′ | 75° 6.16′ |
| 20** | LLasu1S | Exit of Lasuntay L (flows into Shullcas R) | 11° 55.56′ | 75° 3.70′ |
| 21**** | LÑahu1S | Exit of Ñahuinpuquio L(flows into Cunas R) | 12° 4.10′ | 75° 20.40’ |

*Jauja, **Huancayo, ***Concepcion, **** Chupaca

R designates river, L designates lagoon, MR designates Mantaro River, WWTP Wastewater treatment plant, DWTP Drinking water treatment plant

### 2.2.3 Statistical Analysis

Pearson's correlation analysis is a method that measures the linear relationship between two variables and is defined as a correct statistical technique to determine the correlation between water quality parameters (Sharma et al. 2020).

This step began with the standardization of the raw data through the Z-scale transformation that generates a mean of 0 and a variance of 1 in order to eliminate the impact of the dimensions and finally calculate the correlation coefficients, where values close to +1 or −1 indicate a good relationship and those close to 0 show a low relationship between the 2 water quality variables evaluated. The previous analysis was performed using the R program version 4.1.1.

### 2.2.4 Spatial Variation Analysis

Spatial variation analysis was performed in ArcMap 10.8. Data preparation was performed from the digital elevation model (DEM) provided by the Ministry of the Environment (Ministry of the Environment 2022) with a resolution of 30 by 30 m. Using the Arc Hydro Tools package, the drainage lines and 39 subcatchments were calculated (Fig. 2.2). The input data correspond to the average of each monitoring station in the wet and dry seasons.

**GIS Interpolation**. The Inverse Distance Weighted (IDW) method was used through the Geostatistical Analyst tool. This method is one of the most used in the mapping of water quality parameters, and assumes that each value is locally influenced and decreases with distance, therefore, the weights assigned to the interpolation points are based on the inverse of the distance from the point being estimated (Magesh and Elango 2019). The general IDW equation is:

$$\hat{z}(x_0) = \frac{\sum_{i=1}^{n} z(x_1) \cdot d_{ij}^{-p}}{\sum_{i=1}^{n} d_{ij}^{-p}}$$

where Z represents the interpolated value, $Z_1$ represents the nearby or neighboring data points, and $d_{ij}$ are the distances between the data points and the interpolated value.

After interpolation, the values were divided among the subcatchments taking into account the highest value of each parameter in each of them, except for the DO, which included the lowest value. In this last step, 6 subcatchments (23, 24, 25, 26, 27 and 39) were not taken into account; this measure was adopted because there is no monitoring data in these areas and because they are upstream of the other stations, the values obtained were not representative.

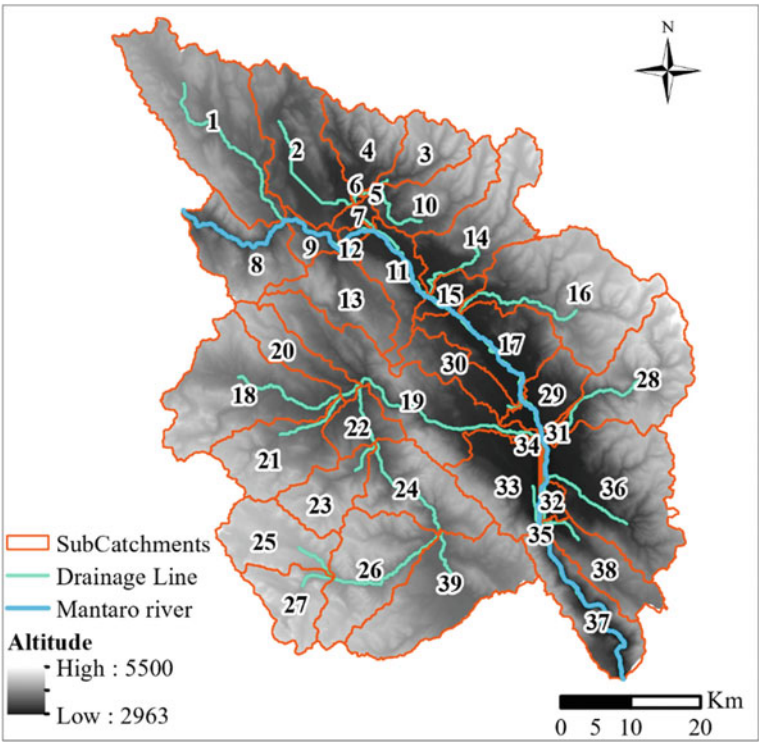


**Fig. 2.2** Study area division into subcatchments

## 2.3 Results and Discussion

### *2.3.1 Correlation Coefficients*

Figure 3a shows a strong positive significant correlation between Pb and Cd ($\rho = 0.58$, $p = 0.001$) and the BOD5 and COD ($\rho = 0.62$, $p = 0.001$), while there is a strong negative significant correlation between $NO^{3-}$ and the variables DO ($\rho = -0.61$, $p = 0.001$), BOD5 ($\rho = -0.62$, $p = 0.001$), and Cd ($\rho = -0.57$, $p = 0.001$) for the dry season. Figure 3b shows a moderately strong positive correlation between COD and BOD5 ($\rho = 0.48$, $p = 0.001$), Fe and the variables Pb ($\rho = 0.47$, $p = 0.001$) and COD ($\rho = 0.35$, $p = 0.001$).

and a strong correlation with Mn ($\rho = 0.63$, $p = 0.001$). Finally, TP has a moderately strong positive correlation with the variables Fe ($\rho = 0.41$, $p = 0.001$), Mn ($\rho = 0.41$, $p = 0.001$), COD ($\rho = 0.41$, $p = 0.001$), and negatively with the metal Cd ($\rho = -0.39$, $p = 0.001$) and the variable DO ($\rho = -0.41$, $p = 0.001$) for the wet season.

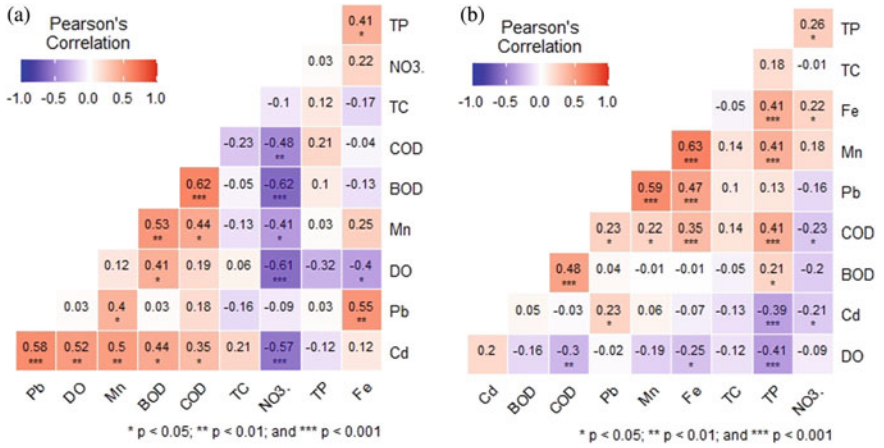


**Fig. 2.3** Correlation matrix of water quality parameters in dry season (**a**) and wet season (**b**)

### *2.3.2 Spatio-Seasonal Variation*

**Physico-chemical parameters**. The DO presents higher average values in the wet season, the maximum value in both seasons is focused on the most populated areas of the Middle sub-basin, considering that the wastewater in the area does not have a WWTP, they are still above the PEQS (4 mg/L) (see Fig. 4a, b).

The concentrations of TP and $NO^{3-}$ increase as the altitude decreases, which is where the agricultural activity begins, even so, the concentrations of nitrates are below the limit values (VL) recommended by the FAO (TP = 2 mg/L, nitrates = 5 mg/L) (FAO 2022), on the contrary, the TP exceeds them in both seasons.

Subcatchment 28, which is where the city of Huancayo, the main urban area, is located, shows TP concentrations twice as the LV (see Fig. 4c, d). $NO^{3-}$ have higher values in the dry season in the area of the Cunas River just before it joins the Mantaro River (Subcatchment 19), understanding this for the potential runoff and the use of fertilizers in agriculture and a lower flow that generates a lower dilution capacity (see Fig. 4e, f); in all cases a lower concentration and below the LV is seen after the only WWTP in the area (Subcatchment 33). (Custodio et al. 2021b) conducted a study at the end of the wet season from 2017 to 2019 in the Cunas river, they found average values of 6.02 mg/L and 0.065 mg/L of DO and TP, respectively, and a maximum value of 1.79 mg/L of the nitrate parameter in 2019, showing lower results than the present study for the last two parameters and a similar result for DO.

The BOD5 and COD values exceed the PEQS (BOD5 = 15 mg/L, COD = 40 mg/L) in the subcatchments located around the urban area and agricultural area, having BOD5 concentrations 8 and 6 times higher in the wet and dry season respectively, and in the case of COD, 7 and 5 times higher in the wet and dry seasons (see Fig. 5a, b). (Custodio et al. 2021b) found average values of 10.22 mg/L for the BOD5

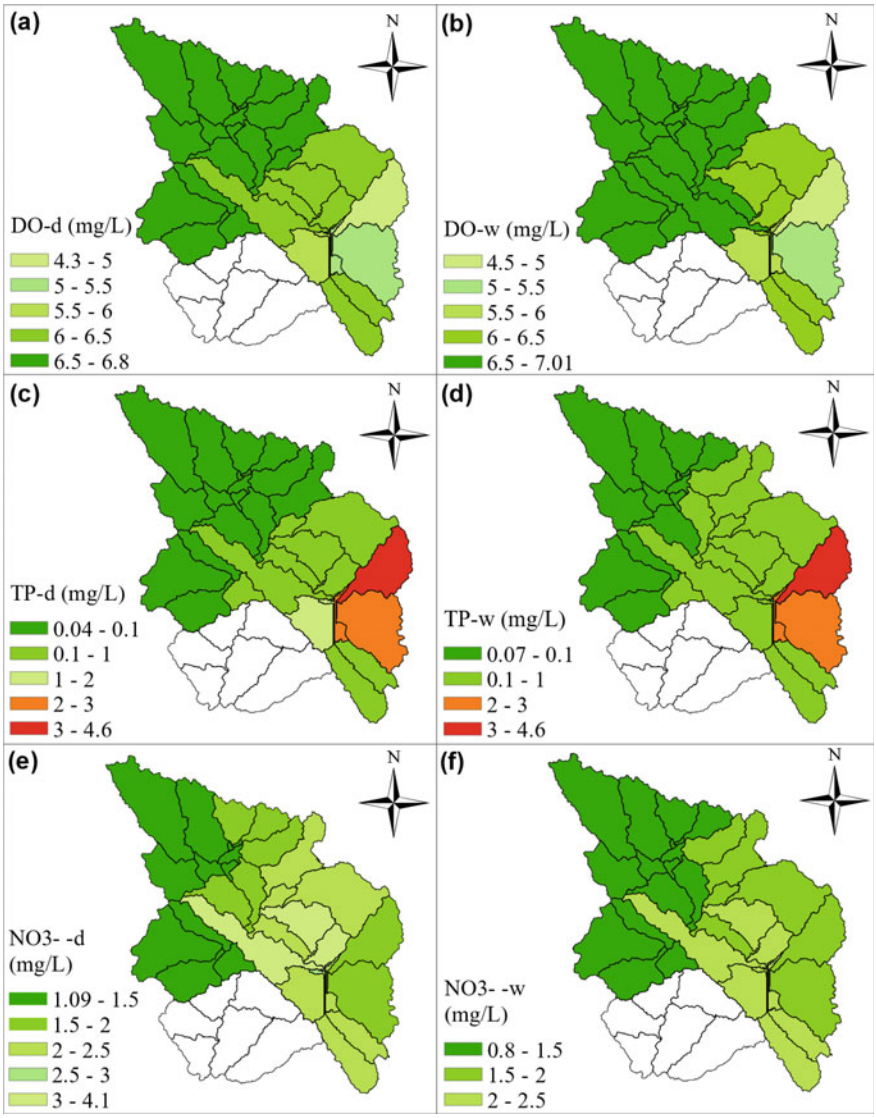


**Fig. 2.4** Spatial distribution of Dissolved Oxygen, Total Phosphorous and nitrates in dry and wet season (left and right side, respectively)

parameter in the wet season, a concentration that is within the range of our study for the Shullcas River.

These values are related to the lack of municipal wastewater treatment plants in one of the main cities of central Peru. The high values of organic matter are also linked to the direct discharge of wastewater from slaughterhouses in the Shullcas, Mantaro, Achamayo and Chanchas rivers and the presence of dumps (National Water

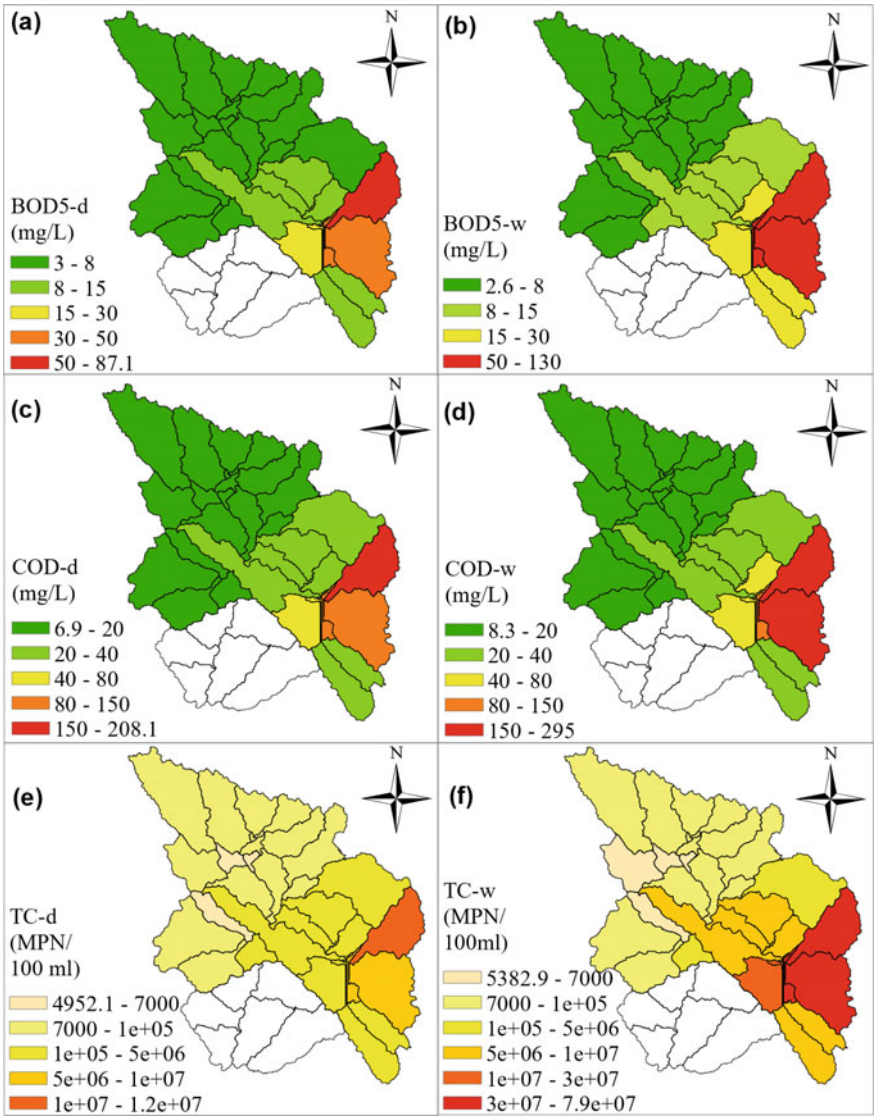


**Fig. 2.5** Spatial distribution of BOD5, COD and TC in dry and wet season (left and right side, respectively)

Authority 2015) that in the wet season generate a greater amount of leachate that enters the Mantaro river.

**Microbiological Parameter**. The concentrations of thermotolerant coliforms do not meet the PEQS values (1000 MPN/100 ml) in any of the subcatchments, reaching excessive values of 79,000,000 MPN/100 ml in the wet season, almost 7 times more

than in the dry season (see Fig. 5e, f). The WNA has identified polluting sources of domestic and municipal wastewater in almost all the districts of the study area (National Water Authority 2022), a fact that generates conflict with all the economic activities in the zone, especially those of direct use and without water treatment such as agriculture.

**Heavy Metals**. The mean concentrations of Mn exceed the PEQS (0.2 mg/L) in the northern and highest part of the study area, as well as in the urban area in the dry season, with maximum values of 0.47 mg/L. The dry season has higher values, but the wet season covers more subcatchments that do not comply with the standard (see Fig. 6a, b). Fe values do not violate the Peruvian law (5 mg/L) in any of the cases; however, unlike Mn, there is an increase in the wet season in both, the north and the south of the study area. Like Fe, the average concentrations of Cd do not violate Peruvian regulations (0.01 mg/L), higher values can be seen in the upper and lower parts of the Mantaro River in the wet season and in the lower part in the dry season (see Fig. 2.6c–f).

The average concentrations of Pb fail to comply with the PEQS (0.05 mg/L) in the wet season with a maximum value of 0.055 mg/L, in both seasons there are higher values in the lower part of the Mantaro River (see Fig. 7a, b). Custodio et al. (2020) reported maximum values of 0.5 mg/L and 0.0045 mg/L of Fe and Pb in the Mantaro River located in the Jauja sector in the wet season, Custodio et al. (2021b) found average values of 1.57 mg/L of Fe and in the year 2020, Custodio et al. (2021a) reported an average value of Fe and Pb of 0.42 mg/L and 0.0065 mg/L, respectively, in the agricultural sector, and of 0.34 and 0.0063 mg/L in the urban sector, being in all cases concentrations below what was found in the study.

The NWA has not identified natural or anthropogenic polluting metal mining sources in the study area (National Water Authority 2022); and despite this, the values of heavy metals exceed the recommended standards. Chira (2021) states that the main cause of the presence of heavy metals is the metallurgical activity of La Oroya, which is located upstream (upper Mantaro sub-basin). Although this activity has directly generated poor water quality for many years, in the 2015–2021 period it can be seen that the highest concentrations of these metals are not found in the initial part of the middle sub-basin, so other activities could be causing this problem.

These concentrations can be explained by the presence of mining deposits, not yet in operation, in the sub-basins where high concentrations of heavy metals have been found, these deposits contain the following metals: Pb, Zn, Cu, Fe, Mn (Junin Regional Technical Commission 2015) that could be naturally contributing these values. Similarly, accumulations of Pb and Fe have been reported in the soils of Jauja and Concepcion, areas that collide with the Mantaro River, with Pb values that exceed the PEQS for soil. This has been generated as a consequence of mining and metallurgical activities of the Upper Sub-basin, and to a lesser degree by industrial waste, use of agrochemicals and urban effluents (Custodio et al. 2021c), which may be a possible source of water contamination. Chira (2021) indicates that there is sufficient statistical evidence to correlate the Cd content in the water and in the soil of the Mantaro Basin. Likewise, 4 non-metallic mining discharges have been identified into the Mantaro River in subcatchment 8 (northern zone), mainly of travertine

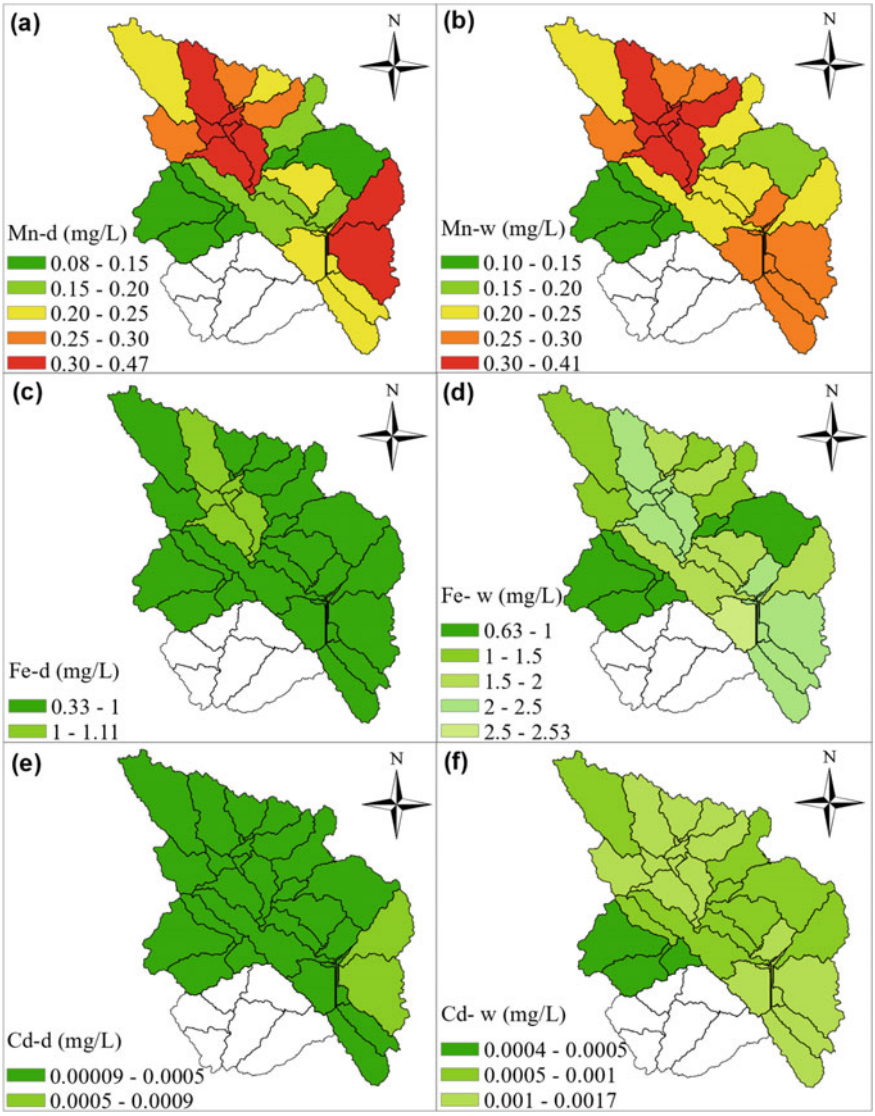


**Fig. 2.6** Spatial distribution of Mn, Fe and Cd in dry and wet season (left and right side, respectively)

(Carpio and Chong 2018) and because its composition includes considerable percentages of Mn and Fe, the non-metallurgical activity could be contributing concentrations of heavy metals, added to this, mining liabilities have been reported in the highest parts of subcatchments 1, 2, 10, 14, 28, and in the lowest parts of subcatchments 17, 32 and 36 (National Water Authority 2015).

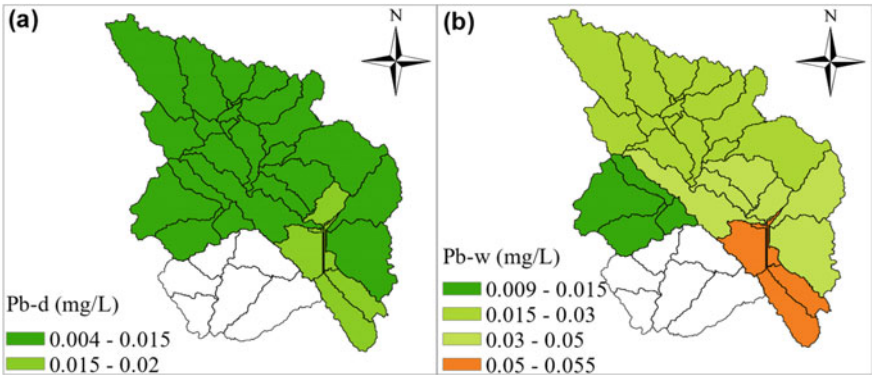


**Fig. 2.7** Spatial distribution of Pd in dry and wet season (left and right side, respectively)

Considering that there are 19,742 agricultural water use rights for surface water from the Shullcas, Mantaro, Cunas, Consac, Chanchas and Achamayo rivers, 2,696 from the Mantaro river, concentrated in subcatchments 11 and 17, and having a farm activity that plans to increase areas with access to irrigation from surface water sources (National Water Authority 2021), it is important to reanalyze the current state of water quality in the Middle Mantaro Sub-basin and generate better control and care of our resource.

## 2.4 Conclusions and Recommendations

The Middle Mantaro Sub-basin presents poor water quality between 2015 and 2021. The main parameters that exceed Peruvian and FAO environmental regulations in the dry season are: total phosphorus, BOD5, COD, thermotolerant coliforms and Mn, and in the wet season: total phosphorus, BOD5, COD, thermotolerant coliforms, Mn and Pb. Concentrations were higher in the wet season for all parameters except for Mn, nitrates and TP. The most affected subcatchments by physical–chemical parameters are 10, 28, 36, 32, 31, 35, 29, 33, 34, 37, 38, which is where the urban area is concentrated; the most affected by the microbiological parameter are all, and by heavy metals are 27, the: 1, 2, 8, 9, 4, 5, 6, 3, 12, 7, 11, 13, 10, 14, 19, 30, 17, 29, 28, 31, 32, 33, 34, 35, 36, 37, 38, the latter being the ones that generate the greatest concern. The sources of contamination for the physical–chemical and microbiological parameters focus on municipal, domestic, slaughterhouse wastewater, dumps and agricultural activities, while for heavy metals they are found in mining liabilities, mining deposits, non-metallic mining, and agrochemicals.

## References

Carpio M, Chong M (2018) Prospecting for rock and industrial mineral resources in the Junin region. INGEMMET, Lima

Chira J (2021) Geochemical dispersion of heavy metals and their impact on the soils of the Mantaro river basin, department of Junín-Peru. Rev Del Inst Investig La Fac Minas, Metal y Ciencias Geográficas 24:47–56

Correa S, Mello C, Chou S, Curi N, Norton L (2016) Soil erosion risk associated with climate change at Mantaro River basin, Peruvian Andes. CATENA 147:110–124

Custodio M, Peñaloza R, Alvarado J, Chanamé F, Maldonado E (2021a) Surface water quality in the mantaro river watershed assessed after the cessation of anthropogenic activities due to the covid-19 pandemic. Polish J Environ Stud 30:3005–3018

Custodio M, Peñaloza R, Chanamé F, Hinostroza-Martínez J, De la Cruz H (2021b) Water quality dynamics of the Cunas River in rural and urban areas in the central region of Peru. Egypt J Aquat Res 47:253–259

Custodio M, Peñaloza R, Ochoa S, Cuadrado W (2021c) Human risk associated with the ingestion of artichokes grown in soils irrigated with water contaminated by potentially toxic elements, Junin, Peru. Saudi J Biol Sci 28:5952–5962

Custodio M, Peñaloza R, Espinoza C, Peralta-Ortiz T, Ordinola-Zapata A, Sánchez-Suárez H, Vyera-Peña E (2020) Data on the concentration of heavy metals and metalloids in lotic water of the Mantaro river watershed and human risk assessment. Peru Data Br 30:105493

FAO (2022) Water quality for agriculture. https://www.fao.org/3/t0234e/T0234E01.htm#ch1.4. Last accessed 28 Feb 2022

Junin Regional Technical Commission (2015) Descriptive memory of the geological study of Junin department at a scale of 1:100000. In: Junin Regional Technical Commission (ed) Economic and ecological zoning of the Junin region. Junin Regional Government, Junin, pp 64–65

Magesh N, Elango L (2019) Spatio-temporal variations of fluoride in the groundwater of Dindigul District, Tamil Nadu, India: a comparative assessment using two interpolation techniques. In: Yong S (ed) GIS Geostatistical Techn Groundwater Science, vol 1. Elsevier, Goa, pp 283–296

Ministry of the Environment (2022) G-DEM Aster. https://geoservidorperu.minam.gob.pe/geoservidor/download_raster.aspx. Last accessed 26 April 2022

National Water Authority (2012) Water resources in Peru, 1st edn. National Water Authority, Lima

National Water Authority (2015) Identification of pollution sources in the Mantaro basin. National Water Authority, Lima, pp 15–52

National Water Authority (2015) Water quality in hydrographic basins at the national level. National Water Authority, Lima, p 213

National Water Authority (2020) Water resources management plan in the Mantaro basin: "Baseline", 1st edn. National Water Authority, Lima

National Water Authority (2021) Water resources management plan in the Mantaro basin. National Water Authority, Lima

National Water Authority (2022) Observatorio del agua. https://snirh.ana.gob.pe/observatorio SNIRH/. Last accessed 26 Feb 2022

Sharma V, Sharma M, Pandita S, Kumar V, Kour J, Sharma N (2020) Assessment of water quality using different pollution indices and multivariate statistical techniques. In: Kumar V, Sharma A (eds) Heavy metals in the environment, vol 1. Elsevier, Jammu and kashmir, pp 165–178

Silva Y, Takahashi K, Chávez R (2008) Dry and wet rainy seasons in the Mantaro river basin (Central Peruvian Andes). Adv Geosci 14:261–264

# Chapter 3
# The Amazon of Central Europe—the Drava River


**Lovorka Gotal Dmitrovic**

**Abstract** The area near the Drava River is characterized by great biodiversity, geodiversity and landscape diversity, as well as a rich cultural and traditional heritage. The Drava River with its tributaries is among the last natural lowland rivers in Central Europe. Wet habitats, which are among the most endangered in Europe, are particularly important. According to its characteristics, it can be compared with the Amazon River. In order to protect the Drava River, a multi-day continuous survey was conducted, during which samples of the Drava River water were collected in laminar and turbulent currents. Statistically processed data show how the concentration of organic matter, ammonia, nitrite and phosphate changes throughout the course of the Drava River in the Republic of Croatia. The Drava River is also the backbone of the UNESCO Transboundary Biosphere Reserve "Mura – Drava – Danube", which is the largest European protected river area (700 km) and the world's first pentalateral (Croatia, Austria, Hungary, Slovenia and Serbia) UNESCO Biosphere Reserve. In addition, the project area and its surroundings contain the largest freshwater reservoir in Croatia.

**Keywords** Organic matter · Ammonia · Nitrates · Phosphates

## 3.1 Basic Characteristics of Drava River

### *3.1.1 Geographical and Hydrological Characteristics*

The Drava is a Central European river with a total catchment area of 42.238 km$^2$, it originates in South Tyrol (near Lake Dobiaco) in Italy, from where it continues to flow eastward through the Austrian province of Kärnten (Carinthia). After that, it flows through Slovenia, then Croatia, and then forms the Croatian-Hungarian border. Considering the volume of the catchment area, the Drava is one of the most important tributaries of the Danube (Trockner and Uehlinger 2009).

L. Gotal Dmitrovic (✉)
University North, University Center Varazdin, Krizaniceva 31, 42000 Varazdin, Croatia
e-mail: lgotaldmitrovic@unin.hr



Z. Yang (ed.), *Environmental Science and Technology: Sustainable Development*,
Environmental Science and Engineering, https://doi.org/10.1007/978-3-031-27431-2_3

In the east of Croatia, it separates from the border and turns south-east into the depths of Croatia, where near the town of Aljmas, it flows into the Danube. The total length of the Drava is 725 km, and its source is located at 1.175 m above sea level. It is a rainy-glacial regime with a small amount of water in winter and a large amount in late spring and early summer.

The Drava enters Croatia near the village of Dubrava Križovljanska, at an altitude of 197 m and ends at the confluence with the Danube near Aljmaš at an altitude of 82 m. The total height difference from the entrance to Croatia to the confluence is 105 m and the length of the river is 323 km (Čuljak 2017).

At the entrance to Croatia, the average flow of the Drava is 315 $m^3$/s at Botovo after the mouth of the largest tributary of the Mura, 530 $m^3$/s and at the mouth of the Danube, 580 $m^3$/s. A total of 22 hydropower plants were built on the Drava River. On its course through Croatia, the Drava was dammed three times upstream from the mouth of the Mura, and 19 times before entering Croatia (11 in Austria, 8 in Slovenia) (Grlica 2008).

### *3.1.2 Habitats*

The Drava River hosts a variety of habitats, including some which are among the most threatened in Europe: alluvial forests, wet grasslands, gravel islands and sand banks, side-arms, steep banks, oxbow lakes, stagnant backwaters, abandoned riverbeds and meanders. Floodplain forests, together with an extensive network of various floodplain water bodies and their typical vegetation are widely distributed in the entire area. However, both habitat types are at risk due to river regulation in the past, riverbed deepening and water level decrease.

Pioneer habitats like gravel, sand and muddy banks are widely distributed within the entire area, in particular on the upper, more dynamic part in North Croatia. Due to river regulation, riverbed deepening, water level decrease and reduced sediment dynamics in the last 100 years, pioneer habitats were reduced by about 92% and steep dynamic banks by about 80% (Adria 2022).

### *3.1.3 Flora and Fauna*

The Drava is home to numerous animal species, especially birds. The gravel and sand banks are a key habitat for gravel and sand breeding birds, such as the little tern (*lat. Sterna albifrons*), the common tern (*lat. Sterna hirundo*), the common sandpiper (*lat. Actitis hypoleucos*) and the little ringed plover (*lat. Charadrius dubius*). The natural steep river banks are home to the sand martin (*lat. Riparia riparia*), the bee-eater (*lat. Merops apiaster*) and the kingfisher (*lat. Alcedo atthis*). The White-tailed eagle (*lat. Haliaeetus albicilla*) and black stork (*lat. Ciconia nigra*) are also present in the

area. All these birds are at risk, as their populations are decreasing due to the loss of habitat and habitat quality.

The Drava also hosts the greatest fish biodiversity in Croatia, with 70 recorded fish species. Five of these species are endemic to the Danube basin: the Danube salmon (*lat. Hucho hucho*), the danubian roach (*lat. Rutilus pigus*), the balon's ruffe (*lat. Gymnocephalus baloni*), the schraetzer (*lat. Gymnocephalus schraetser*) and the streber (*lat. Zingel streber*). In addition, the sterlet (*lat. Acipenser ruthenus*) and the nearly extinct ship sturgeon (*lat. Acipenser nudiventris*), which was recorded two times in the Drava during the last decade, can also be found here. Out of the 70 recorded species, 38 were included in the Red Book of Freshwater Fish, including: the ziege (*lat. Peleceus cultratus*), the asp (*lat. Aspius aspius*), the weather loach (*lat. Misgurnus fossilis*) and the European mudminnow (*lat. Umbra krameri*). The Drava is also home to the beaver (*lat. Castor fiber*), which was extinct in most of Europe, during the second half of the 19th Century and the otter (*lat. Lutra lutra*).

Lastly, also large numbers of amphibians (for example: the Danube crested newt (*lat. Triturus dobrogicu*), the European fire-bellied toad (*lat. Bombina bombina*) and the European tree frog (*lat. Hyla arborea*)) and insects (for example: the dragonflies (*lat. Odonata*) and the green snaketail (*lat. Ophiogomphus cecilia*)) live here (Adria 2022).

## 3.2 Protected Areas Along the Drava River in the Republic of Croatia

There are 14 protected areas along the Drava River in the Republic of Croatia in the following categories: special reserve—ornithological (Veliki Pažut (near the mouth of the Mura and Drava) and Podpanj (near the mouth of the Drava and Danube), regional park (Mura—Drava—covers 87.448.52 ha of the upper reaches of the Drava River), natural monument—botanical (poplars in the Drava Forest near the city of Varaždin and oaks near 214 $m^2$), six significant landscapes, park-forest and two monuments of park architecture.

### *3.2.1 Natura 2000*

Natura 2000 is a network of nature protection areas in the territory of the European Union. It is made up of Special Areas of Conservation and Special Protection Areas designated under the Habitats Directive and the Birds Directive, respectively.

In May 1992 the governments of the European Communities adopted legislation designed to protect the most seriously threatened habitats and species across Europe. The Habitats Directive complements the Birds Directive adopted earlier in 1979 and together they make up the Natura 2000 network of protected areas (Abran 2000).

The Drava River area is part of the European ecological network Natura 2000. The Drava and the areas along the Drava are defined not only as Natura 2000 protection areas, but also as protected areas and natural features. Along the Drava River (including the river itself) there are 12 ecological network areas, namely 8 conservation areas important for species and habitat types and 4 conservation areas important for birds (Public Institution for the Management of Protected Nature Areas of Varaždin County 2022).

### *3.2.2 UNESCO Cross-Border Biosphere Reserve "Mura—Drava—Danube"*

The Drava River is also the backbone of the UNESCO Transboundary Biosphere Reserve "Mura—Drava—Danube". which is the largest European protected river area (700 km) and the world's first pentalateral (Croatia, Austria, Hungary, Slovenia and Serbia) UNESCO Biosphere Reserve. In addition, the project area and its surroundings contain the largest freshwater reservoir in Croatia.

## 3.3 Research of the Water Quality of the Drava River in Croatia Its Course in Laminar and Turbulent Flow

### *3.3.1 Data Collection*

In laminar flow, all particles in the same fluid layer have the same speed, that is, all fluid layers move parallel and the fluid necessarily moves slowly. When the speed increases, the layers mix and the flow becomes turbulent. According to the variability of the speed, there is a difference between: stationary flow, in which the amount of matter that passes through each section is constant and non-stationary flow, in which this amount changes. Depending on whether vortices are created during the flow, there is a difference between eddy flow and potential flow. The flow is eddy if eddies are created and if eddies are not created, the speed of the flow can be represented using the so-called potential function, so such a flow is called potential (Bansal 2010).

At the same place (same river kilometer), a water sample of the Drava River was sampled at:

1. laminar, non-stationary, potential flow;
2. turbulent, non-stationary, eddy flow on larger river kilometers to potential flow on river kilometers closer to the mouth of the Danube.

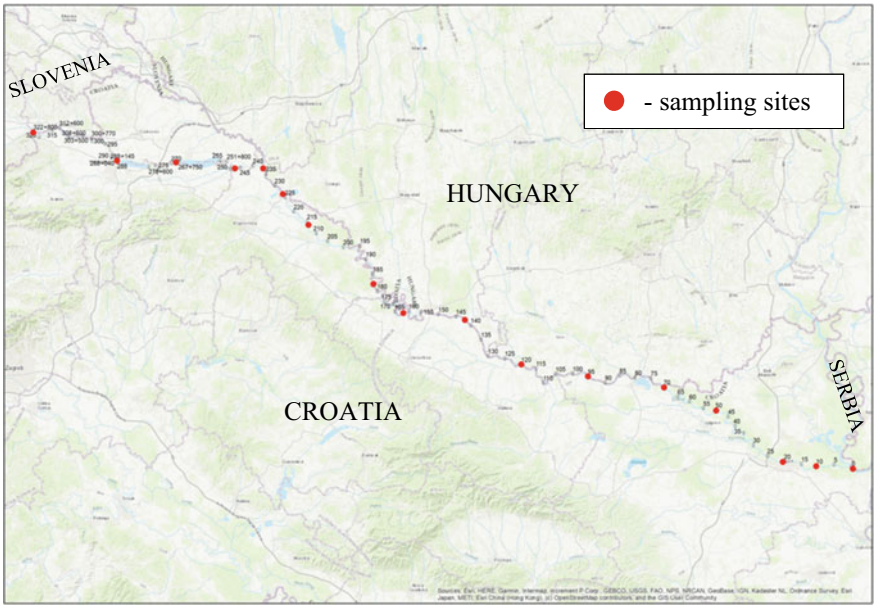


**Fig. 3.1** The Drava river in Croatia

The sampling sites were on river kilometers (see Fig. 3.1):

- 320 rkm (entrance to the Republic of Croatia).
- 288 rkm (near the Varaždin—the second largest city on the Drava River).
- 268 rkm (at the exit from the wastewater treatment system of the city of Varaždin).
- 226 rkm (the mouth of the Mura river into the Drava).
- 214 rkm (near nature monument—botanical).
- 182 rkm.
- 172 rkm (Križnica—here the Drava makes meanders in a small area, in large bends. The Drava is crossed by a scaffold and there is no land connection except for the hanging pedestrian bridge, which was built in 1967/68 year in a length of 250 m. The old course of the Drava River and stagnant water are habitats for many species of fish. Križnica is rich in endangered and protected bird species).
- 162 rkm.
- 142 rkm (near the small city of Virovitica).
- 120 rkm (municipal Sopje).
- 95 rkm.
- 70 rkm.
- 50 rkm (place Nard in the small city of Valpovo).
- 20 rkm (a suburb of the city of Osijek—the largest Croatian city on the Drava).
- 10 rkm.
- 0 rkm (the mouth of the Drava river into the Danube).

From 320 rkm (the entrance of the Drava to the Republic of Croatia) to 268 rkm, sampling was done from the bridge, that is, the shore. After 268 rkm, the Drava River becomes navigable, so sampling was carried out by descent with stops. The test lasted 5 days.

### 3.3.2 *Statistical Data Processing*

At each sampling point, 3 samples were collected. The values of the arithmetic mean are shown in Table 3.1.

The system of functions that describe the dependence of the concentration of organic matter along the coast ($y_{OMc}$) and middle of the stream ($y_{OMs}$) on the sampling location (x) can be shown on the part of the "fast" Drava (1, 2) (Fig. 3.2) and the "slow" Drava (3, 4) (Fig. 3.3).

$$y_{OMc1} = 0.0066\,x^2 - 3.4349\,x + 484.206 \tag{3.1}$$

**Table 3.1** The arithmetic mean

| | Organic matter (mg/l) | | Ammonia (μg/l) | | Nitrites (μg/l) | | Phosphates (mg/l) | |
|---|---|---|---|---|---|---|---|---|
| rkm | Along the coast | Middle of the stream | Along the coast | Middle of the stream | Along the coast | Middle of the stream | Along the coast | Middle of the stream |
| 320 | 46.00 | 45.00 | < 10 | < 10 | 26.67 | 24.33 | 0.45 | 0.14 |
| 288 | 43.67 | 59.67 | < 10 | < 10 | 14.00 | 18.00 | 0.15 | 0.29 |
| 268 | 58.33 | 56.33 | 30.33 | 138.33 | 159.00 | 186.33 | 0.23 | 0.13 |
| 226 | 29.00 | 36.00 | < 10 | < 10 | 15.00 | 16.00 | 0.58 | < 0.05 |
| 214 | 56.50 | 50.50 | 37.00 | 67.00 | < 10 | 7.00 | < 0.05 | < 0.05 |
| 182 | 51.00 | 51.00 | < 10 | < 10 | < 10 | < 10 | < 0.05 | < 0.05 |
| 172 | 69.00 | 97.00 | < 10 | < 10 | < 10 | < 10 | 0.08 | < 0.05 |
| 162 | 135.00 | 118.67 | 37.00 | 76.00 | 8.00 | < 10 | < 0.05 | < 0.05 |
| 142 | 126.33 | 136.33 | 27.00 | 8.00 | < 10 | < 10 | < 0.05 | < 0.05 |
| 120 | 137.33 | 140.66 | 125.00 | 12.00 | 12.67 | 10.00 | < 0.05 | < 0.05 |
| 95 | 26.33 | 32.00 | 8.67 | < 10 | < 10 | < 10 | < 0.05 | < 0.05 |
| 70 | 42.00 | 29.33 | 60.33 | < 10 | 81.00 | < 10 | < 0.05 | < 0.05 |
| 50 | 37.00 | 34.00 | 49.00 | < 10 | 9.00 | 16.00 | < 0.05 | < 0.05 |
| 20 | 143.33 | 115.33 | < 10 | < 10 | < 10 | < 10 | 0.04 | 0.04 |
| 10 | 119.33 | 116.33 | < 10 | < 10 | 9.33 | < 10 | 0.11 | 0.09 |
| 0 | 117.00 | 110.33 | < 10 | < 10 | < 10 | < 10 | 0.10 | 0.09 |

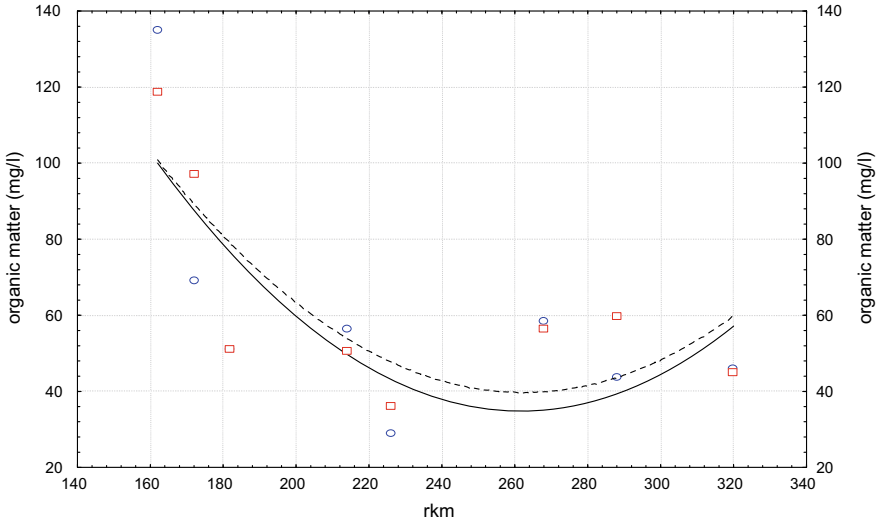


**Fig. 3.2** Organic matter in "fast" Drava (square/dashed line = middle of the stream; circle/solid line = along the coast)

$$y_{OMs1} = 0.0061\,x^2 - 3.1859\,x + 457.6625 \tag{3.2}$$

$$y_{OMc2} = 0.0141\,x^2 - 2.1398\,x + 135.7517 \tag{3.3}$$

$$y_{OMs2} = 0.0129\,x^2 - 1.8863\,x + 121.5789 \tag{3.4}$$

The system of functions that describe the dependence of the concentration of ammonia along the coast ($y_{Ac}$) and middle of the stream ($y_{As}$) on the sampling location (x) can be shown on the part of the "fast" Drava (5, 6) (Fig. 3.4) and the "slow" Drava (7, 8) (Fig. 3.5).

$$y_{Ac1} = -0.0012\,x^2 + 0.5079\,x - 35.0219 \tag{3.5}$$

$$y_{As1} = -0.0058\,x^2 + 2,7482\,x - 271.0664 \tag{3.6}$$

$$y_{Ac2} = -0.0064\,x^2 + 1.3414\,x - 10.5061 \tag{3.7}$$

$$y_{As2} = 0.0054\,x^2 - 0.5717\,x + 6.5084 \tag{3.8}$$

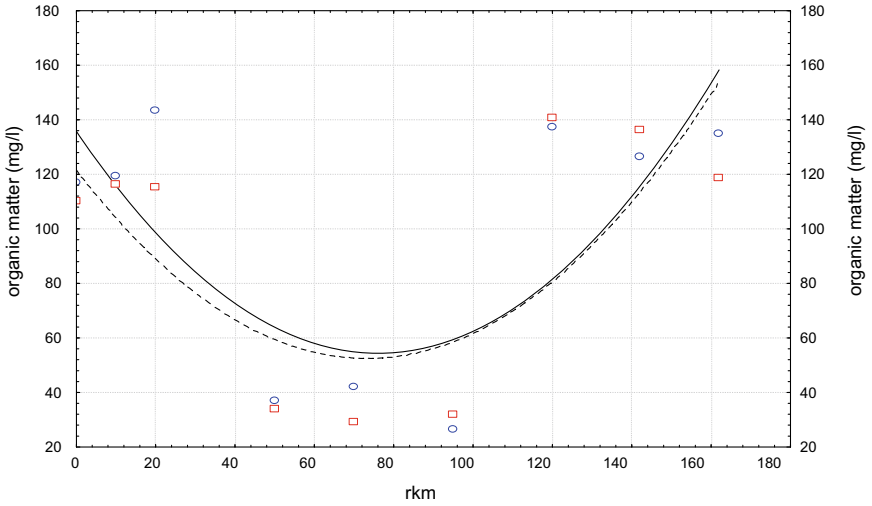


**Fig. 3.3** Organic matter in "slow" Drava (square/dashed line = middle of the stream; circle/solid line = along the coast)

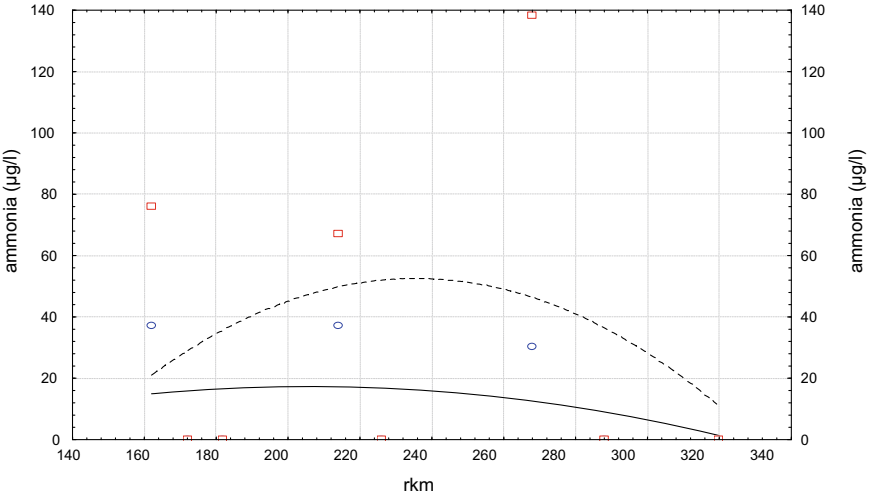


**Fig. 3.4** Ammonia in "fast" Drava (square/dashed line = middle of the stream; circle/solid line = along the coast)

The system of functions that describe the dependence of the concentration of nitrites ions along the coast ($y_{Nc}$) and middle of the stream ($y_{Ns}$) on the sampling location (x) can be shown on the part of the "fast" Drava (9, 10) (Fig. 3.6) and the "slow" Drava (11, 12) (Fig. 3.7).

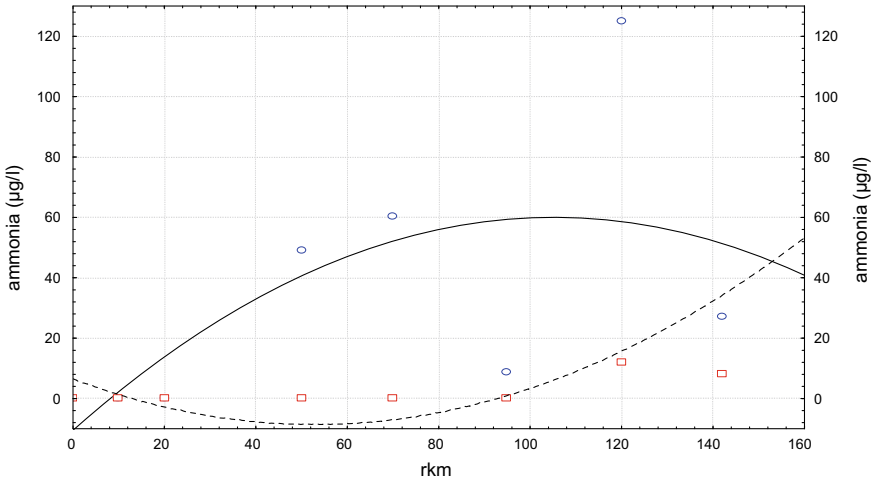


**Fig. 3.5** Ammonia in "slow" Drava (square/dashed line = middle of the stream; circle/solid line = along the coast)

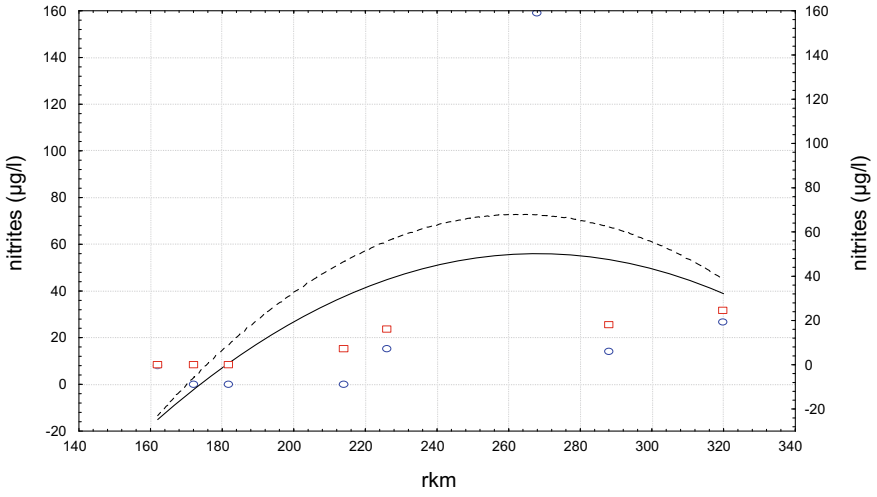


**Fig. 3.6** Nitrites in "fast" Drava (square/dashed line = middle of the stream; circle/solid line = along the coast)

$$y_{Nc1} = -0.0063\,x^2 + 3.3889\,x - 398.0679 \tag{3.9}$$

$$y_{Ns1} = -0.009\,x^2 + 4.7051\,x - 550.2901 \tag{3.10}$$

$$y_{Nc2} = -0.0046\,x^2 + 0.7294\,x - 0.997 \tag{3.11}$$

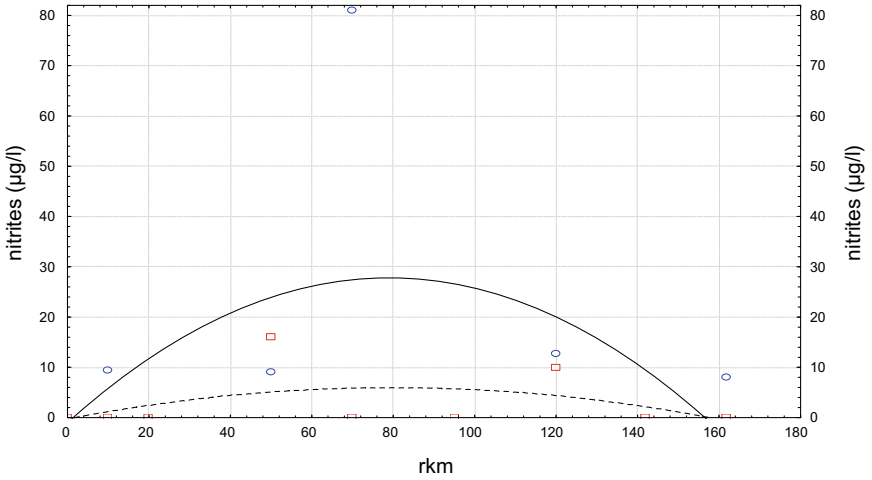


**Fig. 3.7** Nitrites in "slow" Drava (square/dashed line = middle of the stream; circle/solid line = along the coast)

$$y_{Ns2} = -0.001\,x^2 + 0.1564\,x - 0.2696 \tag{3.12}$$

The system of functions that describe the dependence of the concentration of phosphate concentration along the coast ($y_{Pc}$) and middle of the stream ($y_{Ps}$) on the sampling location (x) can be shown on the part of the "fast" Drava (13, 14) (Fig. 3.8) and the "slow" Drava (15, 16) (Fig. 3.9):

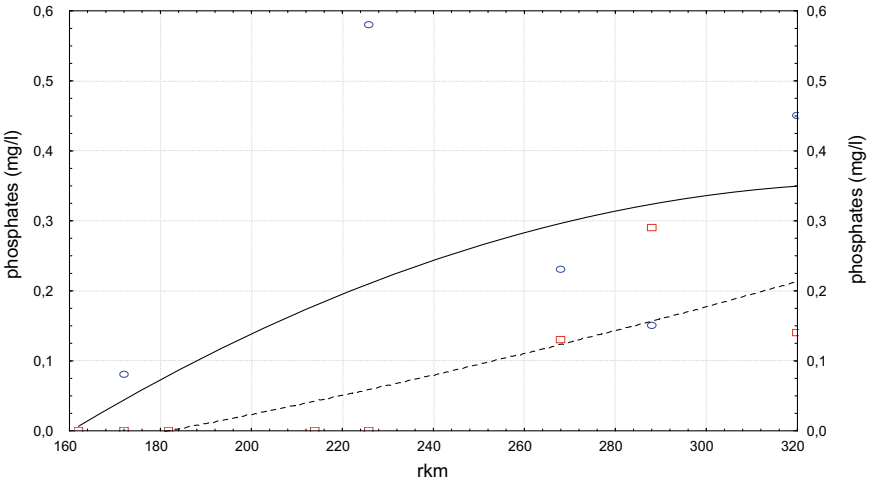


**Fig. 3.8** Phosphates in "fast" Drava (square/dashed line = middle of the stream; circle/solid line = along the coast)

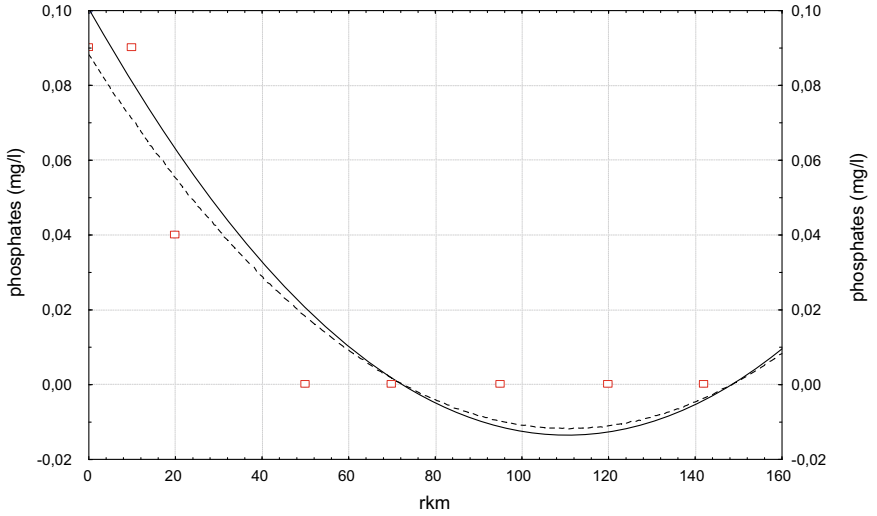


**Fig. 3.9** Phosphates in "slow" Drava (square/dashed line = middle of the stream; circle/solid line = along the coast)

$$y_{Pc1} = -1.0845 \cdot 10^{-5} x^2 + 0.0074 x - 0.9082 \tag{3.13}$$

$$y_{NP1} = 2.171 \cdot 10^{-6} x^2 + 0.0005 x - 0.1543 \tag{3.14}$$

$$y_{Pc2} = 9.3635 \cdot 10^{-6} x^2 - 0.0021 x + 0.1005 \tag{3.15}$$

$$y_{Ps2} = 8.1793 \cdot 10^{-6} x^2 - 0.0018 x + 0.0882 \tag{3.16}$$

Organic matter in both laminar and turbulent motion, and in "fast" and "slow" flow of the Drava forms a convex function. In the case of ammonium ion pollution in the "fast" flow of the Drava in both laminar and turbulent motion, the function is concave, and in the "slow" Drava flow, the function becomes convex in turbulent motion.

With nitrite contamination, all functions are concave. In the case of phosphate pollution in the "fast" Drava Stream in laminar motion, the function is concave, while in the case of turbulent flow, the function is convex. In "slow" flow both functions are convex.

Based on the obtained functions, a computer model can be developed to predict the level of pollution.

## 3.4 Conclusion

Mountains are often responsible for most of the transported material and are often a strong regulatory control on the ecological features of river reaches and lowland floodplains. The Amazon River is an example of this phenomenon. Its murky waters, extensive and highly productive whitewater floodplains are mainly the result of events from the distant Andean mountain ranges. The diversity of organisms can be attributed to adjustments to the annual and perennial cycles of sediment and mineral nutrients transport from the Andes. The Amazon is rich in flora and fauna, as well as floodplains (Čuljak 2017).

In Europe, one of the largest natural rivers is the Drava River, which also flows through the mountains and descends into the lowlands, forming floodplains, backwaters, sandbars and marshes. What also connects these two lowland rivers is the way they shape the landscape they pass through, as well as the meaning they have for the local population, but primarily the wealth of flora and fauna that make them stand out. Both rivers have their origin in the highlands or mountains, both rivers are rich in meanders, they flood their lowlands with fertile sediment. With their natural dynamics, these rivers create a whole range of habitats—from land to water with all transitions. This is what makes them stand out and this is their specialty and the reason for the wealth of plant and animal life. Few areas have such diverse and preserved habitats as these two rivers, the Amazon and the Drava. The habitats are not separated from each other and there are healthy ecosystems and food chains where a large number of species live. All of the above, along with other similarities, gives us the right to call the Drava River the Central European Amazon and to protect it from pollution.

## References

Abran P (2012) Forest management in the Natura 2000 ecological network in Romania—present problems and perspectives. Revista pădurilor 127(1):21–27

Bansal RK (2010) A textbook of fluid mechanics and hydraulic machines. Laxmi Publications Ltd, pp 163–165

Čuljak A (2017) Drava River: Central European Amazon (cro. Rijeka Drava: srednjoeuropska Amazona). https://www.linkedin.com/pulse/rijeka-drava-srednjoeuropska-amazona-alen-culjak. Last accessed 20 Sept 2022

Grlica I (2008) Study of the biological diversity of the Drava River—Drava dead backwaters and separate backwaters, part II. (cro. Studija biološke raznolikosti rijeke Drave—Dravske mrtvice i odvojeni rukavci II dio.) "Drava" Natural History Society (cro. Prirodoslovno društvo "Drava") pp 5–8

Public Institution for the Management of Protected Nature Areas of Varaždin County (2022) Mura-Drava-Danube Regional Park - working material

Trockner K, Uehlinger U, Robinson CT (eds) (2009) Rivers of Europe. Elsevier/Academic Press, San Diego, USA

WWF Adria (2022) Drava Life—integrated river management. https://www.drava-life.hr/en/project/. Last accessed 30 Sept 2022

# Chapter 4
# Development of a Type-2 Fuzzy Bi-level Programming Model Coupling MCDA Analysis for Water Resources Optimization Under Uncertainty


**Ruolin Bai, Lei Jin, Bin Zhuo, Hai Yan Fu, Jing Liu, and Hui Bin Guo**

**Abstract** In view of the contradiction of water use among water use departments, the optimal allocation of water resources can be effectively solved and the efficient utilization of water resources can be realized. The goal of this study is to combine the interval type-2 fuzzy algorithm with bi-level programming (BP) method, propose a type-2 fuzzy bi-level model (T2FBL), and apply it to the water resources planning system in the southern Fujian Province. The main innovations and contributions of this study is that a new type-two fuzzy bilayer model (T2FBL) is proposed by combining type-two fuzzy theory with BP method and applied to water resources planning. The new model balances the needs of decision-makers (DMs) at different levels in southern Fujian Province. The upper level decision aims to maximize the overall social benefit of the region by minimizing the regional water shortage, while the lower level decision focuses on achieving the economic benefit goal by improving the net benefit of regional water supply. The MCDA method is adopted to further analyze the results of water resources allocation. In the future direction, water supply to the service industry can be strengthened. Ideally, 73.79% water supply to the tertiary industry can achieve a scenario with the maximum target benefit. T2FBL model can obtain the results of water resources allocation among different agricultural, industrial and tertiary industries, and reveal the relationship between various competitive users. These findings can provide an in-depth understanding of the interaction between agricultural, industrial and tertiary industry water allocation and provide technical support for water resource planning issues.

**Keywords** Type-2 fuzzy sets · Bi-level programming · MCDA · Water resources

R. Bai · L. Jin (✉) · B. Zhuo · H. Y. Fu · J. Liu · H. B. Guo
Key Laboratory of Environmental Biotechnology (XMUT), Fujian Province University, Xiamen University of Technology, Xiamen 361024, China
e-mail: jinl@xmut.edu.cn



Z. Yang (ed.), *Environmental Science and Technology: Sustainable Development*, Environmental Science and Engineering, https://doi.org/10.1007/978-3-031-27431-2_4

## 4.1 Introduction

With the rapid development of social economy, the contradiction between the increase of human's demand for water and the decrease of water supply is becoming more and more prominent. In view of the contradiction of water use among water use departments, the optimal allocation of water resources can be effectively solved and the efficient utilization of water resources can be realized (Zhou et al. 2017). In the 1970s, D. H. Murks proposed linear decision programming for water resources systems, and Joeres (Joeres et al. 1971) applied linear programming theory to Baltimore's multi-source water supply research. After a long period of continuous research, the optimal allocation method of water resources gradually tends to mature.

Generally, decision making problems are often compounded by uncertainties related to benefits/costs, water availabilities, environmental capacities and objectives (Huang et al. 1993; Li et al. 2008; Yeomans 2008). Many methods have been proposed to handle uncertainties existing in water resources management systems (Zhang et al. 2017; Zhang and Guo 2016). To reflect the tradeoff between two decision-making levels with different concerns, the bi-level programing (BP) approach with a two-level structure was developed for supporting regional water policies formulation (Camacho-Vallejo et al. 2015). A leader-follower decision-making strategy was incorporated into the optimization process of BP to generate satisfied decision-making plan for both the upper-level and the lower-level decision makers. When dealing with a system problem, different decision-makers (DMs) generally have different perspectives and starting points, which leads to conflicts in the design of ideal solutions for certain variables. Although the BP algorithm can effectively balance the needs of decision-makers at different levels, it has limitations in representing uncertain parameters in the planning system. Therefore, different types of fuzzy numbers, interval numbers and BP linear programming can be combined to address the uncertainty in the system, and a suitable algorithm can be used to convert the fuzzy number and interval number into clear values and obtain an effective optimization plan (Ma et al. 2016).

Zadeh (Chen 2013) proposed type-2 fuzzy sets (T2FSs) whose membership grades themselves are type-1 fuzzy sets (T1FSs). As an extension of T1FSs, T2FSs are characterized by primary and secondary membership functions, which can provide greater freedom and flexibility for DMs to better express their uncertain judgments (Chen and Lee 2010). Although T2FS owns a wide range of advantages, it is usually accompanied by high computational difficulty, which results in its low practicality. Currently, trapezoidal interval type-2 fuzzy set (TrIT2FS) (Srinivasan and Geetharamani 2016), as a special form of T2FS, has been extensively applied to fuzzy decision making problems. Hence, this paper employs TrIT2FSs to represent the pairwise comparisons (PCs) of objects and the evaluations of alternatives on criteria.

Therefore, the goal of this study is to combine the interval type-2 fuzzy algorithm with BP method, propose a T2FBL model, and apply it to the water resources planning system in the southern Fujian Province, and analyze and suggest the water resources situation in the southern Fujian Province under the application analysis of MCDA

(Multiple Criteria Decision Analysis). The main innovations and contributions of this study are as follows: (1) a new T2FBL model is proposed by combining type-two fuzzy theory with BP method and applied to water resources planning. (2) The new model balances the needs of decision-makers at different levels in southern Fujian Province. The upper level decision-makers aim to maximize the overall social benefit of the region by minimizing the regional water shortage, while the lower level decision-makers focus on achieving the economic benefit goal by improving the net benefit of regional water supply. (3) By collecting the regional water resources data of the Minnan region of Fujian Province from 2016 to 2020, the water resources utilization situation of the three locations was analyzed. (4) T2FBL model can obtain the results of water resources allocation among different agricultural, industrial and tertiary industries, and reveal the relationship between various competitive users. (5) The MCDA method was used to further analyze the water resources allocation results.

## 4.2 Methodology

### *4.2.1 Bi-level Programming Model*

Bi-level programming is a mathematical optimization model with a two-level hierarchical structure. The upper and lower level problems have their own objective functions and constraints. The objective function and constraints of the upper-level problem are not only related to the upper-level decision variables, but also depend on the optimal solution of the lower-level problem, which in turn is affected by the upper-level decision variables. It can simultaneously consider the interests of both the global and the individual, ensure that the global is first and the local is second, and the final decision result is often a mutually coordinated scheme between all layers, which can well solve complex practical problems (Lv et al. 2009). The general form of bi-level programming model is as follows:

$$\begin{cases} \min f_u(x, y), \\ \min f_l(x, y), \end{cases}$$
$$s.t.\ A(x, y) \leq B, i = 1, 2, \ldots, m \tag{4.1}$$

x is the upper decision variable. y is the lower level decision variable; $f_u$ (x, y) is the upper objective function of the model. $f_l$ (x, y) is the lower objective function of the model. A (x, y) is the constraint condition.

IT2FN is introduced into the bi-level programming model, and the uncertainty parameters in the model are represented by interval type-2 fuzzy numbers. The type-2 fuzzy bilevel model can be expressed as follows:

$$\begin{cases} \min f_u(x, y), \\ \min f_1(x, y) \end{cases}$$
$$s.t.\, \tilde{A}(x, y) \leq \tilde{B}, i = 1, 2, \ldots, m \tag{4.2}$$

where $\tilde{A}$ and $\tilde{B}$ are the IT2FNs and $\overset{\sim}{\leq}$ represents the fuzzy sorting relationship between the left and right sides of the equation.

### 4.2.2 Type 2 Fuzzy Sets

Let X be the universe of discourse. A type-2 fuzzy sets (T2FSs) $\overset{\sim}{\mathrm{A}}$ can be represented by the type-2 membership function $\mu_{\tilde{A}}(x, u)$ such that:

$$\tilde{A} = \{(x, u), \mu_{\tilde{A}}(x, u) | x \in \mathrm{X}, \mathrm{u} \in [0, 1]\} \tag{4.3}$$

The IT2FSs are usually taken in some simplified formations in applications (Aviso et al. 2010). As shown in Fig. 4.1. Let $\overset{\sim}{\mathrm{A}} = [\mathrm{A^L}, \mathrm{A^U}]$ be IT2FS on X. Let $\overset{\sim \mathrm{L}}{\mathrm{A}} = (\mathrm{a_2^L}, \mathrm{a_3^L}, \alpha_\mathrm{L}, \beta_\mathrm{L})$ and $\overset{\sim \mathrm{U}}{\mathrm{A}} = (\mathrm{a_2^U}, \mathrm{a_3^U}, \alpha_\mathrm{U}, \beta_\mathrm{U})$ be the lower and upper trapezoidal fuzzy number, respectively, with respect to $\overset{\sim}{\mathrm{A}}$ defined on the universe of discourse X, where $a_2^L \leq a_3^L \cdot a_2^U \leq a_3^U \cdot \alpha_L, \alpha_U \geq 0$, and $\beta_L, \beta_U \geq 0$, $[a_3^L, a_3^L]$ is the core of $\tilde{A}^L$, and $\alpha_L, \beta_L \geq 0$ are the left-hand and right-hand spreads and $[a_2^U, a_3^U]$ is the core of $\tilde{A}^U$, and $\alpha_U, \beta_U \geq 0$ are the lefthand and right-hand spreads. The membership functions of x in $\tilde{A}^L$ and $\tilde{A}^U$ are expressed as follows:

$$\underline{u}_{\tilde{A}}(x) = \begin{cases} \frac{(x - a_2^L + \alpha_L)}{\alpha_L}, & a_2^L - \alpha_L \leq x \leq a_2^L, \\ 1, & a_2^L \leq x \leq a_3^L, \\ -\frac{(x - a_3^L - \beta_L)}{\beta_L}, & a_3^L \leq x \leq a_3^L + \beta_L, \\ 0, & otherwise, \end{cases} \tag{4.4}$$

$$\overline{u}_{\tilde{A}}(x) = \begin{cases} \frac{(x - a_2^U + \alpha_U)}{\alpha_U}, & a_2^U - \alpha_U \leq x \leq a_2^U, \\ 1, & a_2^U \leq x \leq a_3^U, \\ -\frac{(x - a_3^U - \beta_U)}{\beta_U}, & a_3^U \leq x \leq a_3^U + \beta_U, \\ 0, & otherwise, \end{cases} \tag{4.5}$$

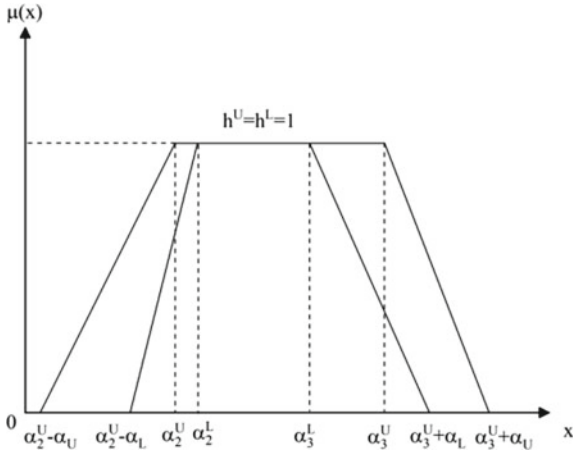


**Fig. 4.1** The upper membership function $\tilde{A}^U$ and the lower membership function $\tilde{A}^L$ of IT2FS $\tilde{A}$

### *4.2.3 Multiple Criteria Decision Analysis (MCDA)*

A Multi Criteria Decision Analysis (MCDA), is a decision-making analysis that evaluates multiple (conflicting) criteria as part of the decision-making process. MCDA resembles a cost–benefit analysis, but with the notable advantage of not being solely limited to monetary units for its comparisons. When making comprehensive or important decisions, multiple criteria and levels of scale need to be accounted for. Analytic hierarchy process (AHP) is a commonly used MCDA method. The AHP is a method that provides a choice between different alternatives (strategies, investments, etc.) based on a series of criteria or variables, which are usually in conflict. The method consists of the following steps.

The starting points are the different possible alternatives that a decision maker faces, shown in Fig. 4.2. The criteria used to make the selection are then specified. Once the alternatives are known and the criteria have been defined, the relative importance of each criterion is determined and weighed. Taking into account the criteria and their weights, the different alternatives are assessed obtaining n matrices, as many as the criteria. From each one of them, the eigenvector is calculated which will show the weight of the alternative as a function of each criterion. From the two previous processes two additional matrices are obtained. A column matrix n $\times$ 1 with the weights for the criteria (for n criteria) and another matrix m $\times$ n formed by the weights of the different alternatives taking into account all the criteria and their importance. The product of both matrices will produce a matrix that will prioritize the different alternatives taking into account all the criteria and their importance.

The result is a matrix w showing the relative importance of each alternative. This figure is the one that allows the ranking of all alternatives from least to most desirable, and quantifies the interest of each alternative with respect to the others as a function of all criteria and their importance, therefore allowing us to choose the best.

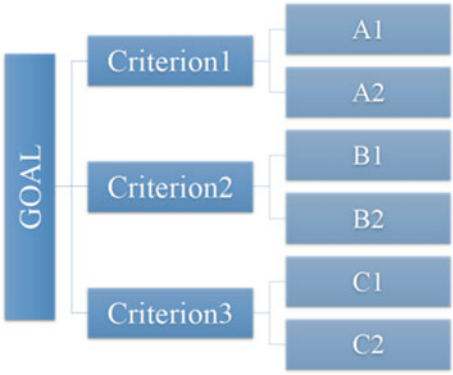


**Fig. 4.2** Graphical representation of a hierarchy

## 4.3 Application

### *4.3.1 Statement of Problem*

The Southern Fujian Triangle is located on the southeast coast of Fujian Province, between the Jiulong River, the largest river system in the province, and the Jinjiang River, the third largest river system. Xiamen, Quanzhou and Zhangzhou belong to the southern Fujian region, which faces Taiwan across the sea and is the central part of the economic zone on the west coast of the Straits. It connects the Jiulong River and Jinjiang River basins together, so that Xiamen, Quanzhou and Zhangzhou occupy a unique position in the town system of southern Fujian. As shown in Fig. 4.3. Jiulong River is the second largest river in Fujian Province, second only to Minjiang River. The total area of Xia, Quan and Zhang is 25,180 $km^2$, accounting for 20.98% of the province. In 2020, the GDP of southern Fujian reached 2108.829 billion Yuan, accounting for 48.03% of Fujian Province, and has become the "locomotive" of Fujian Province's economic development.

However, Xiamen, Quanzhou and Zhangzhou are areas with water scarcity. With the further development of economy, how to protect water resources and rationally allocate water resources is the key to the development of this region. The optimal allocation of water resources in the water receiving area will have a positive impact on the social economy, ecological environment and sustainable utilization of water resources in the region.

### *4.3.2 Interval Type-2 Fuzzy Bi-level Programming Model*

There are three sources of water supply in Fujian Province, which are: surface water supply, underground water supply and other water supply, and surface water supply is divided into water supply from storage projects, water supply from diversion projects


**Fig. 4.3** Study area

and water supply from lifting projects. The water use in Fujian Province is mainly divided into three categories according to different uses, namely: agricultural water, industrial water and domestic water.

According to the requirements of sustainable development, the optimal allocation model of water resources should be a multi-objective model including social, economic and ecological environment. According to the characteristics of water resources system in southern Fujian, social benefits and economic benefits are selected as objective functions, and corresponding constraints are established. Three cities in southern Fujian are regarded as K sub-regions with N public water sources, I(k) independent water sources and J(k) water use departments, and the corresponding objective functions are established.

(1) Social benefit objectives. The minimum regional total water shortage is adopted to indirectly reflect social benefits:

$$\min f_1(x) = \sum_{k=1}^{K} \sum_{j=1}^{J} \left( D_j^k - \sum_{i=1}^{I} x_{ij}^k \right) \tag{4.6}$$

where $D_j^k$ is the water demand of j users in k sub-areas; $x_{ij}^k$ is the water supply from water source i to user j in subzone k.

(2) Economic benefit objectives. It is expressed as the largest net benefit generated by regional water supply:

$$\max f_2(x) = \sum_{k=1}^{K} \sum_{j=1}^{J} \sum_{i=1}^{I} \left( b_{ij}^k - c_{ij}^k \right) x_{ij} \tag{4.7}$$

where $x_{ij}$ is the water supply from source i to user j; $b_{ij}^k$ and $c_{ij}^k$ are the unit water supply benefit coefficient and water supply consumption coefficient of water source i to user j in subarea k, respectively.

For the above objective functions, the relevant constraints are established.

(1) Constraint of water supply.

$$\sum_{j=1}^{J} x_{ij}^k \le W_i^k \tag{4.8}$$

where $W_i^k$ is the water supply from source I to subarea K.

(2) Water demand capacity constraints of users.

$$D_{\min}^{k'} \le \sum_{j=1}^{J} \sum_{i=1}^{I} x_{ij}^k \le D_{\max}^k \tag{4.9}$$

where $D_{\min}^{k'}$ and $D_{\max}^k$ are the minimum and maximum water demand of k subareas, respectively.

(3) Water transmission capacity constraint of water transmission system.

$$x_{ij}^k \le Q_{i\max}^k \tag{4.10}$$

where $Q_{i\max}^k$ is the maximum water transfer capacity of the source to the K subareas.

**Table 4.1** Input the water demand of each sub-district under different water use sectors

| | Water demand from 2016 to 2020 | | | |
|---|---|---|---|---|
| | Agriculture | Industry | Tertiary industry | Sum of max values |
| Xiamen | (1.016, 1.680) | (0.936, 1.788) | (1.608, 3.048) | 6.516 |
| Quanzhou | (6.336, 12.684) | (6.656, 18.720) | (3.392, 5.676) | 37.080 |
| Zhangzhou | (8.968, 16.104) | (2.720, 8.724) | (1.792, 2.976) | 27.804 |

**Table 4.2** Input the economic benefit values of each subdistrict under different water use sectors

| | Economic benefits from 2016 to 2020 | | | |
|---|---|---|---|---|
| | Agriculture | Industry | Tertiary industry | Sum |
| Xiamen | 19.0 | 1584.5 | 1053.0 | 2656.5 |
| Quanzhou | 24.5 | 473.5 | 644.5 | 1142.5 |
| Zhangzhou | 35.5 | 403.0 | 578.5 | 1017 |

(4) Non-negative constraints on variables.

$$x_{ij}^{k} \geq 0 \tag{4.11}$$

As shown in Tables 4.1 and 4.2, the statistical data were entered into the model.

## 4.4 Results and Discussion

### *4.4.1 Results Analysis*

Under different satisfaction levels, there are some changes in the regional water shortage and the net benefits of regional water supply. As shown in Fig. 4.4. When the satisfaction level is 0.9, the water shortage is the smallest and the total amount of available water resources is maximized, which maximizes the net benefits of water supply in southern Fujian, which is 1,951.172 billion yuan. When the satisfaction is 0.2, the total water shortage increases to 10.28146 billion $m^3$ and the net benefit of water supply decreases to 17,550.56 billion yuan, indicating that the value of satisfaction is inversely proportional to the risk of water shortage. This means that the higher the satisfaction level, the closer the total amount of available water is to the minimum. The lower the satisfaction level, the closer the total available water resources are to the maximum value of the statistics.

Figure 4.5 shows the overall water supply structure in southern Fujian under different planning periods and satisfaction levels. When the satisfaction level is the highest, the proportion of agricultural water use in the three cities is the lowest and the proportion of industrial water use is the highest. With the decrease of satisfaction,

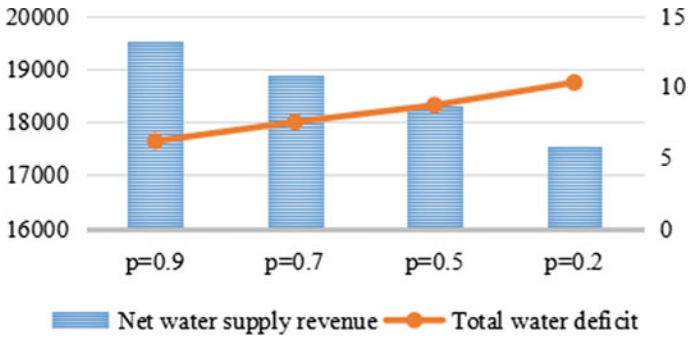


**Fig. 4.4** Regional changes in water scarcity and net benefits of water supply

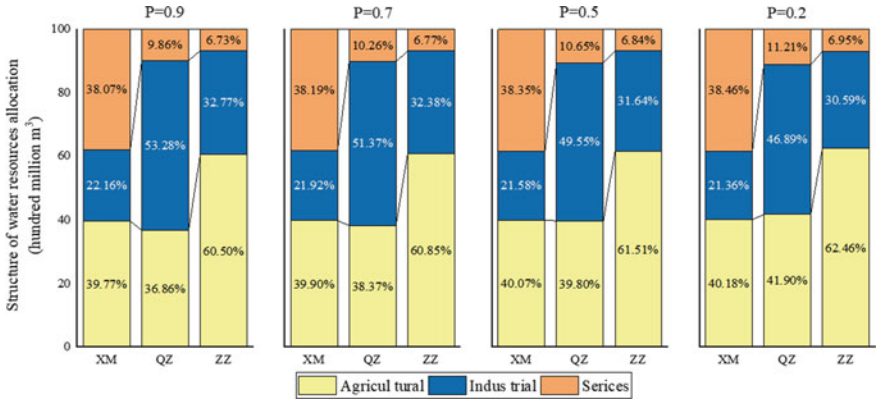


**Fig. 4.5** Water distribution structure in each city in three industries at different α-cut

the proportion of agricultural water use gradually increased, while the proportion of industrial water use decreased. This means that when the water scarcity is minimum, the benefit is highest and the optimal allocation is reached, the benefit from industrial water is greater than that from agricultural water. The government departments in southern Fujian should control the proportion of industrial water consumption, focusing on adjusting the industrial structure and developing high-tech industries.

According to the observation data, when the satisfaction is 0.9, the optimal water allocation of Quanzhou is the closest to the statistical data, so it can be concluded that the water allocation structure of Quanzhou is relatively excellent. The proportions were 9.86, 53.28 and 36.86% respectively. It is the highest proportion of industrial water among the four satisfaction levels. Moreover, due to the development of industry, the economic benefits of industrial water allocation are gradually increasing, which means that the water resources needed to increase the same industrial output value as in the past are gradually decreasing.

This phenomenon also reflects the gradual development of Fujian's industrial industry in the direction of environmental protection and high technology. The tertiary industry and domestic water use generally showed a downward trend, indicating that the development of Fujian's service industry also showed an upward trend year by year. Another factor related to this phenomenon is that government departments pay attention to saving water and have made a series of policies to save water. With the increase of available water resources, the overall water resources planning structure has no obvious fluctuation, only the industrial water consumption shows an upward trend. The reason is that the economic benefit of industrial water distribution is more prominent than that of tertiary industry and agriculture. The model would prioritize allocating more water to industry to maximize economic benefits.

### *4.4.2 Discussion Based on MCDA*

Contributions to solving complex natural resource issues can come from pooling expert opinion, using the Delphi method (Miller 1984). This technique brings together diverse expert opinion on specific, unresolved issues, with the goal of achieving agreement–as close to consensus as possible while respecting minority views. The Delphi method is adopted to value the weights.

The proportion of agricultural output value to gross domestic product is an important index to measure the development stage of agricultural industry. Generally speaking, the summary of expert data shows that the proportion of agriculture in economically developed countries and regions is less than 10%, the proportion of industrial manufacturing is 20–30%, and the proportion of service industry is more than 60%. According to the Delphi method, the weight distribution of agricultural, industrial and service standards under the objective of economic benefits is carried out, and the judgment matrix is generated, and the consistency test is carried out to obtain CR < 1, the ratio of economic benefits of the three is 9.45, 16.76 and 73.79%. This provides a development idea for the water supply structure in southern Fujian. While ensuring the water supply and economic benefits, more water supply will be used to develop the service industry, industry and construction industry, so that the city can achieve the goal of faster economic development while ensuring the quality of life of residents.

## 4.5 Conclusion

In this paper, a bi-level planning method based on T2FBL is proposed to optimize the water resources planning system. T2FBL method comprehensively considers the interests of decision makers at different levels, and uses two kinds of fuzzy ranking algorithms to solve the uncertainty in water resources planning. This method can not only reflect the degree of risk corresponding to uncertain parameters in the system,

but also balance the interest demand between two levels of decision makers. The new model balances the needs of decision-makers at different levels in southern Fujian Province. The upper level decision-makers aim to maximize the overall social benefit of the region by minimizing the regional water shortage, while the lower level decision-makers focus on achieving the economic benefit goal by improving the net benefit of regional water supply. The weight analysis of the data results was carried out through MCDA, and finally the following results were obtained:

(i) Southern Fujian gives priority to adjusting the industrial water supply structure, focuses on adjusting the industrial structure, develops high-tech industries, and greatly alleviates the water pressure.
(ii) This paper adopts T2FBL to calculate the uncertain parameters in the system. As the α-cut decreases and the total amount of water available to the system increases, the concomitant water shortage risk also increases. In this study, water resources allocation schemes under different satisfaction levels in three cities were calculated.
(iii) This paper adopts MCDA to conduct weighted analysis on the data results, and concludes that the future direction of developing into a developed city can strengthen the water supply to the service industry, and 73.79% water supply to the tertiary industry can achieve a scenario with the maximum target benefit.

**Acknowledgements** This work was funded by Fujian provincial industry-university research collaborative innovation (2021Y4005), Fujian Natural Science Foundation (2021J011176), Youth Program of Fujian Provincial Social Sciences Foundation of China (FJ2020C010).

## References

Aviso KB, Tan RR, Culaba AB et al (2010) Bi-level fuzzy optimization approach for water exchange in eco-industrial parks. Process Saf Environ Prot 88(1):31–40

Camacho-Vallejo JF, Gonzalez-Rodriguez E, Almaguer FJ, Gonzaez-Ramirez RG (2015) A bi-level optimization model for aid distribution after the occurrence of a disaster. J Clean Prod 105:134–145

Chen TY (2013) An interactive method for multiple criteria group decision analysis based on interval type-2 fuzzy sets and its application to medical decision making. Fuzzy Optim Decis Mak 12:323–356

Chen SM, Lee LW (2010) Fuzzy multiple attributes group decision-making based on the interval type-2 TOPSIS method. Expert Syst Appl 37:2790–2798

Huang GH, Baetz BW, Patry GG (1993) A Gray fuzzy linear-programming approach for municipal solid-waste management planning under uncertainty. Civ Eng Syst 10(2):123–146

Joeres EF, Liebman JC, Revelle CS (1971) Operating rules for joint operation of raw water sources. Water Res Res 7(2):225–235

Li YP, Huang GH, Xiao HN (2008) Municipal solid waste management under uncertainty: an interval-fuzzy two-stage stochastic programming approach. J Env Inform 12(2):96–104

Lv YB, Wan ZP, Hu TS (2009) A two-tier planning model for optimal allocation of water resources. Syst Eng Theory Pract 29(6):115–120

Ma X, Ma C, Wan Z, Wang K (2016) A fuzzy chance-constrained programming model with type 1 and type 2 fuzzy sets for solid waste management under uncertainty. Eng Optim 496:1040–1056

Miller A (1984) Professional collaboration in environmental management: the effectiveness of expert groups. J Environ Manage 19:365–388

Srinivasan A, Geetharamani G (2016) Linear programming problem with interval type 2 fuzzy coefficients and an interpretation for its constraints. J Appl Math 2016

Yeomans JS (2008) Applications of simulation-optimization methods in environmental policy planning under uncertainty. J Env Inform 12(2):174–186

Zhang D, Guo P (2016) Integrated agriculture water management optimization model for water saving potential analysis. Agric Water Manag 170:5–19

Zhang C, Li M, Guo P (2017) An interval multistage joint-probabilistic chance-constrained programming model with left-hand-side randomness for crop area planning under uncertainty. J Clean Prod 167:1276–1289

Zhou WK, Li JD, Jin CC (2017) Study on the optimal allocation of regional water resources based on multi-objective planning model. Water Technol Econ 23(6):51–56

# Part II
# Urban Design, Ecological Planning and Sustainable Development

# Chapter 5
# Ecological Remediation Technology and Landscape Optimization System Design Based on Improving Landscape Water Pollution

**Chengqi Xu and Juanjuan Zhang**

**Abstract** The current stage, with the development of social economy and the deepening of the urbanization process, people consume a large amount of mineral, forestry and water resources, the discharge into the natural environment of a large amount of waste water, waste gas and harmful substances, caused serious destruction of ecological environment, that some animals and plants has become extinct, and threaten the survival of mankind. In order to be able to find a balance between human development and natural ecological environment, and the natural harmonious coexistence, in this paper, the wetland landscape, for example, standing in the water pollution and the effective governance of the polluted water, the water from the Angle of technology and ecological environmental governance has carried on the thorough analysis, build up a set of computer control as the core of the system maintenance, It is expected to provide reference for the treatment of seriously polluted water bodies in the future.

**Keywords** Water pollution · Ecological restoration technology · Landscape optimization · Ecological environment · The environmental pollution

## 5.1 Introduction

Landscape water remediation technology is a new technology that has been developed worldwide in recent 10 years and has been widely used in the treatment of polluted soil, landscape water and offshore ocean surface. With the rapid development of environmental biotechnology, the scope of research in this field is constantly expanding. Water Treatment Technology has published a paper stating that landscape water remediation technology has become the most effective means to control environmental pollution (Jiewen et al. 2019). At present, the commonly used in landscape

C. Xu (✉)
Department of Hospital Administration, Gansu University of Chinese Medicine, Lanzhou, China
e-mail: xcq80139@21cn.com

J. Zhang
Yuzhong County Liugoudian Primary School, Yuzhong County Education Bureau, Lanzhou, Gansu, China



Z. Yang (ed.), *Environmental Science and Technology: Sustainable Development*, Environmental Science and Engineering, https://doi.org/10.1007/978-3-031-27431-2_5

water body repair technology are mainly constructed wetland technology, biological technology, AFI captive type such as biological floating bed, using the biological method to control pollution of the end product is such as carbon dioxide, water and nitrogen non-toxic harmless substances, therefore, to avoid the secondary pollution to the environment, do real repair of landscape water body.

This study aims to study water pollution. Based on the introduction of current water pollution control and treatment methods, a complementary ecosystem with water environment as the theme and the surrounding ecological landscape as the assistant was constructed by using computer technology. It can control and optimize the water environment and maintain the balance of water environment ecology. This is of great practical significance for the treatment of water pollution.

## 5.2 Environmental Pollution and Ecological Balance

In our current living environment, most of the area there are a lot of due to human caused by the ecological vision problems, although to a large extent can promote human progress continuously, but in this process, people forget the problem a fundamental principle, it is human survival environment and creatures of nature are interdependent. As the top of the food chain, human beings need to constantly obtain the needed energy and materials from the ecological chain, and this process forms a stable cycle. For both nature and human beings, this is a relatively stable internal circulation ecosystem, which is also called ecological balance in biology. However, due to the interference of human behavior and unscrupulous acquisition from the ecology in this cycle system, this stable ecosystem has been gradually broken by human beings (Ruoshui et al. 2016). In ecological system, due to the interaction between biological makes some human pollution behavior can be digested by food chain from the net, but with the continuous development of society, the invasion increasingly serious pollution, and filling self-healing capability has been unable to effectively purify the pollution produced by people, this makes the pollutants in the condition of long-term accumulation, Thus, it has a very serious impact on people's normal life, and the ability of ecological restoration and self-healing cannot restore the ecological environment to its previous appearance. This situation is called environmental pollution.

## 5.3 Water Pollution

As water is the source of life, humans and all organisms in the ecological chain cannot do without water. The distribution of water resources on the earth is shown in Table 5.1 below. Among the environmental pollution, water pollution has the most serious impact on human beings, so water pollution is the most serious pollution problem to be solved at present (Jinzhong et al. 2007). Water environment due to human

**Table 5.1** Distribution of water resources on Earth

| | The total water | | Fresh water | |
|---|---|---|---|---|
| | Volume ($10^4$ $km^3$) | Percentage | Volume ($10^4$ $km^3$) | Percentage |
| The sea water | 133,880 | 96.54 | | |
| The underground salt water | 2340 | 1.69 | | |
| Underground water | 1287 | 0.94 | 1053 | 30.06 |
| Soil water | 1053 | 0.75 | | |
| Glaciers and permanent snow | 1.7 | 0.001 | | |
| Permafrost underwater | 2406 | 1.74 | | |
| Permafrost underwater | 30 | 0.022 | 2406 | 68.68 |
| Salt water lake | 8.5 | 0.006 | 30 | 0.86 |
| Fresh water lake | 9.1 | 0.007 | 9.1 | 0.26 |
| Marsh water | 1.1 | 0.0008 | 1.1 | 0.08 |
| The river water | 0.2 | 0.0002 | 0.2 | 0.006 |
| Biological water | 0.1 | 0.0001 | 0.1 | 0.003 |
| Atmospheric water | 1.3 | 0.001 | 1.3 | 0.04 |

intervention makes suffered severe pollution of water environment, the basic characteristics of water environment pollution in water body changed, leading to water can not be effectively used, will cause serious harm to human body health not only, also aggravated the shortage of water resources, had a great influence on the development of human society. At present, the world consumes about 2,088 $km^3$ of fresh water per year, together with the total amount of water that can be recycled 3300 $km^3$/a, which accounts for about 90% of the global annual total runoff, and the remaining 10% of freshwater flows into the ocean. The focus is on the continuous increase of the world's population and the rapid development of industrial production, people's demand for water is increasing day by day. Moreover, the utilization and distribution of water resources are extremely uneven, and the available water resources are not proportional to the distribution of population. More the main reason lies in man-made water pollution caused by people discharging untreated waste water and wastes into water bodies when using water resources dye. It can be seen that the freshwater resources available for direct human use and easy access are very limited for all countries of the world, as shown in Table 5.2 below. Therefore, water pollution control is the primary goal of environmental protection.

**Table 5.2** World water supply and contaminated water

| Types of water supply | Adopt the total water | | The amount of water is not recovered | | Discharge of sewage | | Polluted natural water | |
|---|---|---|---|---|---|---|---|---|
| | The amount of water ($10^8$ $m^3$) | Percentage | The amount of water ($10^8$ $m^3$) | Percentage | The amount of water ($10^8$ $m^3$) | Percentage | The amount of water ($10^8$ $m^3$) | Percentage |
| Domestic water | 980 | 17.4 | 560 | 39.9 | 420 | 10.0 | 6000 | 10.9 |
| Water power | 2250 | 40.0 | 150 | 10.6 | 2100 | 49.7 | 6000 | 10.9 |
| Industrial water | 2000 | 35.5 | 400 | 28.3 | 1600 | 37.9 | 40,000 | 72.9 |
| Animal husbandry and water | 400 | 7.1 | 300 | 21.2 | 100 | 2.4 | 3000 | 5.5 |
| Total | 5630 | 100 | 1410 | 100 | 4220 | 100 | 55,000 | 100 |

## 5.4 Water Pollution Control and Treatment Methods

### *5.4.1 Control Methods of Water Pollution*

In the treatment of water bodies, the first thing to do is to timely control water pollution (Li 2018; Wan 2016). Only in this way can the accumulation of pollutants be reduced to the maximum, so that the self-healing function of the ecological environment and people's reasonable control can the water pollution be treated.

To control water pollution, people need to use the established municipal and water conservancy engineering system, the combination of maximum to control pollution of water source, subregional, cut off the pollution of rivers, let the pollutants in rivers cannot be accumulated for a long term, so will be able to control water environment pollution degree is no longer intensifying.

### *5.4.2 Treatment Methods of Water Pollution*

In the treatment of water pollution, it is necessary to carry out targeted river water treatment according to different spatial locations. Usually, in situ treatment and ectopic treatment are used to treat river water pollution respectively (See Fig. 5.1).

**Ectopic Management**. The so-called heterotopic treatment method is based on the pollution of the river, to have targeted treatment of the river. Among them, the most important is to use various municipal and water conservancy facilities built by people. The essence of ectopic treatment is to use these engineering facilities to cut off exogenous pollutants and clean up endogenous pollutants in rivers, so as to finally achieve

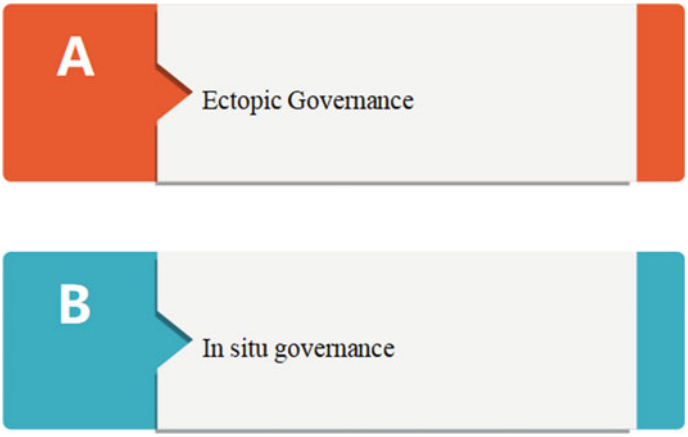


**Fig. 5.1** Treatment of water pollution

the purpose of improving water quality. The so-called exogenous cutoff refers to the use of river tributaries and strict control of water inlet, so that pollutants can be cut off from the source, to ensure that pollutants will not enter the river which has been seriously polluted. Of course, it is impossible to absolutely cut off pollutants from the source, so exogenous treatment is to cut off a large number of pollution sources that the water environment ecosystem cannot purify, so that the water environment ecosystem can effectively self-heal (Haiquan et al. 2021). Endogenous treatment refers to the operation of dredging and improving the water environment for those extremely polluted river courses, so that the water environment can achieve basic ecological self-healing as far as possible. End-source control requires higher requirements for the water conservancy system of the river course. First of all, the whole river shall be blocked in sections so that the river water can go to other watercourses. During this period of closure, the river course shall be cleared and treated at the fastest speed without necessary restoration and reconstruction of the ecological system inside the river course. Combined with the exogenous treatment of pollutants cut off, the river can be re-entered when the river ecosystem is in a good cycle, and the pollution can be self-purification. After the completion of the treatment, it is also necessary to monitor the ecosystem of the river channel and timely adjust the ecological structure inside the river channel, so as to maximize the treatment action to achieve the expected purpose.

**In-situ Treatment**. Although the ectopic treatment method can achieve a purification effect in the short term to some extent, people can not discharge pollutants into the river in the short term because the pollution of water comes from people's life, but in the long term, it will cause serious impact on the development and life of human beings. Therefore, the in-situ treatment method can fundamentally solve the problem of water pollution.

In addition to the traditional dredging treatment methods, we believe that through the overall improvement of the water environment, reduce the water purification load, improve the water self-purification ability, improve the water quality, can achieve the goal of complete control of water pollution (Liuyan et al. 2013). Bioremediation is the core of in-situ management. In simple terms, bioremediation is to repair the damaged water environment and eliminate pollutants in the water environment by using the microorganisms in the water environment and the ecological chain circulation in the water environment under controllable conditions. The main methods of bioremediation are as follows (See Fig. 5.2).

**Increase the Oxygen Content, Put in Microbial Agents**. The main purpose of this method is to change the water, especially the bottom and the bottom of the river water environment of microbial growth environment, through the study of the increase of the oxygen content of the water environment as well as the microbial agents, can quickly produce large quantities of aerobic bacteria, can use the aerobic bacteria for quick decomposition of pollutants in water environment, So as to create a good foundation for the living environment of the organisms in the water.

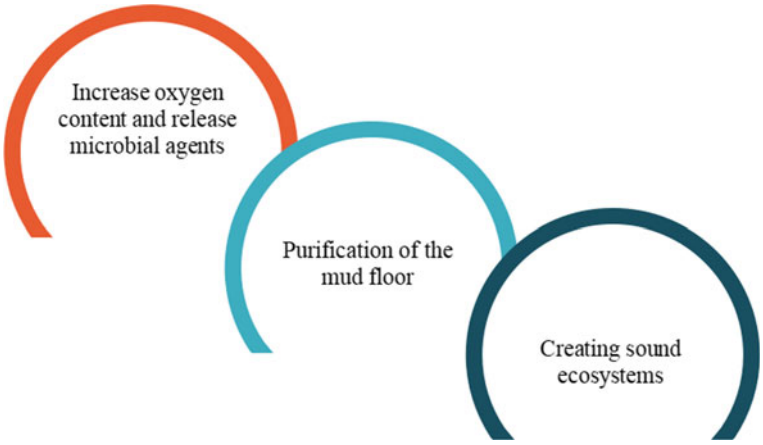


**Fig. 5.2** Bioremediation measures

**Purification of Mud Bottom**. In the long-term polluted river course, a large number of pollutants are accumulated in the mud layer at the bottom of the river course, and due to the influence of these precipitated pollutants, the upper water quality in the water environment is always in a situation of pollution. This is also why the top water purification can not completely change the water quality of the fundamental reason. Although the previous dredging treatment can completely eradicate the pollution sources at the bottom of the river, at the same time, it will also seriously damage the ecological environment in the river. In the short term, the ecological environment inside the river is fragile (Li 2017; Ya 2018). Once the invasion of pollutants, the river will quickly recover to the state before the treatment. And because the ecological chain in the channel has been completely removed, so the black and smelly rivers are created. For the purification of the mud at the bottom of the water environment, still need to use those who can carry on the effective decomposition of microorganism to the pollutant, these microbes can survive in the mud, to complete decomposition of pollutants, and the ability to convert it to become useful to the water environment of the biological survival substance, so you can let the water environment of ecological system is more stable, It can also eradicate the sources of pollution.

**Create a Sound Ecosystem**. In most of the polluted waters, we find that although the ecosystems in them have a certain scale, they are usually relatively fragile due to the biological species and biological chain. Through the long-term pollution of people, these ecosystems are basically on the verge of collapse. Therefore, the establishment of a more perfect water environment ecosystem can solve this problem. Through to the different water environment research, targeted for the perfection of the location of waters ecosystems work, proper move about feeding fish and benthic shellfish effectively to digest of suspended substances in water, to improve of water at the bottom of the environment, so as to improve the clarity of the water quality, long-term effective purify the water.

## 5.5 Wetland Ecological Landscape System Design Under Computer Control

Although the treatment of water environment can effectively purify the water environment to a large extent, the ecological environment around the water area also has a great impact on the water environment from the perspective of the overall environment. Therefore, based on this criterion, the water environment and surrounding environment can be combined to design a complementary ecosystem with the water environment as the theme and the surrounding ecological landscape as the auxiliary. In this system, the most important thing is the governance and improvement of the water environment (Miao and Fanglin 2015). After the water is thoroughly improved, the water environment can meet the basic requirements for the survival of organisms, and then on this basis, perfect supporting landscape facilities are established around the water area. By virtue of the excellent water environment, a wetland park suitable for human recreation and entertainment is created. In this way, not only the water environment can be improved, but also the overall regional environment can be transformed, so as to re-establish a perfect ecological balance system.

In the design of this system, advanced technology can be properly used to upgrade the wetland park. Such as in the landscape of the system management, can create a set of computer control as the core of the curing system, the system can carry on the program control through the line of set in advance, in a certain period of time can be automated to timely maintenance of landscape, so as to ensure the normal development of wetland landscape inside. The core of the system lies in the governance of the water environment, assisted by the intelligent control of computer technology, and finally forms an advanced and perfect ecological circulation system.

## 5.6 Conclusion

To sum up, this paper mainly studies the water pollution control and treatment methods, and combines the previous research results, and designs a new wetland ecological landscape system under computer control from the perspective of combining the water environment and the surrounding environment, so as to innovate and optimize the treatment path of water pollution. However, on the whole, limited by my ability and knowledge, the designed ecological landscape system still has many shortcomings, and its practicality needs to be verified. However, in the future, with the development of science and technology and the update of governance concept, there will be more new technologies and new ideas applied to water pollution control, and the effectiveness of water pollution control will be gradually improved.

## References

Haiquan Y, Jingan C, Wei Y et al (2021) A method for ecological restoration and aquatic ecosystem restoration of polluted water bodies in plateau lakes, CN112607956A

Jiewen M, Yalong Z, Wenbin L et al (2019) Analysis on technical system of water environment control and water ecological restoration. China Strat Emerg Indus (Theor Version) 00(002):1–2

Jinzhong L, Xueju L, Xuegong L (2007) A study on the application of bioecological technology in the improvement of urban landscape river water environment. Haihe Water Resour 000(004):37–39

Li L (2017) Application of water ecological restoration technology in black-smelly river regulation. China Municipal Eng 00(03):40–42

Li X (2018) Water pollution control and restoration water ecology optimization water system to ensure water safety—12th China international symposium on urban water development held in Haikou. Constr Sci Technol 00(01):9

Liuyan Y, Qiankun C, Yining S et al (2013) A comprehensive ecological restoration process for low-pollution river bodies, CN103359886A

Miao L, Fanglin D (2015) Ecological restoration and optimization analysis of landscape water pollution. Mod Hortic 00(18):173–174

Ruoshui Y, Yingfang C, Jiasheng W et al (2016) A study on water quality purification and ecological restoration of urban landscape water. Environ Sci Technol 39(S2):210–214

Wan Z (2016) A study on landscape design of urban artificial lake based on ecological restoration technology. Sichuan Agricultural University

Ya G (2018) Control scheme of overflow pollution and ecological restoration strategy of a landscape lake combined flow system. Water Purif Technol 00(08):122–126

# Chapter 6
# Structural Adjustment and Intensive Use Evaluation of Ecological Mountain Tourism Construction Land—A Case Study of Binglang Valley Scenic Spot in Hainan, China


**Xingmei Huang, Gengjie Zhang, Huiyong Hu, Honggang Zheng, and Shuxia Liu**

**Abstract** Structure determines function. Regional land use structure adjustment should follow the development needs and social, economic, and ecological conditions, and reasonable organization of land layout. This paper took Hainan Binglang Valley tourist scenic spot as the research object based on the current situation of the tourist scenic spot land use, combined with the positioning of Hainan International Tourism Island, Baoting County, and the development planning of the scenic spot, based on the eco-tourism land use classification system, divided the scenic tourist spot into Ecological Natural Scenic Area, Ecological Cultural Landscape Area and Eco-tourism Service Facility area, a total of 14 land types, the scenic area for Land use structure adjustment. At the same time, considered the social, economic, and ecological benefits to evaluate the degree of intensive land use for tourism construction in Binglang Valley. The results indicated that: (1) The adjusted land use structure was in line with the development plan and development orientation of the Binglang Valley Tourism Scenic Spot. (2) By evaluating the intensive use of the construction land in the scenic spot after land use structure adjustment, the comprehensive score was 0.18, and the intensive grade was intensive use. It meant that could keep the status for development with high land use rate, and reasonable land use type. The

X. Huang · G. Zhang (✉) · H. Hu · H. Zheng · S. Liu
Yunnan Agricultural University, Yunnan 650201, China
e-mail: jiegeng@ynau.edu.cn

G. Zhang · H. Zheng · S. Liu
Scientific and Technological Innovation Team for Optimizing the Land Allocation and Ecological Remediation in Southwest China's Diverse Regions, Ministry of Natural Resources, Kunming, China

Field Scientific Observation and Research Bases of Land Use in Yunnan Luliang, Ministry of Natural Resources, Kunming, China

Engineering Laboratory of Land Resources Utilization and Protection in Yunnan Province, Kunming, China



Z. Yang (ed.), *Environmental Science and Technology: Sustainable Development*, Environmental Science and Engineering, https://doi.org/10.1007/978-3-031-27431-2_6

study concluded that in addition to matching development planning, land use restructuring should also focus on the synergy of social, economic, and ecological benefits to ensure sustainable regional development.

**Keywords** Land use structure adjustment · Intensive use evaluation · Binglang valley scenic spot in Hainan

## 6.1 Introduction

The mountain ecosystem is complex, with obvious natural geography and ecological diversity differences. Meanwhile, the mountain tourism construction land has the characteristics of small capacity, the prominent contradiction between supply and demand, and the ecological environment is vulnerable and difficult to restore (Li et al. 2014; He 2015; Chen 2018). The structure of construction land used for mountain tourism refers to the proportional structure used for mountain tourism construction in mountain tourism areas (Sun 2000; Zhang and Li 2013). The connotation includes two aspects of quantitative structure and spatial structure (Song and Yang 2018). Quantitative structure refers to the proportional relationship of the scale of mountain construction land (Yan 2001), and it is the primary way to study the development of mountain tourism land from a quantitative perspective. Spatial structure refers to the spatial distribution of various types of land for mountain tourism (Yan 2001). It is the primary way to study the development of mountain tourism land from the perspective of positioning. Restructuring land for mountain tourism construction is a process of orderly and scientific distribution of mountain tourism resources in different uses and areas in terms of quantity and space to maintain sustainable use. It is also the process of combining specific land use methods with the ecological suitability and socio-economic suitability of land use to form a good mountain tourism land structure and a coordinated spatial layout and pursue the sustainable use of land.

As the tourism market becomes wider and wider (Fu 2019), the number of tourism projects, tourism stores, and public tourism infrastructure in tourist resorts continues to increase, which leads to the expansion of land for mountain tourism construction and the reduction of ecological land in the mountains (Wang et al. 2021). It harms the development of tourism and the improvement of the ecological environment. Due to mountain tourism land's complex topography and biodiversity, topographic and ecological factors should be considered when optimizing the land for tourism construction. In the current land use situation of Binglang Valley Scenic Spot in Hainan, the land of scenic sites and unique sites is small, which is not conducive to the development planning and positioning of the scenic spot. By drawing on the concept of ecological corridors and optimization of the construction land structure, we conducted an evaluation of the intensive use of land, it was hoped that provided a reference for the land use and sustainable development of ecological mountain tourism construction.

## 6.2 Principles of Construction Land Restructuring for Mountain Tourism

Land restructuring is a way to achieve growth in land output and obtain structural effects by reasonably adjusting the proportional relationship of each land area without increasing the land area. Meanwhile, the land use structure determines the overall function of the land (Wang 2006), so land use structure optimization is the core content of land restructuring (Liu et al. 2005). When optimizing the land use structure according to national economic and social development needs and regional social, economic, and ecological conditions. At the same time, under the guidance of the regional development strategy, land use should be organized according to local conditions as the basis for the restructuring of land use (Wang 2006). The following adjustment principles should be observed.

### *6.2.1 Respect the Economic Laws and Save Land Effectively and Intensively*

In adjusting the structure for mountain tourism land, it is necessary to fully consider saving land resources and improving the efficiency of unit land use. Occupy as little land as possible, enhance the standard of economical and intensive land use, fully exploit the economic supply potential of eco-tourism land, and optimize the input–output ratio and land use rate. That is, reasonably arrange the type and scale of mountain tourism land through the trend of mountain tourism development and the specific needs of mountain tourism land. For example, the centralized layout of the same type of tourism facility land so that it can reasonably radiate to the surrounding mountainous tourist areas without increasing the scale of land use can save intensive land use and improve land use benefits.

### *6.2.2 Respect the Superior Plan and Closely Connect the Relevant Plans*

The restructuring of mountain tourism land involves multiple land use types and their mutual transformation and is also influenced by the region's overall land use strategy and layout. Therefore, the optimization of mountain tourism land structure should be combined with the optimization of the general regional land use structure and closely connected with the overall regional land use planning. Specifically, when optimization of mountain tourism land structure, it is necessary to communicate with the overall land use planning closely. First, it is needed to ensure that each land use does not exceed the control indicators set in the comprehensive land use planning at the corresponding level. Second, it is not to break through land scale in the upper

eco-tourism land planning. The third is connected with urban planning, eco-tourism development planning, and other related planning so as not to conflict with related planning (Xu 2021).

### 6.2.3 Dynamicity Principle

Land's natural and economic elements are constantly changing and evolving (Wang 2006), with changes in social factors leading to constant adjustment and optimization of the land use structure. The land use adjustment plan should be adjusted and revised according to regional economic development needs and changes to maintain an optimized state. Thus expressing the dynamics of regional land use on a stable basis.

### 6.2.4 Sustainability Principles

The land use of mountain tourism construction should consider the present and future, that is, its sustainability. The sustainable use of land resources is the reasonable exploitation, use, management and conservation of land resources under the specific period and regional by organizing and coordinating the relationship among people, land, resources and the environment, which to meet the needs of the present and future generations for survival and development (Sustainable Use of Land Resources 2022). The restructuring of mountain tourism construction land must be fundamental and used as a guideline to develop a configuration plan.

## 6.3 Evaluation Method of Intensive Use of Mountain Tourism Construction Land in Binglang Valley

### 6.3.1 Quantitative Evaluation Sub-index Calculation

The sub-indices of the quantitative evaluation of the intensive use of ecological mountain tourism construction land were calculated according to formula (6.1).

$$\alpha_j = \sum (W_{ij} \times S_{ij}) \times 100 \tag{6.1}$$

where $\alpha_j$ is the value of the jth sub-index; $W_{ij}$ is the weight of the ith indicator under the jth sub-index; $S_{ij}$ is the standardized value of the ith indicator under the jth sub-index.

### 6.3.2 Quantitative Evaluation Index Calculation

The indices for quantitatively evaluating the intensive use of ecological mountain tourism construction land should be calculated according to formula (6.2).

$$\beta_k = \sum (W_{jk} \times a_{ij}) \tag{6.2}$$

where $\beta_k$ is the value of the kth index; $W_{jk}$ is the weight of the jth sub-index under the kth index; $\alpha_j$ is the value of the jth sub-index.

### 6.3.3 Calculation of Total Quantitative Evaluation Index

The complete quantitative evaluation index of the intensive use of ecological mountain tourism construction land was calculated according to formula (6.3).

$$I = \sum (W_k \times \beta_K) \tag{6.3}$$

where $W_k$ is the weight of the kth index; $\beta_k$ is the value of the kth index.

### 6.3.4 Evaluation and Classification of Intensive Use of Tourism Land

According to the evaluation need for intensive use of tourism land, divided the evaluation grade into four grades: "excessive use", intensive use", moderate use", and "low use" (Table 6.1). The expert consultation method graded tourism construction land intensive evaluation and divided the grade of tourism construction land intensive use.

## 6.4 The Restructuring of Mountain Tourism Construction Land of Binglang Valley

The original eco-cultural tourist area of Binglang Valley was a multi-ethnic, multi-cultural, multi-modal, multi-type compounded scenic tourist area that integrates sightseeing, leisure and entertainment, and cultural display (Zhu and Liu 2017). With the unique local folk culture characteristics, rich historical activity monuments, and precious biological resources, the Binglang Valley's original cultural tourism scenic area attracted both China and abroad tourists. It was significantly contributing to

**Table 6.1** The intensification rating of tourism construction land

| Intensive grade | Score | Grade description |
|---|---|---|
| Excessive use | $0 < CI \leq 0.15$ | The over-intensification of land in the region is severe, with over-development and land use; the land use structure is unreasonable |
| Intensive use | $0.15 < CI \leq 0.25$ | The land use in the region is more intensive, the land use rate is higher, and the land use type is more reasonable |
| Moderate use | $0.25 < CI \leq 0.50$ | The land use rate in the area is relatively low, and there is a lot of space for intensive use improvement |
| Low use | $0.50 < CI \leq 1.00$ | In this region, the land use rate is low, the idle land is much, the land use structure is unreasonable, the spatial layout is unreasonable, and there is a perfect space for intensive use and improvement |

tourism development in Hainan and driving the growth of the region's economy. According to the requirements of building an ecological civilization, the scenic spot needed to improve the development conditions and pay attention to protecting the environment. The tourism positioning should pay attention to differentiation, based on ecological carrying capacity, with various characteristics as the theme of the tourism industry, to create a unique tourism business card of "Binglang Valley original Li-Miao cultural tourism scenic spot".

### *6.4.1 Current Land Use Structure in Binglang Valley*

Based on the results of the Second National Land Survey in Baoting County and Sanya City and the *Current Land Use Classification (GB/T21010-2017)* national standard (the land classification standard), the land use structure of Binglang Valley tourist scenic spot was shown in Table 6.2. The current map of land use is shown in Fig. 6.1.

It could be seen from the situation of land use in Binglang Valley that the land of scenic sites and unique sites was small, accounting for less than 1% of the total land area, which was not conducive to the development of scenic spots. Therefore, it was necessary to restructure the current land use.

### *6.4.2 Optimization and Restructuring of Land Use Structure of Mountain Tourist Land in Binglang Valley*

The spatial adjustment of the structure of mountain tourism land was to make more rational use of scenic land and promote the intensification of mountain tourism land. It was necessary to classify the land use types that were not previously involved

**Table 6.2** Current land use of Binglang valley

| Name of land type | Area of land type ($m^2$) | The proportion (%) |
|---|---|---|
| Paddy field | 67,740.7573 | 17.58 |
| The Orchard | 83.5577 | 0.02 |
| Closed forest land | 115,016.8031 | 29.85 |
| Other orchards | 156,830.8642 | 40.70 |
| Land of scenic sites and particular sites | 302.1653 | **0.08** |
| Village | 30,380.9053 | 7.88 |
| Town | 14,962.0907 | 3.88 |
| Total | 385,310.8285 | 100.00 |

Significant bold value indicate it means that the area of the land used for scenic and other special utility occupied the whole area is 0.08%. 302.1653/ 385310.8285 = 0.08%

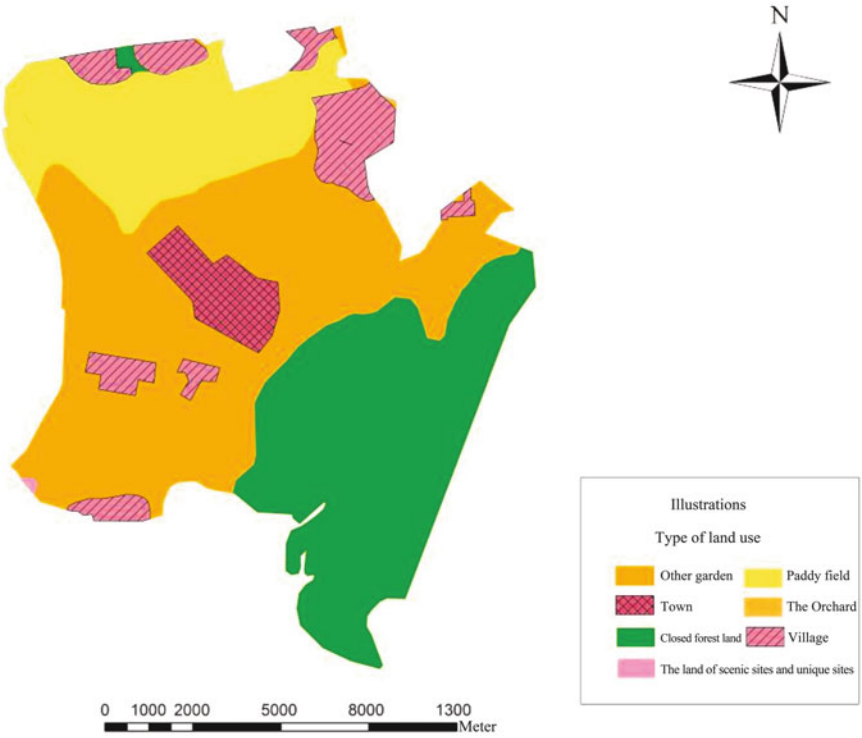


**Fig. 6.1** Map of current land use of Binglang valley

in the scenic spot according to the classification system of ecological tourism land, such as adding new land types; classify and merging existing land types. Combined with the current land use status of the tourist land in the Pinang Valley Scenic Spot, based on the positioning of Hainan International Tourism Island, the development planning of Baoting County, and the intensive development and long-term planning of the scenic spot, according to the ecological tourism land classification system for planning arrangement, the Binglang Valley tourism area was divide into the following functional areas: ① Ecotourism Natural Scenic Area, including land for sightseeing agriculture, forest tourism, and grassland tourism. ② Ecotourism Cultural Landscape Area, including leisure tourism construction land, science and education tourism construction land, cultural tourism construction land, rural tourism construction land, and medical tourism construction land. ③ Ecotourism Service Facility Area, including land for accommodation and catering, shopping and commercial land, tourism infrastructure projects land, management institutions land, comprehensive distribution land, and tourism transportation land. Table 6.3 shows the restructuring of land use.

According to the restructuring table of land use, we could see that the eco-tourism natural scenic spot had the largest area, which was in line with the development plan and development orientation of the original eco-cultural tourism scenic spot in the Binglang Valley. The second was the eco-tourism service facilities area of land. The service facilities in the tourist attractions and the construction of public facilities were relatively complete. The eco-cultural landscape land accounted for 7.58% of the total area. Since Binglang Valley Scenic Area was the first National Cultural 5A Level Scenic Spot (Chen 2020), the cultural landscape has been rich and diverse. Hence there were many types of eco-cultural landscape land in the scenic spot.

## 6.5 Application of Ecological Corridor

Ecological corridors refer to corridors with ecological service functions such as protecting biodiversity, filtering pollutants, preventing soil erosion, wind-break, sand fixation, and regulating floods. Ecological corridors have many ecological functions, for example, establishing reasonable ecological corridors between relatively isolated habitats can increase ecosystem connectivity, provide channels for species exchange and storage, and enhance the resistance and stability of populations to disturbance. The ecological corridors mainly comprise vegetation, water bodies, and other ecological structural elements, representing the same concept as “green corridors” (Ecological Corridor 2022). This study drew on the application of ecological corridors, with forests as the main line. It was a composite corridor composed of plants and organisms such as trees, grasses, and shrubs, with various elements interacting and synergizing to realize its various ecological functions. At the same time, the ecological corridor was a holistic ecological network system which consisted of the primary and secondary corridors and green nodes. Moreover, building the ecological corridor could provide socio-cultural life for people because it had the deep

**Table 6.3** The restructuring table of land use in Binglang valley

| Functional areas | Land type | Area ($m^2$) | Total area ($m^2$) | The proportion (%) | Total proportion (%) |
|---|---|---|---|---|---|
| Ecotourism natural scenic area | Sightseeing agriculture land | 93,556.6318 | 247,344.9802 | 24.28 | 64.19 |
| | Forest tourism land | 140,535.1029 | | 36.47 | |
| | Grassland tourism land | 13,253.2455 | | 3.44 | |
| Ecotourism cultural landscape area | Leisure tourism construction land | 15,938.5707 | 29,216.5537 | 4.14 | 7.58 |
| | Science and education tourism construction land | 2326.0057 | | 0.60 | |
| | Cultural tourism construction land | 1819.3930 | | 0.47 | |
| | Medical tourism construction land | 158.0937 | | 0.04 | |
| | Rural tourism construction land | 8974.4906 | | 2.33 | |
| Ecotourism service facility area | Accommodation and catering land | 11,166.7105 | 108,749.2945 | 2.90 | 28.22 |
| | Shopping and commercial land | 5449.9612 | | 1.41 | |
| | Tourism infrastructure projects land | 11,980.7949 | | 3.11 | |
| | Management institutions land | 2847.8312 | | 0.74 | |
| | Comprehensive distribution land | 6517.1408 | | 1.69 | |
| | Tourism transportation land | 70,786.8558 | | 18.37 | |
| Total | | | 385,310.8285 | 100 | 100 |

cultural and historical connotation. To prevent the continuous expansion of mountain tourism construction land and ensure the stability of the mountain ecosystem, set a 20 m wide ecological corridor boundary outside the existing tourism construction land (Fig. 6.2).

For the construction planning of the ecological corridor boundary, the premise was to maintain and restore the natural form of the mountain tourism scenery. Secondly, attention should also be paid to the organic combination of forest and ecological

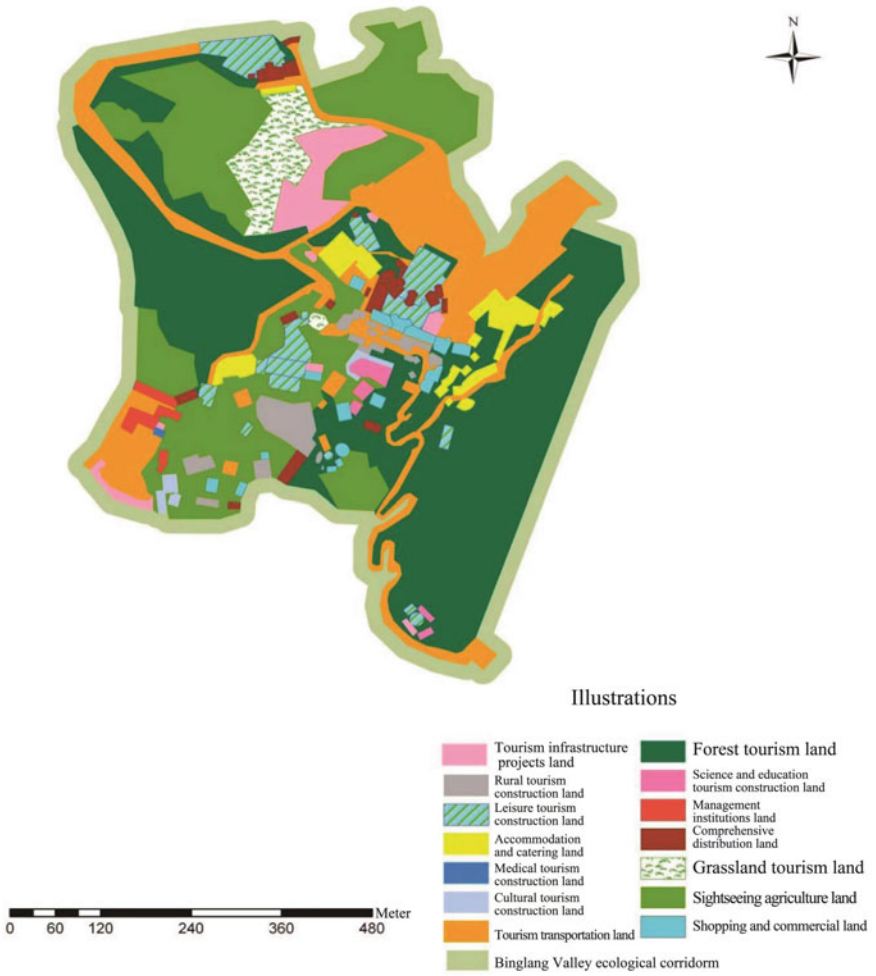


**Fig. 6.2** Ecological corridor map of Binglang valley after land use restructuring

corridors, considering the corridor's openness, ventilation function, and slope limitation. Both sides of the berm were visually sensitive areas, and plant materials were mainly local characteristic herbaceous vegetation. For the local dominant herbaceous vegetation, designed the design of slope protection plants according to the seasonal changes, slope aspect, and the growth requirements of the plants themselves to form an open space and show distinctive rhythmic features in the landscape, such as the opening and closing of space, the undulation of the skyline and color changes.

The demonstration of the construction land intensive control technology of the original Li-Miao cultural tourism scenic spot in the Binglang Valley was bounded by the ecological corridor boundary. The setting of the ecological corridor boundary protected the cultural integrity of the scenic site, protected the scenic land from being

occupied, and limited the continuous expansion of the construction area of the scenic spot due to the expansion of market demand to protect the ecological environment of the mountain. The setting of the mountain ecological corridor boundary could effectively reduce temperature, improve habitat diversity, increase the supply of biological food, control soil erosion, effectively filter pollutants, meet the migration and spread of animals and plants, and enrich the landscape structure. Since the setting of ecological corridors were all dominant indigenous species, which had strong adaptability, low cost, easy growth, strong vitality, and were not easily destroyed by nature or artificial, and could be gradually succeeded by nature in the later stage.

## 6.6 Intensive Use Evaluation

Combined with the characteristics of Hainan's mountain tourism resources, comprehensively considered the three aspects of the economy, society, and ecological benefits to select evaluation indicators and established an evaluation index system for the intensive use of ecological mountain tourism land (Table 6.4). According to the analytical evaluation method, the ideal value of the reference system was determined by the "best of the best" approach. Through the *environmental assessment report* provided by the local department, the *Assessment Report on the Current of Hainan Binglang Valley Tourist Scenic Spot Project*, the *Baoting County Statistical Yearbook*, the *Guidelines for the Verification of the Maximum Carrying Capacity of Scenic Spots*, the *Hainan Provincial Tourism Regulations*, and the *tourism industry statistics*, to determine the value of the scenic index.

Based on the quantitative evaluation total index calculation method to get a total score of 0.18. The eco-tourism construction land intensity classification showed that Binglang Valley tourism construction land was intensive and should maintain the current development.

## 6.7 Conclusions and Recommendations

In order to make the land use structure of Binglang Valley reasonable and in line with the planning and positioning of development, by drawing on the concept of ecological corridors and practicing with the unique local folk culture, it was divided into 3 functional areas: ecotourism natural scenic area, ecotourism cultural landscape area, and ecotourism service facilities area. Furthermore, the land use structure had been adjusted to evaluate the intensive use of land for tourism construction in the mountainous Binglang Valley, and it was considered that the status should be kept for development.

The Binglang Valley's original Li-Miao cultural tourism area was rich in natural, human, and social resources, with a wide variety of resources and a high concentration rate. Still, it needed further excavation and sorting out. Among them, the

**Table 6.4** Evaluation index system for the intensive use of ecological mountain tourism land

| The target layer | Rule layer | Index layer | Indicator extremely | Ideal value | The actual value |
|---|---|---|---|---|---|
| Evaluation of intensive use of ecological mountain tourism land | Economic benefits | Number of tourists per unit area (ten thousand meters$^2$/person) | − | 78.295 | 157.5 |
| | | The input–output ratio of unit construction land (%) | + | 95.96% | 0.3 |
| | | Tourism revenue per unit area | + | 274.133 | 94.73 |
| | | Average investment intensity (%) | − | 250.752 | 207.62 |
| | Social benefits | The proportion of tourism income in GDP (%) | + | 12.44% | 1.68 |
| | | Number of tourism employees per unit area (people/hm$^2$) | + | 5.667 | 8.464 |
| | | Tourism service facilities and infrastructure perfection (unit) | + | 100 | 85 |
| | | Convenience of transportation | + | Optimal | 70 |
| | Ecological benefits | Green rate (%) | + | 70.00% | 22.3 |
| | | Environmental protection investment ($10^4$ CNY/m$^2$) | + | 9.87% | 9.87 |
| | | Air environmental quality (Grade I) | + | One | 100 |
| | | Water environmental quality (Grade I) | + | II | 90 |
| | | Acoustic environmental quality (Grade I) | + | I | 100 |

natural resources of the scenic spot were dominated by tropical rainforests in the natural landscape, with high landscape value. The natural resources in the area had good spatial continuity and composition, connected the scenic spots, and the scenery was different, which was convenient for centralized development. Rich in cultural resources, with the culture related to the Li-Miao ethnic groups.

### *6.7.1 Create a Diverse Tourism Experience Environment*

Relying on the local natural resources and rich cultural and social resources (Du et al. 2022), combined with the local historical monuments and cultural customs to create a diverse tourism experience environment, attracting tourists interested in experiencing the original ecological Li-Miao culture (Chen 2020). As a scenic spot, it is necessary to actively develop various tourism experience services to form a rich experience, such as making pottery, musical instruments, and exquisite embroidery experience (Xia and Liu 2021). At the same time, it should improve the quality of service, strengthen the service consciousness of scenic spot staff (Du et al. 2022), conduct more training, actively guide tourists to experience the local culture, and meet the tourist experience needs of tourists. Tourism service is an important factor affecting tourism development (Cheng 2014). It should adhere to the service idea of "tourist experience-oriented", improving the quality of scenic folk tourism experience products, and implementing personalized services using various carriers in the tour (Du et al. 2022), to enhance the customer's pleasant travel experience. Only by changing the concept of management and service and constantly innovating tourism products around tourists' needs can tourist attractions develop sustainably. For tourism food, using the scenic spots platform promotes Li-Miao special snacks to tourists from all over the world, such as bamboo tube rice and three-color rice (Xia and Liu 2021), to strengthen the development of scenic spots, enrich tourism products, and increase income.

### *6.7.2 Strengthen Regional Tourism Cooperation*

According to relevant agreements, economic entities in different regions conduct tourism exchanges and cooperation spontaneously and mutually beneficially, called inter-regional tourism cooperation (Li 2011). It is a product of this era, and its emergence is inevitable and significant to the region's sustainable development. The first is cooperation between the market and resources. Hainan Province has an advantageous geographical location and unique tourism resources. There are many high-quality tourism resources in and around Hainan Province, and it is easy to form regional tourism cooperation with tourist destinations within a specific range. The Binglang Valley can be used as a tourism distribution center to gather tourists from Hainan and develop a regional loop tour through the guidance of boutique tourism routes, which

is easy to achieve win–win cooperation. Second, regional resources will be incorporated and shared by holding large-scale events, such as food and cultural festivals, the "March 3" festival, and international exhibitions. Third, joint promotions, such as the Maritime Silk Road, integrate the surrounding high-quality tourism resources to create an international eco-tourism city.

### *6.7.3 Create a Brand of Characteristic Amusement and Leisure Tourism*

The original eco-cultural tourist attraction of Binglang Valley is a multi-ethnic, multi-cultural, multi-modal, multi-type compound tourist scenic area that integrates sightseeing, leisure and entertainment, and cultural display (Zhu and Liu 2017). With the unique local folk culture characteristics, rich historical activity monuments, and precious biological resources, the Binglang Valley's original cultural tourism scenic area attracts many tourists. It is making a significant contribution to tourism development in Hainan and driving the growth of the region's economy. At the same time, it is necessary to improve the development conditions and pay attention to protecting the environment. And then, the tourism positioning should be differentiated and not too similar to highlight its highlights, create a unique "Binglang Valley Original Li-Miao Cultural Tourism Scenic Spot", and strengthen exchanges and cooperation with national tourist attractions. Based on the ecological carrying capacity, with various characteristic tourism industries as the theme, create a unique tourism business card.

**Acknowledgements** This work is supported by

(1) Ecological Evaluation of Terraced Fields in Ecological Isolation Zone of Plateau Red Earth Area, supported by Yunnan Provincial Department of Education Fund (Grant No. 2022J0300).

(2) Trade-offs and Synergies of Ecosystem Services in Terraced Fields with Ecological Isolation Zones, supported by Yunnan Provincial Agricultural Joint Special Youth Project (Grant No. 2018FG001-092).

(3) Yunnan Youth Top-notch Talent Support Program (YNWR-QNBJ-2018-338).

## References

Chen X (2018) Study on intensive degree-coordination analysis and promotion strategy of tourist land—a case of Jiangxi province. Nanchang University, p 1

Chen L (2020) A study on the competitive strategy of Hainan Binglang Valley Li&Miao cultural tourism area under the background of cultural tourism integration. Hainan Tropical Ocean University, p 9

Cheng JL (2014) Introduction to tourism studies. Henan University Publishing House, Zhengzhou

Du XM, Huang YJ, Cui XL et al (2022) Evaluating perceived online tourism service quality based on consumer experiences. Shanghai Manag Sci 44(2):92–102

Ecological Corridor. https://www.huanwenwen.com/article-4899.html. 2022/08/11

Fu JH (2019) Analysis of the opportunities and challenges facing the tourism industry. Market Circles 35:138–139
He YY (2015) Research on tourism land use planning and regulation based on tourism environmental capacity—taking the Xueshan ancient city tourism resource area in Lijiang City as an example. Kunming University of Science and Technology, p 10
Li H (2011) International tourism island of Hainan context of regional tourism cooperation. Hainan University, p 1
Li Y, Zhou AW, Zhao ZZ, Yu TH, Zou YF (2014) Problems and solutions of Hainan tourism land based on the quality and capacity strategy. J Hainan Norm Univ (Nat Sci) 27(01):84–86+97
Liu RX, Xue A, Han P, Ni JR (2005) Optimization of land use structure: commentary of methods. Acta Scientiarum Naturalium Universitatis Pekinensis 41(04):655–662
Song JL, Yang J (2018) Analysis of the quantitative structure and spatial characteristics of land use in less developed areas based on landscape ecology. Rural Econ Sci Technol 29(13):28–32
Sun HL (2000) China Encyclopedia of resource science. Encyclopedia of China Publishing House, Beijing
Sustainable use of land resources. https://wiki.mbalib.com/wiki/. 2022/08/11
Wang WM (2006) Planning of land use. Scientific Publishing House, Beijing
Wang XW, Yu L, Wang SJ, Cao WD, Fan DL (2021) Evolution and optimization of ecological land pattern in the Wanjiang area based on construction land expansion. J Northwest A&F Univ (Nat Sci Ed) 49(08):120–132+144
Xia XW, Liu LL (2021) Hainan Penang Valley scenic area tourism product innovation development research. Market Modern 13:158–160
Xu MP (2021) Study on the preparation of village land use planning in the context of rural revitalization strategy. Shanxi Agric Econ 19:70–71
Yan JM (2001) Land use planning in China: theory, methodology, strategy. Economic Management Publishing House, Beijing
Zhang QJ, Li XX (2013) Research review in optimization allocation methods of land use structure. J Tianjin Inst Urban Constr 19(01):10–15+33
Zhu HB, Liu BC (2017) Analysis of the local impact of tourism development in Binglang Valley scenic area. Tour Overview 12:211–212

# Chapter 7
# Assessing Optimal LID Areas for Flood Mitigation: A Case Study on Vancouver Island, Canada


**Z. Zhang and C. Valeo**

**Abstract** Low Impact Development (LID) is considered an effective method for mitigating urban flooding and is often implemented in existing urban areas that are constrained by space. LIDs are getting more attention in peri-urban areas as the dominant stormwater infrastructure in future developments in part because there is a greater availability of space. This paper explores and simulates the potential for mitigating urban development and the possibility of completely replacing conventional urban drainage facilities on a large scale. PCSWMM is used with a proposed framework for identifying the optimal LID implementation size as well as LID parameter settings, in the Tod Creek watershed (10.38 $km^2$) of Saanich on Vancouver Island, British Columbia, Canada. The type of LID considered is the bioretention cell. Local weather and flow data are input to PCSWMM to simulate a varying number of bioretention cells (constituting varying LID areas) to reduce the peak flow as well as total volume. The results show that at the catchment scale, it is necessary to implement default bioretention cells that account for about 9% of the overall area, which results in a return to pre-developed imperviousness (5%) from the developed level of imperviousness of 40%. The implementation area size of the LID is the dominant parameter for reducing the total volume and peak flow.

**Keywords** LID · Bioretention cells · Spatial scale · PCSWMM

## 7.1 Introduction

Urbanization can lead to increased stormwater runoff and flooding (Ahiablame and Shakya 2016; Shaneyfelt et al. 2021), as well as decreased water quality. Low Impact Development (LID) techniques are systems or practices that use or mimic natural processes to mitigate the hydrological risk caused by urbanization (Environmental Protection Agency 2012; Paule-Mercado et al. 2017). Typical LID technologies include green roofs, bioretention cells, and permeable pavements (Golden and

Z. Zhang (✉) · C. Valeo
Department of Mechanical Engineering, University of Victoria, Victoria, Canada
e-mail: zhonghaoz@uvic.ca



Z. Yang (ed.), *Environmental Science and Technology: Sustainable Development*,
Environmental Science and Engineering, https://doi.org/10.1007/978-3-031-27431-2_7

Hoghooghi 2018). They provide numerous hydrological and environmental benefits, including runoff volume and peak reduction, groundwater recharge by increasing stormwater infiltration into the native soil, water quality improvement, heat-island effect mitigation (Xie et al. 2019), as well as reducing soil sealing effects (Rodríguez-Rojas and Grindlay Moreno 2022). Implementing LIDs however, can be difficult due to challenges from limited space and resources, geographic restrictions due to location, financial issues, and vague guidance on LID design, implementation, and maintenance (Cohen-Shacham et al. 2019). Modelling tools such as SWMM5 or PCSWMM that can model LID function in catchments are frequently used in LID design, construction, and operation (Sakshi and Singh 2016; Bai et al. 2018; Jeffers et al. 2022; Bond et al. 2021). These models aid in creating LIDs to ensure a level of effectiveness for reducing the effects of urbanization on water availability and, possibly, water quality throughout the design life. Stormwater management strategies increasingly incorporate urban stormwater computer models that simulate LIDs in urban and peri-urban catchments. LIDs are frequently applied at plot scales partly because they were developed for urban areas. Laboratory, field, and practical studies have shown LIDs to be valuable tools at various small scales (Piro et al. 2019; Stovin et al. 2012; Gülbaz and Kazezyılmaz-Alhan 2017; Palla and Gnecco 2015). At these small or plot scales, LIDs are shown to efficiently reduce, mitigate, and prevent hydrological and meteorological risks (Bai et al. 2018; Palla and Gnecco 2015; Seo et al. 2017; Liu et al. 2017; Jiang et al. 2015; Herrera-Gomez et al. 2017). However, when assessing the LID performance, researchers frequently dissociate it from the hydrological water cycle system and treat it as a separate, unconnected element. This behavior drastically shrinks the evaluation scale, disregards how the many elements of the hydrological process interact with one another and ignore the flow transformation in the upstream and downstream zones (Nika et al. 2020). As a result, it is more likely to overstate small scale LID effectiveness. When LIDs are up-scaled from small scale to larger scales, the implementation area of the LID is the key factor that needs to be considered because it involves the configuration of the internal parameters of the LID, and the optimal configuration of the implementation area. The latest research results show that there is a threshold for the implementation area of LID; rather than the more the better, no more additional hydrological benefits are achieved beyond this threshold (D'Ambrosio et al. 2022).

The objective of this work is to understand the limits of scaling up LIDs to large areas. This research applies the PCSWMM model to the Tod Creek watershed, which is a peri-urban watershed on Vancouver Island, as a case study to answer the following questions:

i. Considering future urban development trends in the Tod Creek watershed, how much areal coverage of LID needs to be implemented in the total area for mitigating the impact of the proposed urbanization?
ii. What are the optimal LID parameters setting for the scale of this application in this region?
iii. What is the uncertainty or challenge of modelling LIDs using PCSWMM as the scales of application change? And what are the potential solutions?

This paper focuses on bioretention cells as the LID due to their water quality and quantity enhancing benefits. PCSWMM output is detailed, analyzed, and conclusions are drawn with the last part of the paper discussing the limitations and uncertainties in the model and potential solutions. This research can provide guidance to stakeholders involved in the future sustainable development of this region, and is useable for any region and scale.

## 7.2 Methodology

PCSWMM is applied to the Tod Creek watershed to model flow rates and total volumes under various LID scenarios. The influence of LID size and parameterization is investigated by comparing the model output for each of those scenarios to a basis of comparison (BOC). We use ArcGIS software with a digital elevation model (DEM) of the Saanich region area of Vancouver Island, BC, Canada, to delineate the watershed, determine water flow direction as well as streamflow order. Open data provided by the Saanich Open Data Set were collected including rainfall data, soil type, and land-use data. Based on flow gauge data, we calibrated PCSWMM for the catchment with minimal urbanization (5% impervious cover). We created a BOC whereby 40% of the catchment is rendered impervious based on future projected land-use changes and with no LIDs implemented. The scenarios were created as progressive increases in bioretention cell area with basic parameters unrelated to area being unchanged. Then we developed an additional set of scenarios that modify important parameters. The comparison to the BOC then suggests optimal bioretention cell area and optimal parameters for mitigating the impact of urban development.

## 7.3 Study Area

Saanich has a total area of 29.61 km of sea coastline and 8.175 $km^2$ of freshwater lakes (Wikipedia 2022). The Tod Creek watershed in the greater Saanich area was chosen as the focus of our study since the majority of its territory is rural with some degree of urbanization and also due to availability of gauge data. This watershed water flow varies greatly over the year, reaching up to 5 $m^3/s$ after winter rains to $5 \times 10^{-4}$ $m^3/s$ at the end of the summer. Hence, flooding is primarily a winter phenomenon in this climate which receives little snow. In addition, there are four large natural lakes in the study area, Maltby Lake, Prospect Lake, Durrance Lake and Quarry Lake. During summer, especially in June and July, the daily evaporation of the nearby lakes is 6,167.4 $m^3$/day. The model catchment is 10.38 $km^2$ and based on the only available streamflow gauge in the area (Tod Creek below Prospect Lake 08HA054). This station (referred to as J300 in this work) has nine years of flow discharge records (1982–1990), as show in Fig. 7.1b is used for model calibration. In addition, the 50 year return period storm for the region was used as the precipitation

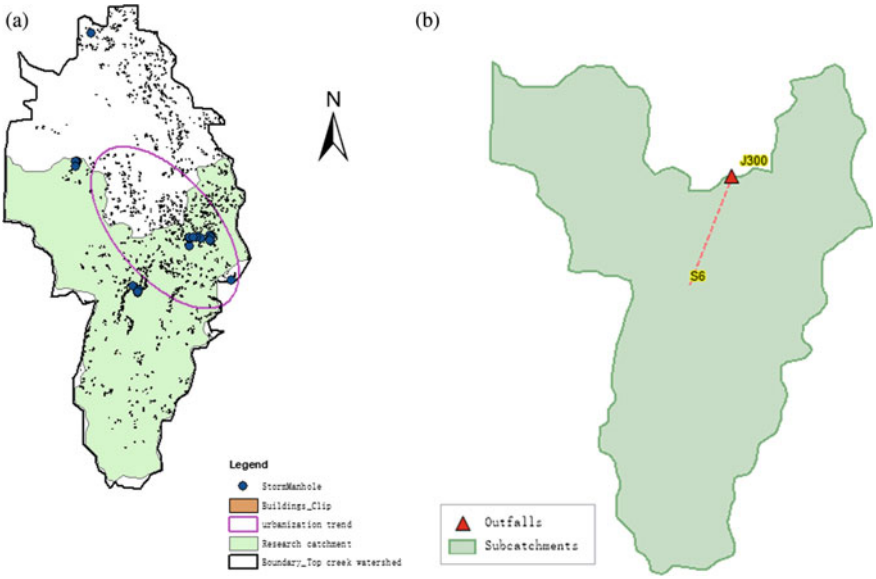


**Fig. 7.1** **a** The urbanization plan for catchment; **b** simplified Tod Creek catchment draining to J300

input under various scenarios in the comparisons of performance at varying scales and with changing parameters.

### *7.3.1 PCSWMM Applied to Tod Creek Catchment*

Based on the distribution data of residential houses and manhole data, Fig. 7.1a illustrates the urbanization trend for the current study area. Figure 7.1b shows the calibrated study area. The Authors calibrated the soil parameters, catchment width as well as the baseflow in the study area according to the 1984 streamflow station data (from April to September) and the meteorological data for that year.

### *7.3.2 Hypothesis for 1984 Scenario, Proposed Scenario, and LID Scenarios*

To compare the performance of LID in mitigating the urbanization process, we examined the historical data for urbanization. The data from 1984 was used to calibrate the model with an imperviousness of 5%. This is the 1984 proposed scenario shown

**Table 7.1** The scenarios setting for spatial scaling impacts analysis

| Scenario | Type of scenario | LID % of area | Remaining % imperviousness | Remaining non-LID % | Adjusted % imperv. |
|---|---|---|---|---|---|
| 1984 | Pre-urbanization | 0 | 5 | 100 | 5 |
| S0 | Full urbanization | 0 | 40 | 100 | 40 |
| S1 | Proposed LID | 1 | 39.6 | 99.6 | 39.75 |
| S2 | Proposed LID | 2 | 39.2 | 99.2 | 39.51 |
| S3 | Proposed LID | 5 | 38 | 98 | 38.77 |
| S4 | Proposed LID | 10 | 36 | 96 | 37.5 |
| S5 | Proposed LID | 15 | 34 | 94 | 36.17 |
| S6 | Proposed LID | 20 | 32 | 92 | 34.78 |
| S7 | Proposed LID | 30 | 28 | 88 | 31.81 |

in Table 7.1. Scenario 0 (S0) is a projected future urbanization of nearly 40% imperviousness and scenarios 1 to 7 represent incremental increases in bioretention cell area and adjusted levels of imperviousness given in the Table.

There are also two equations used for representing the LID performance. Equation 7.1 is used to calculate the basis of comparison for different scenarios (from S1 to S7) compared with No LID scenario (S0) and Eq. 7.2 is a new proposed performance matric used to calculate the LID performance for mitigating urbanization that uses the 1984 scenario.

$$P_{BOC} = \frac{S_i - S_0}{S_0} \tag{7.1}$$

$$P_{LID} = \frac{S_{No\,LID} - S_{LID}}{S_{No\,LID} - S_{1984}} \tag{7.2}$$

where $P_{BOC}$ is the basis of comparison for different LID scenarios; $S_i$ is the proposed scenario with LID implementation, $S_0$ is the proposed urbanized scenario; $P_{LID}$ is the proposed performance metric; $S_{No\,LID}$ is the simulated function after urbanization in different proposed scenarios; $S_{LID}$ is the simulated function after urbanization in different proposed scenarios with LID implementation; and $S_{1984}$ is the observation function of the level before urbanization.

### *7.3.3 Bioretention Cell Parameter Initial Setting and Uncertainty Range for Optimizing Parameters*

Table 7.2 shows the parameters used for the bioretention cell as modelled in PCSWMM for the BOC, as well as the suggested ranges for the parameters given modelling under a 50 year rain event.

**Table 7.2** The optimization range for LID parameter setting as well as the BOC value

| Layers | Parameter | BOC values | 50 Yr rain event range |
|---|---|---|---|
| Surface layer | Berm height (mm) | 150 | [75, 300] |
| | Vegetative cover (fraction) | 0.03 | [0.015, 0.06] |
| | Surface roughness (Manning's n) | 0.1 | [0.05, 0.2] |
| | Surface slope (%) | 1 | 1 |
| Soil layer | Soil thickness (mm) | 650 | [325, 1300] |
| | Porosity (volume fraction) | 0.44 | [0.22, 0.88] |
| | Field capacity* (volume fraction) | 0.11 | 0.11 |
| | Wilting point* (volume fraction) | 0.03 | 0.03 |
| | Soil conductivity (mm/h) | 40 | [20, 80] |
| | Conductivity slope | 7 | [3.5, 14] |
| | Suction head (mm) | 48.26 | 48.26 |
| Storage layer | Storage height (mm) | 200 | [100, 400] |
| | Storage void ratio (voids/solids) | 0.75 | [0.375, 1.5] |
| | Seepage rate (mm/h) | 6 | [3, 12] |
| | Storage clogging factor | 60 | 0.5 |

Note that the uncertainty range could allow stakeholders to propose changes to design based on costs (for engineered soil for example) or future sustainability.

### *7.3.4 Nash–Sutcliffe Model Efficiency Coefficient (NSEA) as the Optimization Criteria*

The NSE index (Eq. 7.3) is used to evaluate the accuracy of the calibrated hydrological model as well as serve as the optimization criteria in the parameter study.

$$\mathrm{NSE} = 1 - \frac{\sum_{i=1}^{n} (\mathrm{O_i} - \mathrm{P_i})^2}{\sum_{i=1}^{n} \left(\mathrm{O_i} - \overline{\mathrm{O}}\right)^2} \tag{7.3}$$

where $\overline{O}$ is the mean of observed discharge; $O_i$ is the modeled discharge; and $P_i$ is the observed discharge. The closer the value of NSE is to 1, the better the fit of the observed value to the model valued. The calibrated NSE for the 1984 rainfall and flowrate was 0.69.

## 7.4 Result

### *7.4.1 Effect of LID Implementation Percentage*

Figure 7.2 shows the results of the impact of bioretention cell area on mitigating peak flows and volumes using both Eqs. 7.1 and 7.2. Technically, S0 (imperviousness is 40%) is at point 0 on the horizontal axis but is not shown as it is a BOC from which all other scenarios compared to in both Eqs. 7.1 and 7.2 and would have a value of 0%. It is not shown because the vertical axis is a log scale of base 2. The vertical axis was drawn this way in order to better illustrate how implementing even a small percentage of bioretention cells in the area can bring the peak flows and volumes to better than pre-developed (1984) circumstances. The blue curves represent impacts on total volumes and the red curves represent peak flowrates.

Focusing on the curves created using Eq. 7.1, the figure shows that different bioretention cell area implementation strategies play varying roles depending on the area. At small LID implementation areas, the impact is greater on volumes than on peak flows but as one gets closer to 10% of the catchment being a bioretention cell, the impacts to peak flow are greater than to volumes. As implementation area increases beyond 10%, there is no additional benefit to reducing peak flows or volumes. This occurs because PCSWMM models bioretention cells as rather simple reservoirs. Increasing LID area simply increases the size of this "reservoir" and at 10%, effectively all the rainfall of the 50 year event is captured and retained and there is no surface runoff generated. Thus, further improvement of water storage capacity will not reduce the total inflow of J300; thus, the implementation area of LID increases but the "performance" of LID does not improve significantly. The LID performance

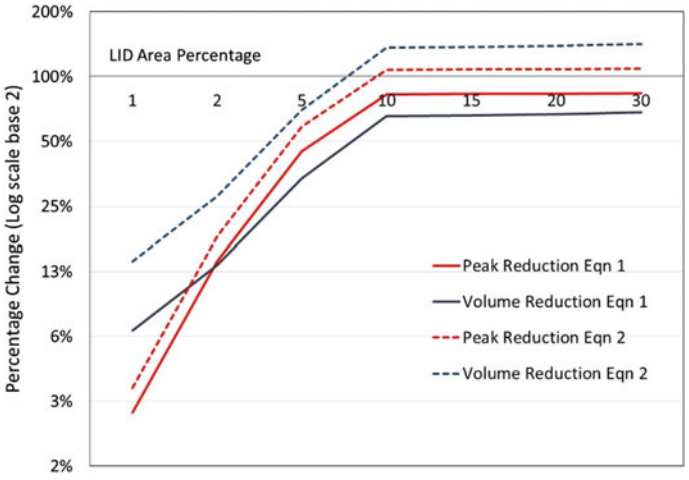


**Fig. 7.2** Percent reductions for scenarios S1–S7 using Eq. 7.1 (only uses S0 and S# values) and 7.2 (uses 1984 flows as well)

metric results show that the optimal percentage of LID implementation should be between scenario AS2 and scenario AS3 because it has already reached the 100% performance. That is, 5–10% of the predesigned bioretention cells in the overall research range need to be implemented to mitigate 40% of the impervious area back to the 5% impervious level in the catchment scale.

Equation 7.1 is the typical relationship used to reflect performance of LIDs, whereas Eq. 7.2 helps to illustrate the levels that can actually total volumes and peak flows to better than pre-developed levels. As seen in Fig. 7.2, Eq. 7.2 shows that at 10%, reductions are better than 1984 values (which is difficult to observe using Eq. 7.1). Whether or not this is desired or even practical is an important question. Over-implementing bioretention cells such that flows are mitigated beyond pre-developed states simply changes the hydrology of the region, which is not desirable from an ecosystem perspective. Having too many LIDs can increase infiltration substantially leading to drier river beds, etc. Certain ecosystem processes rely on some degree of annual flooding, which would be affected by having too much area converted to LIDs.

### *7.4.2 Impacts of LID Parameter Settings*

For this analysis, S3 was used as the BOC case in which 5% of the area is converted to bioretention cells. This was necessary in order to have some runoff generated during the simulations. PCSWMM provides a Sensitivity-based Radio Tuning Calibration (SRTC) tool for the optimization needed. According to the sensitivity analysis results and the area percentage we initially obtained; we further optimize the bioretention cell parameters within a reasonable range. Doing so, not only improves the performance of the bioretention cells but further reduces the required implementation area (which leads to increases in costs as area increases). It is worth noting that any combination of the 11 parameters can be selected in any combination within the intervals given in Table 7.2. Table 7.3 shows the parameters bioretention cell performance was very sensitive too, as well as two options, or changes in parameters, to determine the impact overall.

The results show that reducing the LID implementation area by 20% requires a corresponding increase in berm height by 25% as show in Table 7.3, option 1. If the soil layer and storage layer are modified, reducing the LID implementation area by 20% requires increasing the soil thickness by 30%, and the porosity by 20% as shown in Table 7.3 Option 2. The optimized final LID implementation area for AS3 is 7.5% for both Options, which can meet the requirements of peak flow and total volume. Note that we have modified the configuration of the bioretention cells using different approaches. The first approach (Option 1 in Table 7.3) mainly modifies the parameters of the surface layer, and approach two (Option 2) modifies the parameters of the soil layer. The results show minor sensitivity to the storage layer (based on previous research). Although there are different approaches to changing different components of the model, the modified area required is the same for both

**Table 7.3** AS3 parameters to provide optimal area and LID parameter options leading to reduced areas

| Name | Optimized parameters | Parameter option 1 | Parameter option 2 |
|---|---|---|---|
| Berm height (mm) | 150 | 187.5 | 150 |
| Vegetative cover (fraction) | 0.03 | 0.03 | 0.03 |
| Soil Thickness (mm) | 650 | 650 | 845 |
| Porosity (volume fraction) | 0.44 | 0.44 | 0.528 |
| **LID area required (%)** | **9** | **7.5** | **7.5** |
| Peak flow ($m^3/s$) | 5.495 | 5.695 | 5.842 |
| Total volume ($m^3$) | 136 900 | 135 900 | 136 800 |

Options. This similarity proves that when reducing the implementation area of LID, the internal parameter combination that needs to be modified to achieve this does not have a unique solution. It is worth noting that when the LID implementation area is reduced by 50%, even modifying the LID parameters cannot return the hydrograph to the 1984 level because this change has over-stretched the LIDs parameters beyond the interval allowed. The results show that modifying the parameter configuration of the LID can improve the performance to a certain extent, while reducing the implementation area of the LID. This shows that the optimal LID implementation size will also vary with the LID internal parameterization.

## 7.5 Discussion

When testing the parameters for each bioretention cell layer, we find that the all-around performance can be affected by the ponding layer, soil media, and storage. We can get the best solution, but no unique solution. When making decisions about implementing LIDs, we often need to support stakeholder decision-making based on the model's results. Thus, the best range of uncertainty needs to be carefully decided by stakeholders.

Lacking accurate data is a common limitation for most studies. In this study, highly accurate elevation data for the area was difficult to obtain and low precision DEMs will bring many errors. ArcGIS uses the C8 method (based on elevation data) to determine the water flow direction. However, a low-precision DEM will lead to

inaccuracy in the modelling of surface runoff flow pathways. This 'root' uncertainty will be further amplified in subsequent modelling analysis. In particular, the pattern of surface runoff captured from ArcGIS is highly compatible with the situation in rural areas. However, due to the influence of drainage infrastructure or urban development, the flow direction and surface runoff model may be affected when used in urban areas. Whatever human activity or urban development changes the streamflow pathways, this change will further lead to ambiguity in where LIDs should be implemented at large catchment scales.

An additional source of uncertainty arises from the model structure; that is, the modelling cannot perfectly describe the physical reality, especially the transfer from non-uniform sub-catchments to uniform catchments (arising particularly when modelling large-scale areas). For the simple calculation process, the PCSWMM sets the slope of the area as the average value, and the conductivity value is derived from the regional distribution of the original soil but is also an average value. Many other average values are also used for representing the input parameters. This simplification step dramatically reduces the calculation time but reduces the ability of the model for using relevant and heterogeneous geographic information. PCSWMM also conceptualizes a subcatchment as a rectangular surface with a uniform slope S and a width W that drains to a single outlet channel. When calibrating the model, the most uncertain parameter is width, which greatly affects peak flow and total volume. The result shows that wider widths will make peak flow advance, and a narrower width will allow more time for infiltration and reduce the total volume. Essentially distinctive irregular, catchment features are transformed into uniform rectangular surfaces, and this transformation eventually causes all spatial information to be lost. In addition, the model structure of LIDs is layer by layer where movement is exclusively vertical; which for bioretention cells does not consider the capillary water absorption of the surrounding soil, which may lead to overestimation of infiltration in contact with the original soil on a large scale. Currently, there is a lack of consensus about computing and outputting a hydrograph that accurately reflects the uncertainty and variability in the modelled processes, noisy field data, and other errors. PCSWMM computed output may be presented for a range of values based on probability and error. However, sensitivity analysis is minimal for tracking the propagation of uncertainty. Currently, for parameterizing LIDs using models, effective calibration and validation is difficult due to the sparseness of LID data available from studies and the literature. This limitation of validation data has primarily limited the promotion and development of LIDs, and the process of quantifying the propagation of uncertainty is crucial for stakeholder decision-making and risk analysis.

## 7.6 Conclusions

The results show that the Saanich area needs to implement about 9% of the total LID area to mitigate the proposed urbanization. After optimizing the LID parameters, this percentage can be reduced to 7.5%. However, this comes with trade-offs in

LID designs which may increase costs in other ways. For the 50-year rainfall event, increasing the berm height can effectively reduce the required LID area. Uncertainty mainly arises from data and model structure, such that there is no unique combination of model parameters and areal extent to produce a specific output.

## References

Ahiablame L, Shakya R (2016) Modeling flood reduction effects of low impact development at a watershed scale. J Environ Manag 171. https://doi.org/10.1016/j.jenvman.2016.01.036

Bai Y, Zhao N, Zhang R, Zeng X (2018) Storm water management of low impact development in urban areas based on SWMM. Water (Switzerland) 11(1). https://doi.org/10.3390/w11010033

Bond J, Batchabani E, Fuamba M, Courchesne D, Trudel G (2021) Modeling a bioretention basin and vegetated swale with a trapezoidal cross section using SWMM LID controls. J Water Manag Model 29. https://doi.org/10.14796/JWMM.C474

Cohen-Shacham E et al (2019) Core principles for successfully implementing and upscaling nature-based solutions. Environ Sci Policy 98. https://doi.org/10.1016/j.envsci.2019.04.014

D'Ambrosio R, Balbo A, Longobardi A, Rizzo A (2022) Re-think urban drainage following a SuDS retrofitting approach against urban flooding: a modelling investigation for an Italian case study. Urban For Urban Greening 28:127518. https://doi.org/10.1016/j.ufug.2022.127518

Environmental Protection Agency (2012) Urban runoff: low impact development

Gülbaz S, Kazezyılmaz-Alhan CM (2017) Experimental investigation on hydrologic performance of LID with rainfall-watershed-bioretention system. J Hydrol Eng 22(1). https://doi.org/10.1061/(asce)he.1943-5584.0001450

Golden HE, Hoghooghi N (2018) Green infrastructure and its catchment—scale effects: an emerging science. WIREs Water 5(1). https://doi.org/10.1002/wat2.1254

Herrera-Gomez SS, Quevedo-Nolasco A, Pérez-Urrestarazu L (2017) The role of green roofs in climate change mitigation. A case study in Seville (Spain). Build Environ 123:575–584. https://doi.org/10.1016/j.buildenv.2017.07.036

Jeffers S, Garner B, Hidalgo D, Daoularis D, Warmerdam O (2022) Insights into green roof modeling using SWMM LID controls for detention-based designs. J Water Manag Model 30. https://doi.org/10.14796/JWMM.C484

Jiang Y, Yuan Y, Piza H (2015) A review of applicability and effectiveness of low impact development/green infrastructure practices in arid/semi-arid United States. Environ MDPI 2(2):221–249. MDPI AG, Jun 01, 2015. https://doi.org/10.3390/environments2020221

Liu Y, Engel BA, Flanagan DC, Gitau MW, McMillan SK, Chaubey I (2017) A review on effectiveness of best management practices in improving hydrology and water quality: needs and opportunities. Sci Total Environ 601–602:580–593. Elsevier B.V., Dec 01, 2017. https://doi.org/10.1016/j.scitotenv.2017.05.212

Nika CE, Gusmaroli L, Ghafourian M, Atanasova N, Buttiglieri G, Katsou E (2020) Nature-based solutions as enablers of circularity in water systems: a review on assessment methodologies, tools and indicators. Water Research 183:115988. https://doi.org/10.1016/j.watres.2020.115988

Palla A, Gnecco I (2015) Hydrologic modeling of low impact development systems at the urban catchment scale. J Hydrol (Amst) 528:361–368. https://doi.org/10.1016/j.jhydrol.2015.06.050

Paule-Mercado MA, Lee BY, Memon SA, Umer SR, Salim I, Lee CH (2017) Influence of land development on stormwater runoff from a mixed land use and land cover catchment. Sci Total Environ 599–600. https://doi.org/10.1016/j.scitotenv.2017.05.081

Piro P, Carbone M, Morimanno F, Palermo SA (2019) Simple flowmeter device for LID systems: from laboratory procedure to full-scale implementation. Flow Meas Instrum 65:240–249. https://doi.org/10.1016/j.flowmeasinst.2019.01.008

Rodríguez-Rojas MI, Grindlay Moreno AL (2022) A discussion on the application of terminology for urban soil sealing mitigation practices. Int J Environ Res Public Health 19(14). NLM (Medline), Jul 01, 2022. https://doi.org/10.3390/ijerph19148713

Sakshi S, Singh A (2016) Modeling LID using SWMM5 and MIDS credit calculator: credit valley conservation's Elm drive case study. J Water Manag Model. https://doi.org/10.14796/JWMM.C403

Seo M, Jaber F, Srinivasan R, Jeong J (2017) Evaluating the impact of low impact development (LID) practices on water quantity and quality under different development designs using SWAT. Water (Switzerland) 9(3). https://doi.org/10.3390/w9030193

Shaneyfelt KM, Johnson JP, Hunt WF (2021) Hydrologic modeling of distributed stormwater control measure retrofit and examination of impact of subcatchment discretization in PCSWMM. J Sustain Water Built Environ 7(3). https://doi.org/10.1061/jswbay.0000938

Stovin V, Vesuviano G, Kasmin H (2012) The hydrological performance of a green roof test bed under UK climatic conditions. J Hydrol (Amst) 414–415:148–161. https://doi.org/10.1016/j.jhydrol.2011.10.022

Wikipedia (2022) 'Saanich, British Columbia'. https://en.wikipedia.org/wiki/Saanich,_British_Columbia, Last accessed 01 Oct 2022

Xie N, Akin M, Shi X (2019) Permeable concrete pavements: a review of environmental benefits and durability. J Clean Prod 210. https://doi.org/10.1016/j.jclepro.2018.11.134

# Chapter 8
# The Potential of Peripheral Neighborhoods for the Development of Urban Green in Latin American Cities, the Case of Algeria, Quito, Ecuador


**Susana Moya, Doménica Muñoz, and Franco Ortiz**

**Abstract** This article proposes an analysis of the policies and strategies of the city of Quito for the development of urban green, for which the climate action plan of Quito and the plans to be fulfilled until 2030 have been reviewed, as well as the metropolitan corridor and its potential as a green corridor, after this the characteristics of the sector "La Argelia" have been analyzed. as an example of the characteristics of the peripheral neighborhoods of Quito, in order to show the potential that this type of environment has for the development of urban green, in this case from an urban agriculture approach, which could also provide these spaces not only with an economy, but with a circular metabolism, that contributes to the development of the neighborhood and the city.

**Keywords** Climate action plan · Argelia · Retentive architecture

## 8.1 Introduction

Urbanization has always been linked to the processes of change in ecosystems, but it is since industrialization that urban growth has been a serious problem directly related to climate change and the destruction of ecosystems, despite this, as indicated by León Arévalo in 2018, industrialization is seen as "necessary to achieve living standards of the first world, which is a common global goal" (León 2018).

Although industrialization in a certain way "improved" the quality of life of human beings, little by little these urban comforts have affected the stability of the planet's climate, with the least industrialized countries being affected. However, despite experiencing the consequences, industrialization continues to accelerate, at the last climate summit "COP26" in Glasgow, held in November 2021, where the nations that make up the G20, responsible for 80% of the greenhouse gas emissions, agreements described as "timid" by environmentalists were reached, since they do

S. Moya (✉) · D. Muñoz · F. Ortiz
Faculty of Architecture, Arts and Design (FAAD), Universidad Tecnológica Indoamérica, Sabanilla Street, Quito 170103, Ecuador
e-mail: susanamoya@uti.edu.ec



Z. Yang (ed.), *Environmental Science and Technology: Sustainable Development*, Environmental Science and Engineering, https://doi.org/10.1007/978-3-031-27431-2_8

not minimize the accelerated climate change and prioritize economic factors over environmental ones (France24 2021; Carrillo 2021).

In this conference it has been possible to establish the consequences that the increase in temperature will have, as pointed out by the AFP, where for every 1.5 °C increase in temperature in relation to the pre-industrial era, 3,340 million people will be exposed to water stress, 3.96 billion will be exposed to heat waves, and 40,000 to decreased crop yields, which will increase exponentially as temperatures rise. Taking into account that currently the temperature has already risen 1.1 °C, which has caused disasters such as extreme droughts, loss of territory due to the rise in sea level. (France24 2021; Carrillo 2021).

Added to this problem is the densification of cities, since it is expected that by 2030, 61% of the world population will live in cities, with developing countries concentrating around 89% of their population in cities according to with UN-Habitat. In Latin America, the need to manage the secondary effects of growing urbanization is evident, which according to the Global Risks Report 2020 (World Economic Forum 2020) will affect areas such as economic stability and social cohesion, this uncontrolled climate threat, will accelerate the loss of biodiversity, due to the loss of green spaces and the lack of ecological corridors, necessary to maintain biodiversity and a good quality of life for human beings as several studies have shown, however, the lack of planning for urban growth will put pressure on the already disadvantaged health systems of Latin America. (Carrillo 2021; World Economic Forum 2020).

Architecture plays an important role in managing the organization of the city and mitigating the consequences foreseen by the Global Risks Report. Taking into account the population density that cities will reach, the demand for housing will increase, this being a basic human right, the city must provide adequate infrastructure and services, which avoid marginality and its consequences, within this marginality we find the lack of green spaces that in many Latin American cities have a lower percentage in areas where the population has less purchasing power, since peripheral neighbourhoods are often born from the lack of planning and control by the authorities, generating spaces devoid of equipment necessary, which is evident in the lack of green areas. To solve the lack of these spaces, planning is necessary that includes green infrastructures that run through and ensure an adequate and equitable development of the city (United Nations 2014; BBC News Mundo 2021).

The construction of sustainable housing, in which vegetated infrastructures are integrated, would be able to offer services that would reduce pollution levels and the pressure that the population exerts on water and food supplies, since, as the UN-FAO warns, “hunger and deaths could increase significantly in urban areas that do not have regulations to ensure that poor and vulnerable residents have access to food” (BBC News Mundo 2021).

An urban planning based on the proper management of nature, and the agricultural areas of the growing sectors, would give the city the possibility of facing the challenges and even regenerating its environment by creating a circular economy, where these spaces are capable of ensuring feeding the inhabitants of that environment, and even have the potential to supply other spaces in the city, reducing pollution from cargo transport, and improving the economy of the population, by creating a

favourable relationship between society, economy and nature, capable of generating greater interest in sustainable models (Mangunsong 2018).

## 8.2 Methodology

In this context, the work is developed in two phases: (a) the first analyzes the current reality of the planning of sustainable strategies in the city of Quito -Ecuador. Where the current action plans are analyzed, including the 2020 climate action plan, and the strategies to be applied between 2023 and 2030, the metropolitan corridor is also mentioned, with a term until 2050; and (b) the second, integrates the context of one of the peripheral neighbourhoods of the City of Quito, to show the potentialities of the sector, based on the potentialities found in the first stage of the investigation.

The development of the first phase is based on the compilation and bibliographical analysis of the information available in scientific articles, documents and web pages referring to the city. For the second phase, a bibliographic review is carried out, as well as visits to the site and interviews with the population.

## 8.3 Barriers to Urban Green in City Planning

Developing territories such as Latin America are undergoing an accelerated urbanization process, which has reached them without urban planning that contextualizes the growing needs for space and infrastructure. The political, economic and sociocultural barriers that the Latin American city faces have generated in many of them "two cities", where the periphery is plagued by marginal neighbourhoods whose care or relationship with nature takes a back seat, when they are immersed in food and social insecurity, and the lack of services and minimum infrastructures that cover their basic health and sanitation requirements (United Nations 2014; BBC News Mundo 2021).

Orienting a city towards sustainable development, encompassing a set of planning activities for the growth and design of urban infrastructures, without detaching itself from the determining factors of the political, economic and sociocultural environment, to understand and manage solutions to the problems of the environment, is complicated in the context of developing territories, where this process is often limited by slow government planning and the resistance of a market in search of profitability (BBC News Mundo 2021; Mangunsong 2018).

However, awareness of the influence that politics and economics have on the effects of urbanization have led to new government and community planning processes that include neighbourhoods and communities for the regeneration of the urban ecosystem in close relationship with the natural environment, facing climate change, and the needs that this imposes and will impose on the most vulnerable population. (Mangunsong 2018; United Nations Development Program 2021).

**Table 8.1** Effects of the loss of urban green Quito—Ecuador

| Situation | Risks |
|---|---|
| The amount of rain decreases each year, but in months like April since 2015, it has rained 50% more per month than the average between 2004–2014 | Drought and flood risk—Mudslides and landslides |
| Minimum, lower and maximum, higher temperatures (increase of between 2.3 and 2.5 °C) | Heat island |
| Lack of recreational green spaces | Affects in the quality of life |
| Deforestation, lack of green areas, climatic variations, and the growth of the city | Damage to biodiversity |

## 8.4 Effects of the Loss of Urban Green Quito—Ecuador

To enter into context, Quito is located in the Andes mountain range at 2850 m above sea level, at longitude and latitude 0° 15 "S and 78° 35" W, made up of 65 parishes which are divided into 32 urban and 33 rural, 6 of which due to their proximity and the growth of the city, are currently linked to the district. It has two seasons, the rainy season with a prolonged rainy season (October to May) and the dry season of four months (June to September). However, it presents great climatic contrasts during the course of the same day, being able to go down or up several degrees, taking into account that it covers around fifteen types of climates, with an ambient temperature that ranges between 10 and 25 °C as minimum and maximum averages (Instituto Nacional de Eficiencia Energética y Energías Renovables 2017).

A projection carried out by the Secretary of the Environment of Ecuador in 2014, indicates that the metropolitan district will suffer an increase of between 2.3 and 2.5 °C in temperature at different scales in its territory, as a consequence of the loss of urban and peripheral green, since many spaces previously designated as protection areas are currently occupied with the planning of new homes (Table 8.1) (Instituto Nacional de Eficiencia Energética y Energías Renovables 2017).

## 8.5 Sustainable Strategies in the City of Quito—Ecuador

In the city of Quito, currently the most populous city in Ecuador with more than 2 million inhabitants, the expansion of the urban area extends to the outskirts. Being an elongated city limited by a natural mountainous environment, growing urbanization has invaded natural environments of ecological protection, affecting the natural environment and increasing the risk of potential natural disasters, which mainly affect the population that has built their homes in peripheral spaces and their immediate environment, made up in most cases by the most vulnerable population, since land values are usually lower, due to the fact that they are usually disconnected from the

rest of the city, especially from the economic centers, and from the green areas (To and Fernández 2014; Zareba et al. 2017).

In order to seek solutions to the existing urban problems due to the rapid growth of the city, and with the ideal of achieving UNESCO recognition, Quito hopes to carry out the 17 Sustainable Development Goals of the United Nations—ODS for which has developed the "Quito Climate Action Plan", in which several political and technical strategies are proposed, which should be implemented between 2023 and 2030, improving the quality of life of its inhabitants in an equitable way (Table 8.2) (Grochulska and ZInowiec-Cieplik 2019; Roggema et al. 2021).

However, most of them depend on political will since they are at the mercy of the provision of regulations and tools that have not been resolved to date. Although for 2030 it has been planned to promote the strategies mentioned in Table 8.1, for 2050 the implementation of the structural plan developed by the "Metropolitan Corridor" in 2019 is also proposed, which intervenes along approximately 55 km, where it

**Table 8.2** Sustainable strategies climate action plan

| | |
|---|---|
| Sustainable buildings and dynamics of urban growth | Sustainable and Eco-efficient Buildings to Reduce the Carbon Footprint and Increase Resilience |
| | Eco-efficient neighbourhoods and parks |
| | Decarbonization of the energy matrix |
| | Land occupation conditions aligned to climate neutrality |
| Comprehensive management of water resources | Adaptive water management |
| | Infrastructure to increase resilience to climate change |
| Environmental services | Sustainable land management and provision of environmental services |
| | Wildfire Resilience |
| Sustainable agriculture | Sustainable and climate compatible agriculture |
| Governance and climate research | Climate change resilient monitoring |
| | Governance and capacity building |
| Comprehensive and circular management of solid waste | Circular waste management program for climate neutrality |
| | Use of organic waste |
| | Gas capture and energy use of biogas in the landfill |
| Sustainable mobility | Zero emission public transport |
| | Zero emission historic center |
| | Integrated and efficient public transport |
| | Active mobility for an active city |

*Source* Climate action plan of Quito 2020

seeks to solve problems of the city such as the displacement of residential areas from the center to the periphery, taking advantage of these spaces to generate an axis that will allow connecting various urban green infrastructures such as roofs, facades, urban agriculture or parks and public space, with natural green spaces such as of protection, forests or creek edges, this through a network of connectors throughout the urban fabric linking its inhabitants with a socially and environmentally inclusive environment (Plan Nacional de Eficiencia Energética 2017; Plan de Acción de Cambio Climático de Quito 2020).

## 8.6 Potential of Peripheral Neighborhoods in Quito, for Sustainable Development

On the other hand, the strategy of "Eco-efficient Neighborhoods and Parks" denotes the great potential for the development of sustainable housing, which have peripheral neighborhoods of the city. The La Argelia parish located to the south of the Metropolitan District of Quito, adjoins Simon Bolívar Avenue, one of the main arteries of the city, with an area of around 40.37 hectares located in a peripheral area where, in addition to having agricultural characteristics, its location makes it an ideal area to generate green corridors due to its proximity to other natural environments and green areas within the urban area such as the Metropolitan Park of the South, the Epiclachima, the military fort of the same name that has an important extension of green spaces, and a creek edge that crosses the sector (Fig. 8.1) (Plan Nacional de Eficiencia Energética 2017; Plan de Acción de Cambio Climático de Quito 2020).

In its urban history, the relationship of La Argelia with agricultural production is evident. Initially occupied by a farm destined for agriculture and livestock, in 1974 an attempt was made to convert it into an elite housing area, however, this was not achieved, and later the properties were zoned with residential, agricultural, industrial and protection land uses. ecological, (Fig. 8.2) becoming part of a peripheral space with informal construction characteristics due to lack of planning. With a demography made up largely of a population with limited resources, which, as mentioned by the Territorial Planning Commission, "lacks the resources to satisfy the basic needs that allow an adequate level and quality of life" (Municipio del Distrito Metropolitano de Quito 2021).

Although the agricultural tradition of its population has favored urban green since the houses, mostly with informal construction characteristics, are combined with agricultural land where we can find crops or raise animals, which are usually a means of livelihood, which collaborates by covering part of the needs of the inhabitants of the sector, who mostly work during the day outside of Algeria, due to the lack of equipment that allows the sector to work under the regime of a circular economy (Mangunsong 2018; United Nations Development Program 2021; Zumárraga et al. 2021).

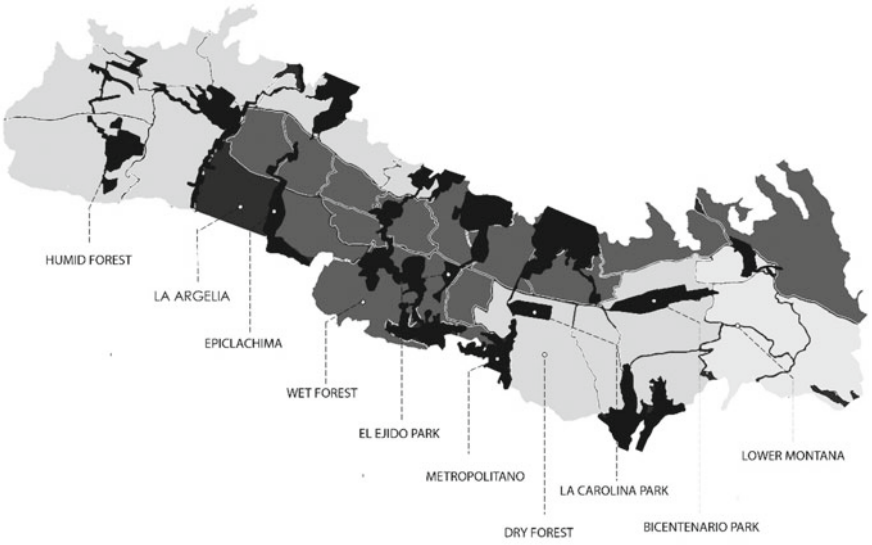


**Fig. 8.1** Identification of natural and urban green areas (urban green infrastructures (parks, public space, natural green areas, protection areas, forests and stream banks)

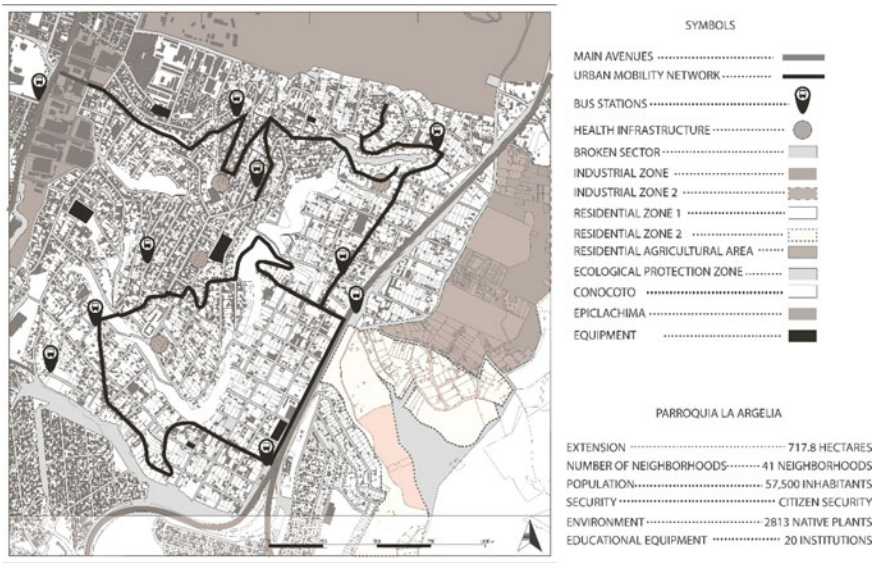


**Fig. 8.2** Land uses and characteristics of La Argelia

To understand the potential of urban green regeneration environments, in peri-urban neighborhoods, we must understand the strong relationship between agriculture and communities in a large part of these environments, taking into account that agriculture also has the potential to achieve a circular metabolism of the city and a sustainable social economy, for this we can take as a comparative example, the "Solidarity Alliance Cooperative in the Recovery of the Ortega Ravine", located south of Quito, in the Quitumbe area, where the social organization was the main tool for the recovery of the sector, through neighbourhood assemblies that allowed shaping its urban environment, generating changes at a social, economic and sustainable level (Zumárraga et al. 2021; Chavez 2014).

Making the majority of the residents aware of the ability to "build neighbourhood networks of local economy" through urban gardens, created from the recovery of the Ortega Ravine, where the production of urban gardens has ceased to be self-consumption for go on to contribute to the economy of the sector through its commercialization (Fig. 8.3) (Zumárraga et al. 2021).

La Argelia, like Quitumbe, is located south of the city where the collective is an important part of the development of the communities, this due to its population composition, which has a large percentage of the population arriving from the countryside, which has migrated in search of a "better quality of life" and that when arriving in the city they find themselves in need of a home, however, as mentioned, in the city the costs depend on the sector where they are located, and they are the peripheries as La Argelia those that allow these new inhabitants to acquire a home owned or rented that allows mixing the urban with the rural, at an affordable value (Zumárraga et al. 2021; Chavez 2014).

This peasant population, mostly from the mountains of the country, brings with it its customs and traditions such as agriculture and community work, which together with the agricultural history of the sector make up an urban and social space with great potential in terms of urban agriculture.

From this predisposition, was born the collective "Family Gardens of La Argelia", whose organization focuses on the development of urban agriculture, within private properties owned by the residents. Prior to the formal configuration of this group, the production of the plots of each family was destined mainly for self-sufficiency, and a fraction of the production was destined for informal marketing. Taking into account that the reality of the labor market in the sector is marked by a large number of people dedicated to informal business and trades, where there is no gender distinction, but if we focus on agriculture, and the trade of its products, it is carried out mainly by women, while men dedicate themselves in greater proportion to other trades that tend to be carried out outside the sector. (Zumárraga et al. 2021; Chavez 2014).

In 2007, a private initiative took advantage of the agricultural trend and informal commerce of the inhabitants of the sector, to organize them in the "Family Gardens of La Argelia" Collective, training them in order to improve the production of family gardens, but also providing them with tools that allow to commercialize their products in a formal way, the intervention of the municipal government provided the residents with a collection center in a municipal property, which improved the logistics of collection, storage and distribution, necessary for the organized commercialization

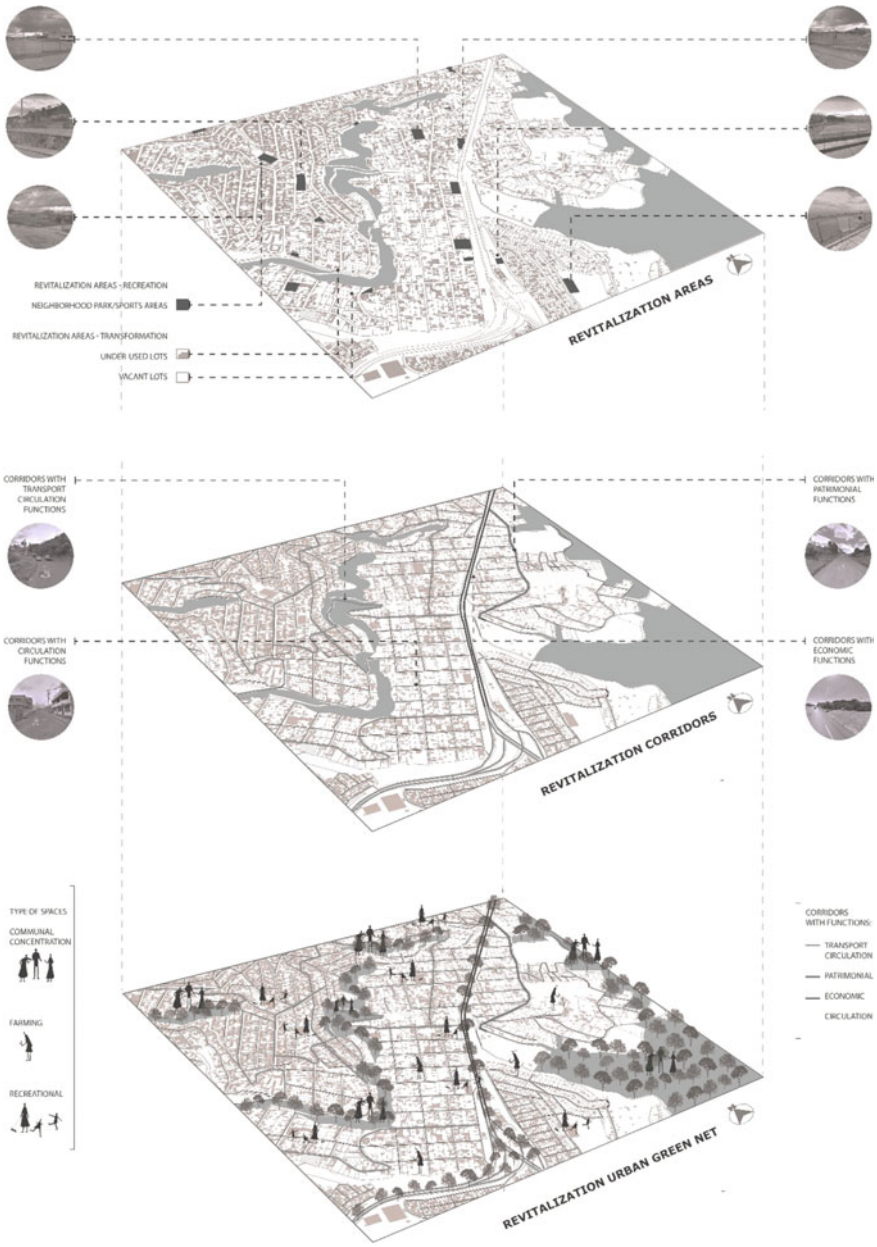


**Fig. 8.3** Revitalization Urban green net

of the products, achieving an efficient implementation of the tools learned (Zumárraga et al. 2021; Chavez 2014).

## 8.7 Conclusions

Currently, the association, made up almost entirely of women, fulfills sovereignty over the city through its relationship with public space through agriculture, aware that the next space to be taken is precisely the public space, allowing them to leave the boundaries of their "family gardens".

There is great potential for development, since green spaces such as the ravine and other properties that, although they are destined for public space, currently have no use or are partially destroyed or lack equipment, and that due to the configuration of the sector would be very useful to promote urban agriculture, taking advantage of them to improve the quality of life and economic capacity of La Argelia (Zumárraga et al. 2021; Chavez 2014).

The model of peripheral neighborhoods such as Quitumbe or La Argelia, in which the community characteristics of the ethnography of these sectors are taken advantage of, makes it possible to develop not only agricultural projects that regenerate the urban environment, but also presents great potential for the economic development of the communities involved, bringing the city closer to achieving its sustainable goals.

## References

BBC News Mundo (2021) 5 Revelaciones del preocupante informe de la ONU sobre cambio climático [Online]. https://www.bbc.com/mundo/noticias-58152731

Carrillo D (2021) WWF Chile 2021 El planeta agota sus recursos este 29 de julio y entra en Sobregiro Ecológico [Online]. https://www.wwf.org.ec/?368250/El-planeta-agota-sus-recursos-este-29-de-julio-y-entra-en-Sobregiro-Ecologico#:~:text=Este%20jueves%2029%20de%20julio,un%20a%C3%B1o%20ya%20est%C3%A1n%20agotado

Chavez M (2014) Mujeres, Agroecología Y Soberanía Alimentaria: Estudio De La (Re)Construcción De La Identidad De Las Campesinas Migrantes En El Barrio La Argelia Alta, Tesis Para Obtener El Título De Maestría En Estudios Socioambientales, Facultad Latinoamericana De Ciencias Sociales

France24 (2021) Países del G20 llegan a la COP26 con un tímido acuerdo sobre el clima[Online]. https://www.france24.com/es/minuto-a-minuto/20211031-pa%C3%ADses-del-g20-llegan-a-la-cop26-con-un-t%C3%ADmido-acuerdo-sobre-el-clima

Grochulska S, ZInowiec-Cieplik K (2019) The regenerative model of the city in view of climatic changes. Redefining cities in view of climatic changes, Warsaw University of Technology Publishing House

Instituto Nacional de Eficiencia Energética y Energías renovables (2017) Estrategias para mejorar las condiciones de habitabilidad y el consumo de energía en viviendas

León K (2018) Análisis de los diferentes sistemas de certificación en construcción sostenible a nivel mundial y sus perspectivas de aplicación y cumplimiento en Colombia. http://hdl.handle.net/10654/20417

Mangunsong R (2018) Tres grandes ideas para lograr ciudades y comunidades sostenibles [Online]. https://www.bancomundial.org/es/news/immersive-story/2018/01/31/3-big-ideas-to-achieve-sustainable-cities-and-communities

Municipio del Distrito Metropolitano de Quito (2021) Plan Metropolitano de Desarrollo y Ordenamiento Territorial del Distrito Metropolitano de Quito, 2021–2033

Plan de Acción de Cambio Climático de Quito 2020 DMQ Neutralidad Climática, (2020) Secretaría de Ambiente del Municipio del Distrito Metropolitano de Quito

Plan Nacional de Eficiencia Energética 2016–2035 (2017) Banco Interamericano de Desarrollo (BID)—Plan Nacional de Eficiencia Energética del Ecuador

Roggema R, Tillie N, Keeffe G, Yan W (2021), Nature-based deployment strategies for multiple paces of change: the case of Oimachi, Japan, planning for rapid change in cities. University of Pretoria, SouthAfrica

To K, Fernández J (2014) Alternative Urban technology for future low-carbon cities: a demonstration project review and discussion springer 10

United Nations (2015) World urbanization prospects. The 2014 revision. United Nations, New York City, NY, USA

United Nations Development Program (2021) Objective 1: sustainable cities and communities [Online]. https://www1.undp.org/content/undp/es/home/sustainable-developmentgoals/goal-11-sustainable-cities-and-communities.html

World Economic Forum (2020) The global risks report 2020 Marsh and McLennan and Zurich insurance group, vol 15. Zurich, Alemania

Zareba A, Krzeminska A, Lanch J (2017) Energy sustainable cities. From eco villages, eco districts towards zero carbon. E3S Web Conf 22(1)

Zumárraga M, Pascual T, Unda M (2021) Acciones colectivas en la recuperación de espacios verdes públicos: Caso Quebrada Ortega, Quitumbe, Quito-Ecuador. Hábitat Y Sociedad (14)

# Part III
# Clean Production and Environmentally Friendly Technology

# Chapter 9
# Development of "DECOAM" Eco-Friendly Detergent that Minimizes Eutrophication


**Betsy Guadalupe Vasquez Orihuela, Karol Adriana Gallardo Rodríguez, and Jose Vladimir Cornejo Tueros**

**Abstract** During the First and Second World Wars, there was a significant increase in wastewater from animal and vegetable fats treated with newly produced detergents. However, these detergents are still conventional and contain in their composition chemical and harmful compounds that affect the aquatic environment. Faced with this problem, it was proposed to develop a biodegradable detergent with low concentrations of phosphorus and nitrogen to minimize eutrophication. The "DECOAM" detergent was made with organic products, its main component being orange peel, which replaces the surfactants contained in conventional detergents. In order to contrast the efficiency of the eco-friendly detergent with conventional detergents, two dirty garments (covered with mud and ash) were washed, one with the conventional detergent and the other with the biodegradable detergent, where both garments were impeccable. Immediately afterward, the samples of each wastewater were taken and the results obtained from the laboratory were: the wastewater from the conventional detergent had the following concentrations: pH (11.15), T° (12.8 °C), Conductivity (11 550 uS/cm), Phosphorus (4. 310 mg/L) and Total Nitrogen (20.24 mg/L); and for the wastewater from the eco-friendly detergent "DECOAM" were: pH (7.01), T° (12.5 °C), Conductivity (448 uS/cm), Phosphorus (0.316 mg/L) and Total Nitrogen (<1.00 mg/L). Finally, it was concluded that the biodegradable detergent has the same efficiency as the conventional detergent in removing the dirt; on the other hand, the concentration of phosphorus and nitrogen were significantly lower compared to the conventional detergent, thus reducing eutrophication in the surface water bodies.

**Keywords** Biodegradable · Eutrophication · Phosphorus · Nitrogen

## 9.1 Introduction

Currently, water pollution has increased significantly, due to the direct discharge of domestic and industrial wastewater into a receiving body, causing the death of aquatic

B. G. Vasquez Orihuela (✉) · K. A. Gallardo Rodríguez · J. V. Cornejo Tueros
Universidad Continental, Huancayo 12000, Peru
e-mail: 74230484@continental.edu.pe



Z. Yang (ed.), *Environmental Science and Technology: Sustainable Development*,
Environmental Science and Engineering, https://doi.org/10.1007/978-3-031-27431-2_9

life (fish), because ammoniacal nitrogen in its free form, as ammonia, is toxic and its toxicity depends on the pH of the water and its temperature (Calvo and Mora 2007).

In the past, the root of the plant called Saqta was used as a soap to wash alpaca wool before spinning, obtaining good results in dirt removal (Gadea et al. 2019), but due to the great demand and the wide need, a great variety of these products have a composition of compounds that are pollutants as they are persistent and are not easily decomposed by bacterial action, and due to their composition they generate negative impacts on the environment (Showell 2006).

Currently, most detergents are sodium compounds of substituted benzene sulphonate, called Linear Alkylbenzene Sulphonates (LAS). Others are branched-chain Alkylbenzene Sulphate (ABS) compounds, which degrade more slowly than LAS (Jurado et al. 2017).

Until the 1970s a common heavy-duty laundry detergent contained 50% sodium tripolyphosphate (phosphate) (Jurado et al. 2017), which when discharged into natural waters lead to environmental problems such as eutrophication.

The dangers to people's health caused by these commercial detergents are due to loss of vision (accident due to contact of detergent in the eyes), gastrointestinal problems, either by inhalation of the detergent or by ingestion, can cause abdominal pain, vomiting, fainting, blood in the feces and excessive use of detergent (hand washing) which can cause irritation of the hands (Jurado et al. 2017).

On the other hand, the effects do not only impact human health but also the ecosystem's health. The most relevant is eutrophication, also known as water ageing, which is caused by the oversaturation or excess of major nutrients such as nitrogen and phosphorus in surface waters, as the presence of total nitrogen, soluble phosphorus and turbidity are indicators of this phenomenon (Jimenez et al. 2016), or explained in another way, these nutrients in excess cause algal growth (proliferation), which with the passage of time decay, producing foul odors as the putrefaction consumes a large amount of dissolved oxygen, causing the interruption of the growth of the aquatic ecosystem and thus leaving the receiving body in a bad state (destruction of the ecosystem) due to such anaerobic conditions (Jimenez et al. 2016). Another effect is generated by the surfactant compounds of synthetic detergents, which also tend to be unfavorable, because they act as inhibitors of bacteria, fungi, etc., as a consequence, these organisms do not fulfill their functions causing an adverse effect on the environment (Waldhoff 2004; Ashforth and Calvin 1993).

Despite these circumstances, in our country, the use of these commercial detergents is still promoted due to their great need, as they cover various sectors such as the automotive, paper, and textile industries, in the production of inks, paints, and dyes and even to remediate contaminated ecosystems, for example, due to oil spills or others (Gadea et al. 2019); they are also widely used in other settings such as homes, educational centers, and health establishments. Furthermore, in recent years, their commercialization has increased and they have positioned themselves as an important sector of the industry in the country's economy. In addition, in the years 2020–2021 (Covid-19 pandemic), there was a disproportionate increase in the use of cleaning products, including conventional detergents, in homes, commercial centers, and health centers, since the World Health Organization recommended that

all spaces, surface areas, clothing, and hands should be clean (Adams et al. 2016). For these reasons, the aim of this article is to reduce the adverse effects caused by the different petroleum-based chemicals found in commercial detergents, through the production of a homemade eco-friendly detergent that represents a beneficial environmental, social and economic alternative.

## 9.2 Materials and Methods

### *9.2.1 A Conventional Detergent Formulations*

Current detergents are mainly composed of one or more surfactants (Anionic, Nonionic, among others) and different components such as silicates, citrates, zeolites, carbonates, bleaching agents, perborates, enzymes, and coloring agents (Warne and Schifko 1999).

### *9.2.2 "DECOAM" Eco-Friendly Detergent Formulations*

The eco-friendly detergent "DECOAM", is composed of natural ingredients as described in Table 9.1. In addition to providing efficient cleaning, this product has a protective effect on the garments and surfaces to which it is applied and even provides a number of desired characteristics in regard to color, odor, feel and others.

The inputs used for the formulation of the eco-friendly detergent are shown in Table 9.2, where the active material is orange peel.

**Pure Coconut Oil**. During the last few years, the use of plant-derived surfactants has increased and they are therefore ecosystem friendly. Table 9.3 shows the nutritional information per 100 g of product.

**Table 9.1** Formulation of eco-friendly detergent according to components

| Components | Detergent biodegradable "DECOAM" |
|---|---|
| Surfactant | Saponin and limonene (orange peel, coconut oil, and clay) |
| Enhancers | Zeolites, sodium citrate, and citric acid (orange peel) |
| Bleaching agents | Citric acid |
| Presentation auxiliary agents (Brighteners) | Clay and coconut oil |

**Table 9.2** Inputs for the production of the eco-friendly detergent

| Products | Quantity | Unit |
|---|---|---|
| Orange peel | 0.25 | kg |
| Clay | 0.25 | kg |
| Pure coconut oil | 50 | ml |

**Table 9.3** Nutritional information

| Totals fats | Percentage (%) |
|---|---|
| Saturated fats | 94.13 |
| Monounsaturated fats | 5.01 |
| Polyunsaturated fats | 0.83 |
| Cholesterol | 0 |
| Lauric acid | 50.46 |
| Myristic acid | 18.31 |
| Palmitic acid | 7.87 |
| Caprylic acid | 7.80 |

Alkylpolyglucosides are certainly a highly recommended type of surfactant because they are produced from vegetable oils and fats, can form small amounts of foam, and are beneficial to the skin (Restrepo et al. 2020).

Currently, coconut is a fruit that is highly valued by most people for its pleasant taste and aroma and is also a quality product for cosmetics and cosmetics (Restrepo et al. 2020).

Coconut oil is mainly composed of saturated fatty acids (SFA), where the predominant fatty acids (FA) are lauric, myristic, palmitic, and caprylic acids (Restrepo et al. 2020). We use Santa Natura coconut oil, a well-known brand in our country (see Fig. 9.1).

**Orange Peel**. For the formulation of the DECOAM detergent we used Washington navel orange peel (see Fig. 9.2) due to its high vitamin C content (38.69 mg/100 ml) and its consumption is high, it also has nutritional properties such as calcium (53.7 mg/l), phosphorus (157 mg/l), manganese (0.05 mg/l), zinc (2.34 mg/l), magnesium (96.6 mg/l), sodium (12.7 mg), potassium (255 mg/l) and pH (3.62) (Topuz et al. 2005).

**Clay**. It is a natural, non-toxic, and inexpensive mineral, generally used for the removal of ultra-small particles (see Fig. 9.3), and is therefore efficient in adsorbing organic pollutants from water (Ewis et al. 2022).


**Fig. 9.1** "Santa Natura" coconut oil

**Fig. 9.2** Prepared orange peel


**Fig. 9.3** Weighing of clay

### *9.2.3 Procedure for the Elaboration of Eco-Friendly Detergents*

In this point, the different activities for obtaining the inputs for their respective formulation and elaboration are detailed (see Fig. 9.4).

### *9.2.4 Efficacy of "DECOAM" Eco-Friendly Detergent*

An efficacy test of the eco-friendly detergent was carried out against a conventional detergent.

The test consisted of soiling two white garments homogeneously with mud and ashes (see Fig. 9.5), and then washing one garment with the conventional detergent and the other with the "DECOAM" detergent, with the same amount of each.

From this study, it was deduced that the eco-friendly detergent proved to be a very good quality cleaner and remover as it completely removed the sludge and ash from the garment, and its effectiveness is similar to that of the conventional detergent as shown in Fig. 9.6.

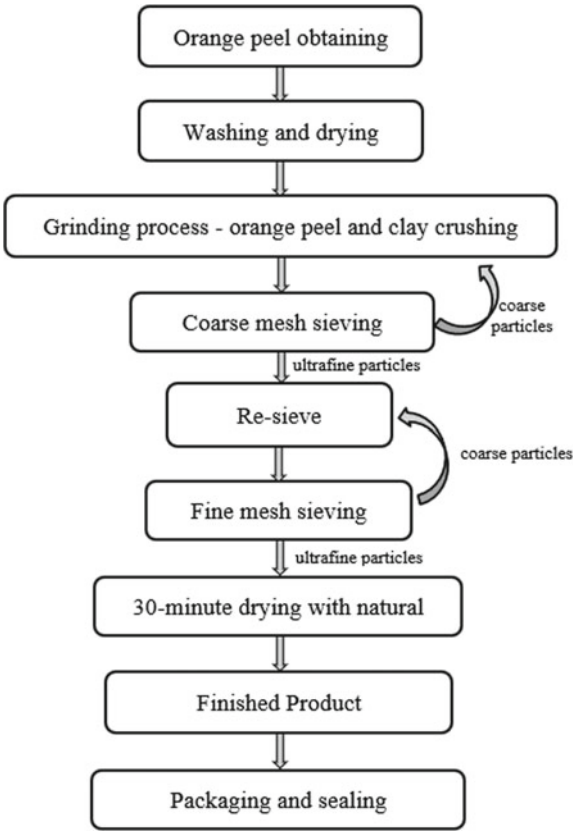


**Fig. 9.4** Diagram of detergent production

**Fig. 9.5** Sample of garments soiled with mud and ash


**Fig. 9.6** Results of both detergents

### *9.2.5 Sample Collection*

The process of experimentation and sample collection was carried out under the same environmental conditions. Samples were taken for each container, so two different samples of wastewater were obtained, which were stored and duly labelled to be taken to the corresponding laboratory.

## 9.3 Results

### *9.3.1 Test Methodology*

Table 9.4 shows the test methodology that was established by the laboratory where the analysis of the parameters was carried out; this accredited laboratory is Servicios Analíticos Generales S.A.C.

### *9.3.2 Sample Analysis*

The samples were analyzed by the laboratory Servicios Analíticos Generales S.A.C. (testing laboratory accredited by the accreditation body INACAL-DA with registration No. LE-047).

**Table 9.4** Analysis methods

| Essay | Method | L.C | Units |
|---|---|---|---|
| pH (field measurement) | SMEWW-APHA-AWWA-WEF Part 4500-H + B, 23rd Ed. 2017. Ph Value. Electrometric Method | Not applicable | pH |
| Temperature (field measurement) | SMEWW-APHA-AWWA-WEF Part 2550 B, 23rd Ed. 2017. Temperature. Laboratory and Field Method | – | °C |
| Conductivity (field measurement) | SMEWW-APHA-AWWA-WEF Part 2510 B, 23rd Ed. 2017. Conductivity. Laboratory Method | – | uS/cm |
| Total nitrogen (NTK) | SMEWW-APHA-AWWA-WEF Part 4500-$N_{org}$-B, 23rd Ed. 2017 Nitrogen (organic). Macro Method | 1.00 | $NH_3^+$ –N mg/L |
| Total phosphorus or phosphorus (P) | SMEWW-APHA-AWWA-WEF Part 4500-P E, 23rd Ed. 2017. Phosphorus. Ascorbic Acid Method | 0.013 | P mg/L |

*Note Q.L.* Limit of quantification

Table 9.5 shows the results obtained for the parameters analyzed for each residual sample, these results were provided in Test Report No. 163758 -2022 with official value.

According to the results, a descriptive comparison was made, and since the cost of analysis per sample in this laboratory is expensive, a careful analysis was made for each parameter.

**Hydrogen Potential**. According to the results obtained for the biodegradable detergent "DECOAM" a pH of 7.01 Unit was obtained, while for the conventional detergent it was 11.15 Unit, Therefore, it can be seen that the "DECOAM" (biodegradable) detergent has a neutral pH similar to that of drinking water and if we talk about

**Table 9.5** Analytical results of water quality—I.E. No. 163758–2022 with official value

| | Unit | Detergent biodegradable "DECOAM" | Detergent conventional |
|---|---|---|---|
| pH | Unid. pH | 7.01 | 11.15 |
| Temperature | °C | 12.5 | 12.8 |
| Conductivity | U/com | 448 | 11.550 |
| Phosphorus (P) | mg/L | 0.316 | 4.310 |
| Total nitrogen (N) | mg/L | <1.00 | 20.34 |

*Note I.E.* Assay Report

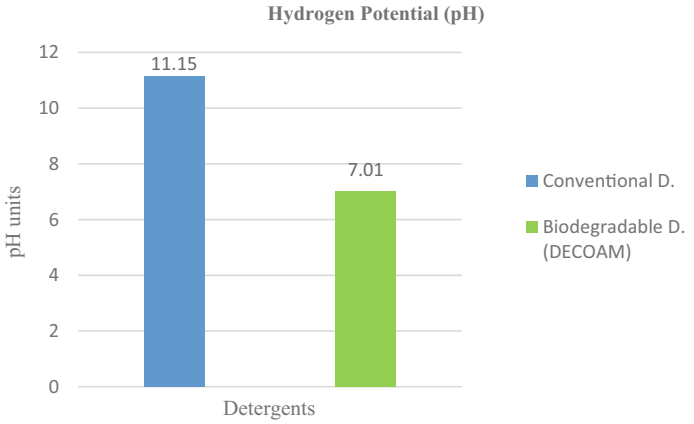


**Fig. 9.7** Analysis of the pH parameter—conventional detergent versus biodegradable detergent "DECOAM"

synthetic detergents, these contain phosphate additives (tripolyphosphate), which makes the water alkaline, that is to say, producing a high pH, as shown in the Fig. 9.7.

In general, pH is one of the most important parameters for determining the quality of water, where it has adverse consequences if it is acidic or alkaline, since these extremes can cause damage to health; however, if it has a neutral pH that varies between 6.5 and 8.5 (where the pH of the biodegradable detergent "DECOAM" is found), it is acceptable and has no harmful effects on health (Pérez 2016).

**Temperature**. For the temperature parameter, it is shown in Fig. 9.8 that for the eco-friendly detergent "DECOAM" a temperature of 12.5 °C was obtained, while for the conventional detergent it was 12.8 °C. It is shown that both temperatures have no significant variation because they were measured under the same conditions of time and space.

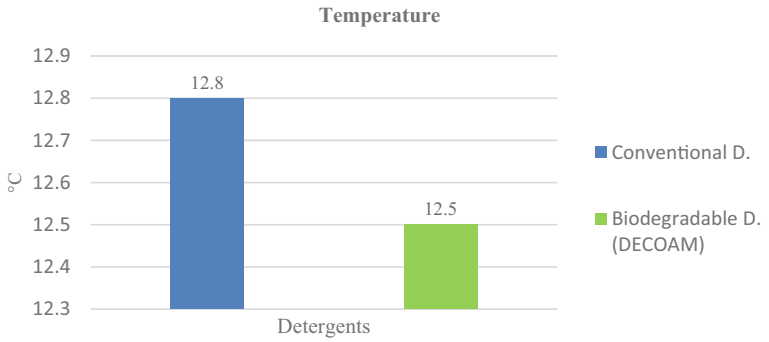


**Fig. 9.8** Analysis of the parameter temperature—conventional detergent versus biodegradable detergent "DECOAM"

**Conductivity**. The results obtained for the conductivity parameter in the biodegradable detergent "DECOAM" were 448 uS/cm while for the conventional detergent 11 550 uS/cm. taking into account that having a high value of electrical conductivity (increase of water hardness) the performance of a detergent decreases significantly (Guevara 2013), as shown in the Fig. 9.9.

**Total Phosphorus or Phosphorus**. Figure 9.10 shows the results obtained for the parameter Total Phosphorus or Phosphorus (includes all types of phosphorus). A value of 0.316 mg/L was obtained for the biodegradable detergent "DECOAM" and 4.31 mg/L for the conventional detergent. In this section we will mention sodium tripolyphosphate (TPFS), which acts as a coadjuvant and is the phosphate of excellence in synthetic detergents, fulfilling its function as a softener, auxiliary surfactant and stabilizer; however, it is one of the elements that enrich surface bodies with nutrients and is therefore one of the compounds that cause eutrophication (Mousavi and Khodadoost 2019; Kogawa et al. 2017).

As for the biodegradable detergent, orange peel is used as a surfactant, which is used as a solvent (cleaning agent) due to the limonene found in the peel (Achimón and Zygadio 2022). And the highlight of its characteristics is that, according to the results in Fig. 9.10, the biodegradable detergent contains minimal and/or almost negligible amounts of phosphorus.

**Total Nitrogen**. The results obtained for the Total Nitrogen parameter were as follows: for the biodegradable detergent "DECOAM" a value of <1.00 mg/L was obtained and for the conventional detergent a value of 20.34 mg/L was obtained.

Conventional detergents contain nitrogen in their composition as well as phosphorus, which are usually a problem in wastewater since these components are not biodegradable (they are not degraded by microorganisms) (Kogawa et al. 2017), on the contrary, they accumulate and cause eutrophication on their way through the receiving bodies, however, the concentration of nitrogen in the biodegradable detergent as shown in Fig. 9.11, unlike the conventional detergent, is approximately 20

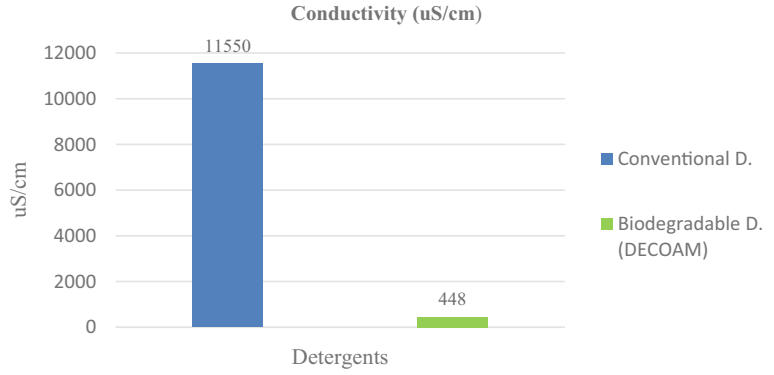


**Fig. 9.9** Conductivity parameter analysis—conventional detergent versus biodegradable detergent "DECOAM"

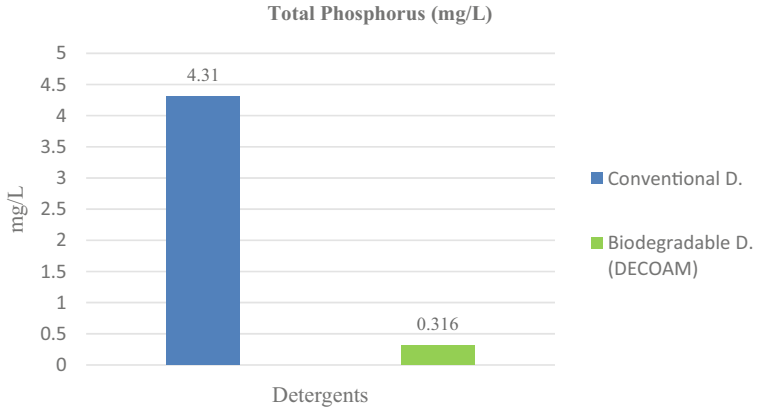


**Fig. 9.10** Analysis of the Total Phosphorus parameter for conventional detergent versus biodegradable detergent "DECOAM"

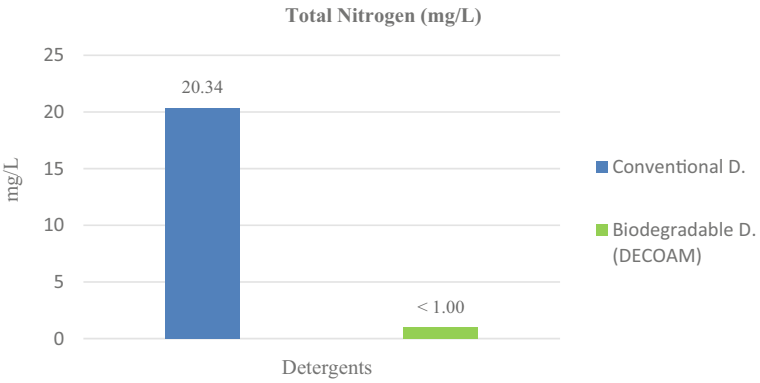


**Fig. 9.11** Analysis of the Total Nitrogen parameter for conventional detergent versus biodegradable detergent "DECOAM"

times less in concentration, which evidently is usually environmentally advantageous compared to synthetic detergents.

## 9.4 Conclusion

It is concluded that the eco-friendly detergent "DECOAM" is indeed a product that minimizes eutrophication due to its low phosphorus and nitrogen content, and it has the same efficiency as conventional detergents.

## References

Achimón F, Zygadio J (2022) Insecticidal and antifungal effects of lemon, orange, and grapefruit peel essential oils from Argentina. AgriScientia 71–82

Adams J, Bartram J, Chartier Y (2016) Normas básicas de higiene del entorno en la atención sanitaria (OMS) 1–62

Ashforth, G., Calvin. G (1993) Safety evaluation of substitutes for phosphates in detergents. Water Res 7(1):309–320

Calvo G, Mora J (2007) Evaluación y clasificación preliminar de la calidad de agua de la cuenca del río Tárcoles y el Reventazón Parte I: Análisis de la contaminación de cuatro ríos del área metropolitana. Tecnología En Marcha 20(2):1–9

Ewis D, Ba-Abbad M, Benamor A, El-Naas M (2022) Adsorption of organic water pollutants by clays and clay minerals composites: a comprehensive review. Appl Clay Sci

Gadea G, Hernández S, Mamani T, Nieves J, Rivera M (2019) Detergente eco amigable: Saphi. UPC, Peru

Guevara R (2013) Proceso de desarrollo y formulación de detergentes. Mexico City

Jimenez L, Jahuira F, Ibañez V (2016) Tratamiento de aguas eutrofizadas de la bahía interior de Puno, Perú uso de dos Macrófitas. Inv Altoandinas 18(4):403–410

Jurado E, Saenz D, Velásquez M, Azáldegui A, Benavides O (2020) Riesgos del uso de detergentes domésticos en la calidad del agua en poblaciones en transición de lo rural a lo urbano: Churín 2017. Alternativa Financiera

Kogawa A, Cernic B, Domingos do Couto L, Nunez H (2017) Synthetic detergents: 100 years of history. Saudi Pharm J 25(6):934–938

Mousavi S, Khodadoost F (2019) Effects of detergents on natural ecosystems and wastewater treatment processes: a review. Environ Sci Pollut Res 26(26):26439–26448

Pérez E (2016) Control de calidad en aguas para consumo humano en la región occidental de Costa Rica. Tecnología En Marcha 29(3):3–14

Restrepo M, Zavala L, Guiot L (2020) Aceite de coco: características nutricionales y posibles aportes a la salud humana. Corporación Universitaria Lasallista, Caldas-Antioquia

Showell M (2006) Handbook of detergents Part D: formulation. Taylor & Francis Group, EE. UU (2006).

Topuz A, Topakci M, Canakci M, Akinci I, Ozdemir F (2005) Physical and nutritional properties of four orange varieties. J Food Eng 66:519–523

Waldhoff H (2004) Handbook of detergents Part C: analysis. California, Boca Raton

Warne M, Schifko A (1999) Toxicity of laundry detergent components to a freshwater cladoceran and their contribution to detergent toxicity. Ecotoxicol Environ Saf 44:196–206

# Chapter 10
# Essential Oils of Plants as Biocides Against Microorganisms Isolated from Portuguese Convent of Christ in Tomar


**Dina M. R. Mateus, Fernando M. C. Costa, and Ricardo P. Triães**

**Abstract** Biodeterioration observed in art and architectural works holding patrimonial value is primarily due to the proliferation of various microorganisms, that through their energy-producing metabolisms lead to the formation of biotic substances that can attack the physicochemical structures of artworks' constitutive materials. In conservation-restoration, different biocides of synthetic origin which exhibit some human and environmental toxicity are traditionally used. Natural resources exploitation awareness and side effects of common disinfectants and inhibitors led to the need for natural compounds with biocidal effects. This work aimed to evaluate the possible use of essential oils (EOs) extracted from endogenous plants as novel conservation products against the biocolonization of cultural heritage materials. The biocidal potential of five EOs extracted from the indigenous plants *Thymus mastichina* (Tm), *Helichrysum stoechas* (Hs), *Mentha pulegium* (Mp), *Foeniculum vulgare* (Fv) and *Lavandula viridis* (Lv) were evaluated. Microorganisms collected at an emblematic site of the country's cultural heritage, Convent of Christ in Tomar, were used to evaluate the biocidal activity of the EOs at concentrations of 2, 10 and 20% (v/v), emulsified in water with 0.2% SDS (m/v). For the tested conditions and comparatively to the commercial biocide Biotin T (1% v/v), it can be concluded that: (i) Hs didn't exhibit fungicidal nor bactericidal activity; (ii) Tm exhibited only bactericidal activity; (iii) in contrast, the other EOs exhibited both fungicidal and bactericidal activity. The results allow considering the use of Tm, Mp, Fv and Lv EOs as a valid alternative to commercial biocides, providing a prospective of application in the field of green conservation of Cultural Heritage.

**Keywords** Biodeterioration · Built heritage · Essential oils · Green biocides · Plant extracts

D. M. R. Mateus (✉) · F. M. C. Costa · R. P. Triães
Technology, Restoration and Arts Enhancement Center (Techn&Art), Instituto Politécnico de Tomar, Tomar, Portugal
e-mail: dinamateus@ipt.pt

D. M. R. Mateus
Bioenergy and Applied Biotechnology Lab (BIOTEC.IPT), Instituto Politécnico de Tomar, Tomar, Portugal



Z. Yang (ed.), *Environmental Science and Technology: Sustainable Development*, Environmental Science and Engineering, https://doi.org/10.1007/978-3-031-27431-2_10

## 10.1 Introduction

The safeguard of cultural assets is contemporary with the purpose of enhancement and use of cultural heritage. In this protective and forestalling action, various conservation and restoration interventions aim to minimize the degradation of the materials of cultural interest. On the other hand, the twenty-first century brought, along with a touristic boom, environmental concerns which led to many studies on the safety of chemicals used in the Conservation and Restoration of cultural heritage elements (Allsopp 2011).

Biological agents that contribute to deterioration, commonly associated symbiotically in biofilms, comprise fungi and bacteria playing as major culprits in the biodeterioration of organic and inorganic materials (Martin-Sanchez et al. 2012; Mateus et al. 2013; Meng et al. 2017). Given their complex metabolic activities, which include the production of organic and inorganic acids (Allsopp 2011; Sterflinger and Piñar 2013), further convoluted by ecological succession when combined with micro-climatic characteristics, most solutions focus on destroying such microorganisms. Common biocides are produced to eliminate and inhibit the growth of microorganisms, but most biocides can cause damage to heritage artefacts. Biocides such as quaternary ammonium compounds, phenol, aldehydes and alcohol are clear examples of disinfectant biocides, with temporary results and long-term damage to preservation (Mateus et al. 2013; Meng et al. 2017; Zhang et al. 2018). Where current biocide solutions have failed, either due to their environmental hazards or toxicity, the future embraces the need for the development of new materials, including plant essential oils (Mota et al. 2015). These may hold the key to effective conservation of cultural heritage, combining the environmental safety with non-destructive action. At present, marketed biocides have a specific action mechanism that affects cell wall synthesis causing DNA and RNA damage and are highly toxic to humans, even to the touch, leaving conservators at high risk (Varnai et al. 2011; Ashraf et al. 2014). Plants, on the other hand, have lower toxicity and environmental suitability, and can be easily handled.

Natural resources exploitation awareness and side effects of disinfectants and inhibitors led to the need for new materials with biocidal effects. Biocides with a wide spectrum of activity and low cost, favouring natural materials with easy handling, environmental stability and lower toxicities, are currently preferred (Kakakhel et al. 2019). Some characteristics of plants are relatively well known in alternative medicine, the conservation market, however, does not hold such an important economic relevance, hence the lack of research. Research on plants, lichens and mushrooms brought to the biodeterioration field knowledge that such groups can be used as the most promising biocides which are environmentally and ecologically friendly. Plant species such as *Schinus mole*, *Mentha piperita*, *Lavandula angustifolia*, *Rosmarinus officinalis*, *Foeniculum vulgare*, and *Origanum vulgare*, among others, have proven effective antifungal and antibacterial characteristics (Mota et al. 2015; Kakakhel et al. 2019; Jeong et al. 2018; Stupar et al. 2014). Undoubtedly, plant extracts represent a research opportunity.

The idea underlying this study is focused on the use of green biocides in the conservation of cultural heritage, protecting biodiversity, strengthening natural resources and optimizing their use, increasing land productivity and avoiding pollution along the whole life cycle, thus contributing to the achievement of sustainable preservation of cultural heritage. The main objective of this study is to encounter new natural materials extracted from plants that can be used as biocides in the preservation of cultural heritage. The biocidal potential of five EOs extracted from Portugal endogenous plants, namely *Thymus mastielina* (Tm), *Helichrysum stoechas* (Hs), *Mentha pulegium* (Mp), *Foeniculum vulgare* (Fv) and *Lavandula viridis* (Lv), were evaluated. Microorganisms collected from the emblematic site of the country's cultural heritage Convent of Christ in Tomar, Portugal (classified UNESCO world heritage), were used to assess the biocidal activity of the EOs. The use of mixed cultures for in vitro biocidal tests was one of the main innovations of the present study. In the authors' knowledge, only studies with pure isolated cultures are reported in the literature.

## 10.2 Experimental

### *10.2.1 Site Description*

Convent of Christ is the name usually given to the monument ensemble consisting of the Templar Castle of Tomar (Portugal), the Order of Christ Convent of Rebirth, the conventual wall, the Immaculate Conception Hermitage and the conventual aqueduct. The castle had its foundation in 1160 and comprised the walled village, the yard and the military house situated and the knight's round-shaped Oratorium known as Charola, finished in 1190. This group of spaces, built throughout the centuries, makes the Convent of Christ a grandiose monument complex that earned the UNESCO Heritage of Mankind distinction (Cristo 2022). The Main Cloister (MC) of the Convent of Christ is the masterpiece of the Renaissance convent built by King John III, situated outside the castle walls and surrounding the nave that his father—King Manuel I—used to extend the Templar church. It is a part of the set of four large cloisters in which the formal structure of the conventual spatiality is placed. The MC, adjacent to the conventual church, flanks the Southern façade of the Manueline nave. Its outline is diverse from the rest of the Castilian conventual architecture. Redone in a Mannerist Italian Cinquecento style by Diogo de Torralva, after Castilho's passing, this cloister receives its water from the conventual aqueduct—in a work by Fernandes Torres (Cristo 2022). The MC has a quadrangular shape, measuring approximately 38 m × 43 m and consists of four galleries and 3 floors, the last one comprising a terrace (Fig. 10.1). The material used in its construction was predominantly limestone. In the interior of the cloister and in the architectural elements of the galleries, the rigged stone blocks predominate. The walls of the galleries exhibit irregular mortar masonry, the vaults have limestone staves and keys, and roof is made

**Fig. 10.1** South elevation of the Main Cloister of Convent of Christ in Tomar

of brick and plastered. The cloister limestones are similar to the ones found in the region, described as dolomitic limestones from the Jurassic. They are slightly granular, with yellowish, whitish and sometimes greyish colours (Machado 1992). As in the sampling sites (south elevation), most of the elevations reveal intense biological colonization, mainly biofilms and lichens but also mosses and higher plants. The existence of fissures, gaps, and old and recent detachments, as well as differential erosion and limestone concretions, can also be observed.

### *10.2.2 Microorganism Collection and Characterization*

The microbial population to be used in the biocidal evaluation of the EOs was collected by swabbing from pigmented biofilms formed on the limestone walls and columns of the MC (Fig. 10.2). Four samples were collected from different locations selected by visual inspection of the pigmented areas. The swabs were immersed in 9 ml of sterile Ringer's solution and kept sealed at 4 °C for later usage.

Two media were used for isolation and subculture of heterotrophic microorganisms: Tryptic Soy Agar (TSA) (HiMedia) as a specific medium for bacteria; Potato Dextrose Agar (PDA) (HiMedia) supplemented with chlortetracycline for the growth of fungi. Autotrophic organisms were selected with BG-11 media agar.

Heterotrophic microorganisms were grown in an incubator without light and autotrophic microorganisms in an incubator with a photoperiod of natural light, both at a temperature of 22 °C.

Gram stain colouration and tests for the presence of catalase and oxidase were performed for the bacterial isolates. Classification of the fungal isolates was based on their macro and microscopic observation, under a light microscope (Olympus CH30) with particular attention to reproductive structures.

**Fig. 10.2** Sample collection from various pigmented biofilms formed on the limestone walls of the Main Cloister

### *10.2.3 Essential Oils and Preparation*

Five essential oils from the Portuguese endogenous plants *Thymus mastichina*, *Helichrysum stoechas*, *Mentha pulegium*, *Foeniculum vulgare* and *Lavandula viridis* were selected for their easy access and reference in the literature to biocidal activity (Fidanza and Caneva 2019; Palla et al. 2020; Marco et al. 2020), or popular belief of antiseptic properties. The EOs were kindly provided by the company Dalenguadiana, located in the Guadiana Valley Natural Park—Corte Sines (Mértola, Portugal). The EOs were produced in organically by hand-harvesting the plants and then by hydro-distilling them in stainless-steel stills. The EOs composition was previously characterized through gas chromatography-mass spectrometry (Baptista et al. 2022). The EOs were tested in three concentrations, 2, 10 and 20% (v/v). Sodium dodecyl sulfate (SDS) (Duchefa Biochemie) was used to emulsify the EOs in sterile deionised water at a fixed final concentration of 0.2% (m/v).

### *10.2.4 Assessment of Antifungal and Antibacterial Activity of Eos*

Evaluations of antibacterial and antifungal activity of the EOs were performed by the well-known agar disk-diffusion method. The tube swabs, kept at 4 °C, were stirred in a vortex for approximately two periods of 30 s. A volume of 200 µl of the microorganism's suspension was then smeared onto agar Petri dishes via the spread plate method. Then, for each tested essential oil, one to three 6 mm filter paper disks (Macherey–Nagel) containing the tested EO were placed on the agar surface. The Petri dishes were incubated at 22 °C for four days, after which the diameters of growth inhibition zones were measured. PDA agar medium, supplemented with

chlortetracycline to inhibit the growth of bacteria, was used for the assessment of antifungal activity. TSA agar medium was used to assess bacteria sensibility to the EOs.

The commercial biocide Biotin T (CTS SRL) was selected as the positive control. Biotin T (BT) is a concentrated liquid preparation of the active substances n-octyl-isothiazolinone and a quaternary ammonium salt. BT is widely used in the preservation of surfaces like stone materials, mortars, frescoes, bricks, etc., from microbiological attacks (Mateus et al. 2013; C.T.S. S.r.l. 2022). BT was used at the concentration recommended by the supplier of 1% (v/v), the dilution was made with sterile deionized water. A solution of DNS (0.2% m/v) in deionized water was used as the negative control. All procedures were conducted under sterile conditions and in triplicate.

## 10.3 Results and Discussion

### *10.3.1 Isolation and Characterization of Microorganisms*

A total of four fungal species and one bacterial specie were originally isolated from the specimens collected from the limestone supporting walls and pillars of the Main Cloister's of the Convent of Christ. Fungi of the genus *Penicillium* were the main cultivable microorganisms detected, which is in agreement with previous studies (Rosado et al. 2016). In the second round of isolation, the following microorganisms were identified (Fig. 10.3): (i) four fungi, including a specie of the genera *Penicillium*, two species of the genera *Cladosporium* and the black yeast *Aureobasidium pullulans*; (ii) one staphylococcus bacterium (yellow colonies, Gram-negative and catalase and oxidase positive). No autotrophic microorganisms cultivable in the laboratory were detected, despite one of the sampled biofilms being visibly contaminated with green colonization (Fig. 10.2).

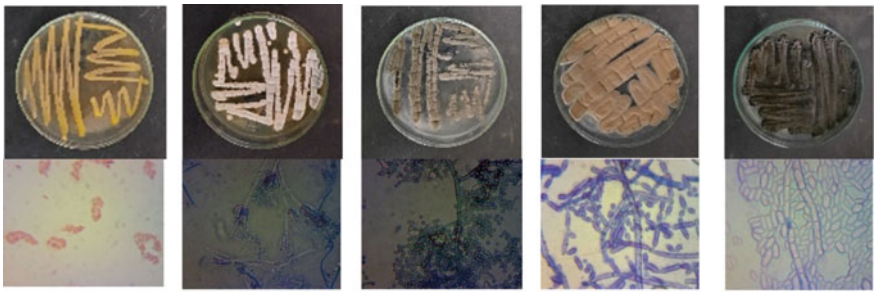


**Fig. 10.3** Isolated colonies and their microscopic observation (1000× for bacteria and 400× for fungi): **a** Staphylococcus bacterium; **b** *Penicillium sp.*; **c**, **d** *Cladosporium sp.*; **e** *Aureobasidium pullulans*

Microbiology identification techniques based on morphological appearance and biochemical characteristics are very useful and have a strong impact due to the ability to cover biotic and abiotic aspects, representing and added-value to characterization of the unseen effects and problems of biodeterioration induced by microbial colonization. Due to the importance of accurate identification of the species, the identification of microflora by molecular biology techniques is foreseen for future works.

### *10.3.2 Assessment of Antifungal and Antibacterial Activity of Eos*

With the goal of setting up green conservation strategies, the antimicrobial activities of *Thymus mastichina*, *Helichrysum stoechas*, *Mentha pulegium*, *Foeniculum vulgare* and *Lavandula viridis* essential oils were assayed in vitro against the mixed population of microorganisms present in the samples collected from the MC. The biodeteriorative action in historic monuments is exerted by several microorganisms, which live symbiotically in biofilms developed on the surface of the monuments' support materials. To evaluate the biocidal activity of the EOs close to real field conditions, it was decided to carry out the biocidal assays with the mixed populations of the microorganisms collected, and in the same proportion of the sampling. Thus, the suspensions of microorganisms collected in the sampling sites were directly used in the biocidal experiments. Assays were carried out in TSA medium for heterotrophic bacteria and in PDA medium for fungi, and this was the only enrichment performed. The use of mixed cultures for in vitro biocidal tests was one of the main innovations of the present study. In the authors' knowledge, only studies with pure isolated cultures are reported in the literature. Biocidal assays with BG11 medium were not performed because autotroph microorganisms cultivable in laboratory were not isolated from the samples collected.

Figures 10.4 and 10.5 show examples of the growth-inhibition-halo diameters.

The diameter of the inhibition halos was used as a measure of the antimicrobial action (sensible >0.6 cm, resistant <0.6 cm). To standardize conditions, and better

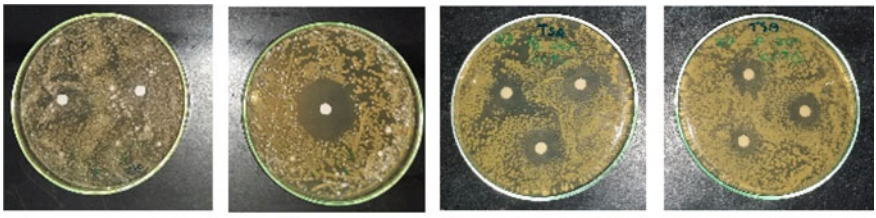


**Fig. 10.4** Agar disc diffusion method inhibition halo of growth for antibacterial activity (inoculation on TSA medium): **a** Negative control (DNS aqueous solution, 0.2% m/v); **b** Positive control (BT 1% v/v); **c** Mp EO (20%); **d** Fv EO (20%)

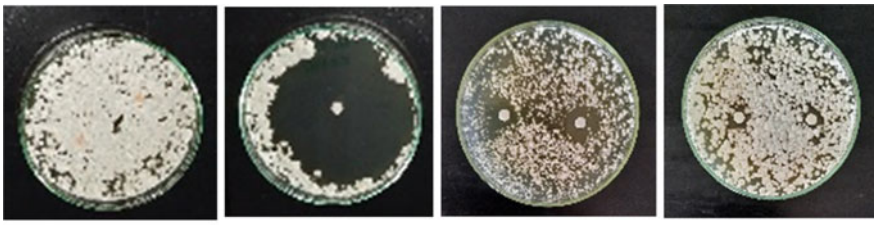


**Fig. 10.5** Agar disc diffusion method inhibition halo of growth for antifungal activity (inoculation on PDA medium): **a** Negative control (DNS aqueous solution, 0.2% m/v); **b** Positive control (BT 1% v/v); **c** Mp EO (10%); **d** Fv EO (10%)

compare results from different experiments, the relative diameter of the inhibition halos was calculated. The relative diameter was calculated by dividing the diameter of the inhibition halo by the diameter of the halo of the positive control (BT) of the respective set of experiments. The results obtained for the five EOs are presented in Table 10.1.

The results of the antibacterial assays showed that among the five EOs tested, the only one that did not demonstrate bactericidal activity in any of the concentrations tested (2, 10 and 20%) was the EO obtained from Hs. Lv EO has proven to be the most effective in concentrations of 10 and 20%, with an inhibitory effect corresponding to 36 and 63% of the commercial biocide BT. The aqueous solution of BT was more

**Table 10.1** Relative average diameter (±standard deviation) of the EOs inhibition halos, using Biotin T inhibition halos as reference (4.2 ± 1.0 cm for bacterial and 6.7 ± 0.4 cm for fungal assays). Resistant (R) corresponds to absolute inhibition halos <0.6 cm

| Biocide | Concentration (v/v %) | Relative inhibition halo (Antibacterial action) | Relative inhibition halo (Antifungal action) |
|---|---|---|---|
| *Thymus mastichina* (Tm) | 2<br>10<br>20 | R<br>0.32 ± 0.04<br>0.44 ± 0.03 | R<br>R<br>R |
| *Helichrysum stoechas* (Hs) | 2<br>10<br>20 | R<br>R<br>R | R<br>R<br>R |
| *Mentha pulegium* (Mp) | 2<br>10<br>20 | R<br>0.31 ± 0.01<br>0.58 ± 0.04 | R<br>0.24 ± 0.01<br>0.37 ± 0.03 |
| *Foeniculum vulgare* (Fv) | 2<br>10<br>20 | 0.22 ± 0.05<br>0.27 ± 0.03<br>0.52 ± 0.03 | R<br>0.16 ± 0.01<br>0.30 ± 0.02 |
| *Lavandula viridis* (Lv) | 2<br>10<br>20 | R<br>0.36 ± 0.03<br>0.63 ± 0.12 | R<br>0.18 ± 0.07<br>0.25 ± 0.07 |

effective against the bacteria colonizing the limestone of the CCT than the EOs. This result is not unexpected due to the high toxicity of the active components of BT (n-octyl-isothiazolinone and a quaternary ammonium salt). Natural biocides are intended to be a compromise solution that allows the control of the biodeterioration of cultural heritage while being more ecological and environmentally friendly.

It could also be observed that for the EOs Tm, Mp, Fv and Lv, and within the range of concentrations tested, the inhibitory effect increases with increasing EO concentration. The EO obtained from Fv was the only one that revealed biocidal activity at the lower concentration (2%).

These results confirm results from previous studies, where *Thymus*, *Mentha*, *Foeniculum* and *Lavandula* EOs were active against bacterial pathogens and human normal microflora species (Roldán et al. 2010). Despite the importance of bacterial species in the biodeterioration of cultural heritage, very few studies address the use of EOs against bacterial species isolated from supporting materials of artworks and architectural heritage (Fidanza and Caneva 2019).

In line with what was observed for bacteria, the aqueous solution of the commercial biocide BT was also more effective against fungi colonizing the CCT limestone than the tested EOs.

Table 10.1 also contains the antifungal activity of the five EOs tested. Tm and Hs EOs did not reveal biocidal activity at any of the concentrations tested. On the other hand, the EOs obtained from Mp, Fv and Lv, despite not showing biocidal activity at a concentration of 2%, showed activity at the concentrations of 10 and 20%.

Mp EO proved to be the most effective, showing an inhibitory effect of 24% and 37% at concentrations of 10 and 20%, respectively. In the literature, a low efficacy for *Menta piperita* against fungus of genera *Alternia*, *Aspergillus, Cladosporium*, *Penicillium* and *Rhizopus* is reported (Levinskaitė and Paškevičius 2013). On the other hand, moderate antifungal activity was reported by Sakr et al.(Sakr et al. 2012) for *Mentha spicata* against fungi of genera *Candida*, *Saccharomyces* and *Lodderomyces.*

Fv EO had an inhibition halo of 16 and 30% at the concentration of 10 and 20%, respectively. Different results were found in the literature for Fv EO. The effect reported in the literature varies from no inhibition or low inhibition against fungi of genera *Candida*, *Lodderomyces* and *Saccharomyces* (Sakr et al. 2012), but high efficacy for the genera *Penicillium*, *Alternaria* and *Epicoccum* (Mironescu and Georgescu 2010).

Lv EO had a moderate fungicide activity of 18% and 25% when compared to BT. The literature reports values from low to high fungicidal efficacy for *Lavandula sp.* (Stupar et al. 2014; Mansour 2013).

The effectiveness of EOs reported in literature is markedly variable, and this can be ascribed to the variability in the methodologies of testing.

In our work, Tm EO did not show fungicide activity against the fungi present in the samples collected (*Penicillium sp.*, *Cladosporium sp.* and *Aureobasidiun pullulans*). Contradictory results were found in the literature for EOs of *Thymus sp.* High biocidal activity of essential oils extracted from the species *Thymus vulgaris* and *Thymus serpyllum* against species of the genera *Penicillium*, *Alternaria* and *Aureobasidium* were reported by Mironescu et al. (2010). However, low efficacy is reported by

Levinskaitè and Paškevičius (2013) for *Thymus pulegioides* against fungus of the genera *Alternaria*, *Aspergillus*, *Cladosporium*, *Penicillium* and *Rhizopus*.

## 10.4 Conclusions

For the cultivable microorganisms present in the sample collected from the limestone supporting walls and pillars of the Main Cloister's of the Convent of Christ, under the tested conditions and comparatively to the commercial biocide Biotin T (0,1% v/v), it can be concluded that:

(i) *Helichrysum stoechas* essential oil did not exhibit fungicidal nor bactericidal activity.
(ii) *Thymus mastichina* EO did not exhibit fungicidal activity.
(iii) The EOs from *Mentha pulegium*, *Foeniculum vulgare* and *Lavandula viridis* all exhibited fungicidal and bactericidal activity; for aqueous emulsions of these essential oils, it was found that the biocidal efficacy increases with increasing concentration of essential oil.
(iv) For the concentration of 20% (v/v) the EOs of *Thymus mastichina*, *Mentha pulegium*, *Foeniculum vulgare* and *Lavandula viridis* showed high efficacy, respectively 44, 58, 52 and 63%, against the cultivable bacterium present in the collected samples.
(v) For the concentration of 20% (v/v) it can be reported that the EOs obtained from *Mentha pulegium*, *Foeniculum vulgare* and *Lavandula viridis* showed average efficacy, respectively 37, 30 and 25% against the mixed culture of fungi belonging to genera *Penicillium*, *Cladosporium* and *Aureobasidium*.

From this research, it can also be concluded that the biocidal activity depends on the concentration and species of the microorganisms assayed, as well as the method used, which makes the comparison between different studies in the literature difficult. For instance, research reporting higher biocidal activity of EOs is usually associated with use of higher concentrations of essential oils, and sometimes the efficacy is compared with commercial biocides at concentrations lower than the recommended by the producers (Palla et al. 2020).

The results obtained so far must, however, be considered as the first promising step in a novel research field, which discloses new opportunities and stimulates further investigations. In this perspective, more in vitro assays need to be performed to evaluate the inhibition activity of the identified EOs against other cultural heritage biodeteriogens, as well as ecotoxicological tests to evaluate human and environmental toxicity of EOs. Afterwards, experimental studies must be carried out to evaluate the possible interaction between the biocide compounds and cultural heritage materials. Among them, the long-lasting biocidal effect shown by the EOs must be underlined. Although more studies are needed to evaluate their permanence and durability in the thermo-hygrometric conditions of storage and usage, we consider that the natural biocides *Thymus mastichina, Mentha pulegium*, *Foeniculum vulgare* and *Lavandula*

*viridis* could be used as a valid alternative to commercial biocides. They provide a perspective of the possible future in the field of green conservation of Cultural Heritage.

**Acknowledgements** Work funded by national funds through the Portuguese National Funding Agency for Science, Research and Technology (FCT) under the project UID/05488/2020. The authors also acknowledge the support of BIOTEC.IPT and LAB.IPT.

## References

Allsopp D (2011) Microbiol Tod 38:150–153
Ashraf M, Ullah S, Ahmad I, Qureshi A, Balkhair K, Rehman M (2014) J Sci Food Agr 94:388–403
Baptista C, Santos S, Amaral M, Silva L (2022) Chemical characterization of essential oils with a biocide base for conservation and restoration. 1st International Proceedings FibEn techn international congress, pp 80-–90. KnE Publishing, Covilhã
C.T.S. S.r.l. (2022). https://www.ctseurope.com/gb/415-biotin-t
Convento de Cristo, Património Cultural, DGPC 2022. http://www.conventocristo.gov.pt/pt/
Fidanza M, Caneva G (2019) J Cult Herit 38:271–286
Jeong S, Lee H, Kim D, Chung Y (2018) Int Biodeter Biodegr 131:19–28
Kakakhel M, Wu F, Gu J, Feng H, Shah K, Wang W (2019) Int Biodeterior Biodegrad 143:104721
Levinskaitė L, Paškevičius A (2013) S. Indoor Built Environ 22:766–775
Machado A (1992) Sedimentary rocks as building materials in the region of Tomar. MSc Thesis Polytechnic Institute of Tomar (in Portuguese)
Mansour M (2013) J Appl Sci Res 3:1917–1930
Marco A, Santos S, Caetano J, Pintado M, Vieira E, Moreira P (2020) Build Environ 167:106459
Martin-Sanchez P, Nováková A, Bastian F, Alabouvette C, Saiz-Jimenez C (2012) Environ Sci 46:3762–3770
Mateus D, Silva R, Costa F, Coroado J (2013) Conserv Patrim 17:11–20
Meng H, Katayama Y, Gu J (2017) Int Biodeter Biodegr 117:78–88
Mironescu M, Georgescu C (2010) Acta Universitatis Cibiniensis. Series e Food Technol 14:41–46
Mota A, Martin M, Arantes S, Lopes V, Bettencourt E, Pombal S, Gomes A, Silva L (2015) Nat Prod Commun 10:673–676
Palla F, Bruno M, Mercurio F, Tantillo A, Rotolo V (2020) Molecules 25:730
Roldán L, Diaz G, Duringer J (2010) Rev Colomb Cienc Pecu 23:451–461
Rosado T, Silva M, Galvão A, Mirão J, Candeias A, Caldeira A (2016) Appl Phys A 122:1012
Sakr A, Ghaly M, Abdel-Haliem M (2012) The efficacy of specific essential oils on yeasts isolated from the royal tomb paintings at tanis, Egypt. Int J Conserv Sci 3:87–92
Sterflinger K, Piñar G (2013) Appl Microbiol Biotechnol 97:9637–9646
Stupar M, Grbić M, Džamić A, Unković N, Ristić M, Jelikić A, Vukojević J (2014) Antifungal activity of selected essential oils and biocide benzalkonium chloride against the fungi isolated from cultural heritage objects. S Afr J Bot 93:118–124
Varnai V, Macan J, Ljubičić A, Prester L, Kanceljak B (2011) Occup Med 61:45–52
Zhang X, Ge Q, Zhu Z, Deng Y, Gu J (2018) Microbiological community of the Royal Palace in Angkor Thom and Beng Mealea of Cambodia by illumina sequencing based on 16S rRNA gene. Int Biodeter Biodegr 134:127–135

# Chapter 11
# Numerical Investigation of a 600 MW Tangentially Fired Boiler with Different Particle Sizes of Pulverized Coal


**Zhiwei Li, Pengfei Cui, Ruixiao Ma, Songhan Wang, Ruicai Si, Zhongyan Wang, and Jia Li**

**Abstract** In this study, three different cases (the average diameter of pulverized coal are 50, 60, and 70 μm, respectively) of a 600 MW tangentially fired pulverized-coal boiler are studied. The numerical calculative results show that the high temperature region of furnace expands and the pulverized-coal burnout rate rises with the decrease of particle size because of the much more intense combustion of pulverized coal. The $NO_x$ emission decreases as the decrease of particle size since the stronger reducing atmosphere strain the generation of $NO_x$ and smaller particle size promotes the reduction reaction of $NO_x$.

**Keywords** Pulverized coal · Particle size · $NO_x$ emissions

## 11.1 Introduction

Tangentially fired pulverized-coal boiler possess good ignition stability, uniform air powder mixing and strong adaptability of coal (Habib et al. 2010; Yan et al. 2012). Coal combustion of coal-fired power stations produces a large number of pollutants, nitrogen oxide ($NO_x$) is one of the main pollutants formed during the coal combustion process. $NO_x$ emission into the air not only cause acid rain, causing damage to plants and animals and destroying buildings, but also directly affecting human health. Therefore, reducing $NO_x$ emission is of great significance to environmental protection. With the rapid development of the economy, the demand for electricity has become more prominent.

In recent decades, many researchers conducted numerical simulation on tangentially fired pulverized-coal boilers. Choi and Kim (2009) investigated the characteristics of the flow, combustion, temperature and $NO_x$ emissions in the 500 MW tangentially fired pulverized-coal boiler. Tan et al. (2017) investigated the effect

Z. Li (✉) · P. Cui · R. Ma
Northeast Electric Power University, Jilin City, Jilin, China
e-mail: 657580390@qq.com

S. Wang · R. Si · Z. Wang · J. Li
State Grid Jilin Electric Power Research Institute, Jilin City, Jilin, China



Z. Yang (ed.), *Environmental Science and Technology: Sustainable Development*,
Environmental Science and Engineering, https://doi.org/10.1007/978-3-031-27431-2_11

of the burner tilt angle on the combustion and $NO_x$ emission characteristics of a 700 MW pulverized-coal-fired boiler with deep-air-staging technology. Zha et al. (2017) studied numerically the forming mechanism of gas velocity and temperature deviations from the perspective of nonlinear flow characteristics in an ultra-supercritical utility boiler. Launder and Spalding (1972) simulated and analyzed the gas flow, temperature profile, and heat transfer of a 600 MW tangentially fired boiler with three different burner arrangements. However, there are very few studies that are focused on how characteristics of the heat transfer, combustion and $NO_x$ emission is affected by change in particle size of pulverized coal.

In this study, the characteristics of the flow, temperature, species concentration and $NO_x$ emissions in the 600 MW tangentially fired pulverized-coal boiler have been numerically investigated using comprehensive models for the combustion processes and $NO_x$ formation. The simulated results were validated with the measured results on-site. On the basis of the comparisons, the effects of particle size on combustion process and $NO_x$ emission were discussed.

## 11.2 Tangentially Fired Boiler

The tangentially fired pulverized-coal boiler considered in this study is a 600 MW, subcritical pressure, once intermediate reheat boiler. The height of the furnace is 65 m, and the cross-section of the furnace is a rectangle with a width of 19.6 m and a depth of 17.4 m. Figure 11.1a shows the schematic configuration of the boiler.

The burners are arranged at four corners, and six layers of primary air nozzles are arranged at each corner. Two layers of secondary air are arranged between each two layers of primary air nozzles. One layer is sprayed in the same direction as the primary air, and the other layer is deflected by 22° relative to the primary air, which generates a stronger oxidizing atmosphere in the area close to the furnace wall. Two-level close coupled over-fire air (CCOFA) and two group separated over-fire air (SOFA) are placed above the primary combustion zone.

## 11.3 Numerical Analysis Procedure

### *11.3.1 Calculation Domain and Mesh System*

The calculation domain is considered to be from the hopper to the reheater, as shown in Fig. 11.1. Since the overall geometric model of the boiler is an irregular geometry, the boiler is divided into several sub-geometry, and each sub-geometry is separately meshed. It should be noted that since the flow, heat transfer and combustion process of the burner area are the most complicated, it is necessary to perform mesh encryption processing on the burner area, especially in the vicinity of the nozzles, as shown

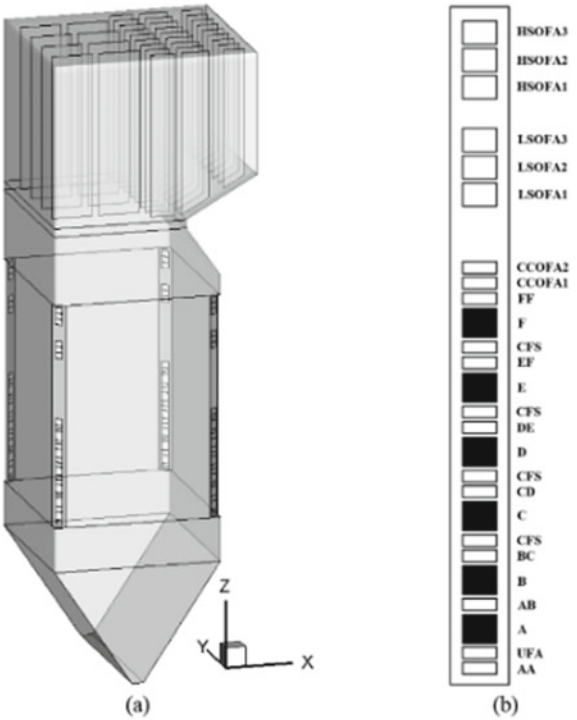


**Fig. 11.1** Burner nozzles distribution of furnace

in Fig. 11.2. To balance accuracy and computation time consumption, a gird independence test was conducted. This study considered 3 sets of grids of 820,135 cells, 1,327,890 cells and 1,892,632 cells. Figure 11.3 compares the average temperature distributions along the furnace height of 3 sets of grids. The calculation results of 1,327,890 cells and 1,892,632 cells are relatively close, and the 820,135 cells have a larger error, so the final selection is 1327890 cells.

Average temperature distributions along the furnace height are shown in Fig. 11.4. The temperature level of the cold ash hopper is low, mainly because most of the high-temperature gas flows toward the upper part of the furnace, and only part of the ash falls into the cold ash hopper. When approaching the burner area, the temperature rises rapidly along the height of the furnace increases. In the burner zone, the jet of pulverized coal ejected from the burners at each corner is subjected to the impact and heating from the high temperature flame that is burning intensely upstream.

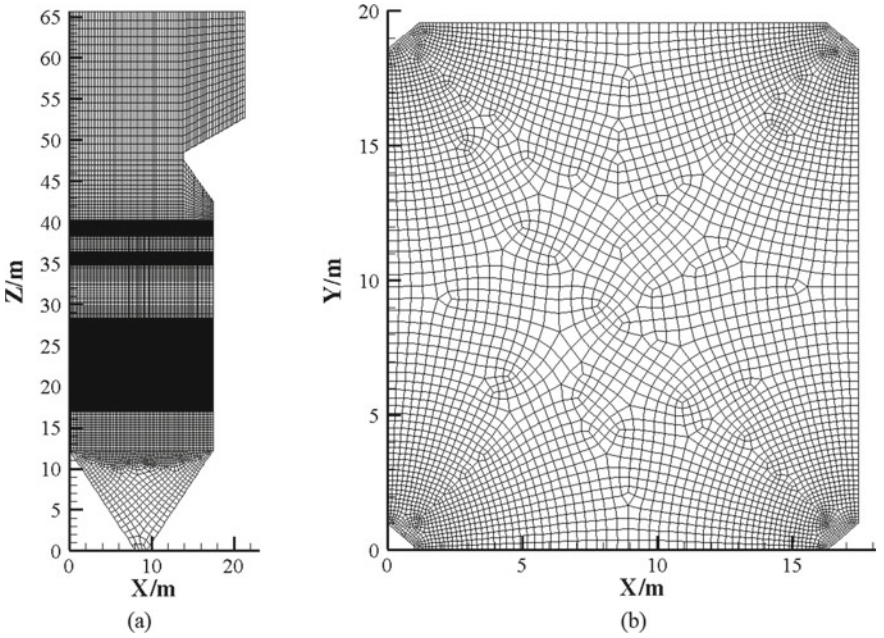


**Fig. 11.2** Grids of the vertical central cross-section and the horizontal cross-section in the burner zone

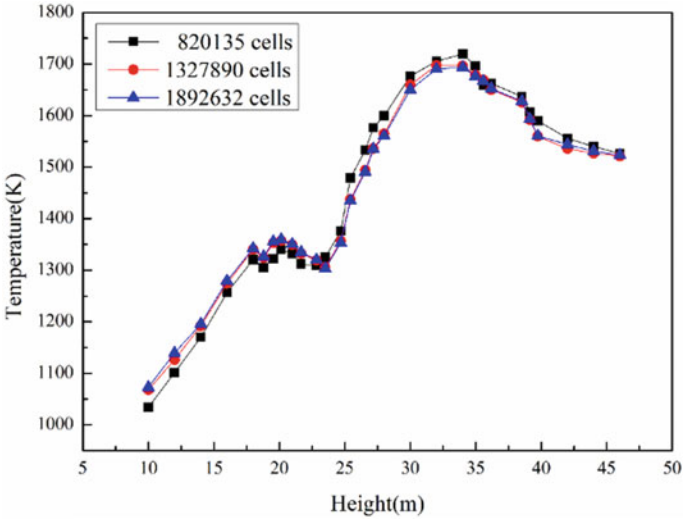


**Fig. 11.3** Grid independence test

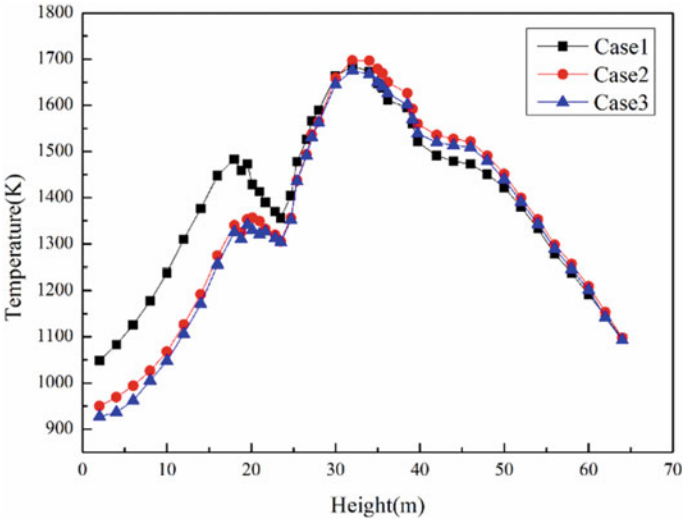


**Fig. 11.4** Temperature distribution along the furnace height

### *11.3.2 Numerical Models*

The numerical simulation of the combustion process in the furnace of a tangentially fired pulverized-coal boiler can be mathematically described by the basic conservation equation, turbulence model, radiation model, discrete phase model, devolatilization model, homogeneous combustion model and char heterogeneous combustion model.

For the combustion of tangentially fired boilers, all physical quantities satisfy the basic conservation equation, which including mass conservation equation, momentum conservation equation, energy conservation equation, and component conservation equation. If $\phi$ is used to represent a general variable, each of the above control equation can be written in the general form:

$$\frac{\partial(\rho\phi)}{\partial t} + div(\rho u\phi) = div(\Gamma grad\phi) + S \tag{11.1}$$

where $\rho$ is the density, $t$ is the time, $\boldsymbol{u}$ is the velocity vector, $\Gamma$ is the generalized diffusion coefficient, and $S$ is the generalized source term. The flow of gas in the furnace is almost turbulent. The Standard $k$-$\varepsilon$ model is used in simulation. And the P-1 model is used to simulate the radiation heat transfer (Launder and Spalding 1972).

$$Y_d = e^{-(\frac{d}{\bar{d}})^n} \tag{11.2}$$

The study simulates the trajectory of pulverized coal particles by a stochastic trajectory model described by Lagrangian. The model first solves the particle momentum equation, and then uses the Monte-Carlo method to calculate the particle flow field trajectory. The stochastic trajectory model assumes that the gas velocity pulsation is isotropic and conforms to the Gaussian distribution. In addition, the Rosin–Rammler model is adopted to simulate the particle size distribution. The model assumes an exponential relationship between the particle diameter $d$ and the mass fraction $Y_d$ of the particles larger than this diameter:

Where $\overline{d}$ is the average diameter and $n$ is the distribution index. After the pulverized coal enter the furnace, the combustion process includes devolatilization, homogeneous combustion and char heterogeneous combustion. Coal devolatilization is described by the two-competing-rates model. The homogeneous combustion process is described by non-premixed model. The heterogeneous combustion is computed according to the kinetics/diffusion-limited model. The $NO_x$ produced by coal combustion mainly refers to NO, $NO_2$ and $N_2O$, of which NO accounts for about 90%.

### *11.3.3 Simulation Conditions*

The total mass flow rate of the coal introduced into the furnace through the burners is 236.36 t/h and the total mass flow rate of the air is 229.3 t/h. The nozzle section of the burner disposed at the four corners of the furnace is used as the inlet boundary of the calculation zone. Gas phase at the inlet boundary are directly given according to the operating parameters of the boiler, as shown in Table 11.1.

The type of coal used is bituminous coal. The coal properties are presented in Table 11.2, including the proximate analysis, ultimate analysis and lower heating value. The change of pulverized coal size has an important influence on combustion, heat transfer and $NO_x$ emissions of boiler. To research the effects of particle size on combustion process and $NO_x$ emission, this study calculated three cases. The average diameters of pulverized coal under case1, case2 (the basic case), and case3 is 50, 60, and 70 μm, respectively.

**Table 11.1** Operating parameters of the boiler

| Type | Air rate (%) | Air temperature (K) | Air velocity (m/s) |
|---|---|---|---|
| Primary air | 20 | 349 | 25 |
| Secondary air | 39.75 | 593 | 54 |
| CCOFA | 5.25 | 593 | 54 |
| SOFA | 30 | 593 | 54 |

**Table 11.2** Coal property

| Type | | Data |
|---|---|---|
| Lower heating value (kJ/kg) | | 23,790 |
| Proximate analysis (%) | Moisture | 14.5 |
| | Ash | 7.7 |
| | Volatile matter | 30.2 |
| | Fixed carbon | 47.6 |
| Ultimate analysis (%) | C | 65.1 |
| | H | 3.25 |
| | O | 8.08 |
| | N | 0.66 |
| | S | 0.71 |

**Table 11.3** Comparison between the simulated and measured results

| Type | Measured | Simulated | Error (%) |
|---|---|---|---|
| Temperature of furnace exit | 1642 K | 1509 K | 8.1 |
| Temperature of final reheater outlet | 1060 K | 1076 K | 1.5 |
| Burnout rate | 99.51% | 99.69% | 0.2 |

## 11.4 Results and Discussion

### *11.4.1 Validation of the Combustion Simulation Results*

The simulated and measured values of these parameters are listed in Table 11.3. The measured results of the burnout rate, the temperature of furnace exit and final reheater outlet are 99.51%, 1642, and 1060 K, respectively. The simulated results of the burnout rate, the temperature of furnace exit and final reheater outlet are 99.69%, 1509, and 1076 K, respectively. And the errors are 0.2, 8.1, and 1.5%, respectively. It can be observed that the simulated values are consistent with the measured values. It means that the numerical models and mesh system adopted are reasonable.

### *11.4.2 Flow Fields*

The contours of the velocity on the vertical central cross-section are shown in Fig. 11.5.

The distribution of the velocity field within the furnace is substantially symmetrical. The high-speed zone is concentrated in the burner nozzle area, and the airflow velocity in other areas is relatively low.

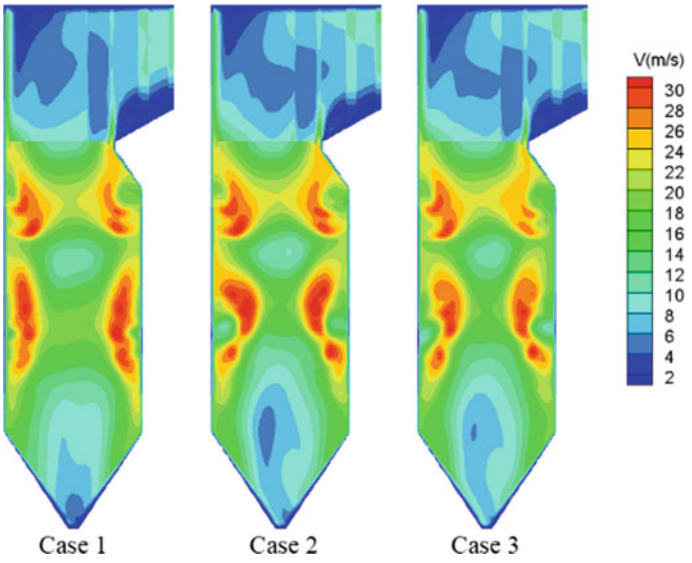


**Fig. 11.5** Contours of the velocity on the vertical central cross-section

The airflow forms a rotating upward flow field in the furnace, and the airflow in the burner area rotates sharply along the height of the furnace, and the rotation intensity gradually decreases above the height of the arch nose. The rotating rising airflow prolongs the residence time of the pulverized coal particles in the furnace, which is beneficial to the mixing of the coal powder and the airflow and promote the burning of the coal powder.

As shown in Fig. 11.6, the high-temperature zone is concentrated in the burner nozzle area, and the temperature in other areas is relatively low. In addition, due to the large amount of oxygen consumed in the initial stage of pulverized coal combustion and the formation of air tangential circle, the combustion reaction in the central region of the primary combustion zone is slower than that in the burner outlet region, so the temperature in the central region of the primary combustion zone is relatively lower than the burner outlet region.

In Fig. 11.7, the airflow is sprayed into the furnace from the four corners of the furnace, forming a tangential circle in the center of the furnace, which conforms to the tangentially fired pulverized-coal boiler.

### *11.4.3 Species Distribution*

As shown in Figs. 11.8 and 11.9, $O_2$ has the high concentration at the burner nozzle area. With the injection of $O_2$, the coal powder burns violently in the burner area, and $O_2$ is consumed in large quantities.

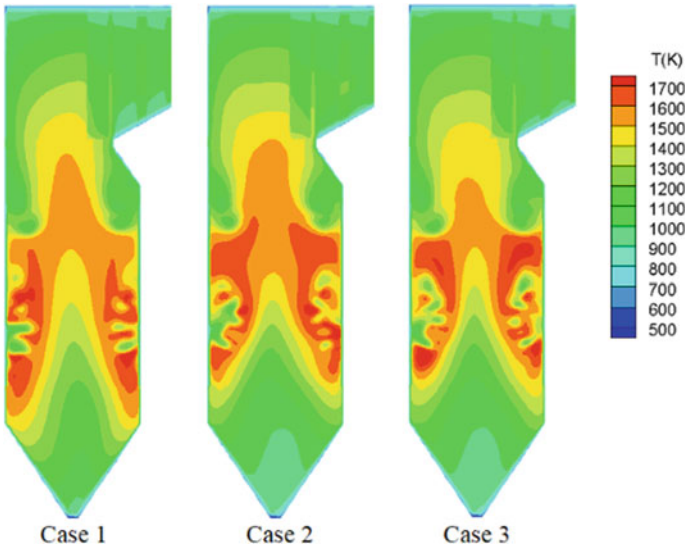


**Fig. 11.6** Contours of the temperature on the vertical central cross-section

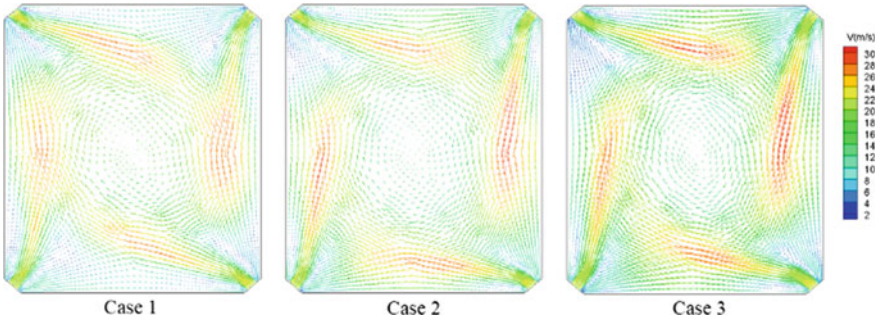


**Fig. 11.7** Vectors of the velocity on the horizontal cross-section of the fourth primary air

Since two sections of SOFA are arranged in the upper part of the primary combustion zone, the burner area is a low-oxygen fuel-rich zone, and under high temperature and anoxic conditions, the coal powder is burned to generate a large amount of CO. Therefore, in the high temperature zone of the burner area, the CO concentration is higher and the $O_2$ concentration is lower. Above the primary combustion zone, the $O_2$ concentration increases due to the input of the SOFA. The CO generated in the burner area reacts with $O_2$ to form $CO_2$, and the concentration of CO is lowered.

Figures 11.10 and 11.11 show the average concentration (mole fraction) distributions of $O_2$ and CO along the furnace height. The CO concentration increases first and then decreases along the height of the furnace, and the CO is generated most in the high temperature zone of the burner area. The $O_2$ concentration at the bottom of

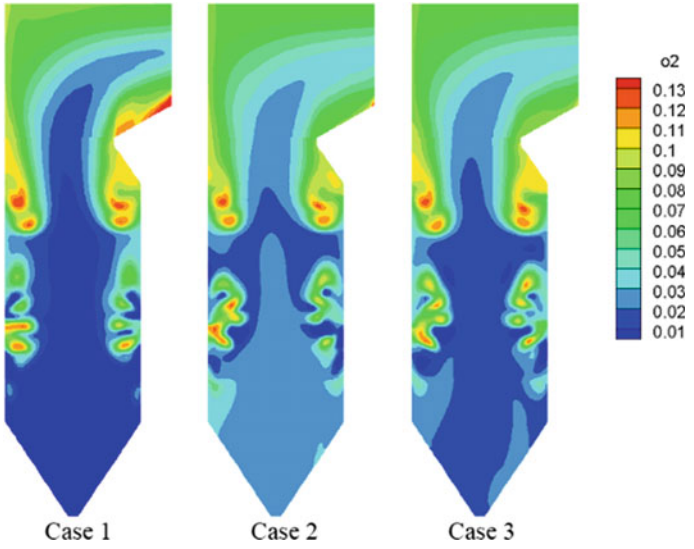


**Fig. 11.8** Contours of the concentration (mole fraction) of $O_2$

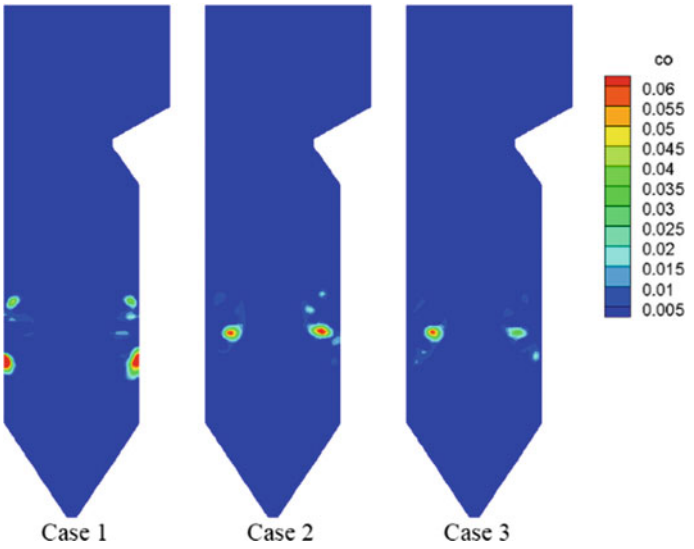


**Fig. 11.9** Contours of the concentration (mole fraction) of CO

the furnace is low. In the burner area, the $O_2$ concentration suddenly rises. From the upper part of the primary combustion zone to the lower part of the SOFA zone, the $O_2$ concentration gradually decreases due to the large amount of $O_2$ consumed by

the combustion of pulverized coal. The $O_2$ concentration rises again after the SOFA is applied.

It can be evidently seen from Figs. 11.8, 11.9, 11.10 and 11.11, that as the particle size of pulverized coal decreases, the $O_2$ concentration in the primary combustion

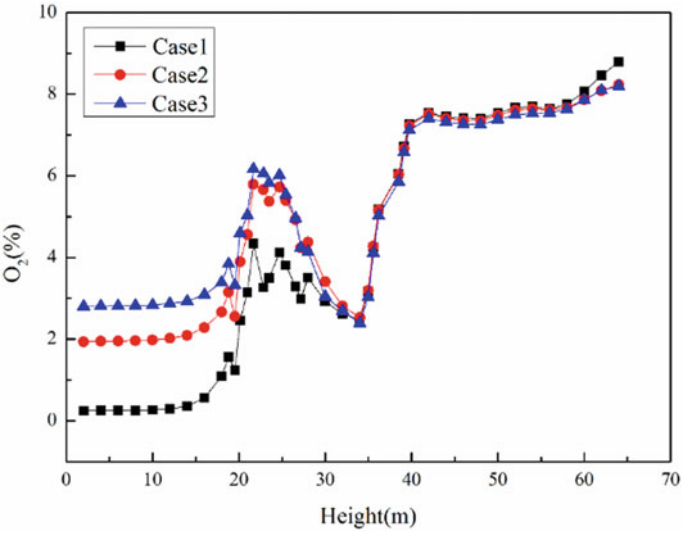


**Fig. 11.10** Average concentration (mole fraction) distributions of $O_2$ along the height

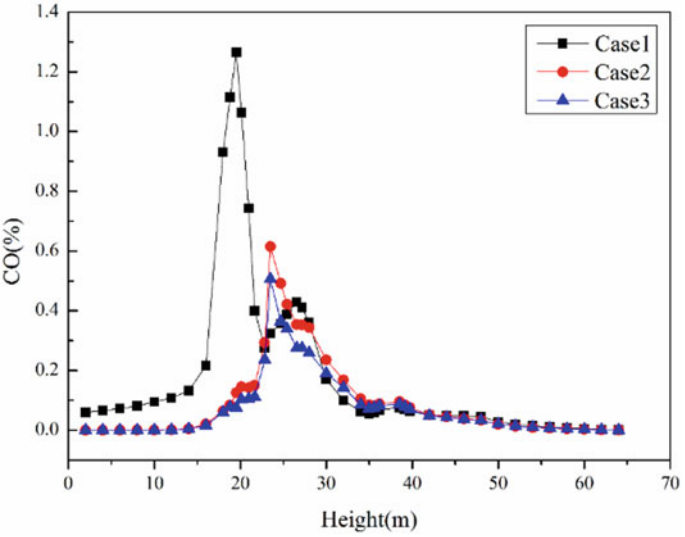


**Fig. 11.11** Average concentration (mole fraction) distributions of CO along the height

zone and the lower part of primary combustion zone decreases, and the CO concentration increases. It is principally because the smaller the particle size of the pulverized coal, the larger the reaction surface area of the particles, the more intense the combustion reaction, the faster the $O_2$ consumption, and the more CO is produced.

### *11.4.4 $NO_x$ Emissions*

Considering NO accounts for more than 90% of NOx. This study mainly discusses the generation of NO.

It can be seen from Fig. 11.12 that most of NO is formed in a high temperature and high oxygen region. In the vicinity of the burners, a large amount of volatile matter is precipitated, and the nitrogen compound is rapidly oxidized to form intermediate products such as HCN and $NH_3$. Then, intermediate products are further reacted with $O_2$ to form NO. After the SOFA is injected, the thermal NO is greatly reduced due to the temperature decrease. And on the same time, due to the dilution effect of the SOFA on the generated NO, the NO concentration decreases as the furnace height increases.

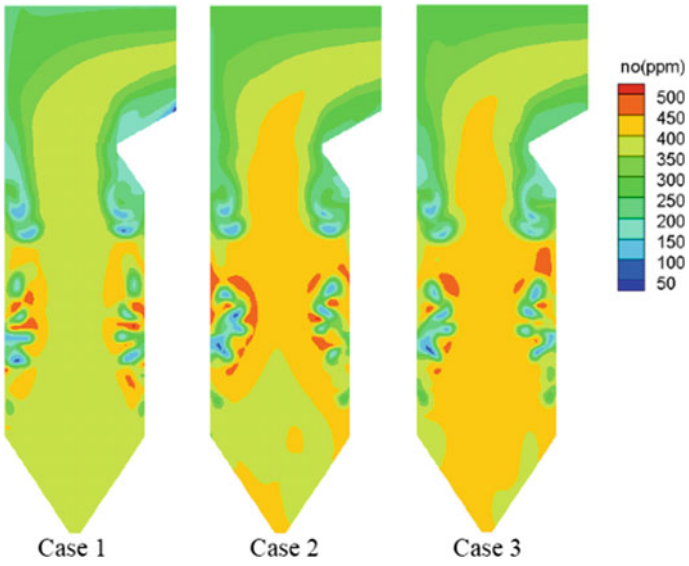


**Fig. 11.12** Distribution of NO on the vertical central cross-section

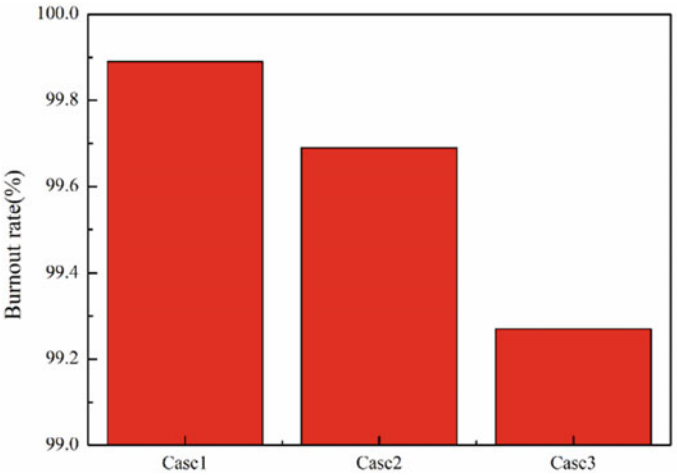


**Fig. 11.13** Burnout rate of pulverized coal

### *11.4.5 Pulverized Coal Burnout Performance*

As shown in Fig. 11.13, it can be clearly seen that the smaller the particle size of pulverized coal, the higher the burnout rate. The smaller the particle size of pulverized coal, the larger the surface area for the combustion reaction, and the lower the thermal resistance of the pulverized coal itself, so that the reaction speed can be accelerated and the pulverized coal burnout rate can be increased.

## 11.5 Conclusions

In this study, the characteristics of the flow, temperature, species concentration and $NO_x$ emissions in the 600 MW tangentially fired pulverized-coal boiler have been numerically investigated using comprehensive models for the combustion processes and $NO_x$ formation. The simulated results were validated with the measured results on-site. Simulation results were compared among three cases (the average diameters of pulverized coal are 50, 60, and 70 μm, respectively). On the basis of the comparisons, the effects of pulverized coal size on combustion process and $NO_x$ emission were discussed.

- As the decrease of particle size of pulverized coal, the temperature distribution in the furnace changes significantly, and the high temperature region expands. It is owing to that smaller particle size heats up the burning degree.
- The $O_2$ concentration in the primary combustion zone is diminished with decrease of particle size, which results from that intense combustion of pulverized coal consumes more $O_2$.

- The CO concentration in the primary combustion zone is increased and the high concentration region is enlarged with decrease of particle size.
- As the decrease of particle size, the $NO_x$ emission decrease. More intense combustion and longer residence time of pulverized coal in the primary combustion zone, the burnout rate rises with the decrease of particle size.

## 11.6 Funding Statement

This work is supported by the Science and Technology Research Projects of the Education Office of Jilin Province [Grant number: JJKH20220112KJ].

## References

Choi CR, Kim CN (2009) Numerical investigation on the flow, combustion and NOx emission characteristics in a 500 MWe tangentially fired pulverized-coal boiler. Fuel 88(9):1720–1731

Habib MA, Ben-Mansour R, Abualhamayel HI (2010) Thermal and emission characteristics in a tangentially fired boiler model furnace. J Energ Res 34(13):1164–1182

Launder BE, Spalding DB (1972) Lectures in mathematical models of turbulence. Academic Press, London

Tan P, Tian DF, Fang QY et al (2017) Effects of burner tilt angle on the combustion and NOX emission characteristics of a 700 MWe deep-air-staged tangentially pulverized-coal-fired boiler. Fuel 196(15):314–324

Yan L, He B, Yao F et al (2012) Numerical simulation of a 600 MW utility boiler with different tangential arrangements of burners. Energy Fuels 26(9):5491–5502

Zha Q, Li D, Wang C et al (2017) Numerical evaluation of heat transfer and NOX emissions under deep-air-staging conditions within a 600 MWe tangentially fired pulverized-coal boiler. Appl Therm Eng 116:170–181

# Chapter 12
# Impact of Climate on COVID-19 Epidemic in New South Wales, Australia


**Manxi Luo and Mingyu He**

**Abstract** Coronavirus-2 (SARS-CoV-2), which is an infectious coronavirus disease, has become a world of concern since the end of 2019. Emerging studies have found that there are many factors that could impact the transmission of coronavirus. Climate change has been a world of concern over centuries. It is inevitable to discover the connections between COVID-19 transmission and climate factors. Some researchers have conducted studies on the relationship mainly in the Northern Hemisphere during the early COVID19 period. As COVID-19 is evolving all the time, we want to discover the relationship from a relatively long-time range in the Southern Hemisphere – New South Wales in Australia in specific. We used a Linear regression model and generalized additive model (GAM) to estimate the interaction of meteorological, air pollutants variables and COVID-19 cases. We found that Temperature at 9 a.m., PM2.5 and PM10 have a positive relationship with covid whereas Relative humidity at 3 p.m., NO, Temperature at 3 p.m. and $NO_2$ have a negative relationship with Covid case number. A better understanding of the relationship does good to generating better pandemic response initiatives and surveillance and could be a reference to other religions.

**Keywords** Climate change · Covid-19 transmission · Air emissions · Relative humidity · Temperature

## 12.1 Introduction

The prevalence of Coronavirus-2 (SARS-CoV-2), which is an infectious coronavirus disease that causes severe comprehensive fatal respiratory symptoms in humans, has been existing for over 2 years. COVID-19 has now been a worldwide pandemic of

M. Luo (✉)
New South Wales Ministry of Health, Sydney 2065, Australia
e-mail: lmxlmx0318@gmail.com

M. He
Department of Biology, University of Auckland, Auckland 1010, New Zealand
e-mail: mhe384@aucklanduni.ac.nz



Z. Yang (ed.), *Environmental Science and Technology: Sustainable Development*,
Environmental Science and Engineering, https://doi.org/10.1007/978-3-031-27431-2_12

more than 496 million infections and more than 6.17 million deaths which have had a dramatic impact on the global economy and social structure (World Health Organization 2022).

Counter-measurements made by most of the countries worldwide initially at the beginning of the covid-19 outbreak are mostly by enforcing lockdown of regions and cities in the effort of reducing the possibilities of close distance social contact. On 21 January 2020, the first COVID-19 case in Australia was reported in Sydney, New South Wales and now New South Wales is the state that has the greatest number of cases in Australia according to the NSW Health (2022). New South Wales was locked down on 26 June to limit the spread of the delta variant, and people could only leave home for essential reasons like buying food. Moreover, the rules were gradually tightened by limiting people's travel to 5 kms and conducting curfews in some areas.

The spread of SARS-CoV-2 between people appears to be mainly through respiratory droplets (World Health Organization 2022). The lockdown on various aspects of air emission in specific regions. The city traffic, personnel flow control, industries activities, and economic facilities closures are of great contribution to air emission of nitrogen monoxide (NO), carbon monoxide (CO), carbon dioxide ($CO_2$), diesel-exhaust particles, and ozone ($O_3$), and nitrogen dioxide ($NO_2$) (Lian et al. 2020). Moreover, for air pollutants, OZONE, PM10 and PM2.5 are playing an important role in causing respiratory-related illnesses (Sicard et al. 2019). Temperature and relative humidity also have been important perspectives that impact the transmission and survival rate of various types of viruses including the SARS-CoV-2 virus. The infectivity of the virus was stronger under lower-temperature, lower-humidity conditions. The infection rate was 75–100% in an environment where the temperature was 5°C and relative humidity was 35 and 50% (Wang et al. 2020).

According to Dragone et al. (2022), the transmission of the virus is likely to occur through respiratory secretions in the form of droplets (>5 μm) and aerosols (<5 μm). In this regard, it is worth considering the stability of the virus in the air, because it may directly affect its transmission (Dragone et al. 2022). Furthermore, Zhu et al. (2020) have done the research for 12 cities in China and have found evidence that the air pollutants PM2.5, PM10, $SO_2$, and $NO_2$ have an impact on COVID-19.

Meanwhile, similar findings were also obtained by Conticini et al. (2020) when conducting research in Northern Italy. Pansini and Fornacca (2021) had also discovered similar evidence on the effects in China, Iran, Italy, Spain, France, Germany, UK and US. On the other hand, Guionie et al. (2013) have in the fields of epidemiology and laboratory that discovered temperature and humidity possibly impact the spread of diseases that is correlated to coronavirus. Moreover, Ward et al. (2020a) have also discovered that humidity is playing a role in SARS-CoV-2 transmission in New South Wales, Australia. Similar findings were achieved by Wang et al. (2021), who discovered the evidence of effects of temperature and humidity on SARS-CoV-2 in both the USA and China.

The purpose of this study was to investigate the association of COVID-19 cases with meteorological variables of humidity and temperature and air pollutants such as NO, $NO_2$, $SO_2$, Ozone PM2.5 and PM10 based in New South Wales, Australia data.

A better understanding of the association is conducive to generating better pandemic response initiatives and surveillance. Most importantly, the relationship between covid-19 and climate factors can be a valuable reference to other regions with pandemic response policies that might improve COVID-19 surveillance and control in the future.

## 12.2 Methodologies

### *12.2.1 Dataset Description*

We mainly collected data for climate change elements, meteorological variables, and covid-19 quantification. The data for climate change variables and meteorological aspects come mainly from the Bureau of Meteorology Australian Government and NSW government, whereas the data for covid-19 quantification is from NSW Health.

We collect the data specified in the range of covid-19 epidemic period. The following charts are the summary statistics of temperature, humidity, and air emission of the 6 selected sites for our research, which include mean values and median values with maximum and minimum values for each variable. The data collected is at a considerable scale for daily capturing in one to two years (Tables 12.1, 12.2, 12.3 and 12.4).

### *12.2.2 Dataset Processing and Statistical Analysis*

Daily Covid case data was collected from March 2021 to March 2022 in NSW, Australia from the 4 LHDs of our interests, which are further calculated into case rate per 100,0000 in each LHD. Climate data was also collected from the nearest weather observation station for these 4 LHDs. Meteorological variables of daily basis were downloaded: temperature (°C), CO, NO, $NO_2$, $SO_2$, OZONE, relative humidity (%) recorded at 9 a.m. and at 3 p.m., PM2.5 and PM10.

A time series of the data was generated for these 4 LHDs. Missing values of the datasets were replaced by the mean value.

In order to see the temporal changes for the variables interested, variables of concern are visualized upon different sites and statistical summary tables were created for each site. Afterwards, decomposition plots were created to discover the trends and seasonality of our variables during our time period of interest. Additionally, to

**Table 12.1** The summary statistics of the values of variables in time series data format for Sydney district between March 2021 to April 2022. The mean values and ranges of the increasing and descending trends of temperature, humidity, $SO_2$, NO, $NO_2$, Ozone, PM10, PM2.5, CO, and covid-19 cases during the epidemic period were recorded in the weather observation stations that cover the area of the LHD of interest

| Sydney LHD | | | | | | |
|---|---|---|---|---|---|---|
| Tempera-ture_9am | Min: 6.1 | 1st Qu: 14.1 | Median: 18.0 | Mean: 17.5 | 3rd Qu: 20.8 | Max: 27.1 |
| Humidity_9am | Min: 26 | 1st Qu: 59 | Median: 72 | Mean: 72 | 3rd Qu: 84 | Max: 100 |
| Tempera-ture_3pm | Min: 10 | 1st Qu: 18 | Median: 21 | Mean: 21 | 3rd Qu: 24 | Max: 34 |
| Humidity_3pm | Min: 10 | 1st Qu: 42 | Median: 56 | Mean: 57 | 3rd Qu: 69 | Max: 100 |
| $NO_2$ | Min: −0.2 | 1st Qu: 0.2 | Median: 0.4 | Mean: 0.52 | 3rd Qu: 0.70 | Max: 2.00 |
| PM10 | Min: 4 | 1st Qu: 12 | Median: 16 | Mean: 16 | 3rd Qu: 20 | Max: 37 |
| PM2.5 | Min: 0.3 | 1st Qu: 4.4 | Median: 5.9 | Mean: 6.3 | 3rd Qu: 7.4 | Max: 31.2 |
| $SO_2$ | Min: 0.0 | 1st Qu: 0.0 | Median: 0.1 | Mean: 0.07 | 3rd Qu: 0.10 | Max: 0.40 |
| NO | Min: −0.1 | 1st Qu: 0.0 | Median: 0.1 | Mean: 0.4 | 3rd Qu: 0.4 | Max: 8.1 |
| Ozone | Min: 0.2 | 1st Qu: 1.5 | Median: 1.9 | Mean: 1.9 | 3rd Qu: 2.3 | Max: 3.7 |
| Cases_num | Min: 0 | 1st Qu: 1 | Median: 20 | Mean: 130 | 3rd Qu: 146 | Max: 978 |
| Case_rate | Min: 0 | 1st Qu: 0 | Median: 3 | Mean: 19 | 3rd Qu: 21 | Max: 140 |

avoid multicollinearity in the analysis, a correlation matrix was adopted to locate reasonable and logical meteorological and air pollutants variables.

The variables will then be included in linear regression and multivariate generalized additive model (GAM) with the daily corona-virus infection number per 100,000 residents, followed by a P-value analysis. The best-fitting model for both linear regression and GAM according to AIC.

**Table 12.2** The summary statistics of the values of variables in time series data format for Hunter New England district between March 2021 to April 2022. The mean values and ranges of the increasing and descending trends of temperature, humidity, $SO_2$, NO, $NO_2$, Ozone, PM10, PM2.5, CO, and covid-19 cases during the epidemic period were recorded in the weather observation stations that cover the area of the LHD of interest

| Hunter New England LHD | | | | | | |
|---|---|---|---|---|---|---|
| Temperature_9am | Min: 10 | 1st Qu: 18 | Median: 21 | Mean: 21 | 3rd Qu: 23 | Max: 32 |
| Humidity_9am | Min: 41 | 1st Qu: 67 | Median: 76 | Mean: 76 | 3rd Qu: 38 | Max: 100 |
| Temperature_3pm | Min: 20 | 1st Qu: 57 | Median: 68 | Mean: 67 | 3rd Qu: 78 | Max: 100 |
| Humidity_3pm | Min: 0.0 | 1st Qu: 0.0 | Median: 0.1 | Mean: 0.1 | 3rd Qu: 0.1 | Max: 0.6 |
| $NO_2$ | Min: 0.0 | 1st Qu: 0.1 | Median: 0.2 | Mean: 0.5 | 3rd Qu: 0.6 | Max: 5.3 |
| PM10 | Min: 0.2 | 1st Qu: 0.1 | Median: 0.5 | Mean: 0.5 | 3rd Qu: 0.8 | Max: 1.8 |
| PM2.5 | Min: 0.10 | 1st Qu: 1.30 | Median: 1.70 | Mean: 1.69 | 3rd Qu: 2.10 | Max: 3.10 |
| $SO_2$ | Min: 2 | 1st Qu: 15 | Median: 19 | Mean: 20 | 3rd Qu: 24 | Max: 44 |
| NO | Min: 1.3 | 1st Qu: 4.3 | Median: 5.7 | Mean: 6.2 | 3rd Qu: 7.6 | Max: 21.1 |
| OZONE | Min: 0.1 | 1st Qu: 0.2 | Median: 0.2 | Mean: 0.2 | 3rd Qu: 0.2 | Max: 0.5 |
| Cases_num | Min: 0 | 1st Qu: 0 | Median: 4 | Mean: 118 | 3rd: 58 | Max: 976 |
| Case_rate | Min: 0 | 1st Qu: 0 | Median: 1 | Mean: 24 | 3rd Qu: 13 | Max: 237 |

## 12.3 Results

The average total number of covid cases acquired between 01 March 2021 and 31 March 2022 is 54555 for Sydney, Hunter New England, New blue mountains and Illawarra Shoalhaven LHDs when Hunter new England had the most number of cases. It is shown in the graph that all LHDs have their covid case number left-skewed while the meteorological and air pollutants remain relatively constant with a slight increase or decrease trend. Covid-19 case numbers are further calculated by the rate of the total population in each LHD.

It can be observed from the graph that all LHDs had experienced an extremely low temperature around 10 June 2021, which was due to a large mass of cold air crossing New South Wales according to the Australia Bureau of Meteorology (2022). The days with outliers in air pollutants variables, such as PM2.5 and PM10 are due to hazard reduction burns (Australia Bureau of Meteorology 2022).

The meteorological and air pollutants data is obtained from 4 weather observation stations within each LHDs. According to the correlation coefficient matrix produced (Fig. 12.1), the variables of air emission and climate variables have different levels of both positive and negative correlations. However, most of the variables can be defined as very weakly correlated or no correlation as the values are close to 0 such as SO and temperature. This suggests that most of the variables that are considered in this study for the four districts are in a weak correlation without specific patterns. However,

**Table 12.3** The summary statistics of the values of variables in time series data format for the Nepean Blue Mountains district between March 2021 to April 2022. The mean values and ranges of the increasing and descending trends of temperature, humidity, $SO_2$, NO, $NO_2$, Ozone, PM10, PM2.5, CO, and covid-19 cases in the range of SARS-CoV-2 epidemic period were recorded by the weather observation stations that cover the area of the LHD of interest

| New Blue Mountain LHD | | | | | | |
|---|---|---|---|---|---|---|
| Tempera-ture_9am | Min: 4.6 | 1st Qu: 13.4 | Median: 17.8 | Mean: 16.8 | 3rd Qu: 20.3 | Max: 25.6 |
| Tempera-ture_3pm | Min: 8 | 1st Qu: 19 | Median: 22 | Mean: 23 | 3rd Qu: 26 | Max: 37 |
| Humidity_9am | Min: 34 | 1st Qu: 70 | Median: 83 | Mean: 80 | 3rd Qu: 98 | Max: 99 |
| Humidity_3pm | Min: 16 | 1st Qu: 39 | Median: 51 | Mean: 55 | 3rd Qu: 68 | Max: 99 |
| $SO_2$ | Min: 0 | 1st Qu: 0 | Median: 0.1 | Mean: 0.07 | 3rd Qu: 0.1 | Max: 0.4 |
| NO | Min: 0 | 1st Qu: 0.2 | Median: 0.3 | Mean: 0.5 | 3rd Qu: 0.6 | Max: 3.3 |
| $NO_2$ | Min: 0.1 | 1st Qu: 0.3 | Median: 0.47 | Mean: 0.47 | 3rd Qu: 0.7 | Max: 1.4 |
| Ozone | Min: 0 | 1st Qu: 1.1 | Median: 1.5 | Mean: 1.5 | 3rd Qu: 1.9 | Max: 3.7 |
| PM10 | Min: 0 | 1st Qu: 12 | Median: 15 | Mean: 16 | 3rd Qu: 20 | Max: 74 |
| PM2.5 | Min: 0 | 1st Qu: 5 | Median: 6 | Mean: 8 | 3rd Qu: 9 | Max: 72 |
| CO | Min: 0.1 | 1st Qu: 0.1 | Median: 0.2 | Mean: 0.18 | 3rd: 0.2 | Max: 0.7 |
| Case_num | Min: 0 | 1st Qu: 0 | Median: 7 | Mean: 109 | 3rd Qu: 88 | Max: 951 |
| Case_rate | Min: 0 | 1st Qu: 0 | Median: 1 | Mean: 12 | 3rd Qu: 10 | Max: 139 |

for Hunter New England LHD, the correlation coefficient matrix demonstrates that a relatively strong positive correlation is shown ($p = 0.730$) between NO and $NO_2$. Also, for the Nepean Blue Mountains LHD, a fairly strong correlation is shown ($p = 0.723$) between PM2.5 and CO levels. For the Illawarra Shoalhaven District, a relative correlation is demonstrated ($p = 0.761$) between $NO_2$ level and NO level (Table 12.5).

By using AIC, which is the backward model selection method after fitting the linear regression models, we obtained our final linear regression model. It suggests a statistical significance for Relative humidity at 3 p.m. ($p = 0.03$ in Hunter New England LHD), Temperature at 9 a.m. ($p = 0.008$ in Illawarra Shoalhaven LHD) and 3 p.m. ($p = 0.004$ in Hunter New England LHD), NO ($p = 0.015$ in Illawarra Shoalhaven LHD and $p = 0.012$ in Sydney LHD), $NO_2$ ($p = 0.018$ in New Blue Mountains LHD), PM2.5 ($p = 0.01$ in Hunter New England LHD and $p = 0.043$ in Sydney LHD) and PM10 ($p = 0.008$ in New Blue Mountains LHD).

**Table 12.4** The summary statistics of Temperature 9 a.m. and 3 p.m., $SO_2$, NO, $NO_2$, Ozone, PM10, PM2.5, CO, Covid-19 case number, Relative humidity 9 a.m., and 3 p.m. and Covid-19 case rate for Illawarra Shoalhaven LHD between March 2021 to March 2022

| Illawarra Shoalhaven LHD | | | | | | |
|---|---|---|---|---|---|---|
| Tempera-ture_9am | Min: 9.4 | 1st Qu: 16.8 | Median: 18.5 | Mean: 18.5 | 3rd Qu: 20.5 | Max: 25.6 |
| Tempera-ture_3pm | Min: 10.1 | 1st Qu: 18.3 | Median: 20.4 | Mean: 20.4 | 3rd Qu: 22.3 | Max: 37 |
| Humidity_9am | Min: 29 | 1st Qu: 57 | Median: 69 | Mean: 69 | 3rd Qu: 81 | Max: 99 |
| Humidity_3pm | Min: 12 | 1st Qu: 55 | Median: 66 | Mean: 65 | 3rd Qu: 78 | Max: 99 |
| $SO_2$ | Min: −0.1 | 1st Qu: 0 | Median: 0 | Mean: 0.07 | 3rd Qu: 0.1 | Max: 0.4 |
| NO | Min: 0 | 1st Qu: 0.1 | Median: 0.2 | Mean: 0.4 | 3rd Qu: 0.4 | Max: 3.3 |
| $NO_2$ | Min: −0.2 | 1st Qu: 0.2 | Median: 0.4 | Mean: 0.45 | 3rd Qu: 0.6 | Max: 1.4 |
| Ozone | Min: 0.3 | 1st Qu: 1.3 | Median: 1.7 | Mean: 1.7 | 3rd Qu: 2.1 | Max: 3.7 |
| PM10 | Min: 3 | 1st Qu: 10 | Median: 14 | Mean: 15 | 3rd Qu: 19 | Max: 74 |
| PM2.5 | Min: 0.3 | 1st Qu: 3.8 | Median: 5.3 | Mean: 5.6 | 3rd Qu: 7 | Max: 72 |
| CO | Min: 0 | 1st Qu: 0.1 | Median: 0.18 | Mean: 0.16 | 3rd: 0.2 | Max: 0.7 |
| Case_num | Min: 0 | 1st Qu: 0 | Median: 4 | Mean: 88 | 3rd Qu: 88 | Max: 944 |
| Case_rate | Min: 0 | 1st Qu: 0 | Median: 0 | Mean: 10 | 3rd Qu: 10 | Max: 103 |

A generalized additive model (GAM) is also fitted and the best GAM model was selected from the model selection method AIC. The summary output of the best-fitting GAM model reconfirms the statistical significance of $NO_2$ ($p = 0.00029$ in New Blue Mountains LHD, $p = 0.0011$ in Illawarra Shoalhaven LHD, $p = 0.029$ in Hunter New England LHD) and Temperature at 9 a.m. ($p = 0.035$ in New Blue Mountains LHD). Furthermore, it was shown by both the best linear regression model and the best Generalized additive model that Temperature at 9 a.m., PM2.5 and PM10 have a positive relationship with covid whereas Relative humidity at 3 p.m., NO, Temperature of the time range of 3 p.m. and $NO_2$ have a negative relationship with Covid case number.

We found a negative association between Relative humidity in the period of 3 p.m. range and temperature of the same time period. Lower relative humidity at 3 p.m. was corresponded to increased cases; for every decrease of relative humidity by 1% approximately causes an increase in COVID-19 case rate by 0.92. Lower 3 p.m. Temperature leads to an increase of cases; a decrease in temperature of 1 degree presumably gives an increase in COVID-19 case rate by 7.48. Ward et al. (2020b),

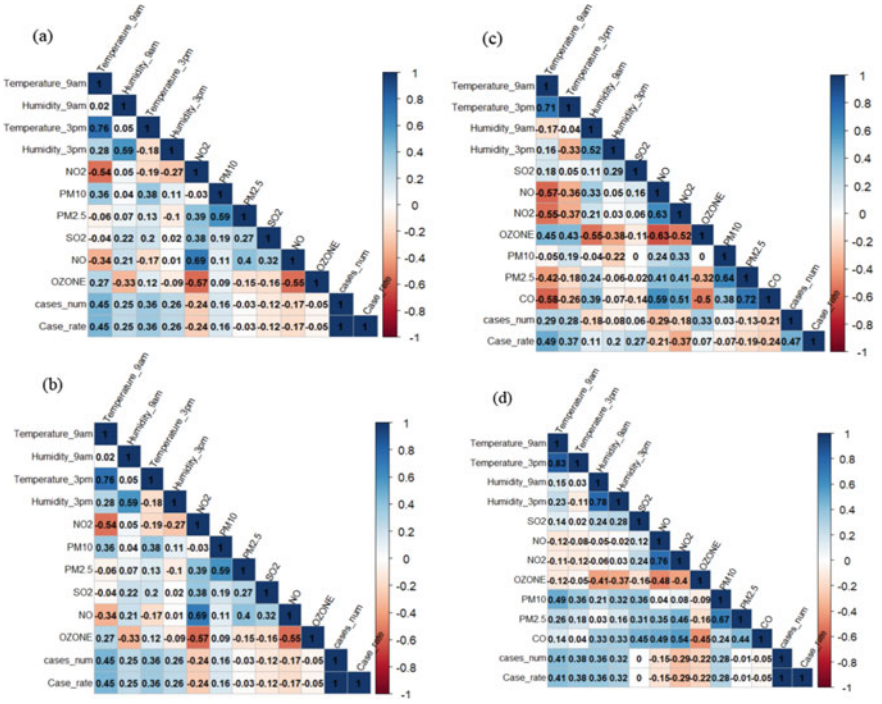


**Fig. 12.1** Correlation coefficient plot of all variables including climate and air emission with covid-19 cases number for Sydney District (**a**), Hunter New England (**b**), Nepean Blue Mountains District (**c**), Illawarra Shoalhaven District (**d**)

who have done similar research discovered the same negative relationship between COVID-19 and relative humidity instead of temperature.

We also found a positive relationship between both PM2.5 and PM10 and the evolving in the range of SARS-CoV-2 epidemic. Increased case number with higher level of PM2.5 and PM10; an increase in PM2.5 of 1 $\mu g/m^3$ presumably leads to an increase of COVID-19 case rate by 9.85 and 5.72 respectively in Hunter New England and Sydney LHD. PM10 of 1 1 $\mu g/m^3$ and the COVID-19 indicates a positive relationship with a case rate by 0.81. Zhu et al. (2020) have found similar positive relationships in 120 cities in China.

What's more, the R-squared of all 4 final linear regression models is high with Hunter New England reaching the highest with 0.994, which means that 99.4% of the variability observed in our retained variables is explained by the regression model. Meanwhile, Sydney LHD has the lowest R-squared at 0.981, which suggests that 98.1% of the variability observed in our retained variables is explained by the regression model.

**Table 12.5** Summary of the best linear regression models of meteorological variables and air pollutants variables and COVID case rate for 4 LHDs of interest

| | Hunter New England | | | Nepean Blue Mountains | | | Illawarra Shoalhaven | | | Sydney | | |
|---|---|---|---|---|---|---|---|---|---|---|---|---|
| Predictors | Estimates | CI | p | Estimates | CI | p | Estimates | CI | p | Estimates | CI | p |
| (Intercept) | −75.22 | (−180.58, 30.13) | 0.151 | −28.73 | (−96.68, 39.22) | 0.39 | −81.95 | (−137.62, −26.28) | 0.006 | −63.19 | (−180.29, 53.91) | 0.274 |
| CO | 188.47 | (−47.48, 424.43) | 0.111 | 33.86 | (−57.19, 124.90) | 0.449 | 12.3 | (−67.02, 91.63) | 0.75 | | | |
| Humidity_3pm | −0.92 | (−1.74, −0.10) | 0.03 | 0.45 | (−0.03, 00.93) | 0.063 | −0.18 | (−0.58, 0.22) | 0.354 | −0.5 | (−1.31, 0.31) | 0.212 |
| Humidity_9am | 0.67 | (−0.34, 1.69) | 0.179 | −0.24 | (−0.67, 0.19) | 0.254 | 0.22 | (−0.25, 0.69) | 0.343 | 0.35 | (−0.5, 1.19) | 0.403 |
| NO | 25.26 | (−17.85, 68.37) | 0.235 | | | | −13.86 | (−24.7, −3.01) | 0.015 | −46.46 | (−81.81, −11.11) | 0.012 |
| $NO_2$ | −23.70 | (−66.40, 19.00) | 0.26 | −25.04 | (−45.31, −4.77) | 0.018 | 3.91 | (−16.49, 24.32) | 0.693 | 14.78 | (−38.85, 68.41) | 0.573 |
| Ozone | 7.26 | (−14.16, 28.68) | 0.487 | | | | | | | −14.65 | (−51.26, 21.95) | 0.415 |
| PM10 | −0.69 | (−2.61, 1.24) | 0.466 | 0.81 | (0.23, 1.39) | 0.008 | 0.33 | (−0.54, 1.19) | 0.441 | 1.01 | (−0.92, 2.94) | 0.29 |
| PM2.5 | 9.85 | (2.66, 17.04) | 0.01 | | | | 1.11 | (−1.7, 3.91) | 0.42 | 5.72 | (0.19, 11.25) | 0.043 |
| $SO_2$ | 59.44 | (−23.29, 142.17) | 0.149 | 15.71 | (−49.63, 81.04) | 0.623 | −17.26 | (−63.43, 28.91) | 0.445 | | | |
| Temperature_3pm | −7.48 | (−12.30, −2.66) | 0.004 | 0.67 | (−1.78, 3.13) | 0.576 | −1.24 | (−3.38, 0.90) | 0.24 | −1.75 | (−8.64, 5.13) | 0.602 |
| Temperature_9am | 5.42 | (−0.27, 11.11) | 0.061 | −0.96 | (−4.45, 2.63) | 0.585 | 3.7 | (1.09, 6.31) | 0.008 | 3.09 | (−5.75, 11.93) | 0.476 |
| trend | 0.33 | (0.29, 0.36) | <0.001 | 0.08 | (0.06, 0.09) | <0.001 | 0.11 | (0.1, 0.13) | <0.001 | 0.22 | (0.18, 0.27) | <0.001 |
| Observation | 396 | | | 396 | | | 396 | | | 396 | | |
| $R^2$/$R^2$ adjusted | 0.994/0.883 | | | 0.991/0.845 | | | 0.992/0.844 | | | 0.981/0.636 | | |

## 12.4 Discussion

As our results demonstrated a negative relationship between relative humidity at 3 p.m., $NO_2$, the temperature at 3 p.m. and the COVID-19 cases rate in New Blue Mountains LHD. To explain this result, the establishment that enveloped viruses, including influenza virus, are sensitive to low pH (Luo et al. 2022) holds a powerful point. $NO_2$ is one of the acidic ambient air pollutants that can react with the water

molecule in the air (humidity) to enrich $HNO_3$, which is the reason why $NO_2$ is not excluded under a relatively high correlation in our research. Also, aerosol pH depends on the composition of the aerosol particle and the surrounding air, and it is well characterized by particulate matter equilibrated with inorganic acids (Luo et al. 2022). Biochemically, virus inactivation happens rapidly when the air is acidic with a PH value of 4 and drops faster with every decrease of the PH value of 2. The faster the viral inactivation proceeds, the less risk of viral transmission for the COVID-19 virus.

Air pollutants such as PM2.5 and PM10 are known for being risk substances for respiratory-related disease morbidity and mortality worldwide (Dragone et al. 2022). Our results indicate there is a positive relationship between PM2.5 and covid-19 case rate in two sites of interest, while there is a positive relationship between PM10 and covid-19 case rate in one site of interest. Exposure to PM2.5 and PM10 promotes pro-inflammatory status that reduces the resistance of the human defense mechanism and increases the risks of COVID-19 virus infection. Moreover, PM2.5 and PM10 are relatively larger particulates in the air, which is highly likely that viruses could potentially adhere to the particulate matter as a COVID-19 virus carrier. Importantly, positive correlations have been found between PM2.5 and other respiratory viruses such as the influenza virus, emphasizing the possibility of particulate matter as a transport carrier for SARS-CoV-2 (Nor et al. 2021).

Intriguingly, temperatures at different times of the day of the two sites of interest have an opposite result on the COVID-19 case rate. A positive relationship between temperature at 9 am and COVID case rate in Illawarra Shoalhaven and a negative relationship between temperature at 3 p.m. and COVID case rate in Hunter New England. The effects of large daily temperature ranges (DTRs) can differ between the cool and the warm ends of the range of naturally occurring temperatures, presumably reflecting nonlinearities in the relationship between extrinsic incubation rates and temperature that become evident when portions of the day are beyond the virus' thermal limits (Danforth et al. 2016). The temperature has significant effects on virus survival and transmission levels. There might also be an optimum temperature coupled with specific relative humidity. The inconsistency that shows relative humidity plays a role in COVID-19 spreading is complex for different evolving periods of the COVID-19 pandemic and there are many other factors that can affect those variables, which is also a limitation of our study. A previous study on the virus and temperature with humidity took into account that improved persistence of released virus would increase the amount of viable virus shed and would furthermore augment amplification of virus in the nasal passages through re-infection. The block in transmission at 30 °C and 35% RH could be explained by the opposite effect: warming of the nasal mucosa may lead to more rapid inactivation of virus particles (Lowen et al., n.d.). As we observed a positive relationship between covid-19 cases and temperature for three sites, it suggests that covid-19 is sensitive to the change of temperature for the level of viral transmission and survival. Studies of temperature effects on the Covid-19 virus allow unveiling the specific changes such as possible optimum conditions for the Covid-19 virus to be active and survive. Furthermore, in a study on swine flu performed in 2007 in a strictly controlled indoor

environment other factors, researchers found that, after they excluded the possibility of immune system impact from the low temperature, the virus could be transmitted through aerosol. The study also found that the infectivity of the virus was stronger under lower-temperature, lower-humidity conditions (Wang et al. 2021). COVID-19 transmission is predicted to be enhanced under the condition of lower temperature, whereas a higher temperature reduces the possibility of viral transmission and risk of COVID-19 for the negative effects on virus survival.

## 12.5 Conclusion

The variables of relative humidity, $NO_2$, temperature, and aerosol particles PM 2.5 and PM 10 have effects on the Covid-19 epidemic in diversified perspectives. For starters, $NO_2$ in the atmosphere associates with the dihydrogen monoxide molecules in the atmosphere and air environment in the range of human habitats creating acidic aerosol environment that promotes viral inactivation that lowers virus survival rate of Covid-19 virus. Furthermore, airborne particles PM 2.5 and PM 10, which have been related to various respiratory problems, provides space for covid-19 to adhere to as carrier, which promotes covid-19 air transmission. Additionally, various combinations of different degree of temperature and different level of humidity have versatile effects of covid-19 virus activation and survival. The study was based on the data of climate and environment specifically in New South Wales, Australia. Moreover, climate changes are known for being affected by anthropogenic activities in various ways with the consideration of economical and sociological aspects contributing to covid-19 epidemic. Increasing level of comprehensive logical and experimental studies will be contributed to the study that concerns climate elements and epidemic issues.

**Acknowledgements** NSW Ministry of Health is thanked for freely making available COVID-19 case notification data. Manxi Luo and Mingyu He contributed equally to this work and should be considered co-first authors.

## References

Australia Bureau of Meteorology (2022) New South Wales in 2021: very wet overall and relatively cool. http://www.bom.gov.au/climate/current/annual/nsw/summary.shtml. Accessed 3 Apr 2022

Conticini E, Frediani B, Caro D (2020) Can atmospheric pollution be considered a co-factor in extremely high level of SARS-CoV-2 lethality in Northern Italy? Environ Pollut 261:114465

Danforth ME, Reisen WK, Barker CM (2016) The impact of cycling temperature on the transmission of West Nile virus. J Med Entomol 53(3):681–686

Dragone R, Licciardi G, Grasso G, Del Gaudio C, Chanussot J (2022) Analysis of the chemical and physical environmental aspects that promoted the spread of SARS-COV-2 in the Lombard area. MDPI. https://doi.org/10.3390/ijerph18031226

Guionie O, Courtillon C, Allee C, Maurel S, Queguiner M, Eterradossi N (2013) An experimental study of the survival of turkey coronavirus at room temperature and+ 4 C. Avian Pathol 42(3):248–252

NSW Health (2022) COVID-19 (Coronavirus). https://www.health.nsw.gov.au/Infectious/covid-19/Pages/default.aspx. Accessed 3 Apr 2022

Lian X, Huang J, Huang R, Liu C, Wang L, Zhang T (2020) Impact of city lockdown on the air quality of COVID-19-hit of Wuhan city. Sci Total Environ 742:140556

Lowen AC, Mubareka S, Steel J, Palese P (n.d.) Influenza virus transmission is dependent on relative humidity and temperature. PLOS Pathog. https://journals.plos.org/plospathogens/article?id=10.1371%2Fjournal.ppat.0030151. Accessed 1 May 2022

Luo B, Schaub A, Glas I, Klein LK, David SC, Bluvshtein N, … Kohn T (2022) Acidity of expiratory aerosols controls the infectivity of airborne influenza virus and SARS-CoV-2. medRxiv

Nor NSM, Yip CW, Ibrahim N, Jaafar MH, Rashid ZZ, Mustafa N, Hamid HHA, Chandru K, Latif MT, Saw PE, Lin CY, Alhasa KM, Hashim JH, Nadzir MSM (2021) Particulate matter (PM2.5) as a potential SARS-COV-2 carrier. Nature News, January 28. https://www.nature.com/articles/s41598-021-81935-9. Accessed 6 May 2022

Pansini R, Fornacca D (2021) Early spread of COVID-19 in the air-polluted regions of eight severely affected countries. Atmosphere 12(6):795. https://doi.org/10.3390/atmos12060795

Sicard P, Khaniabadi YO, Perez S, Gualtieri M, De Marco A (2019) Effect of $O_3$, PM10 and PM2.5 on cardiovascular and respiratory diseases in cities of France, Iran and Italy. Environ Sci Pollut Res 26(31):32645–32665

Wang J, Tang K, Feng K, Lin X, Lv W, Chen K, Wang F (2021) Impact of temperature and relative humidity on the transmission of COVID-19: a modelling study in China and the United States. BMJ Open 11(2):e043863

Wang M, Jiang A, Gong L, Lu L, Guo W, Li C, Zheng J, Li C, Yang B, Zeng J, Chen Y, Zheng K, Li H (2020). Temperature significantly change COVID-19 transmission in 429 cities. medRxiv, January 1. https://doi.org/10.1101/2020.02.22.20025791v1. Accessed 1 May 2022

Ward MP, Xiao S, Zhang Z (2020a) Humidity is a consistent climatic factor contributing to SARS-CoV-2 transmission. Transbound Emerg Dis 67(6):3069–3074

Ward MP, Xiao S, Zhang Z (2020b) The role of climate during the COVID-19 epidemic in New South Wales, Australia. Transbound Emerg Dis 67(6):2313–2317

World Health Organization (2022) Coronavirus disease (COVID-19) pandemic. https://www.who.int/emergencies/diseases/novel-coronavirus-2019. Accessed 3 Apr 2022

Zhu Y, Xie J, Huang F, Cao L (2020) Association between short-term exposure to air pollution and COVID-19 infection: evidence from China. Sci Total Environ 727:138704

# Chapter 13
# Cultural Challenges in the Implementation of COVID-19 Public Health Measures


**Safwan Qadri, Shixiang Chen, Syed Usman Qadri, and Wardah Naeem Bukhari**

**Abstract** Culture is a combination of religion, rituals, beliefs, language, and expressions of different kinds of human interactions. The public culture of the Punjab province of Pakistan has impacted the spread of COVID-19 in several ways. Punjab is famous for cultural and religious activities. During pandemic government authorities enforced that religious congregations should be limited to control the spread of virus as opposed by believers. Punjab province is rich in culture and builds a collective tradition of festivity and religious devotions. These activities include Ramadan, Eid-ul-Fitr, Eid-ul-Adha, Muharram, Eid Milad-un-Nabi (SAW), and Urs in the framework of COVID-19. This research investigates the religious and cultural responses and reveal the difficulties in implementing public health initiatives in Pakistan. Though, it has been seen that greetings such as handshakes and embracing are common in these events and breaches social distancing. This study observed that the number of corona cases and causality started increasing in the holy month of Ramadan, and the situation became worst before and after Eid-ul-Fitr. COVID-19 cases and death rates indicated that the people did not follow most of the social distancing protocols while attending these cultural and religious events. As a result, these kinds of events have been the catalyst for spreading COVID-19 and following variants.

**Keywords** COVID-19 · Health · Social · Cultural · Pakistan · Public participation

S. Qadri (✉) · S. Chen (✉)
School of Political Science and Public Administration, Local Government Public Service Innovation Research Center, Wuhan University, Wuhan 430072, China
e-mail: safwangillani81@yahoo.com

S. Chen
e-mail: chensx@whu.edu.cn

S. U. Qadri
School of Management, Jiangsu University, Zhenjiang 212013, China

W. N. Bukhari
Lahore College for Women University, Lahore 54700, Pakistan



Z. Yang (ed.), *Environmental Science and Technology: Sustainable Development*, Environmental Science and Engineering, https://doi.org/10.1007/978-3-031-27431-2_13

## 13.1 Introduction

COVID-19 has engulfed the world as global public health and medical emergency of international concern (Kim and Park 2022). Thought to have originated in bats and later jumped to humans at one of Wuhan's open-air wet markets. Although coronaviruses, like MERS and SARS, have infected humans in the past, the outbreaks were not as severe as the current pandemic, infecting millions and killing thousands (Huang et al. 2020). After the 1918 flu pandemic, the fifth pandemic can be traced back to its first reporting from a cluster of human cases with pneumonic symptoms in Wuhan City, China, in late December 2019. Common symptoms amongst the cases were fever, malaise, dry cough, and dyspnea, causing mild upper respiratory diseases. Since then, the virus has continuously evolved and has become a global threat (Liu et al. 2020). COVID-19, as evidence suggests, is spread between people through direct contact with infected people, through droplets released in saliva or respiratory secretions, when the infected person coughs, sneezes sings, or speaks. Several recommendations have been made since the emergence, a few mentionable to control the spread, maybe by limiting close contact with infectious people. Since many patients may be asymptomatic or silent carriers of the infection, the overall protective strategy of social distancing must be implied and protecting the mouth and nose by wearing masks and coughing and sneezing while covering the nose and the mouth. The infected must be isolated and close contacts quarantined for at least 14 days or until symptoms resolve, and the test is negative. Well-ventilated indoor settings and avoiding crowded public places have an essential role (Ehsanifar 2021).

In times of epidemics, it could be hard to deal with religious congregations (CORG). Most world religions require their followers to get together in groups on a local, national, and international level. This mobilization and gathering could be a place where new harmful bacteria, especially those that spread through the respiratory system, could spread. Events related to COVID-19 that were talked about in religious groups seem to support this. The best way to avoid this possibility is to stop gatherings of people at these times. A lot of COVID-19 cases started in a Christian congregation in South Korea. After people were able to stop the disease from spreading at first, there was a sudden rise in cases starting in the third week of February 2020. This was caused by a sick person who went to the Shincheonji Church of Jesus. This cult thinks that illness is a sin, and that the person who is sick must go to prayers to make up for the sin (Park 2020). This belief led its followers to avoid tests, and some of them continued to go to Mass in secret. This made the problem even worse. Up to April 8, 2020, a lot of the Cult's followers were tested, and 5209 of them tested positive (Statista Research Department 2020).

Israel were disproportionately high relative to the rest of the population. Up to forty percent of people in an ultra-orthodox community are suspected to be infected. Aside from having a lot of children and living in a small space, one of the most important reasons is that people don't miss religious services. On March 9, 2020, the Jewish holiday of Purim, a lot of people went to the synagogues in this neighborhood. After

that, the community kept having religious gatherings and refused to stop (Tarnopolsky 2020).

A 70-year-old Sikh priest in the Indian state of Punjab refused to isolate himself after returning from Italy and Germany. He then attended other religious events, including a Sikh festival that attracts 300,000 people every day in a different city. After his passing, many of his intimate connections tested positive for the COVID-19 virus (Naib 2020). Tens of thousands of people may visit these venues every day. Every ten years, on the banks of the Ganges, tens of millions of believers converge for the Kumbh Mela (Singh and Haigh 2015). All Hindu religious sites were to be closed by March 20, 2020. At the time, COVID-19 transmission in India was in stage 2 and no clusters have been found at these sites.

Public gatherings have evidently increased the transmission of the disease, leading to an increase in the number of cases and deaths due to COVID-19. More challenging is to deal with religious congregations in times of pandemics (Ting et al. 2021). Such mobilizations and gatherings serve as focal points for dispersing infectious pathogens to geographically distanced areas since the individuals forming the masses may have gathered at a specific time and place from far-flung areas. This had a direct bearing on the epidemic curve and its global spread (Anastasiou and Duquenne 2021). Gathering for congregational prayers in Islam five times a day, Hajj—annual gathering and Umrah at any other time of the year in Makkah, Saudi Arabia; Communal gatherings such as Tablighi Jamaat and commemoration events of the Shiites at shrines are some of the many events worth mentioning where observance without following the SOPs for prevention may lead to a spike in the number of potential causes (Quadri 2020). Since the pandemic's beginning, the virus has affected multiple aspects, including social, political, and economic aspects of many countries worldwide (Qadri et al. 2022). Pakistan had its first case in February 2020, diagnosed in Karachi, Sindh. It was diagnosed in a student who had returned from Iran, where the spiritual leaders had refused to ban religious gatherings at shrines despite the World Health Organization labeling the disease as a pandemic and a public health emergency of international concern. This caused the virus to spill into neighboring countries.

The primary objective of this research is to examine religious and cultural festivities' response to COVID-19. The past studies were mostly focused on discussing socioeconomic scenarios, infections and deaths before and after COVID-19 pandemic. So, it was a need to research religious and cultural events during COVID-19. In this study, we focused to explores the public gathering on Shrines to attend six famous cultural/religious events in Pakistan during COVID-19 in Punjab province. These are the main religious events of Muslims that are rooted deeply in Sufism, for instance, *Ramadan*, *Eid-ul-fitar*, *Eid-ul-Adha*, *Muharram*, *Eid Milad un Nabi*, and *Urs* on Shrines. During the COVID pandemic, a large number of researchers have centered their attention on diverse demographic and religious contexts in developed countries. In the case of Pakistan, however, very few studies have examined the religio-cultural and pandemic issues. Islam is the state religion of Pakistan, which is the second-most populous Muslim country after Indonesia. Therefore, it is extremely interesting to learn the religious responses of individuals

to various Muslim events during a pandemic. During the COVID-19 pandemic, illiteracy and a lack of understanding of viral disease were also significant factors in people's refusal to follow government instructions at various Muslim events (Zakar et al. 2021). On the basis of this study, the following goals have been established:

- To study the impact of people's gatherings on various events are the reason for increasing COVID-19 spread in Pakistan.
- To analyze the Public health measure to cope with religious cultural challenges in case of Pakistan.
- To talk about the smart lockdown control as a key way to stop the spread of COVID-19 at cultural events.

## 13.2 Theoretical Background and Research Framework

### *13.2.1 Ramadan and Eid-ul-Fitr*

Keeping in view the sacredness of Ramadan and the spiritual healing it brings with itself, the government allowed religious clerics to hold large gatherings for prayers during COVID-19. This decision was severely opposed by the medical fraternity as the virus was on its boom, with no treatment and proper diagnosis of the cause. Moreover, the medical officials were highly critical of the infrastructural deficiencies in the country. They even predicted exponential growth in the cases. During Ramadan, Muslims usually visit mosques on a routine basis and also the markets as the schedule changes and there is a strict routine to be followed during fasting.

The public expected a ban on mass prayers that are offered during Ramadan as social or even religious gatherings were unfavorable under the context of uncontrollable upshot of the coronavirus. However, Imran Khan, the Prime Minister of Pakistan, provided relaxation to the religious gatherings while advising strict follow-up of SOPs (mainly social distancing) during prayers. The idea behind the gesture was to provide a hope to the hopeless third world dwellers. He urged religious clerics to instruct the public to follow SOPs while visiting mosques strictly (Khan and Shams 2022).

The maximum violation of SOPs provided by the government was done during *Ramadan* and *Eid* (Malik 2020) as the general public was reluctant to adopt the change named as precautionary measures. Resultantly, health care providers across the globe were severely affected by this pandemic. They were the frontline workers and they had to cope with physical and mental health issues eventually (Malik 2020). The relaxation regarding mobility before *Eid-ul-Fitr* in order to maintain economic stability badly affected the country's health system. Muslim countries worldwide observed a lockdown of mosques during the holy month of *Ramadan* as a response to the pandemic, while Pakistan remained the only exception. Pakistan did not impose a ban on religious gatherings even though the media reported several violations of SOPs in the mosques (Ittefaq et al. 2020). Pakistan tried to cope up with the

emergency situation differently with the context of low literacy rate, a large number of daily wage earners and depression due to already deteriorating financial setups. The partial lockdown saved the public spiritually but affected them physically and hence psychologically.

### *13.2.2 Eid-ul-Adha*

*Eid-ul-Adha* is also a religious festival of Muslims celebrated annually involving the mass sacrifice of animals. In Pakistan, this festival is celebrated on 10th Dhul Hijjah, a month of Islamic (Hijri) calendar. During pandemic, *Eid-ul-Adha* was celebrated in August 2020. Celebration of this festival was again a challenge for medical workers because it threatened resurgence of positive cases nationwide. In Pakistan, cattle farmers travel from villages to cities to sell animals during *Eid-ul-Adha* in order to get a better price for their well-bred cattle. Moreover, 64% population of Pakistan lives in rural areas with low literacy rate. So, cattle owners traveling from rural to urban areas for the sake of business activity caused a major threat as there was a high risk that virus may spread to virus-free areas as well. Furthermore, due lack of awareness of COVID-19 and its safety protocols in some of those areas, it was expected that the travelers will not follow the measures as they cannot comprehend it and can consider it a mere propaganda. It was an alarming situation as the naked eye cannot see the virus and hence it can spread easily and rapidly. The health department was again concerned about this rural–urban migratory activity which caused a surge in COVID-19 cases in Pakistan.

Although the Punjab government provided strict guidelines for establishing cattle markets but violation of these guidelines was widely expected. These guidelines included instructions such as maintaining social distance during the purchase, establishing markets in designated places only, provision of sanitizers, masks, and gloves being mandatory for all. It was even emphasized that strict action will be taken against illegal cattle markets i.e. those that do not follow COVID-19 protocols. Unfortunately, this could not stop the spread of COVID-19; however, the government kept a strict check on the SOPs. The festival of *Eid-ul-Adha* also resulted in the surge of COVID-19 cases like the festival of *Eid-ul-Fitr* (Mallhi et al. 2020) as congested animal sales stations were another problem during this festival because they could have been a source of virus transmission.

### *13.2.3 Muharram*

Muharram is the month in which the Muslims begin their lunar Hijrah Calendar. The 10th of Muharram is honored as Ashura in memory of Hazrat Imam Hussain (A.S), the Prophet's great-grandson and Hazrat Ali's (A.S) son. On Ashura, 680 AD, Hazrat Imam Hussain (A.S) was martyred in the battle of Karbala. In contrast

to other Islamic events, Muharram is a month of mourning and prayer in which no celebrations take place. An important cultural and religious event in Multan, a historical city in Pakistan, is the commemoration of Hazrat Imam Hussain's (A.S) martyrdom with more than fifty *tazia* and *zuljinna* procession. This moveable tomb can be of numerous shapes or sizes and is often a duplicate of the original one. *Tazia* is a significant rite of the Shia sect in Pakistan. On the first 10 days of Muharram, thousands of Shias decorate the *tazia* and lead a procession in commemoration of Karbala.

The marketplace environment inevitably causes the violation of one of the essential precautions, i.e., social distancing. It is the need of time to avoid any gatherings that may result in the widespread virus (Quadri 2020) be it of religious nature or of economic, to avoid the spread of this virus. After a decline in cases observed in Pakistan, the government opened several businesses and entertainment sectors that threatened the healthy stability and stimulated the second wave of COVID-19.

During the holy month of *Muharram*, *majalis*, assemblies, processions of *zuljinnah,* and gatherings also caused violations of several SOPs. Resurface of the virus was seen during Muharram congregations as well. Although, the government issued strict SOPs, including hand-washing, social distancing, wearing masks, sanitizing, and disinfection during *majalis.* Masses violated SOPs across the country during the holy month of *Muharram.*

### *13.2.4 Eid Milad-un-Nabi (SAW)*

It is a public holiday in Pakistan, *Eid Milad-un-Nabi*, also known as the birthday of Prophet Muhammad (SAW). On 12th *Rabi-ul-Awwal* (the Islamic calendar's third month), Muslims celebrate *Eid Milad-un-Nabi.* During the holy month of *Rabi-ul-Awwal, Eid Milad-un Nabi* is widely celebrated in Pakistan. Government also prescribed different SOPs for the *Seerat* conference, including the fact that *Milads* should be held in spacious areas ensuring proper ventilation, the social distancing of six feet should be maintained for everyone, thermal scanners would be added on all entry points, mask and hand sanitizers to be provided on all venues, and all the *Na'at* recites and clerics to be tested for coronavirus. But still people across Pakistan did not follow these SOPs, resulting in many positive cases. Due to these events and gatherings, the second wave of the coronavirus has hit Pakistan very seriously (Web Desk 2022).

### *13.2.5 Urs*

The term '*aroos*,' which means union or marriage, is the root of the name *Urs*. Sufis believe that after death, a person is united with their Lord, which is the greatest pleasure a person may experience. For this reason, it is a joyous occasion to commemorate

the saint's passing because it signifies the saint's union with God. Those who adhere to the Sufi faith believe that the world is simply a short-term residence where there are several tests and challenges. In the end, a man's destiny is sealed when he meets his Savior face to face. One of Multan's most important *Urs(es)*, that of Hazrat Bahauddin Zakariya, and the other of Hazrat Shah Rukn-i-Alam, is known throughout Pakistan (Chaudhry 2002). Hazrat Shah Rukn-i-Alam and Hazrat Bahauddin Zakariya's *Urs* represent the importance of religious festivals. Sufi celebrations have become a big part of the culture and a sign of the philosophy of Sufism. The government also issued SOPs for visits to religious places such as shrines. These SOPs included face masks, temperature checks, and social distancing. The custodians of these shrines are responsible for ensuring all the SOPs and violations that may result in the closure of the shrine (DAWN 2022). But a custodian cannot assure what a responsible individual can. So, even instead of the strictness at the shrines by the managing bodies there were still violations that can be the cause of transmission of virus at some point during pandemic.

### *13.2.6 Research Design*

This is a descriptive type of study. The study has used the secondary data via various sources to collect the information regarding covid 19 pandemic. The data[1] were collected for six religious and cultural festivals of Punjab Province that caused the COVID-19 spread in the province. These six religious and cultural events are *Ramadan*, *Eid-ul-Fitr*, *Eid Ul Adha*, *Muharram*, *Eid Milad-un-Nabi*, and *Urs*. Punjab province was chosen for this study because it has rich cultural and religious recognition. Religious people are called "Saints" that mostly belong to Punjab province, and religious events authorized with them are still happening. Furthermore, the other religious events have great recognition among the people of Punjab and are happening and celebrating with full enthusiasm. However, this research is conducted because these cultural and religious events object to gathering people in the province, even with strict government restrictions and SOPs, which are violated. The purpose of the study is to examine the number of cases reported in each event and the number of deaths recorded. In this regard, the research framework is developed, which is given below in Fig. 13.1.

[1] Source covid data: https://covid.gov.pk/.

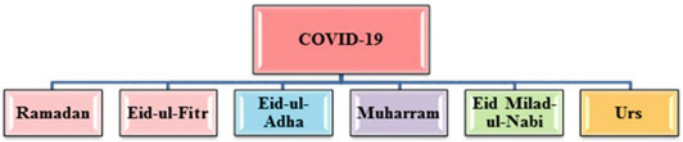


**Fig. 13.1** The above framework indicates the six religious and cultural events found as the leading cause of the COVID-19 variant in the Punjab province of Pakistan

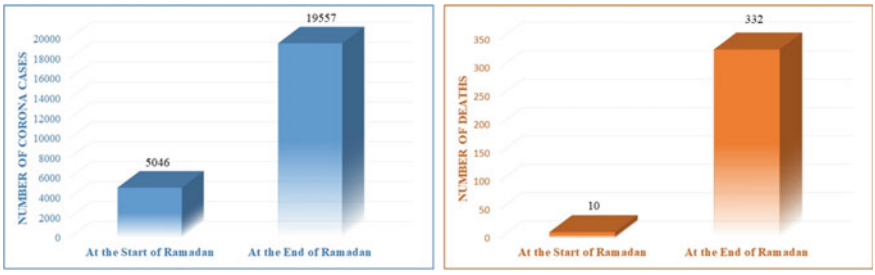


**Fig. 13.2** The number of corona cases and deaths at the start and end of Ramadan shows a rapid increase due to maximum violation of SOPs

## 13.3 Findings

### *13.3.1 Ramadan*

Ramadan is the holy month of Muslims and people of Pakistani. During this holy month, the corona cases in Pakistan increased rapidly. This holy month commenced on the 24th of April, and corona cases in Punjab that were reported on the same day were 5046. On 22nd May 2020, at the end of this holy month of *Ramadan*, the number of corona cases in Punjab increased drastically and reached to 19,557 Moreover, 332 deaths were reported due to COVID-19 during *Ramadan* (Fig. 13.2).

### *13.3.2 Eid ul Fitr*

*Eid-ul-Fitr* is another festival of Muslims and Pakistan. In 2020, Pakistan celebrated this festival with some restrictions due to worldwide spread of coronavirus. *Eid-ul-Fitr* is celebrated after the last day of Ramadan. At this festival, people meet and greet each other. Family gatherings are organized. After this festival of *Eid-ul-Fitr*, the number of corona cases in Punjab increased rapidly. On 7th June 2020 in Punjab, Pakistan, after 15 days of *Eid-ul-Fitr*, the reported corona cases were 38,903, and the number of deaths reached to 715. Undoubtedly, this resulted from family gatherings and not following the proper SOPs for the celebrations of *Eid-ul-Fitr* (Fig. 13.3).

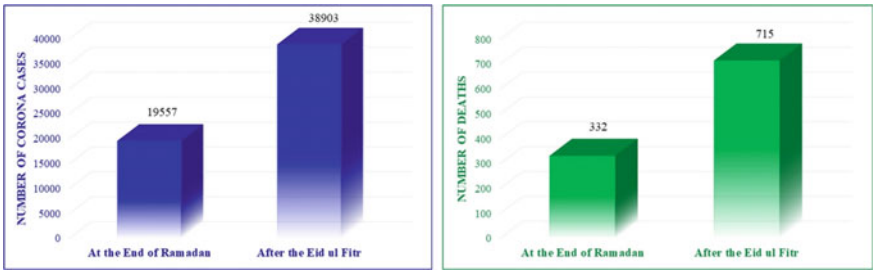


**Fig. 13.3** The number of corona cases and death at the end of Ramadan and after the Eid-ul-Fitr festival

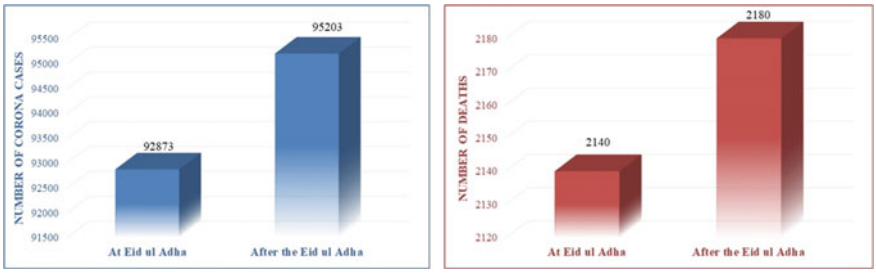


**Fig. 13.4** A number of corona cases and death at Eid-ul-Adha and after the Eid-ul-Adha festival. Eid-ul-Adha was celebrated with full SOPs, which witnessed fewer worst conditions than Ramadan and Eid-ul-Fitr

### *13.3.3 Eid ul Adha*

In Punjab, Pakistan, *Eid-ul-Adha* was celebrated on Thursday, 30th of July, 2020. This festival was celebrated with complete corona SOPs. The total number of corona cases in Punjab was 92,873, and deaths reported were 2140. After 15 days of this festival, on 15th August 2020, the total number of corona cases was reported as 95,203, and deaths were 2180. The results showed the government's strict policies and smart lockdown during this *Eid-ul-Adha* event (Fig. 13.4).

### *13.3.4 Muharram*

Muharram is another sacred month for Muslims and Pakistan. In Pakistan, Ashura in *Muharram* was mourned on the 30th of August 2020, with proper corona SOPs. The total number of corona cases in Punjab was 96,769, and deaths reported were 2198 after Ashura. This is the result of good government policies and National Command and Operation Centre (NCOC) guidelines. Otherwise, the number of cases and death


**Fig. 13.5** The number of corona cases and death before and after the Ashura and less number of corona cases and deaths were reported in this event compared to previous events and government-imposed smart lockdown

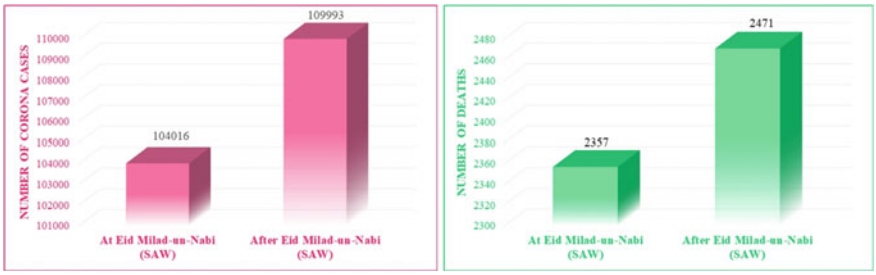


**Fig. 13.6** Number of corona cases and death before and after the Eid Milad-un-Nabi (SAW)

rate would have been severe after Ashura. However, the much-affected areas adopted smart lockdown (Fig. 13.5).

### *13.3.5 Eid Milad-un-Nabi (SAW)*

*Eid Milad-un-Nabi* (SAW) was celebrated in Punjab on 30th October 2020. This was the time when Punjab stopped following the NCOC and Corona SOPs. On 30th October 2020, the total number of corona cases in Punjab was reported as 104,016, and the number of deaths was 2357. After 15 days of this event, on 14th November 2020, the total number of corona cases was 109,993, and deaths were reported at 2471 (Fig. 13.6).

### *13.3.6 Urs*

During the uncertain situation of COVID-19 in the country, most of the *Urs* in much-affected areas of Punjab province were postponed. However, some urs of highly

spiritual and influentially famous names, especially from Southern Punjab, held on the same date. However, it is also the concern of impossible to collect data on every *Urs* held in Punjab. Therefore, we have chosen the most famous *Urs* held in Punjab with the availability of accurate figures of corona cases and deaths in Punjab. So, we have discussed the COVID-19 situations in the *Urs* of Hazrat Bahauddin Zakariya and Hazrat Shah Rukn-e-Alam.

**Hazrat Bahauddin Zakariya**. Hazrat Bahauddin Zakariya is a very famous saint of Muslims and Pakistanis. His *Urs* is celebrated in the Multan City of Punjab every year. However, in 2020, due to COVID-19, the celebrations of *Urs* were organized with proper Corona SOPs and strict rules. The *Urs* activities were kept short and limited due to COVID-19 on the day of Urs i.e. 24th September 2020. On this day, the total number of cases in Punjab was 98,864, and death was reported **at** 2229 (Fig. 13.7-first row). However, this was the time when Punjab decided to stop following the **NCOC** guidelines and Corona SOPs, and it was one of the the worst situation after the *Eid Milad-un-Nabi* (SAW).

**Hazrat Shah Rukn e Alam**. The *Urs* of Hazrat Shah Rukn-e-Alam was planned to be organized in Multan Punjab at the end of December 2020. However, due to the spread of COVID-19 from the its second wave the *Urs* celebrations were postponed to 15th December 2020. At that time, the number of corona cases in Punjab was reported at 128,673, and number of deaths was 3452. After 15 days of this, on 31st December 2020, the total number of cases increased rapidly and was 138,608, and

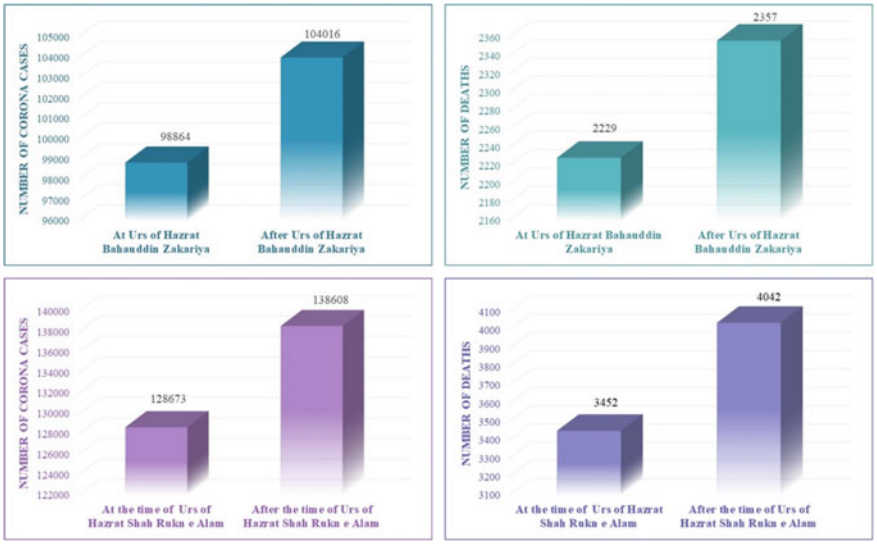


**Fig. 13.7** The first row shows the number of corona cases and death at and after Urs of Hazrat Bahauddin Zakariya, and the second row shows the number of corona cases and death at and after Urs of Hazrat Shah Rukn e Alam at Multan city in Punjab province

**Table 13.1** Before and after the main six festival-wise breakups total number of cases and deaths in Punjab province

| | Festivities | | | Cases | Deaths |
|---|---|---|---|---|---|
| 1 | Ramadan | | Before | 05,046 | – |
| | | | After | 19,557 | 332 |
| 2 | Eid ul Fitr | | Before | – | – |
| | | | After | 38,903 | 715 |
| 3 | Eid ul Adha | | Before | 92,873 | 2140 |
| | | | After | 95,203 | 2180 |
| 4 | Muharram (Ashura) | | Before | 95,203 | 2180 |
| | | | After | 96,769 | 2198 |
| 5 | Eid Milad-un-Nabi (SAW) | | Before | 104,016 | 2357 |
| | | | After | 109,993 | 2471 |
| 6 | Urs | Hazrat Bahauddin Zakariya | Before | 98,864 | 2229 |
| | | | After | 104,016 | 2357 |
| | | Hazrat Shah Rukn-e-Alam | Before | 128,673 | 3452 |
| | | | After | 138,608 | 4042 |

*Source* Covid data: https://covid.gov.pk/

death was reported at 4042 (Fig. 13.7-second row). This was the result of ignoring corona SOPs and NCOC instructions. Before and after the main six festival-wise breakups, and the total number of cases and deaths in Punjab province are given in Table 13.1.

## 13.4 Discussion

The spread of COVID-19 is a major challenge for governments worldwide (Bayeh et al. 2021). The people of the Punjab province of Pakistan did not follow the SOPs and attended religious events regularly. These events include *Ramdan*, *Eid-ul-fitar*, *Eid-ul-Adha*, *Muharram*, *Eid Milad-un-Nabi*, and the celebration of *Urs*. According to the findings, the negligence in SOPs cost us the second wave of COVID-19 in Punjab (Pakistan). Regarding this, it was noticed that the number of corona cases and deaths started increasing in the holy month of Ramadan, and the situation was worse before and after *Eid-ul-Fitr*. However, the next event of *Eid-ul-Adha* was celebrated with full SOPs, which actually witnessed less worsened conditions than Ramadan and *Eid-ul-Fitr*. Furthermore, *Muharram* (*Ashura*) is mourned under strict government policies and NCOC guidelines. We have noticed the least number of corona cases and deaths in this event compared to all previous events under consideration. After this, people in Punjab did not follow the NCOC and corona SOPs, and the worst situation was witnessed after *Eid Milad-un-Nabi* (SAW).

During the COVID-19, we observed a complete lockdown for a short time, which resulted in the country's economic crisis. After that Government of Pakistan announced the smart locked down to control the COVID-19 spread without affecting socio-economic wellbeing. In smart locked down, we saw severe COVID-19 cases in areas where the SOPs were not followed. *Ramadan* and *Eid-ul-Fitr* are examples of the province's economic benefits, but the province has gone through a disastrous situation. After that Government of Pakistan announced strict SOPs during the smart lockdown, and we have noticed that the events of *Eid-ul-Adha* and *Muharram* went well, and we witnessed less number of COVID-19 infections and deaths. So, after these successful events and a better situation in the province, the government announced a mild locked-down. During this lockdown basically, the SOPs were less strict. People can easily travel and the number of people allowed in gatherings such as weddings, etc., by wearing masks and hand sanitizer increased. However, we have seen that the people did not take it seriously and moved to the regular routine without following soft SOPs, and the results are witnessed in the events of *Urs* and *Eid-Milad-un-Nabi* (SAW). Pakistan has announced standard operating procedures (SOPs) for public gatherings in order to slow the spread of COVID-19 as the country is currently in the grip of the second wave of the pandemic. The *Urs* of Hazrat Shah Rukn-e-Alam conference has been cancelled due to coronavirus pandemic in the country. Due to the ongoing second wave, many other religious events and Shrine rituals that the caretakers traditionally performed were not observed. The government has requested devotees not to attend the *Urs* due to the virus's possible spread.

## 13.5 Conclusion

Pakistan is a developing country struggling with its economic situation, and it cannot negotiate with full strict lockdown. However, the findings suggest that Government should impose smart lockdown with complete SOPs, and it should continue until the zero policy. The use of masks and hand sanitizer should be compulsory, and there should be strict punishment if someone finds it violating. This study's genuine concern is social distancing, which should be adopted without any negligence. These findings are inferable from the above discussion that government should refocus on the sensitivity of time because any province of Pakistan cannot afford a lockdown, same as recently China imposed a lockdown in Shenzhen, Shanghai, and Beijing due to the SARS-CoV-2 outbreak (Zhang et al. 2022; Chen and Chen 2022). Based on this research, it is proposed that:

- Government should increase the vaccination coverage network because only 56.1% (124 million people) of the population is fully vaccinated, which is a very low rate (COVID Vaccination in Pakistan 2022) while this ratio in China is 89.1%.
- All religious and cultural festivities should monitor properly and be held according to SOP, wearing face masks and keeping social distance.

- For mild COVID cases, the government should train local healthcare staff to provide better services.
- Reduce in-person patients by expanding online clinical services.
- Smart lock down policy should be implemented to reduce the economical side effects.
- More awareness programme should be lunched for the religious scholars regarding the awareness about the Pandemic.
- Religious scholers should give the awareness regarding the Pendemic to the public in their religious speeches.

The danger is not over yet, and regardless of when the COVID pandemic ends, measures must be made in advance to face the challenges.

There are a few limitations of this research. This study is limited in its area i.e. Punjab province of Pakistan. Furthermore, the data availability was limited as the data of more events. But from the point of view of future research, this research can be extended by accessing the information of other provinces of Pakistan. Eventually, the data will be collected for more events held in other provinces that will result in more research outcomes. Furthermore, this research can be enhanced by studying the indicators of socio-economic concerns and post-pandemic strategies.

**Funding** This research was funded by the key art project of the National Social Science Foundation of China (15AH007), the independent scientific research project of Wuhan University (1203/41050028), and the project of Hubei think tank in 2020 (1203/413000071).

## References

Anastasiou E, Duquenne MN (2021) What about the "Social Aspect of Covid"? Exploring the determinants of social isolation on the Greek population during the Covid-19 lockdown. Soc Sci 10:1–13. https://doi.org/10.3390/socsci10010027

Bayeh R, Yampolsky MA, Ryder AG (2021) The social lives of infectious diseases: why culture matters to COVID-19. Front Psychol 12:1–21. https://doi.org/10.3389/fpsyg.2021.648086

Chaudhry NA (2002) Multan glimpses: with an account of siege and surrender. Sang-e-Meel Publications. ISBN 9789693513516

Chen J-M, Chen Y-Q (2022) China can prepare to end its zero-COVID policy. Nat Med. https://doi.org/10.1038/s41591-022-01794-3

COVID Vaccination in Pakistan (2022). https://covid.gov.pk/vaccine-details. Accessed on 12 June 2022

DAWN (2022) Limited activity at Shah Rukn-i-Alam's Urs in Multan. Newspaper, DAWN.COM. https://www.dawn.com/news/1596927. Accessed on 22 May 2022

Khan S, Shams S (2020) COVID-19: why Ramadan could be a disastrous month for Pakistan | Asia | An in-Depth Look at News from across the Continent | DW | 24.04.2020. https://www.dw.com/en/covid-19-why-ramadan-could-be-a-disastrous-month-for-pakistan/a-53231304. Accessed on 22 May 2022

Ehsanifar M (2021) Airborne aerosols particles and COVID-19 transition. Environ Res 200:111752

Huang C, Wang Y, Li X, Ren L, Zhao J, Hu Y, Zhang L, Fan G, Xu J, Gu X et al (2020) Clinical features of patients infected with 2019 novel coronavirus in Wuhan, China. Lancet 395:497–506

Ittefaq M, Hussain SA, Fatima M (2020) COVID-19 and social-politics of medical misinformation on social media in Pakistan. Media Asia 47:75–80. https://doi.org/10.1080/01296612.2020.1817264

Kim Y, Park Y (2022) International health cooperation in the post-pandemic era: possibilities for and limitations of middle powers in international cooperation. Soc Sci 11:259. https://doi.org/10.3390/socsci11060259

Liu YC, Kuo RL, Shih SR (2020) COVID-19: the first documented coronavirus pandemic in history. Biomed J 43:328–333. https://doi.org/10.1016/j.bj.2020.04.007

Malik S (2020) Knowledge of COVID-19 symptoms and prevention among Pakistani adults. Rawal Med J 45:786–789

Mallhi TH, Khan YH, Alotaibi NH, Alzarea AI, Tanveer N, Khan A (2020) Celebrating Eid-Ul-Adha in the Era of the COVID-19 pandemic in Pakistan: potential threats and precautionary measures. Clin Microbiol Infect 26:1714–1715. https://doi.org/10.1016/j.cmi.2020.07.019

Naib M (2020) At least 40,000 quarantined in India after a single priest spread coronavirus. NBC News

Park SN (2020) Cults and conservatives spread coronavirus in South Korea Seoul seemed to have the virus under control. But religion and politics have derailed plans. Foreign Policy Online 27

Qadri S, Chen S, Usman Qadri S (2022) How does COVID-19 affect demographic, administrative, and social economic domain? Empirical evidence from an emerging economy. Int J Ment Health Promot 24:1–14. https://doi.org/10.32604/ijmhp.2022.021689

Quadri SA (2020) COVID-19 and religious congregations: implications for spread of novel pathogens. Int J Infect Dis 96:219–221. https://doi.org/10.1016/j.ijid.2020.05.007

Singh RPB, Haigh MJ (2015) Hindu pilgrimages: the contemporary scene. Springer, In The changing world religion map, pp 783–801

Statista Research Department (2020) Coronavirus (COVID-19) cases related to Shincheonji Church in South Korea. https://www.statista.com/statistics/1103080/south-korea-covid-19-cases-related-to-shincheonji-church/. Accessed on 24 April 2020

Tarnopolsky N (2020) Ultra-orthodox jews hit disproportionately hard by Israel's coronavirus outbreak. Los Angeles Times

Ting RSK, Aw Yong YY, Tan MM, Yap CK (2021) Cultural responses to covid-19 pandemic: religions, illness perception, and perceived stress. Front Psychol 12:1–19. https://doi.org/10.3389/fpsyg.2021.634863

Web Desk (2022) Eid Milad un Nabi: Sindh issues coronavirus guidelines for conferences, events. https://www.geo.tv/latest/315833-eid-milad-un-nabi-sindh-issues-coronavirus-guidelines-for-conferences-events. Accessed on 22 May 2022

Zakar R, Iqbal S, Zakar MZ, Fischer F (2021) COVID-19 and health information seeking behavior: digital health literacy survey amongst University Students in Pakistan

Zhang X, Zhang W, Chen S (2022) Shanghai's life-saving efforts against the current Omicron wave of the COVID-19 pandemic. Lancet 399:2011–2012. https://doi.org/10.1016/s0140-6736(22)00838-8

# Chapter 14
# Experimental Investigation of Magnetic Field Influence on Viscosity of Waxy Crude Oil Emulsion

**Xueying Li, Lei Hou, Sichen He, Chong Chai, and Ya'nan Huang**

**Abstract** Magnetic treatment is a widely physical technique used in oilfields. The effects of magnetic field on waxy crude oil emulsion have drawn much attention. This study aims to explore the relationship of the change of viscosity of emulsion and magnetic treatment conditions and viscosity reduction mechanism. The static permanent magnet device was constructed. The viscosity of crude oil and emulsion, oil–water interfacial tension and the distribution characters of emulsion droplets before and after magnetic field were experimentally studied. The results showed that when the magnetic treatment temperature was wax appearance temperature, the magnetic field intensity of 200 mT and magnetic treatment time of 10 min, the viscosity of emulsion decreased the most and reached 14.5%. Meanwhile, the viscosity of crude oil and oil–water interfacial tension decreased after magnetic treatment. The droplet distribution did not change obviously after applying different magnetic treatment conditions. The magnetic field reduced the viscosity of the emulsion by reducing the viscosity of crude oil and the oil–water interfacial tension.

**Keywords** Magnetic field · Viscosity · Waxy crude oil emulsion · Interfacial tension

## 14.1 Introduction

In recent years, the production and exploitation of oilfields in China have been the late stage with high water content. Due to the natural emulsifiers, the fluids in oilfield

X. Li · L. Hou (✉) · S. He
China University of Petroleum, Beijing, China
e-mail: houleicup@126.com

X. Li
e-mail: 2927750073@qq.com

C. Chai
National Pipe Network Group Science and Technology Research Institute, Beijing, China

Y. Huang
China Merchants Bank Beijing Branch, Beijing, China



Z. Yang (ed.), *Environmental Science and Technology: Sustainable Development*, Environmental Science and Engineering, https://doi.org/10.1007/978-3-031-27431-2_14

mostly exist in the form of oil–water emulsion especially water-in-oil emulsion, whose apparent viscosity is often several times or even ten times higher than that of crude oil (Li et al. 2014; Li 2018). How to reduce viscosity of emulsion economically and efficiently has become an important challenge. Magnetic treatment technology, as a physical modification method, can be easy to operate and environmentally friendly. It presents the broad application prospect and becomes an attractive research focus to improve the fluidity of emulsion.

Studies have been developed to explore the effect of magnetic field on the viscosity of crude oil. Loskutova et al. (2004), Loskutova and Yudina (2006) selected 16 kinds of Russian oils for magnetic experiments. The results showed that the key factors affecting the magnetic treatment effects were as follows: the magnetic field intensity (B), flow form, treatment time and flow rate. Li et al. (2008) carried out the electromagnetic research on viscosity of heavy oil. The viscosity decreased with the increase of the magnetic field strength, and then remained basically constant. However, Rocha et al. (2000) put forward to the opposite point of view. There was no correlation between viscosity and magnetic treatment time or magnetic field intensity. The viscosity of high waxy crude oil decreased by 40% when magnetic treatment temperature was lower than the wax precipitation point. The Vietnam's White Tiger and Dragon Crude Oils were used for magnetic experiments. The 10 °C higher than the pour point of crude oil is the optimal magnetic treatment temperature (Tung et al. 2001, 2003). Tao and Xu (2006) found that the sensitivity of asphalt-based crude oil to magnetic field was lower than that of paraffin-based crude oil.

The above experiments focus on the macroscopic viscosity of crude oil under magnetic field. However, a few preliminary explorations about the influence of magnetic field on the viscosity of emulsion were carried out. Zhang et al. (2012) proposed that the presence of emulsified water could enhance the viscosity reduction effects of emulsion. The magnetic field made the wax crystal bands aggregate near the equatorial area of droplets, while the wax crystals at two poles were sparse. The droplets could aggregate easily and then the viscosity of emulsion decreased. Gonçalves et al. (2010, 2011) conducted magnetization experiments of six oil samples. The viscosity of the only oil sample decreased by 39%. The oil sample had the highest water content, lowest aromatic/aliphatic hydrocarbon ratio, and trace elements such as Mn, Sr and Br. The magnetic treatment research mainly focuses on the viscosity of crude oil. The systematized studies involving waxy crude oil emulsion have not yet been conducted, and most of them stay in the qualitative analysis. There is still a lack of the mechanism in viscosity change from microscopic level. Therefore, it is necessary to carry out the relevant research.

In this study, the influence of magnetic field on the waxy crude oil emulsion was experimentally investigated by self-developed static magnetic apparatus. Then, the viscosity of crude oil and emulsion, droplet distribution, and oil–water interfacial tension before and after magnetic treatment were observed. Finally, the mechanism interpretation of viscosity change was analyzed from microscopic perspective. It can provide technical and theoretical guidance for viscosity reduction and transportation of waxy crude oil emulsion.

**Table 14.1** The properties and composition (SARA) of the Jilin crude oil

| Density (kg/m$^3$) | Wax appearance temperature (°C) | SARA (wt%) | | | |
|---|---|---|---|---|---|
| | | Saturates | Aromatics | Resins | Asphaltenes |
| 847 | 58 | 60.59 | 13.16 | 11.17 | 0.63 |

## 14.2 Material and Methods

### *14.2.1 Material*

The waxy crude oil used in this work was provided by Jilin oilfield. The differential scanning calorimetry and four-component separation method were used to determine of wax, resin and asphaltene content of crude oil. Properties and SARA (saturates, aromatics, resins, and asphaltenes) composition of the crude oil were listed in Table 14.1. The distilled water was used to prepare the emulsion. Although crude oil has undergone the dehydration process, it still contains a small amount of emulsified water. The deep dehydration treatment is carried out by using DTS-IV(4C) petroleum airtight dehydrator before the experiments. The Condensation point of Jilin crude oil was 36 °C.

### *14.2.2 Magnetic Treatment Device*

The static magnetic treatment device is shown as in Fig. 14.1. It is mainly composed of a rectangular parallelepiped welded with austenitic stainless steel 1Cr18Ni9Ti material and N43 NdFeB permanent magnets. The external dimensions of parallelepiped are 30, 14 and 14 cm. The dimensions of magnetic treatment cavity are 20, 10 and 10 cm. The magnetic treatment parameters can be entered in the control panel. Under the control of PLC programmable logic controller, the servo motor drives the S magnet to move by adjusting the lead screw to achieve the set parameters. The experimental temperature is controlled by the water bath. The magnetic strength range of the device is 0–300 mT. The magnetic treatment temperature range is 0–75 °C.

### *14.2.3 Macroscopic Viscosity Determination*

The macroscopic viscosity of crude oil and emulsion was measured by the Anton Paar RheolabQC rheometer with the shear rate range of 0.1–1000 $s^{-1}$. A sample volume of 30 mL was used to measure viscosity. In the testing temperature range from 38 °C to 55 °C, the samples presented a non-Newtonian fluid behavior whose

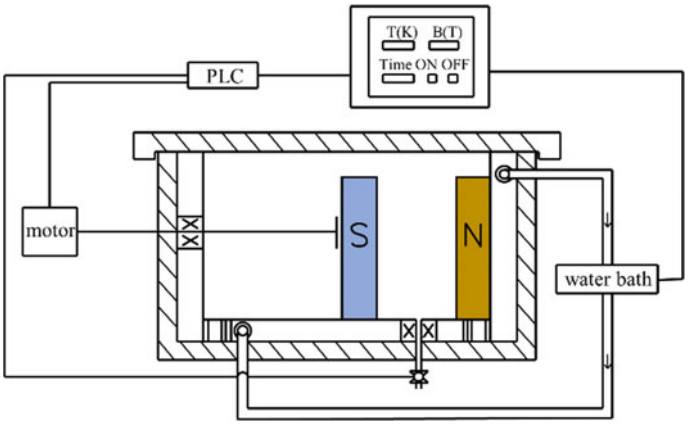


**Fig. 14.1** The static magnetic treatment device

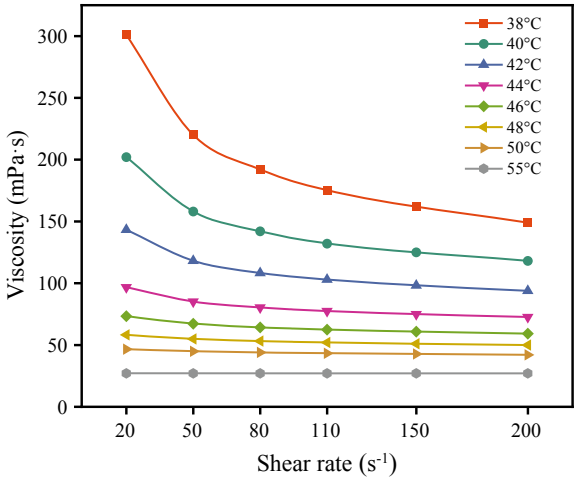


**Fig. 14.2** The relationship of apparent viscosity and temperature of Jilin crude oil

apparent viscosity depended on temperature and shear rate. Figure 14.2 illustrates the relationship of apparent viscosity and temperature of Jilin crude oil.

### *14.2.4 Emulsion Preparation*

The water-in-oil emulsion is prepared by oil–water two-phase emulsification device shown in Fig. 14.3. The volume ratio of water and oil was set at 7/3. The oil sample was treated at 80 °C for two hours to eliminate shear and thermal history. Then it was cooled naturally to ambient temperature for more than 48 h. In this experiment, a

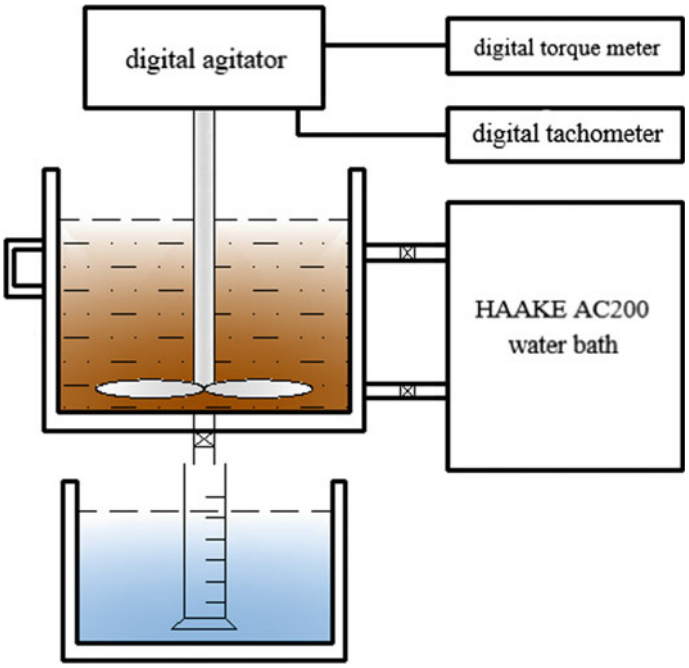


**Fig. 14.3** The oil–water two-phase emulsification device

four-bladed 45° stirring paddle with a diameter of 50 mm was used. A total volume of 50 mL mixture of water and oil sample was placed in a 250 mL beaker. The position of the stirring paddle was about 0.5 cm from the bottom of the beaker, and water was added at one time. The mixture was emulsified for 15 min at 800 rpm using the IKA RW20 digital agitator.

## 14.3 Results and Discussion

### *14.3.1 The Viscosity Variation of Crude Oil Under Magnetic Field*

The large molecules such as wax or asphaltene are treated as suspended particles in low viscosity light oil, and the crude oil is regarded as the liquid suspension. Based on the theory, it is reported that the magnetic field can reduce the apparent viscosity of the waxy crude oil. The following magnetic treatment conditions were applied: the magnetic field intensity of 40–200 mT, the magnetic treatment temperature of 55–62 °C, and the treatment time of 5–20 min. The test temperature of emulsion is 42 °C. The viscosity change rate $\varphi$ was used to evaluate the magnetic treatment

effects. The equation is as follows:

$$\varphi = (\mu - \mu_0)/\mu_0 \tag{14.1}$$

where $\varphi$ is the viscosity change rate, %. $\mu$ and $\mu_0$ are the viscosity of the experimental samples after and before magnetic field, mPa·s.

Figures 14.4, 14.5 and 14.6 shows the viscosity change rate when the magnetic treatment temperature is 55, 58 and 60 °C. The results showed that there was no positive correlation between viscosity change rates and magnetic field intensity. Under the same magnetic treatment temperature and time, the viscosity change rates of crude oil showed multi-extremal changes, not strictly increasing or decreasing with the increase in magnetic field intensity. The difference of viscosity change rate under different magnetic field intensity was up to 53.23%, indicating that the magnetic field intensity has a great influence on the viscosity of crude oil. Especially at B = 200 mT in Table 14.2, the reduction of viscosity was relatively stable and the average reduction rate was more than 10%. The maximum viscosity reduction rate is 20.3%.

When the magnetic treatment temperature was 55 °C in Fig. 14.4 (below the wax appearance temperature), the viscosity of crude oil increased at most test points. Taking the magnetic treatment time of 15 min as an example, the viscosity only reduced by 0.75–5.24% at 80 mT, and the viscosity of other test points all increased. While the magnetic treatment was carried out at 60 °C (above the wax appearance temperature), the viscosity decreased in most magnetic field intensity points. In Fig. 14.6b, the viscosity of crude oil decreased and the maximum reduction rate reached 17.31% except for slight increase at 80 and 160 mT. The results demonstrated that the selection of magnetic treatment temperature was important for the viscosity of crude oil. When magnetic treatment is performed below the wax appearance temperature, there is no obvious viscosity reduction, even the increase of viscosity would occur. However, when the magnetic treatment was performed above the wax appearance temperature, the significant viscosity reduction effects could be obtained if the magnetic field intensity and treatment time were selected appropriately.

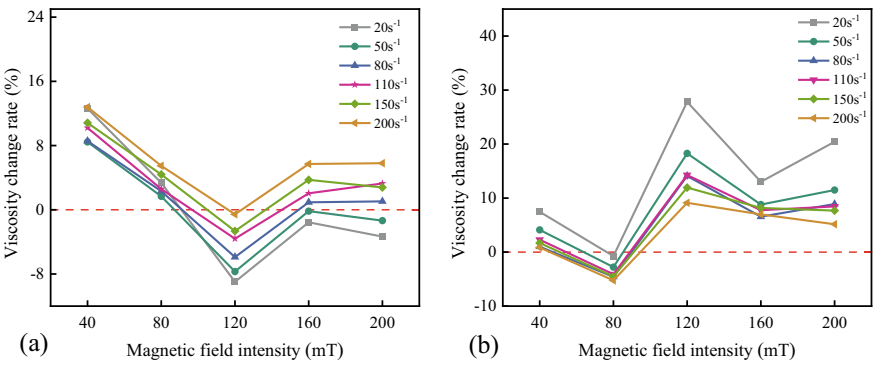


**Fig. 14.4** The change rate of viscosity of crude oil at 55 °C. **a** 5 min, **b** 15 min

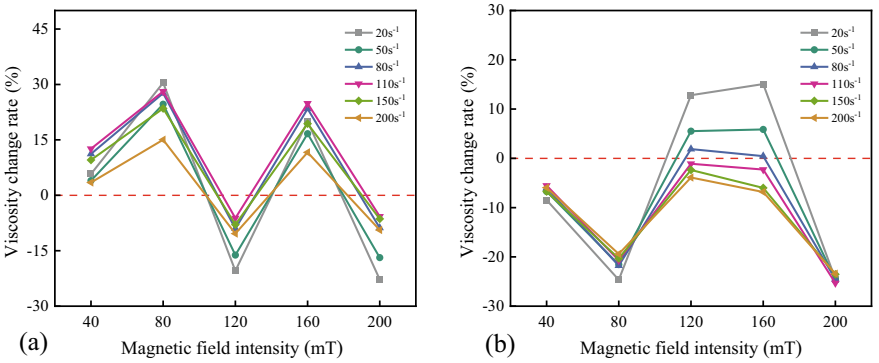


**Fig. 14.5** The change rate of viscosity of crude oil at 58 °C. **a** 5 min, **b** 15 min

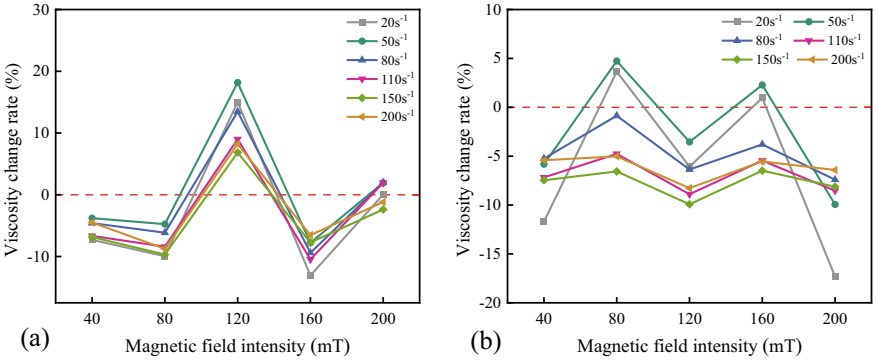


**Fig. 14.6** The change rate of viscosity of crude oil at 60 °C. **a** 5 min, **b** 15 min

**Table 14.2** The maximum change rate of viscosity when B = 200 mT

| *T* (°C) | Magnetic treatment time (min) | Maximum change rate (%) |
|---|---|---|
| 55 | 5 | −22.78 |
| | 10 | 7.11 |
| | 15 | −23.53 |
| | 20 | −12.52 |
| 60 | 5 | −2.38 |
| | 10 | −20.29 |
| | 15 | −17.31 |
| 62 | 5 | −11.81 |
| | 10 | −12.77 |
| | 15 | −0.55 |

### 14.3.2 The Viscosity Variation of Emulsion Under Magnetic Field

Figures 14.7, 14.8 and 14.9 show the viscosity change rates of the emulsion with and without applying magnetic field at 55 °C, 58 °C and 60 °C, respectively. When the magnetic field was applied at 55 °C in Fig. 14.7, the viscosity of the emulsion did not change significantly with the increase of the magnetic field intensity. The change rates of viscosity for the most test points were within 6%, close to the 5% error limitation of the Anton Paar RheolabQC rheometer. The maximum viscosity reduction rate is 11.48% at only B = 40 mT for 15 min. The results indicated that the magnetic effects below the wax appearance temperature did not affect the viscosity of emulsion. When the magnetic treatment temperature was 58 °C (wax precipitation point) as seen in Fig. 14.8, the viscosity of the emulsion all increased at B = 40 mT, 80 mT and 120 mT. The maximum decreasing rate of viscosity reached 20.5% at B = 80 mT for 15 min. The viscosity at 160 mT and 200 mT appeared decreased. When the magnetic field intensity was 160 mT, the viscosity of the emulsion decreased after magnetically treated for 5 min and 10 min. The decreasing rate reached the largest value 15.9% at B = 200 mT for 10 min. As for the magnetic treatment at 60 °C in Fig. 14.9, the viscosity of emulsion increased under different magnetic field intensity. And the maximum increasing rate of viscosity was 15.7% when B = 120 mT for 5 min. Although there was a slight viscosity reduction in some cases such as 40 mT for 5 min and 200 mT for 10 min, the maximum decreasing rate was 3.9% within error limitation.

In summary, the response of viscosity to magnetic treatment temperature was significantly different. Below the wax appearance temperature, the emulsion viscosity did not respond to the magnetic treatment. Above the wax appearance temperature, the viscosity of the emulsion all increased. At the wax appearance temperature, the viscosity of the emulsion appeared the decreasing trends. It

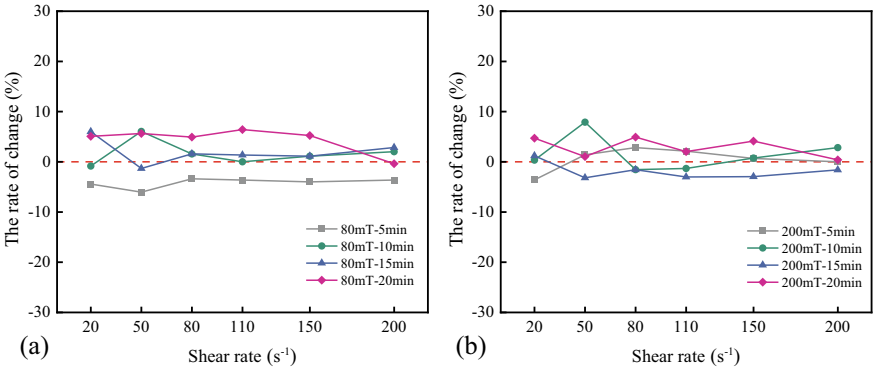


**Fig. 14.7** The change rate of viscosity of emulsion at 55 °C. **a** 80 mT, **b** 200 mT

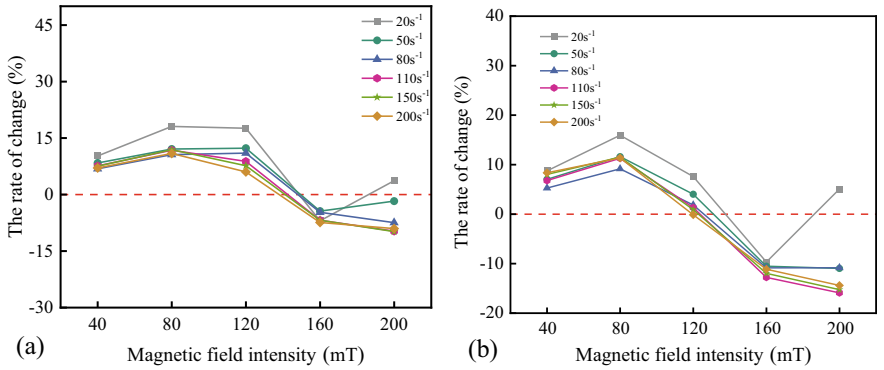


**Fig. 14.8** The change rate of viscosity of emulsion at 58 °C. **a** 5 min, **b** 10 min

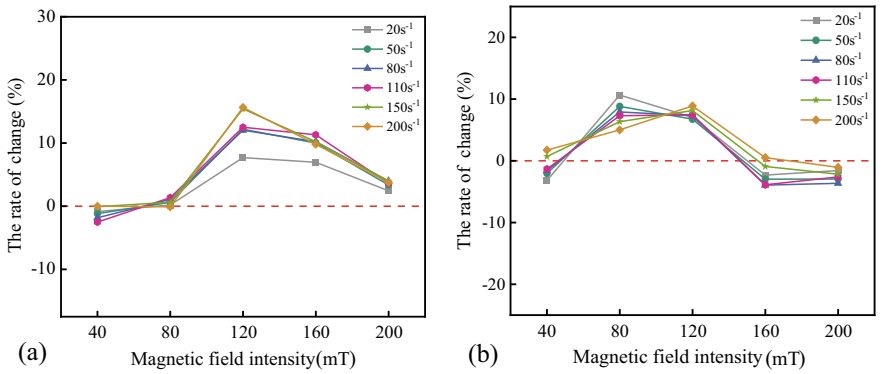


**Fig. 14.9** The change rate of viscosity of emulsion at 60 °C. **a** 5 min, **b** 10 min

could be found that the viscosity of emulsion was very sensitive to the magnetic treatment temperature and magnetic field intensity.

### *14.3.3 The Droplet Diameter Distribution and Interfacial Tension*

To study the mechanism of viscosity change of emulsion from microscopic perspective, the droplet diameter distribution and interfacial tension were discussed. Considering the decrease of viscosity at 58 °C, the droplet diameter distribution of emulsion was analyzed in Fig. 14.10. The results indicated that the distribution of droplets did not change significantly after applying magnetic field. When the droplets were at low magnetic field intensity such as 40 mT, the smaller diameter droplets of standing 15 min dominated more than those of 5 min or

10 min. The results were in agreement with the fact that the viscosity (40 mT and 15 min) is higher than other conditions (40 mT, 5 min or 10 min). The long magnetic treatment time easily leads to the coalescence of droplets. Therefore, the small droplets are more numerous when the magnetic treatment time is short. The magnetic treatments under 40 mT and 80 mT were taken as an example in Fig. 14.10a, b. The distribution curves of small droplets of 15 min were higher than that of 5 min, indicating that the small droplets dominated with the increase of magnetic treatment time. It proved that the magnetic field could inhibit the coalescence of droplets to some extent. To further compare the differences under different conditions, the exponential function "$y = a - b * c^x$" was used to fit the curves of droplet diameter distribution shown in Table 14.3. When the 160 mT was applied, the fitting parameters were basically unchanged and the largest change rate was only 2.89%.

The interfacial properties of the droplets are also one of the factors affecting the viscosity of the emulsion. Table 14.4 lists the oil–water interfacial tension of emulsion with and without magnetic treatment at 58 °C. The oil–water interfacial tension

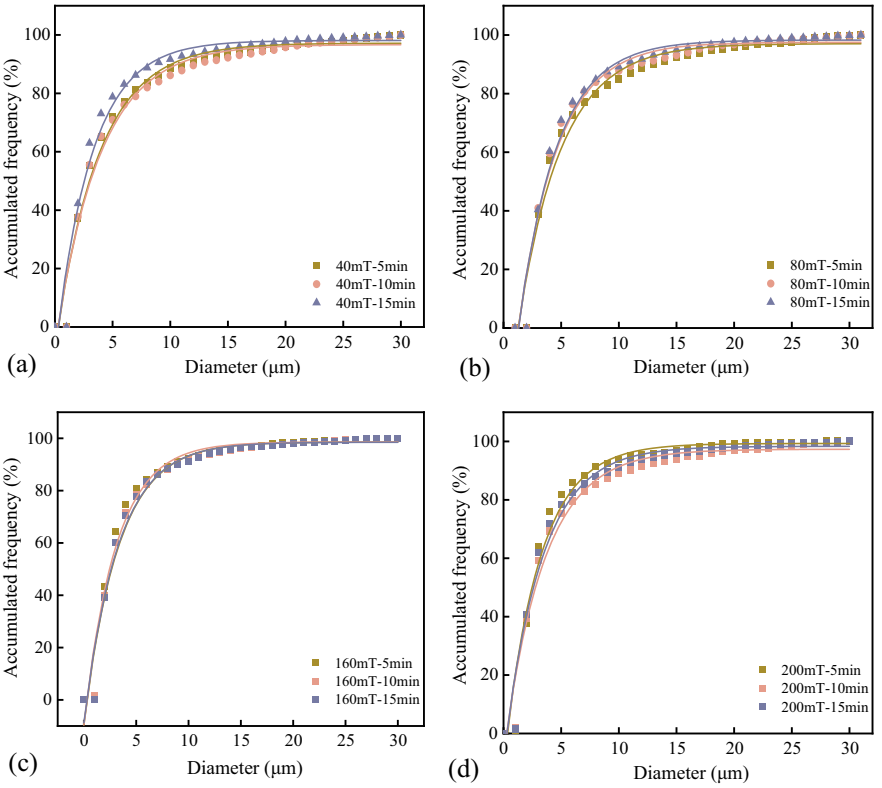


**Fig. 14.10** The droplet diameter distribution of emulsion under different magnetic field intensity. **a** 40 mT, **b** 80 mT, **c** 160 mT, **d** 200 mT

**Table 14.3** The parameters of exponential functions at 58 °C

| Magnetic field intensity (mT) | Treatment time (min) | a | b | c |
|---|---|---|---|---|
| 40 | 5 | 97.18 | 104.78 | 0.767 |
| | 10 | 96.70 | 103.23 | 0.773 |
| | 15 | 98.11 | 107.46 | 0.729 |
| 80 | 5 | 97.06 | 135.58 | 0.767 |
| | 10 | 97.53 | 141.77 | 0.746 |
| | 15 | 98.28 | 144.13 | 0.743 |
| 160 | 5 | 98.60 | 108.23 | 0.723 |
| | 10 | 98.50 | 107.29 | 0.739 |
| | 15 | 98.60 | 108.18 | 0.740 |
| 200 | 5 | 99.30 | 110.39 | 0.722 |
| | 10 | 97.32 | 104.72 | 0.751 |
| | 15 | 98.33 | 106.98 | 0.736 |

**Table 14.4** The interfacial tension of droplets before and after magnetic treatment at T = 58 °C

| Treatment time (min) | Interfacial tension under different magnetic field intensity (mN/m) | | | |
|---|---|---|---|---|
| | 40 mT | 80 mT | 160 mT | 200 mT |
| 0 | 25.29 | 25.29 | 25.29 | 25.29 |
| 5 | 26.87 | 26.27 | 24.48 | 23.16 |
| 10 | 27.00 | 26.40 | 24.52 | 23.26 |
| 15 | 27.33 | 26.58 | 24.64 | 23.41 |

increased at 40 mT and 80 mT, while the oil–water interfacial tension decreased at B = 160 mT and 200 mT. The maximum decreasing rate was about 8.4%. With the increase of magnetic treatment time, the interfacial tension basically did not change.

Based on the above analysis, it was found that when the magnetic treatment was applied at 58 °C and 200 mT, the largest decreasing rate of viscosity for emulsion reached 15.1%. Meanwhile, the decreasing rate of viscosity for crude oil was 6.87%, and the oil–water interfacial tension was reduced by about 8%. Therefore, the viscosity of emulsion can decrease under the magnetic field by reducing the viscosity of crude oil and interfacial tension.

## 14.4 Conclusion

Three indicators of crude oil viscosity, oil–water interfacial tension and droplet distribution were selected to explore the viscosity reduction mechanism of emulsion under magnetic field. The viscosity of waxy crude oil emulsion could decrease after magnetic treatment. When the magnetic treatment temperature was the wax appearance temperature, the viscosity of emulsion decreased apparently. The viscosity reduction of crude oil did not change linearly with the magnetic treatment time and magnetic field intensity. When the magnetic treatment temperature was at or above the wax appearance temperature, the viscosity of the crude oil decreased effectively. The distribution of droplets was basically unchanged after applying magnetic field. The decrease of viscosity of crude oil and the oil-water interfacial tension led to the decrease of viscosity of emulsion.

## References

Gonçalves JL, Bombard AJF, Soares DAW et al (2010) Reduction of paraffin precipitation and viscosity of Brazilian crude oil exposed to magnetic fields. Energy Fuels 24(5):3144–3149

Gonçalves JL, Bombard AJF, Soares DAW et al (2011) Study of the factors responsible for the rheology change of a Brazilian crude oil under magnetic fields. Energy Fuels 25(8):3537–3543

Li S, Huang Q, He M et al (2014) Effect of water fraction on rheological properties of waxy crude oil emulsions. J Dispersion Sci Technol 35:1114–1125

Li GX (2008) The mechanism analysis and experimentation of paraffin controlling and viscosity reducing in crude oil using the magnetism-based treatment. Harbin Institute of Technology, pp 37–49

Li SY (2018) The effect of magnetic field on viscosity and wax deposition of waxy crude oil. China University of Petroleum, Beijing, pp 14–72

Loskutov YV, Yudina NV (2006) Rheological behavior of oils in a magnetic field. J Eng Phys Thermophys 79(1):105–113

Loskutova YV, Prozorova IV, Yudina NV et al (2004) Change in the rheological properties of high-paraffin petroleum under the action of vibrojet magnetic activation. J Eng Phys Thermophys 77(5):1034–1039

Rocha N, González C, Marques LC et al (2000) A preliminary study on the magnetic treatment of fluids. Pet Sci Technol 18(1):33–50

Tao R, Xu X (2006) Reducing the viscosity of crude oil by pulsed electric or magnetic field. Energy Fuels 20(5):2046–2051

Tung NP, Vinh NQ, Phong N et al (2003) Perspective for using Nd–Fe–B magnets as a tool for the improvement of the production and transportation of Vietnamese crude oil with high paraffin content. Phys B Phys Condens Matter 327:443–447

Tung NP, Vuong N, Quang KB et al (2001) Studying the mechanism of magnetic field influence on paraffin crude oil viscosity and wax deposition reductions. In: SPE, vol 68749

Zhang WW (2012) Study on the mechanism and key technologies of paraffin control resulting from electromagnetic field treatment of crude oil. Harbin Institute of Technology, pp 36–64

# Chapter 15
# Application and Mechanism of Catechol-Based Amide Lubricant in Water-Based Drilling Fluid


**Xunkun Yang and Guancheng Jiang**

**Abstract** Common water-based drilling fluid ester lubricants have weak adsorption on the metal friction interface, and it is difficult to form a compact and shear resistant lubricating film, and the high temperature resistance and hydrolysis resistance of ester lubricants are insufficient. These shortcomings often lead to high drilling friction and torque, and lead to downhole accidents such as blockage and sticking, which limits the use of ester lubricants in water-based drilling fluids. In order to improve the adsorption capacity of lubricant on the surface of metal drilling tools, a strong adsorption amide lubricant was prepared by dehydration condensation with protocatechuic acid and long-chain primary amine as raw materials. Its extreme pressure friction, mud cake adhesion and "point-to-point" friction performance are good, and the temperature resistance is up to 180 °C; The action mechanism of bonding lubricant was studied by four ball friction experiment, scanning electron microscope observation and X-ray photo electron spectroscopy, which showed that its catechol structure could form a bonding adsorption stronger than the ordinary adsorption with Fe element, so that a dense and shear resistant lubricating film with a thickness of more than 100 nm could be formed on the surface of metal drilling tools, which could greatly improve the lubrication performance of high-temperature water-based drilling fluid.

**Keywords** Water based drilling fluid · Lubricant · Amide group · Metal surface adsorption · Film

## 15.1 Introduction

In the process of oil drilling, due to the special well type and complex formation environment faced by some extended reach wells and multi branch horizontal wells, it often leads to high friction and torque between the drilling tool and the well wall in the drilling process of strong deflecting section and long horizontal section, and the phenomena of blocking, sticking and mud wrapped bit occur frequently, which

X. Yang · G. Jiang (✉)
College of Petroleum Engineering, China University of Petroleum (Beijing), Changping District, Beijing 102249, China
e-mail: 15600263100_1@163.com



Z. Yang (ed.), *Environmental Science and Technology: Sustainable Development*, Environmental Science and Engineering, https://doi.org/10.1007/978-3-031-27431-2_15

leads to slow penetration rate, high wear of drilling tools, and even serious drilling tool fracture accidents (Jiang et al. 2021; Liu and Rui 2022; Elrod and Nance 1980; Nance and Calkins 1985). Drilling fluid has the function of lubricating drilling tools, which is the key technical means to reduce friction and torque. However, compared with oil-based drilling fluid, water-based drilling fluid has poor natural lubrication performance, so high-performance lubricants must be used to improve the lubrication performance (Patel 1998; Mueller et al. 2004).

In the process of drilling, the friction and torque come from the friction between metal drilling tools and drilling fluid, the internal friction of drilling fluid and the friction between drilling fluid and well wall. There is also friction caused by the direct contact between drilling tools and well wall. The friction involving drilling tools is the main cause of sticking and sticking accidents. A large number of studies have shown that if there is a lubricating "oil film" or flowing solid particles on the friction interface, the friction resistance can be effectively reduced. Especially on the premise that there are a large number of particles in the drilling fluid, forming a dense, stable and shear resistant "oil film" is the most critical step to improve the lubrication performance of water-based drilling fluid (James et al. 2006; Navarro and Dannels 2011). In this regard, vegetable oil, mineral oil, lotion and other oils are commonly used as lubricants in water-based drilling fluids, but due to the poor dispersion of oils in water, especially on the metal surface, there is almost no adsorption except for the weak interaction of van der Waals force, so the lubrication effect is not ideal (Qu et al. 2012; Tseng et al. 1992). In recent years, many studies have found that the catechol structure in the chemical structure can greatly improve the adsorption capacity of organic compounds on a variety of substrate surfaces. By analyzing its key structure of catechol group and introducing it into the field of drilling fluid, many studies have invented treatment agents with strong adhesion, such as biomimetic wall strengthening agents and inhibitors. The adhesion test shows that the o-phenol hydroxyl group structure has strong adsorption on the surface of metal, glass, resin and other substrates except rock, especially on the metal surface (Reddy et al. 2013; Weihofen et al. 2005; Kim et al. 2015). However, there are few reports on lubricants using the adsorption property of catechol.

Secondly, the most commonly used lubricant in water-based drilling fluid is oil ester lubricant. Although this kind of lubricant has excellent lubrication performance, the ester lubricant has poor high-temperature resistance and poor hydrolysis stability. It is easy to hydrolyze in water and produce small molecules such as organic alcohols and acids that have corrosive effect on the surface of metal drilling tools, causing corrosion and wear of equipment and seriously affecting its service life, Generally, water-based drilling fluid lubricants will inevitably contact with water in the actual use process, so it is of great significance to improve the hydrolysis stability and temperature resistance of synthetic ester lubricants.

Because the amide bond has better high temperature resistance and hydrolysis resistance than the ester bond, in view of the above problems, a new strong adsorption amide lubricant A1 containing catechol structure was prepared by synthesizing protocatechuic acid and octadecylamine. This lubricant is a side chain copolymer containing amide bond, which has better thermal stability, hydrolysis resistance and

oxidation stability. The lubricating performance was comprehensively evaluated, and its mechanism was explained by various test and analysis methods, which provided an important idea for the development of strong adsorption and high temperature resistant lubricants.

## 15.2 Materials and Methods

### *15.2.1 Materials*

The main test materials include: protocatechuic acid (90%, analytically pure), octadecylamine (90%, analytically pure), petroleum ether (99%, analytically pure), dimethyl sulfoxide (DMSO, 99%, analytically pure), molecular sieve (4a), p-toluene sulfonic acid (99%, analytically pure), sodium bentonite (industrial grade).

### *15.2.2 Synthesis and Structural Characterization of Amide Lubricants*

Pour 0.1 mol of protocatechuic acid into a three port flask, mix it with a certain amount of octadecylamine, then add 120 ml of petroleum ether/DMSO mixed solvent, stir it until it is fully dissolved, then add 0.05 g of 4A molecular sieve and 0.05 g of catalyst p-toluene sulfonic acid, stir it until it is fully dissolved; Connect the three port flask to the mixing, heating and condensing water separation device, set the reaction temperature to 115 °C and the reaction time to 24 h, and carry out $N_2$ protection during the reaction process to reduce the occurrence of side reactions; After the reaction, the solvent is evaporated with a rotary evaporator and distilled under reduced pressure to remove the residual water in the product to the greatest extent to obtain a dark brown viscous liquid product, which is a strongly adsorbed amide lubricant. The amine group of octadecylamine is primary amine, which can react with protocatechuic acid. Similarly, the secondary amine and tertiary amine in the by-product produced by the reaction of primary amine may also be dehydrated and condensed with protocatechuic acid. Therefore, by controlling the proportion of raw materials in the reaction, the main body of the product is the product of protocatechuic acid and primary amine.

The product was characterized by Hoffen-10 infrared spectrum analyzer and Picospin 80 nuclear magnetic resonance hydrogen spectrometer to judge whether the target product was successfully synthesized.

### 15.2.3 Evaluation Method of Lubricating Performance

**Determination of Extreme Pressure Lubrication Coefficient**. Add 4% bentonite and 0.2% anhydrous sodium carbonate into the water to prepare the base slurry, which is used in all subsequent tests. Use the FANN extreme pressure lubricator (Model 212, Fann instrument company, America) to measure the extreme pressure lubrication coefficient of the base slurry under the dosage of 1% lubricant, set the torque value to 150 pound per inch, and record the stable reading under this torque after 5 min. The lubricator shall be calibrated with distilled water before testing each sample, and the reading shall be controlled between 34 and 40; Before testing different samples, it is necessary to repeatedly clean the metal slider and metal ring with petroleum ether and ethanol to prevent the test error caused by the residue of the previous sample on the metal surface. According to the operating instructions of FANN extreme pressure lubricator, EP extreme pressure lubrication coefficient is determined by Eq. (15.1),

$$f_{lub} = \frac{36}{N_{water}} \times \frac{N_{sample}}{100} \tag{15.1}$$

where: $N_{water}$ is the reading of lubrication coefficient of distilled water under 150 lb·in torque; $N_{sample}$ is the reading of the lubrication coefficient of the sample under different torques.

Extreme pressure lubricator was used to test the lubrication coefficient of amide lubricant A1 in water, bentonite base slurry and bentonite base slurry after compounding with solvent, then the compounding scheme with the best lubrication performance was optimized.

**Determination of Mud Cake Adhesion Coefficient**. Take bentonite base slurry, add 1% lubricant A1 and stir it at high speed until it is uniform, and obtain API mud cake according to API filtration test method; Use the mud cake adhesion coefficient tester to measure the minimum torque required when the stainless steel disc rotates, and calculate the mud cake adhesion coefficient according to formula (15.2):

$$f = M \times 0.845 \times 10^{-2} \tag{15.2}$$

where: F is the adhesion coefficient of mud cake, and M is the minimum torque (N m) for rotation.

**Determination of Foaming Rate of Lubricants**. Generally, the bentonite base slurry with lubricant will bubble after high-speed mixing, and the volume changes greatly. Therefore, the volume change rate of the base slurry is used to express the foaming of the lubricant. Take base slurry 400 mL, add 1% amide lubricant at 12,000 rpm, stir it at high speed for 20 min, then age it for 16 h, use a measuring cylinder to measure the volume $V_1$ after aging, then stir it at 12,000 rpm at high speed for 20 min, and measure the volume $V_2$ after high stirring again. The volume change rate $V_{\%}$ is calculated by the following formula (15.3):

$$V_{\%} = \frac{V_2 - V_1}{V_1} \times 100\% \tag{15.3}$$

**Four Ball Friction Experiment and SEM Scanning of Wear Spots**. A four ball friction tester was used to simulate the "point-to-point" friction, and the lubricating performance of the lubricant was further evaluated in bentonite slurry.

Take 400 ml of base slurry, add 1% amide lubricant, stir the solution at high speed for 20 min, and then stand at room temperature for 16 h. MRS series four ball friction testing machine is selected for the four ball friction test. The friction steel ball is a two-stage bearing steel ball with a diameter of 12.7 mm, made of GCr15. The rotation speed is fixed at 300 rpm, the applied force is fixed at 300 N, and the test time is fixed at 20 min.

After the four ball friction test, the steel balls were ultrasonically cleaned with petroleum ether and absolute ethanol respectively to remove the residual lubricant and clay minerals on the surface of the steel ball friction spots. After natural drying, the steel ball wear spots were scanned by SEM, and the wear resistance of the lubricant was evaluated by comparing the wear spot diameter of the steel balls.

**Determination of Temperature Resistance**. Take 400 ml of base slurry, add 1% amide lubricant a 112,000 rpm, stir at high speed for 20 min, and then use the FANN extreme pressure lubricator to measure the extreme pressure lubrication coefficient and mud cake adhesion coefficient after aging for 16 h at different temperatures. The aging temperatures are 120 °C, 150 °C, 180 °C and 210 °C respectively. When determining the extreme pressure lubrication coefficient, the rotating speed is fixed at 60 rpm and the torque is fixed at 150 pound per inch.

**XPS Energy Spectrum Analysis**. After the four ball friction test, the steel balls were ultrasonically cleaned with petroleum ether and absolute ethanol to remove the residual lubricants and clay minerals on the surface of the steel ball wear marks. After natural drying, the steel ball wear spots were analyzed by XPS. K-alpha XPS spectrometer is selected for XPS test. The X-ray source is al-k-alpha source. The test voltage is 12.5 kV, the current is 20 mA, the deep section ion sputtering speed is 0.5 nm/s, and the total depth is 100 nm.

## 15.3 Results and Discussion

### *15.3.1 Characterization of Amide Lubricants*

The molecular structure of amide lubricant was characterized by infrared spectrum, as shown in Fig. 15.1. The single peak at about 3409.52 $cm^{-1}$ was the N–H stretching vibration peak of secondary amine, the C–O characteristic peak of amide at 1609.6 $cm^{-1}$, and the C–N stretching vibration peak of secondary amine at 1251.82 $cm^{-1}$, which proved that the carboxyl group in protocatechuic acid and the primary amine of octadecylamine were successfully dehydrated and condensed to form secondary amide bond; 2923.27 and 2852.59 $cm^{-1}$ are the characteristic vibrational absorption peaks of methyl-$CH_3$ and methylene-$CH_2$- on the long chain of octadecylamine. The above structural characterization structure shows that the reaction proceeds as expected, and a strong adsorption amide lubricant with o-phenol hydroxylamide structure as the main structure is successfully synthesized.

The NMR hydrogen spectrum of the synthetic product is shown in the Fig. 15.2. It can be determined that amide lubricant has been successfully synthesized according to this experimental scheme to obtain the target product.

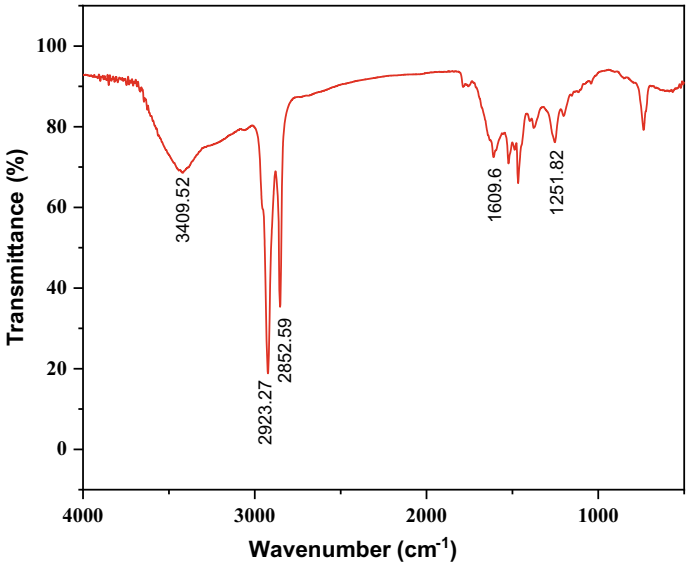


**Fig. 15.1** Infrared spectrum of amide lubricant A1

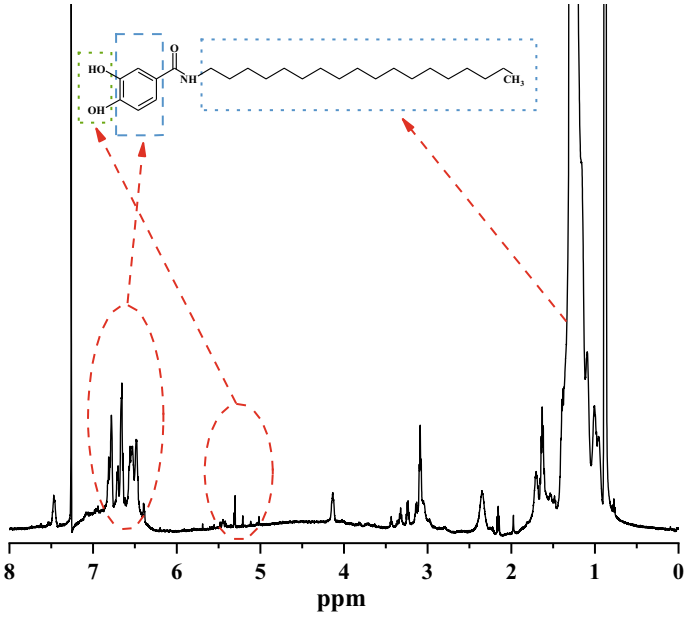


**Fig. 15.2** NMR hydrogen spectrum of the product

### *15.3.2 Extreme Pressure Lubrication Coefficient*

**Determination of Extreme Pressure Lubrication Coefficient in Base Slurry**. It can be seen from Table 15.1 that amide lubricant A1 with 1% dosage can reduce the EP lubrication coefficient of the base slurry by more than 75% before and after aging at 150 °C, and the lubrication effect is good.

**Determination of Lubrication Coefficient After Compounding**. In order to further improve the EP lubricating performance of synthetic ester lubricant, we need to compound a lubricating additive. On the one hand, it can form a stronger adsorption film on the metal surface to improve the EP lubricating performance, on the other

**Table 15.1** Extreme pressure lubrication coefficient of amide lubricant A1 in base slurry

| Samples | EP | Reduction rate (%) |
|---|---|---|
| Water | 0.30 | |
| Base slurry | 0.51 | |
| Base slurry + 1% Amide lubricant | 0.12 | 76.5 |
| After aging at 150 °C | | |
| Water | 0.31 | |
| Base slurry | 0.51 | |
| Base slurry + 1% Amide lubricant | 0.11 | 78.4 |

hand, it can not bubble and affect the density of drilling fluid and the quality of mud cake. Dodecyl mercaptan (R-SH) has the function of strong adsorption and defoaming on the metal surface, which is suitable for compounding with amide to improve extreme pressure lubrication performance. In addition, the lubricant oleyl alcohol commonly used in industry was compounded with amide lubricant A1 and its lubricity was investigated.

First, dodecyl mercaptan and oleyl alcohol are used to dilute the synthetic amide lubricant in different proportions in order to achieve the best lubrication effect. Adding 1% diluted amide lubricant into the base slurry, the EP lubrication coefficients of different solvents and dilution ratios were compared, and the foaming phenomenon was observed. It can be seen from Fig. 15.3 that when the ratio of amide lubricant to oleyl alcohol (OA) is 15:85, the lubrication coefficient of lubricant in the base slurry reaches the lowest 0.09, and the reduction rate of lubrication coefficient reaches 82%. When the ratio of amide lubricant to n-dodecyl mercaptan (SH) is 30:70, the lubricant performs best, the lubrication coefficient reaches the lowest 0.07, and the reduction rate of lubrication coefficient reaches 86%. Therefore, the lubricant product A1 after the combination of amide lubricant and dodecyl mercaptan is used in the later evaluation.

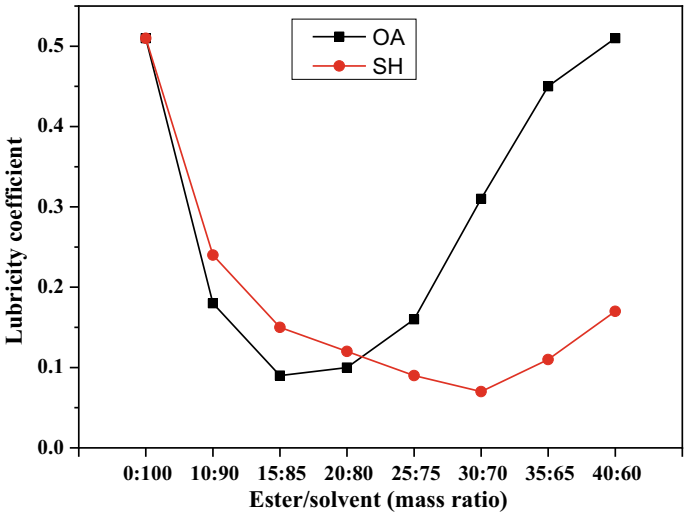


**Fig. 15.3** Lubrication coefficient of amide lubricant and different proportion of oleyl alcohol/dodecyl mercaptan

### 15.3.3 Evaluation of Lubrication and Wear Resistance

**Test of Mud Cake Adhesion Coefficient and Foaming Rate**. Table 15.2 shows the effect of different lubrication on the adhesion coefficient of bentonite base slurry API mud cake. Consistent with the above evaluation results, the amide lubricant A1 synthesized in this paper has excellent lubrication performance and can effectively reduce the mud cake adhesion coefficient. The adhesion coefficient of mud cake of base slurry was reduced by 61.0% before hot rolling and 84.7% after aging.

In addition, the foaming of drilling fluid will seriously threaten the safety of drilling operations. The foaming of drilling fluid will directly lead to the decline of mud density, causing wellbore instability, downhole overflow, blowout and other malignant accidents. Usually, the fresh water base slurry with ester lubricant will be hydrolyzed to a certain extent after high temperature aging, which will cause foaming and increase the volume of the base slurry. In order to investigate the foaming of amide lubricant A1, after rolling aging at 150 °C for 16 h, the volume of base slurry before and after high stirring was recorded respectively. The high stirring condition was fixed at 12,000 rpm and stirred for 20 min. The results of volume increase after high stirring are shown in Table 15.2. Amide lubricant A1 contains polar ends of two hydroxyl groups, but it also contains 18 carbon length non-polar saturated hydrocarbon chains, so that its overall hydrophilic lipophilic balance value is small and foaming will not occur.

**Evaluation of Anti-wear Properties of Lubricants**. Put the steel balls into the common base slurry and the base slurry with 1% lubricant A1 respectively, and conduct four ball friction experiments respectively. The wear spots on the steel ball surface after four ball friction were analyzed by SEM, and the SEM picture is shown in Fig. 15.4. By comparing the friction coefficient analysis, it can be seen that the larger the friction coefficient is, the larger the wear spot diameter is. The wear spot diameter of base slurry is 720.38 μm. At the same time, there are several deep scratches on the surface of the wear spot, and the diameter of the wear spot of the steel ball added with amide lubricant A1 is reduced to 527 μm. It shows that amide lubricant A1 can effectively improve the lubrication and wear resistance of steel balls compared with ordinary base slurry.

**Table 15.2** Effect of amide lubricant on mud cake adhesion coefficient

| Samples | Adhesion coefficient | Reduction rate of adhesion coefficient | Volume increase rate |
|---|---|---|---|
| Base slurry | 0.2672 | / | / |
| Base slurry + 1% A1 | 0.1043 | 61.0% | 0 |
| After aging in 150 °C | | | |
| Base slurry | 0.2195 | / | / |
| Base slurry + 1% A1 | 0.0336 | 84.7% | 0 |

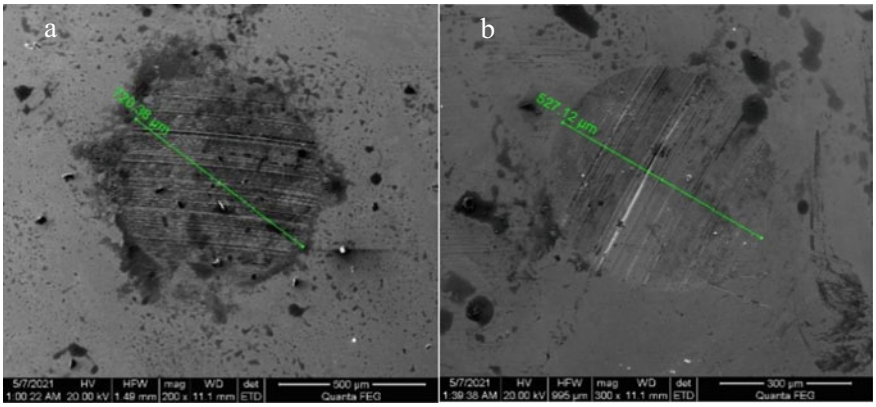


**Fig. 15.4** SEM of wear scar (**a** wear scar of steel ball in base slurry; **b** wear scar of steel ball in base slurry + A1)

**Evaluation of Temperature Resistance of Lubricants**. High temperature aging will promote the hydrolysis of amide, resulting in hydrolysis, foaming and degradation of lubricating performance of amide lubricant. The temperature resistance of amide lubricant A1 was investigated in terms of the volume increase rate of base slurry, extreme pressure lubrication coefficient and mud cake adhesion coefficient after aging. The test results are shown in Table 15.3.

In terms of foaming, when the aging temperature is lower than 150 °C, the volume of base slurry added with 1% amide lubricant A1 will hardly increase after high stirring. When the aging temperature rises to 180 °C, the volume increase rate of fresh water base slurry after high stirring reaches 15.6%, and after aging at 210 °C, its volume increase rate rises significantly to 43.2%, indicating that lubricant A1 appears partial hydrolysis after aging at 180 °C, and serious hydrolysis after aging at 210 °C, resulting in more foam. For extreme pressure lubrication performance, the extreme pressure lubrication performance of lubricant A1 after aging is basically the

**Table 15.3** Lubricating performance of base slurry after aging at different temperatures

| Aging temperature | Volume increase rate (%) | Extreme pressure lubrication coefficient | | Adhesion coefficient | |
|---|---|---|---|---|---|
| | | Blank | Base slurry + A1 | Blank | Base slurry + A1 |
| Room temperature (°C) | 4.8 | 0.51 | 0.10 | 0.2671 | 0.1048 |
| 120 | 0 | 0.52 | 0.10 | 0.2356 | 0.0554 |
| 150 | 0 | 0.52 | 0.09 | 0.2195 | 0.0336 |
| 180 | 15.6 | 0.51 | 0.08 | 0.2505 | 0.0576 |
| 210 | 43.2 | 0.50 | 0.12 | 0.2601 | 0.0959 |

same under 180 °C; The extreme pressure lubrication coefficient began to rise after aging at 210 °C, which was mainly due to the hydrolysis of amide lubricant to a certain extent after high temperature aging, resulting in more foam, and its extreme pressure lubrication coefficient was affected and increased. For the adhesion performance of mud cake, when the temperature is below 180 °C, the adhesion coefficient of mud cake after aging of amide lubricant is relatively consistent, and the adhesion coefficient increases significantly after aging at 210 °C, which is mainly due to the poor quality of mud cake caused by foaming after aging at this temperature. According to the results of foaming, extreme pressure lubrication and mud cake adhesion coefficient after aging at different temperatures, the temperature resistance of lubricant A1 can reach 180 °C.

### *15.3.4 Film Thickness Measurement and Lubrication Mechanism Analysis*

Finally, k-alpha XPS was used to analyze the chemical elements at different depths of the wear marks on the surface of the steel ball in the four ball friction experiment. Through the peak analysis of Fe2p of the scratches, the thickness of the lubricating film on the surface of the wear marks was obtained. It can be seen from Fig. 15.5 that the Fe element on the wear mark of the steel ball is mainly contained in the $Fe_2O_3$ structure; Solid line is Fe2p spectrum of steel ball in base slurry in different etching depths. When the steel ball is not etched (at 0 nm), no signal is observed on the characteristic peak of Fe2p spectrum, indicating that the wear mark surface of the steel ball is covered by a layer of organic film. After the first etching (20 nm), the characteristic peak of Fe2p energy spectrum appeared, indicating that the thickness of this film did not exceed 20 nm. Dotted line is Fe2p spectrum of steel ball in base slurry + lubricant A1 in different etching depths. Compared with the steel ball wear mark in the base slurry, the characteristic peak of Fe2p energy spectrum of the steel ball wear mark containing amide lubricant A1 has no signal during the five times etching, which proves that the amide lubricant adsorbs on the metal and forms a lubricating film with a thickness of more than 100 nm, masking the characteristic peak signal of Fe2p energy spectrum in the steel ball.

## 15.4 Conclusion

Based on the strong adsorption of catechol structure on the substrate surface, a strong adsorption amide lubricant was synthesized from protocatechuic acid and octadecylamine. The lubricant performance test results show that the synthesized amide lubricant has good performance in base slurry, extreme pressure friction and "point-to-point" friction, and the temperature resistance is up to 180 °C.

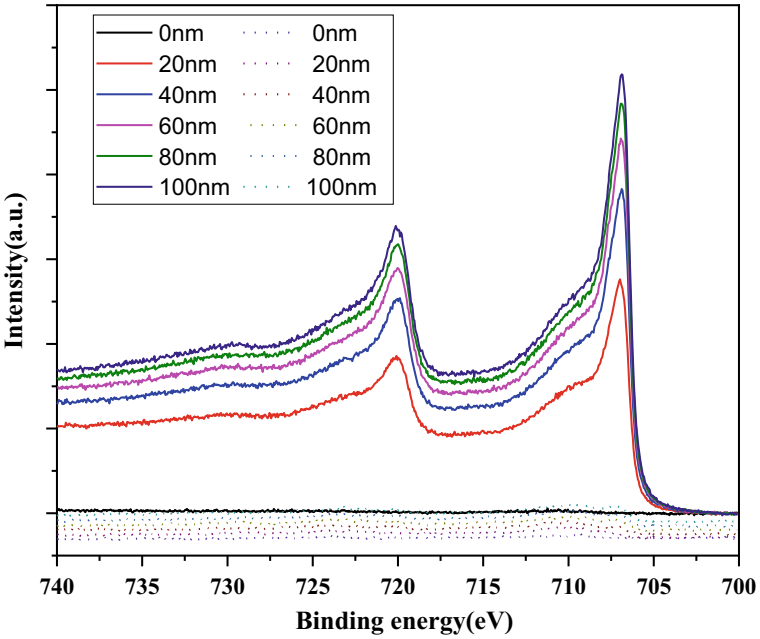


**Fig. 15.5** Fe2p spectrum with different scanning depth (Solid line is Fe2p spectrum of steel ball in base slurry in different etching depths; Dotted line is Fe2p steel ball in spectrum of base slurry + lubricant A1 in different etching depths)

Based on the strength of lubricating film, the micro morphology of friction scratch surface and element analysis, the lubrication mechanism of amide lubricant is revealed. It is found that the metal coordination bond formed by catechol and Fe has a higher adsorption strength than the physical adsorption of ordinary lubricants, which can form a denser and more wear-resistant lubricating film with a thickness of more than 100 nm, which is adsorbed on the metal surface, which is conducive to reducing the friction between drilling tools and well walls, effectively reducing friction resistance, and improving the blocking and sticking during drilling. This amide lubricant still has stable performance and good lubrication performance at a high temperature of 180 °C.

**Acknowledgements** This work was supported by the National Natural Science Foundation of China (grant numbers 51874329, 52004297, 51991361) and the China Postdoctoral Innovative Talent Support Program (BX20200384).

## References

Elrod SH, Nance WB (1980) Aqueous drilling fluid and lubricant composition. US
Jiang G, Sun J, He Y et al (2021) Novel water-based drilling and completion fluid technology to improve wellbore quality during drilling and protect unconventional reservoirs. Engineering
James FV, Kerchevile JD, Pober KW (2006) Silicic acid mud lubricants
Kim BJ, Cheong H, Hwang BH et al (2015) Mussel-inspired protein nanoparticles containing iron (III)-DOPA complexes for pH-responsive drug delivery. Angew Chem
Liu Y, Rui Z (2022) A storage-driven $CO_2$ EOR for a net-zero emission target. Engineering
Mueller H, Herold CP, Von Tapavicza S (2004) Use of selected fatty alcohols and their mixtures with carboxylic acid esters as lubricant components in water-based drilling fluid systems for soil exploration. US
Nance WB, Calkins JM (1985) Lubricating wellbore fluid and method of drilling. US
Navarro AR, Dannels WR (2011) Maximizing drilling operations by mitigating the adverse affects of friction through advanced drilling fluid technology
Patel AD (1998) Silicone based fluids for drilling applications. US
Qu J, Bansal DG, Yu B et al (2012) Anti-wear performance and mechanism of an oil-miscible ionic liquid as a lubricant additive. ACS Appl Mater Interfaces 4(2):997
Reddy ST, Tarafdar PK, Kamlekar RK et al (2013) Structure and thermotropic phase behavior of a homologous series of bioactive N-acyldopamines. J Phys Chem B 117(29):8747–8757
Tseng CF, Iwakami S, Mikajiri A et al (1992) Inhibition of in vitro prostaglandin and leukotriene biosyntheses by cinnamoyl-beta-phenethylamine and N-acyldopamine derivatives. Chem Pharm Bull 40(2):396
Weihofen A, Lavoie MJ, Selkoe DJ (2005) Dopamine covalently modifies and functionally inactivates parkin

# Part IV
# Environmental Pollution Assessment and Management

# Chapter 16
# Pollution Characteristics of VOCs in Atmospheric Background Air of Jinan Cities


**Feng-Ju Zhang, Wen-Jing Han, Fang-Fang Cao, Xi-Hua You, and Yang Xu**

**Abstract** The concentration composition and distribution characteristics of 106 VOCs, chlorofluorocarbon concentration levels and pollution sources in Paomaling air background point in Jinan from May to September 2021 were investigated. The results showed that the average VOCs mass concentration in the high $O_3$ period was 60.1 μg/m$^3$, lower than it in the low $O_3$ period (78.5 μg/m$^3$), which could be attributed to the seasonal difference of the photochemical reaction rates and pollution sources. Furthermore, the mass concentration of chlorofluorocarbons was in the middle level compared with the concentration of common mountain and national background points. However, compared to the high $O_3$ period, the ratio of benzene/toluene and i-pentane/n-pentane decreased in the low $O_3$ period, indicated the important influence of vehicle exhaust and fuel volatilization in the high $O_3$ period and the increasing influence of coal combustion in the low $O_3$ period.

**Keywords** Pollution characteristics · VOCs · Jinan

## 16.1 Introduction

Volatile organic compounds (VOCs) are $O_3$ and secondary fine particles PM2.5 and important precursors of secondary organic aerosol (SOA), $O_3$ and PM2.5 has become China's two mountains to win the blue sky defense war. In summer, $O_3$ pollution was serious and PM2.5 was the main culprit of haze weather in winter (Shi 2013). VOCs had a wide variety and complex components. Some VOCs were toxic and carcinogenic, endangering human health (Li et al. 2013; Xu et al. 2015). With the acceleration of China's industrialization, $O_3$ and PM2.5 and photochemical smog were becoming increasingly prominent (Liu et al. 2012), so VOCs were used as $O_3$

F.-J. Zhang (✉) · F.-F. Cao · X.-H. You · Y. Xu
Shandong Provincial Eco-Environment Monitoring Centre, Jinan 250101, China
e-mail: zhangfengju2008@163.com

W.-J. Han
Shandong Ecological Environment Protection Publicity and Education Center, Jinan 250012, China



Z. Yang (ed.), *Environmental Science and Technology: Sustainable Development*, Environmental Science and Engineering, https://doi.org/10.1007/978-3-031-27431-2_16

and PM2.5, the pollution characteristics, content, composition, spatial distribution and source of VOCs in ambient air had become the focus of routine monitoring in the field of environmental monitoring and the research hotspot of scientific researchers in China. Paomaling was far away from the urban area, with no industrial pollution sources and few mobile traffic sources nearby. It was the air cleaning control point in Jinan, which could better reflect the VOCs concentration level and pollution characteristics of the background point in Jinan.

At present, the research on the emission law, temporal and spatial distribution and photochemical activity of VOCs in China was mainly focused on the Yangtze River Delta, Pearl River Delta, Beijing Tianjin Hebei and other regions and some first-line and provincial capital cities (Nanjing, Shanghai, Beijing, Tianjin, Hangzhou, etc. (Liu et al. 2012; Wang et al. 2004; Wang and Zhao 2008; Cai et al. 2010; Zhang et al. 2020; Gao et al. 2020; Shen et al. 2020)), while the research on the pollution characteristics of VOCs in the atmosphere at urban air background points, the concentration level and source of plant-derived VOCs and chlorofluorocarbons had been submitted. There were few studies on the concentration level of plant derived VOCs in the ambient air at the air background point, the correlation analysis between VOCs Pollution Characteristics and atmospheric conventional 6 kinds of parameters, and the concentration level and source analysis of chlorofluorocarbons. Therefore, this study analyzed the concentration level and pollution characteristics, chemical activity analysis, SOA generation potential and health risk assessment of 106 VOCs (including 29 kinds of alkanes, 16 kinds of olefins, 1 kind of alkyne, 24 kinds of aromatic hydrocarbons, 10 kinds of aldehydes and ketones, 22 kinds of halogenated hydrocarbons, 3 kinds of plant derived VOCs and 1 kind of sulfide) in the ambient air of Paomaling in spring and autumn, in order to reduced VOCs in the ambient air of Jinan Provide more precise technical support for supervision, prevention and control of atmospheric compound pollution, control measures and improvement of ambient air quality.

## 16.2 Materials and Methods

### *16.2.1 Ampling Point*

In order to systematically study the VOCs Pollution Characteristics in the ambient air of Jinan urban area, a representative point of ambient air monitoring that could comprehensively reflected the atmospheric background of Jinan was selected for VOCs sample collection. The observation station of this study was the roof of Jinan Paomaling air station at an altitude of about 900 m. It was located in the National Forest Park of Paomaling scenic spot, with a forest coverage rate of 98% and no industrial emission sources around.

### *16.2.2 Sample Collection*

From May 11 to May 14, 2022 and from September 22 to September 24, 2022, the ENTECH 1900 automatic sampler was used to collect samples continuously and intensively, with a sampling interval of 3 h. The specific sampling periods were 00:00–03:00, 03:00–06:00, 06:00–09:00, 09:00–12:00, 12:00–15:00, 15:00–18:00, 18:00–21:00 and 21:00–24:00. A total of 60 effective ambient air samples were collected.

### *16.2.3 Sample Analysis*

The markets electronic refrigeration system was used to concentrate and inject samples, and cooperated with the Dean switch central cutting technology. Ethane, ethylene, acetylene, propane and propylene were detected on the FID detector, and other VOCs were detected on the MS detector. FID column was alumina bond/$Na_2SO_4$ (30 m × 0.53 mm × 10 μm), MS column was DB-624 (60 m × 0.32 mm × 1.8 μm. FID was qualitative by retention time and quantitative by external standard method; MS was analyzed by selective ion scanning (SIM) mode and quantified by internal standard method.

Test conditions of electronic refrigeration system: transmission line temperature: 160 °C; Cold trap temperature: −30 °C; Analytical temperature: 300 °C; Analysis time: 5 min; Heating rate: Max; Sampling flow rate: 25 ml/min; Internal standard injection pressure: 23 psi; Sample flow rate: 20 ml/min, injection volume: 1 ml/min. The sampling volume was 100 ml. Sampling flow: 60 ml/min.

Test conditions of gas chromatography-mass spectrometer: programmed temperature raised: kept 40 °C for 3 min, raised the temperature to 50 °C (2 min) at 8 °C/min, then raised the temperature to 150 °C at 8 °C/min for 10 min, and then raised the temperature to 185 °C at 15 °C/min for 16.5 min; Chromatographic column flow: 1.5 ml/min; Inlet temperature: 220 °C. Cutting time: 8.4 min, interface temperature: 280 °C; Ion source temperature: 230 °C; Four stage rod temperature: 150 °C; Solvent delay: 4 min; Scanning mode: quantitative analysis of samples in SIM mode and quantitative analyzed by internal standard method.

## 16.3 Result

### *16.3.1 Concentration Composition and Distribution Characteristics of VOCs*

The average TVOCs mass concentration of 106 VOCs in the air of Paomaling air background point in ozone season was 60.1 μg/$m^3$, which was significantly lower

than that in non ozone season (78.4 μg/m$^3$). The average annual mass concentrations of alkanes, olefins, alkynes, halogenated hydrocarbons, aromatic hydrocarbons, oxygenated VOCs, sulfides and plant derived VOCs were 22.1, 2.72, 1.39, 16.6, 10.1, 14.1, 0.96 and 1.32 μg/m$^3$ respectively. It could be seen from the VOCs components of atmospheric samples (Fig. 16.1) that alkanes and halogenated hydrocarbons contributed the most to VOCs, Accounting for 31.9 and 24.0% respectively; Followed by oxygenated VOCs and aromatic hydrocarbons, accounted for 20.3 and 14.6%; The components with less content were olefins, alkynes, plant derived VOCs and sulfides, accounting for 3.92, 2.00, 1.90 and 1.38% respectively. The top 10 components of VOCs concentration were ethanol, ethane, propane, chloroform, ethyl acetate, dichloromethane, dichlorodifluoromethane, dodecane, 2-methylpentane and cyclopentane, accounting for 49.6% of the total mass concentration of VOCs. Chloroform, a secondary carcinogen, was a toxic and harmful air pollutant published by USEPA. Relevant studies showed that ethanol in the air mainly comed from the exhaust gas produced by incomplete combustion of motor vehicles; Ethane and propane in ambient air mainly comed from coal-fired sources (Liang et al. 2021); Dichloromethane, cyclopentane, trichloromethane and 2-2-methylpentane in the ambient air mainly comed from the volatilization of fuels such as liquefied petroleum gas and gasoline vapor. The differences between ozone season and non ozone season of VOCs in Jinan atmosphere were listed in Table 16.1. The average mass concentration of VOCs in ozone season was 60.1 μg/m$^3$, which was significantly lower than that in non ozone season (78.5 μg/m$^3$). The mean temperature of ozone season was 28.3 °C, which was 6 °C higher than that of non-ozone season. Therefore, high temperature and ultraviolet radiation promoted the occurrence of ozone seasonal photochemical reaction, and the ozone seasonal ozone concentration 157 μg/m$^3$ was about 2 times of the non-ozone seasonal ozone concentration (88.3 μg/m$^3$). In addition, the average $SO_2$ concentration in ozone season and non ozone season in Jinan was very approach, about 9.0 μg/m$^3$, indicated that the coal consumption in ozone season and non ozone season in Jinan was the same. It could be seen from Table 16.2 that the fine particulate matter PM10 and PM2.5 in non ozone season. The concentration of PM2.5 was significantly lower than the seasonal concentration of ozone, which was consistent with the change trend of mass concentration of $SO_2$, NOx, CO and VOCs, but opposited to the change of ozone concentration. Co mainly comed from incomplete combustion process due to VOCs and NOx reacted photo chemically under high temperature light to produced ozone, formaldehyde, acetaldehyde and other secondary pollutants. Therefore, the low VOCs concentration in ozone season may be related to the increase of VOCs photochemical loss, the change of emission sources and the change of meteorological conditions such as wind direction, humidity, air temperature and light.

In addition, the mass concentration and proportion of plant VOCs were higher in ozone season than in non-ozone season, and the mass concentration and proportion of other components were higher in non-ozone season than in ozone season. Plant-derived VOCs tracers isoprene, a-pinene and limonene had higher concentrations in May when they were in full foliage because of higher rates of isoprene and monoterpene emissions from vegetation such as poplar and ponderosa pine.

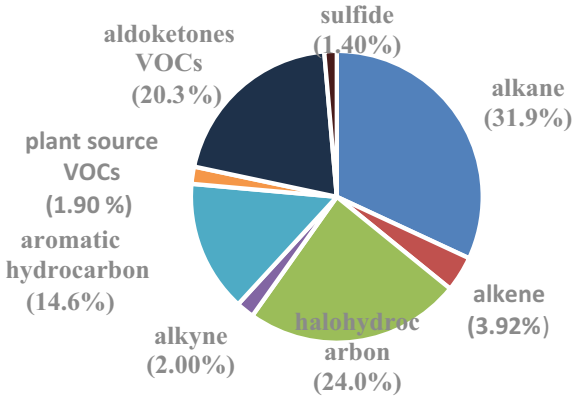


**Fig. 16.1** Compositions of VOCs in Paomaling district

**Table 16.1** Mixing ratios of VOCs, concentrations of $O_3$, NOx and $SO_2$ in the high $O_3$ period and the low $O_3$ period $\mu g/m^3$

| Projects | The season of none ozone | The season of ozone |
|---|---|---|
| VOCs | 78.5 ± 9.37 | 60.1 ± 7.24 |
| Alkane | 26.1 ± 1.09 | 18.2 ± 1.07 |
| Alkene | 3.58 ± 0.42 | 1.86 ± 0.25 |
| Alkyne | 1.65 ± 0.49 | 1.13 ± 0.53 |
| Halohydrocarbon | 17.9 ± 1.05 | 15.3 ± 0.97 |
| Aromatic hydrocarbon | 12.3 ± 0.73 | 7.93 ± 0.41 |
| Oxygen VOCs | 14.6 ± 2.81 | 13.6 ± 2.78 |
| Sulfide | 1.09 ± 0.15 | 0.82 ± 0.19 |
| Plant source VOCs | 1.28 ± 0.23 | 1.36 ± 0.27 |
| $SO_2$ | 9.50 ± 0.72 | 9.19 ± 0.81 |
| $NO_x$ | 9.92 ± 2.84 | 8.18 ± 1.70 |
| CO | 1.40 ± 0.38 | 0.70 ± 0.12 |
| $O_3$-8 h | 88.3 ± 7.93 | 157 ± 29.0 |
| PM10 | 60.6 ± 14.4 | 39.1 ± 7.96 |
| PM2.5 | 39.3 ± 11.5 | 17.3 ± 5.93 |
| Temperature/°C | 22.3 ± 5.34 | 28.3 ± 11.5 |

The concentrations of isoprene, A-pinene and limonene were significantly higher in the daytime than at night, and isoprene, A-pinene and limonene were not detected in some night monitoring periods, which may be related to environmental factors, metabolism and enzyme activities of plants. The monitoring results of isoprene, a-pinene and limonene showed that the contribution of natural source emissions to VOCs concentration in non-ozone season was greater than that in ozone season.

**Table 16.2** Comparison of the mass concentration of chlorofluorocarbons in paomaling atmosphere and other high mountains in China μg/m$^3$

| Mass concentration of constituent | Wuyishan mountain (Lu et al. 2013) | Taishan mountain (Mao et al. 2009) | Gongga mountain (Zhang et al. 2014) | Shenlongjia (Zhang et al. 2014) | Lushan (Seinfeld and Pandis 2006) | Paomaling |
|---|---|---|---|---|---|---|
| CFC-12 | 1.02 ± 0.03 | – | – | 0.22 ± 0.07 | 4.18 ± 1.23 | 2.58 ± 0.20 |
| CFC-114 | <0.05 | – | 0.15 ± 0.03 | 0.17 ± 0.11 | 0.34 ± 0.12 | 0.18 ± 0.14 |
| CFC-11 | 0.56 ± 0.01 | 1.58 ± 0.16 | 1.70 ± 0.25 | 0.20 ± 0.09 | 2.12 ± 0.47 | 1.48 ± 0.17 |
| CFC-113 | 0.18 ± 0.05 | 0.58 ± 0.05 | 0.75 ± 0.08 | 0.31 ± 0.31 | 1.01 ± 0.23 | 0.63 ± 0.14 |
| Carbon tetrachloride | | | | | | 0.71 ± 0.14 |

The seasonal ozone mass concentrations of alkanes, olefins, alkynes, halogenated hydrocarbons, aromatic hydrocarbons, oxygenated VOCs, plant derived VOCs and sulfides were 26.1 ± 1.09, 3.58 ± 0.42, 1.65 ± 0.49, 17.9 ± 1.05 12.3 ± 0.73, 14.6 ± 2.81, 1.28 ± 0.23 and 1.09 ± 0.15 μg/m$^3$ respectively, accounted for 33.2, 4.56, 2.10, 22.9, 15.6, 18.6, 1.63 and 1.39%. The mass concentrations in non ozone seasons were 18.2 ± 1.07, 1.86 ± 0.25, 1.13 ± 0.53, 15.3 ± 0.97, 7.93 ± 0.41, 13.6 ± 2.78, 1.36 ± 0.27 and 0.82 ± 0.19 μg/m$^3$, accounting for 30.3, 3.09, 1.88, 25.6%, 13.2, 22.6, 2.26 and 1.36% respectively. Excepted that the mass concentration and proportion of VOCs from plants were higher in ozone season than in non ozone season, the mass concentration and proportion of other components were higher in non ozone season than in ozone season. The concentrations of plant derived VOCs tracers isoprene, a-pinene and limonene were higher in May when the branches and leaves were luxuriant, because the emission rates of isoprene and monoterpene from vegetation such as poplar and western yellow pine were higher. The mass concentration of isoprene, a-pinene and limonene during the day was significantly higher than that at night. In some night monitoring periods, isoprene, a-pinene and limonene were not detected, which may be related to external environmental factors, plant metabolism and enzyme activity. The monitoring results of isoprene, a-pinene and limonene showed that the contribution of natural source emissions to VOCs concentration in non ozone season was greater than that in ozone season.

### *16.3.2 CFC Concentration Level*

CFC-11, CFC-12 and CFC-113 were ozone depleting substances phased out by the Montreal Protocol, of which CFC-114 was a controlled species (Zhao et al. 2022). The concentration of five chlorofluorocarbons in the atmosphere of Paomaling was listed in Table 16.2. It could be seen from Table 16.2 that the average concentration of five chlorofluorocarbons in the atmosphere of Paomaling was CFC-12 > CFC-11 >

carbon tetrachloride > CFC-113 > CFC-114 from high to low, which was consistent with the analysis results of four chlorofluorocarbons in Wuyishan (Lu et al. 2013) in Guangdong and Lushan (Zhang et al. 2016) in Jiangxi. The concentration of CFC-11 in the atmosphere of Paomaling was lower than that of Lushan Mountain in Jiangxi, Taishan Mountain in Shandong (Mao et al. 2009) and Gongga Mountain in Sichuan (Zhang et al. 2014), but higher than that of Wuyi Mountain in Guangdong and Shenlongjia in Hubei (Zhang et al. 2014). As Wuyi Mountain in Guangdong and Shenlongjia in Hubei were national atmospheric background points, they had a complete natural ecosystem, were far away from cities and industrial belts, and there were no pollutant emission sources around. Compared with Taishan Mountain in Shandong, Gongga Mountain in Sichuan, Wuyi Mountain in Guangdong, Shenlongjia in Hubei and Lushan in Jiangxi, the concentrations of CFC-12, CFC-113 and CFC-114 in the atmosphere of Paomaling were at the middle level.

Although CFC-11, CFC-12, CFC-113 and CFC-114 were obsolete or controlled ozone depleting substances, dued to the long service life of chlorofluorocarbons, their concentration distribution was mainly affected by the interaction between emission sources, long-range transport and volatilization of chemical solvents in the atmosphere. The main source of CFCs in the atmosphere was the release of human behavior (Seinfeld and Pandis 2006). Although the content of chlorofluorocarbons in the atmosphere of Paomaling was significantly higher than that of Wuyishan in Guangdong and Shenlongjia in Hubei, its content was significantly lower than that of Lushan in Jiangxi, Shenyang and Tianjin (Cao et al. 2012). The average mass concentration of carbon tetrachloride in the atmosphere of Paomaling was $0.71 \pm 0.14\ \mu g/m^3$. There were few literature reports on the mass concentration of carbon tetrachloride, which was not compared with other high mountain atmospheric mass concentrations.

### *16.3.3 The Ratio of Characteristic Pollutant*

For some VOCs species, the emission proportion of different pollution sources was different, and the characteristic VOCs component ratio could indicate the impact of pollution sources on VOCs (Sheng et al. 2018). The characteristic concentration ratio (B/T) of benzene to toluene was often used to indicated the source analysis of VOCs in ambient air (Deng et al. 2018). When the B/T ratio was about 0.5, it reflected that VOCs in urban ambient air mainly comed from motor vehicle emissions (Deng et al. 2018; Bricco et al. 1997). When the B/T ratio was greater than 0.5, VOCs in the atmosphere were caused by the use of petrochemical or fossil fuels in addition to the contribution of traffic exhaust; When B/T value >1, it indicated that VOCs mainly comed from the combustion of biofuels and charcoal. When the ratio was much higher than 1, it indicated that it was caused by coal combustion; Less than 0.5 indicated that in addition to the contribution of traffic exhaust, the used of coatings and the volatilization of solvents released aromatic hydrocarbons into the ambient air. The average B/T ratio of VOCs in the ambient air of Paomaling atmospheric

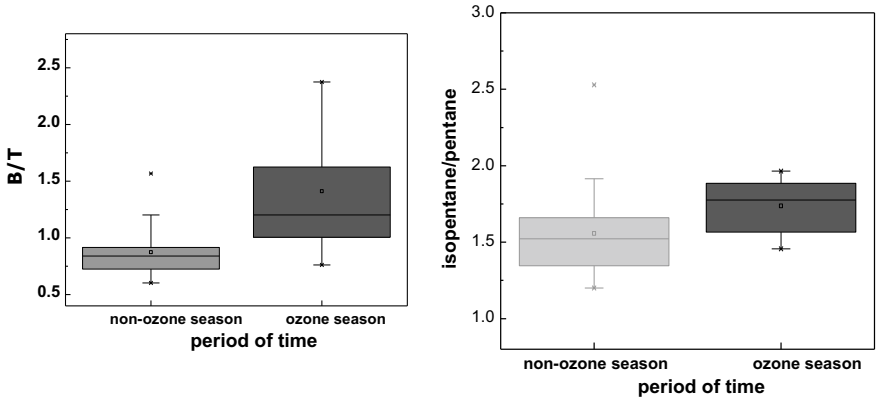


**Fig. 16.2** The ratio of benzene to toluene (B/T), and the ratio of *i*-pentane to *n*-pentane. *Note* The box plot from bottom to top was minimum, 10th percentile, 25th percentile, arithmetic mean (square), median (horizontal line), 75th percentile, 90th percentile and maximum

background point in Jinan in non ozone season and ozone season was 0.91 and 1.35 respectively. The B/T value in non ozone season was significantly lower than that in ozone season (Fig. 16.2), reflected that VOCs in non ozone season mainly comed from the contribution of traffic exhaust, volatilization caused by petrochemical or fossil fuel use, etc.; The impact of coal combustion increased in the ozone season.

Isopentane/n-pentane values could be used to indicate the contribution of pollution sources (included vehicle emissions, oil and gas emissions, combustion and other pollution sources (Li et al. 2019)). When coal combustion was the main contribution, isopentane/n-pentane was usually low (0.56–0.80) (Yan et al. 2017); When the emission of motor vehicles was dominated, the isopentane/n-pentane number was 2.2–3.8; When oil volatilization was the main influence, the value of isopentane/n-pentane was usually 1.8–4.6 (Russo et al. 2010; McGaughey et al. 2004; Jobson 2004). The average annual value of isopentane/n-pentane in Jinan was 1.64, indicated that it was mainly affected by oil and gas volatilization. In Jinan, the average values of isopentane/n-pentane in non ozone season and ozone season were 1.51 and 1.78 respectively (Fig. 16.2). The ratio of isopentane/n-pentane in ozone season was significantly higher than that in non ozone season, and the temperature in ozone season was significantly higher than that in non ozone season. It colud be found that high temperature conditions promoted the volatilization of isopentane.

## 16.4 Conclusion

(1) VOCs, $SO_2$, NOx, CO and PM2.5 in the atmosphere of Jinan background point was investigatd. The mass concentration of PM10 in non ozone season was significantly higher than that in ozone season, while the mass concentration of

$O_3$ in ozone season was about twice that in non ozone season. The average mass concentration of VOCs from plants was $1.321 \pm 0.14$ $\mu g/m^3$, the mass concentration and proportion of VOCs in ozone season were higher than those in non ozone season, and the mass concentration in daytime was significantly higher than that at night.

(2) Compared with Taishan Mountain in Shandong, Gongga Mountain in Sichuan, Wuyi Mountain in Guangdong, Shenlongjia in Hubei and Lushan in Jiangxi, the concentrations of CFC-12, CFC-113 and CFC-114 in Paomaling atmosphere were at the middle level.

(3) The average B/T ratios of VOCs in the ambient air of Paomaling atmospheric background point in Jinan in non ozone season and ozone season were 0.91 and 1.35 respectively. VOCs in non ozone season mainly comed from the contribution of traffic exhaust, volatilization caused by the use of petrochemical or fossil fuels, etc.; The impact of coal combustion increased in the ozone season. The average annual value of isopentane/n-pentane in Jinan was 1.64, indicated that it was mainly affected by oil and gas volatilization

## References

Bricco D, Fratarcangeli R, Lepore L et al (1997) Determination of aromatic hydrocarbons in urban air of Rome. Atmos Environ 31(2):557–566

Cai CJ, Geng FH, Tie XX et al (2010) Characteristics and source apportionment of VOCs measured in Shanghai, China. Atmos Environ 44(38):5005–5014

Cao WW, Shi JW, Han B et al (2012) Composition and distribution of VOCs in the ambient air of typical cities in Northern of China 32(2):200–206

Deng YY, Li J, Li YQ et al (2018) Characteristics of ambient VOCs at the Shuangliu site in Chengdu, China, during summer and autumn. Environ Sci 39(12):5323–5333

Gao JY, Tang M, Chen K et al (2020) Pollution characteristics and source analysis of atmospheric volatile organic compounds in different function areas. Environ Pollut Prot 38(5):43–47

Jobson BT (2004) Hydrocarbon source signatures in Houston, Texas: influence of the petrochemical industry. J Geophys Res 109:D24035

Li L, Li H, Wang XZ (2013) Pollution characteristics and health risk assessment of atmospheric VOCs in the Downtown area of Guangzhou, China. Environ Sci 34(12):4558–4564

Li B, Ho SSH, Gong S et al (2019) Characterization of VOCs and their related atmospheric processes in a central Chinese city during severe ozone pollution periods. Atmos Chem Phys 19(1):617–638

Liang SY, Wang S, Gao S et al (2021) Characteristics of volatile organic compounds and its impact on $o_3$ formation in Beijing urban area. Environ Monit China 37(6):21–30

Liu W, Hsieh H, Chen S et al (2012) Diagnosis of air quality through observation and modeling of volatile organic compounds (VOCs) as pollution tracers. Atmos Environ 55:56–63

Lu YB, Tan L, Teng EJ et al (2013) Concentration levels and composition characteristics of VOCs at the background locations in China. Environ Sci 32(5):726–732

Mao T, Wang YS, Xu HH et al (2009) A study of the atmospheric VOCs of Mount Tai in June 2006. Atmos Environ 43(15):2503–2508

Mcgaughey GR, Desai NR, Allen DT et al (2004) Analysis of motor vehicle emissions in a Houston tunnel during the Texas air quality study 2000. Atmos Environ 38(20):3363–3372

Russo RS, Zhou Y, White ML et al (2010) Multi-year (2004–2008) record of nonmethane hydrocarbons and halocarbons in New England: seasonal variations and regional sources. Atmos Chem Phys 10(10):4909–4929
Seinfeld JH, Pandis SN (2006) Atmospheric chemistry and physics: from air pollution to climate change. Wiley, New York
Shen JD, Ye XH, Zhu YJ et al (2020) Study on the concentration characteristics and chemical reactivity of ambient VOCs in Hangzhou. Environ Monit China 36(5):80–87
Sheng T, Chen XJ, Gao S et al (2018) Process in the research of application of VOCs ratio method. Environ Sci Technol 41(12):122–130
Shi YC (2013) Frog haze production mechanism & treatment strategy in China. Shaanxi Electric Power 41(4):1–4
Wang P, Zhao W (2008) Assessment of ambient volatile organic compounds (VOCs) near major roads in urban Nanjing, China. Atmos Res 89(2):289–297
Wang BG, Zhang YH, Shao M (2004) Special and temporal distribution character of VOCs in the ambient air of peal river delta region. Environ Sci 25(S1):7–15
Xu H, Deng JJ, Xing ZY et al (2015) Pollution characteristics and health risk assessment of VOCs in different functional zones of Xiame. Acta Sci Circumst 35(9):2701–2709
Yan Y, Peng L, Li R et al (2017) Concentration, ozone formation potential and source analysis of volatile organic compounds (VOCs) in a thermal power station centralized area: a study in Shuozhou, China. Environ Pollut 223:295–304
Zhang J, Sun Y, Wu F, Sun J, Wang Y (2014) The characteristics, seasonal variation and source apportionment of VOCs at Gongga Mountain, China. Atmos Environ 88(1):297–305
Zhang FJ, Jin LR, Li HL et al (2016) Determination of chlorofluorocarbons in the atmosphere of high mountain with pre-concentration-GC/MS. Environ Monit China 32(3):105–109
Zhang LH, Wu ZH, Li B et al (2020) Pollution characterizations of atmospheric volatile organic compounds in spring of Beijing urban area. Res Environ Sci 33(3):526–535
Zhao F, Chen TS, Dong C et al (2022) Long-term trends and sources of atmospheric Halocarbons at mount Taishan, Northern China. Environ Sci 43(2):723–735

# Chapter 17
# Fine-Grained Traffic Pollution Monitoring and Estimation: A Case Study in Chengdu


**Xin Peng, Zhanbo Sun, Runzhe Liu, and Feilong Yang**

**Abstract** Accurate, fine-grained monitoring and estimation of traffic pollution are essential for preventing people from the health issues caused by air pollution. In this paper, we illustrated the concept of conducting fine-grained spatial interpolation of near-road traffic pollution distribution with mobile monitoring data. Different spatial interpolation techniques, including Kriging, Natural Neighbor Tessellation (NNT), and Inverse Distance Weighted (IDW) were compared. Results show NNT outperforms others especially in the cases of sparse data. This conclusion contributes to the monitoring and estimation of traffic pollution in smart cities.

**Keywords** Mobile monitoring · Traffic pollution · Spatial interpolation

## 17.1 Introduction

Traffic pollution is a major source of urban air pollution. The closer the area with a large number of vehicles, such as ports and railway stations, the stronger the pollutant is Chen (2022). Furthermore, air pollution level typically varies across short distances (10 m–1 km) caused by the unevenly distributed source of emissions, dispersion, and physical/chemical reactions (Karner et al. 2010; Marshall et al. 2008; Yifang et al. 2002). Evidence reveals that near-road concentrations of pollutants could be 30% to 100% higher than that away from major roads (Sabin et al. 2005). Therefore, monitoring and estimating near-road traffic pollutants are important to understand

X. Peng (✉) · Z. Sun · R. Liu
Southwest Jiaotong University, Chengdu, China
e-mail: alicehssy@my.swjtu.edu.cn

R. Liu
e-mail: lrz1997@my.swjtu.edu.cn

National Engineering Laboratory of Integrated Transportation Big Data Application Technology, Chengdu, China

F. Yang
Panzhihua University, Panzhihua, China
e-mail: yangfl@daqsoft.com



Z. Yang (ed.), *Environmental Science and Technology: Sustainable Development*, Environmental Science and Engineering, https://doi.org/10.1007/978-3-031-27431-2_17

how traffic pollution is produced and transferred in smart cities and prevent people from the health issues caused by air pollution, such as premature death, respiratory and cardiovascular health problems (Zhang et al. 2020).

The common practice to monitor urban air pollution is via fixed-location air quality monitoring stations. These stations are restricted to sparse locations and typically far away from local emission hotspots since complex installation processes and high maintenance costs, although they exhibit high precision and notable persistence. Enabled by advances and ubiquitous applications of the Internet of Things (IoT) and wireless networks in smart cities, fine-grained air pollutants data can be collected via portable air quality sensors. Gao et al. (2016) outlined a low-cost mobile sensing system for personal mobile phones to dynamically monitor air quality. Deshmukh et al. (2020) used mobile monitoring to describe the spatial variability and gradient of $NO_2$, black carbon, and ultrafine particles in Kansas, USA. Lim et al. (2019) analyzed the pollutant distribution pattern in Cambridge based on a low-cost air quality sensor and found that fine particles tended to be concentrated on busy roads. Wong et al. (2021) conducted mobile monitoring of CO, $NO_2$, and $O_3$ before and after the COVID-19 lockdown in Nanjing, China, which proved the perception ability of mobile monitoring on urban air pollution. Alas et al. (2018) applied mobile monitoring to present the results of the first intensive characterization experiment in Metro Manila, Philippines. Mobile monitoring based on portable air quality sensors has been successfully applied by many scholars, but the scope of research area is still limited.

Current estimation methods for pollution are divided into two main categories: (1) model-based method, which involves the simulation of transport mechanisms using emission source data and the knowledge of the chemical transformations in the atmosphere. Unfortunately, emission inventory inputs and initial conditions may be lacking in some regions, while geophysical characteristics might further complicate the implementation of these models. Recent studies further show that the traditional deterministic models struggle to capture the non-linear relationship between the concentration of contaminants and their sources of emission and dispersion (Chen et al. 2017; Shimadera et al. 2016), especially in a model application in regions of complex terrain (Ritter et al. 2013). (2) Statistical techniques, e.g., spatial interpolation, regression, machine learning, use historical data to predict air quality without considering physical and chemical processes. They do not explicitly simulate the environmental processes while they generally exhibit higher predictive performance than Chemical Transport Models (CTMs) on fine-grained spatiotemporal distribution in the presence of extensive monitoring data (Marshall et al. 2008; Adam-Poupart et al. 2014). Spatial interpolations are often used in air pollutant estimation for quality providing suitable results without establishing additional meteorological parameters (Eslami and Ghasemi 2018; Haofei et al. 2018; Rodríguez-Amigo et al. 2017). Marshall et al. (2008) further proved Kriging, Natural Neighbor Tessellation (NNT), and Inverse Distance Weighting (IDW) exhibit characteristics that are similar to those of the LUR method and CMAQ model, and they are suitable for secondary pollutants. However, few studies have applied spatial interpolation to fine-grained urban traffic pollution estimation.

In Chengdu, the number of vehicles has become the second in China, and the special climate also makes it difficult to disperse a large amount of traffic pollution, resulting in serious air pollution in recent years. Although the government has proposed traffic pollution control policies, the effectiveness of implementation needs to be verified by accurate monitoring and estimation. Inspired by the above literature, we explored the variability of near-road air pollution under high spatial resolution (~10 m) based on portable air quality monitor and verified the inferred quality of Kriging, NNT, and IDW.

The rest of the paper is organized as follows. Section 17.2 introduces the mechanism of spatial interpolations. Section 17.3 provides the experiments and numerical results based on a case study in Chengdu, China, followed by the concluding remarks in Sect. 17.4.

## 17.2 Method

The spatial interpolation was started in the 1950s, which is mainly used to predict unknown spatial data from existing spatial data. It is of great significance to acquire, manage and analyze spatial information related to geographical position. Based on the measured data of near-road traffic pollution in Chengdu, the estimation accuracy of Kriging, Natural Neighbor Tessellation (NNT), and Inverse Distance Weighting (IDW) would be verified respectively from qualitative and quantitative aspects.

### *17.2.1 Kriging*

Kriging (Burrough 1986; Oliver and Webster 1990) is based on random functions: the surface or volume is assumed to be one realization of a random function with a certain spatial covariance. Using the measurements with the size of $N$ at discrete points $z(r)$ and an assumption of stationarity that can estimate a semivariogram $\gamma(h)$ defined in (17.1):

$$\gamma(h) = \frac{1}{2Var[\{z(r+h) - z(r)\}]} \approx \frac{1}{(2N_h)\sum_{(ij)}^{N_h}[z(r_i) - z(r_j)]^2} \tag{17.1}$$

which is related to the spatial covariance $C(h)$ in (17.2):

$$\gamma(h) = C(0) - C(h) \tag{17.2}$$

where $C(0)$ is the semivariogram value at infinity (sill). The summation in (17.1) runs over the number $N_h$ of pairs measurements that are separated by vector $h$ within a small tolerance $\Delta h$. The interpolated surface is then constructed using statistical

conditions of unbiasedness and minimum variance. In its dual form the universal Kriging interpolation function can be written in (17.3):

$$F(r) = T(r) + \sum_{j=1}^{N} \lambda_j C\left(r - r_j\right) \tag{17.3}$$

where $F_{Kriging}(r)$ is a function describing the air pollutant distribution in smart city, $T(r)$ represents its non-random component expressed as a linear combination of low-order monomial. The monomial and $\{\lambda_j\}$ coefficients are found by solving a system of linear equations. After confirming the coefficients, the unsampled concentration can be estimated by Kriging.

### *17.2.2 Natural Neighbor Tessellation*

Natural Neighbor Tessellation (NNT) (Hagen and Roller 1991) applies a weighted average of local data based on Thiessen polygons in the bivariate case and Thiessen polyhedra in the trivariate case. To estimate the overall air pollutant distribution in smart city, the value in an unsampled location is firstly computed as a weighted average of the nearest neighbor measurements with weights dependent on areas or volumes rather than distances. The number of measurements used for the computation at each unsampled point is variable, dependent on the spatial configuration of measurements.

### *17.2.3 Inverse Distance Weighting*

Inverse Distance Weighting (IDW) (Longley 1999) is one of the simplest and most readily available methods. It is based on the assumption that the value at any unsampled point can be approximated as a weighted average of measurements within a certain cutoff distance. Given the M values of measurements in the area of interest. The assigned weights are usually inversely proportional to a certain power of the distance, which, at the unsampled location, leads to the estimator in (17.4):

$$F(r) = \sum_{i=1}^{M} w_i z(r_i) = \frac{\sum_{i=1}^{M} z(r_i)/|r - r_i|^p}{\sum_{j=1}^{M} 1/|r - r_i|^p} \tag{17.4}$$

where $|r - r_i|$ indicates the distance between discrete points and interpolation points and $p$ is a parameter (typically $p = 2$).

### *17.2.4 Evaluation Indicator*

To verify the estimation quality of spatial interpolation, the goodness of fit ($R^2$) is used to evaluate the interpretability of spatial interpolation estimates for the overall pollution distribution. Let the total sample size be $N$, the measured pollutant concentration at each location is $y_i (i = 1, 2, ...N)$, the average measured pollutant concentration is $\overline{y}$, and the spatial interpolation estimator is $y_i^{'} (i = 1, 2, ...N)$. The $R^2$ is calculated as follows:

$$R^2 = 1 - \frac{\sum_{i=1}^{N} \left(y_i - y_i'\right)^2}{\sum_{i=1}^{N} \left(y_i - \overline{y}\right)^2} \tag{17.5}$$

## 17.3 Case Study

The area of interest contains diverse land-use types and is located near the Southwest Jiaotong University in Xipu town (E 103°58′, W 34°45′), Chengdu, China, 1 km away from the Metro Station and East Railway Station. As the eastern part of the area was under construction during the data collection period, certain roads were removed from the monitoring route. The final route is shown in Fig. 17.1.

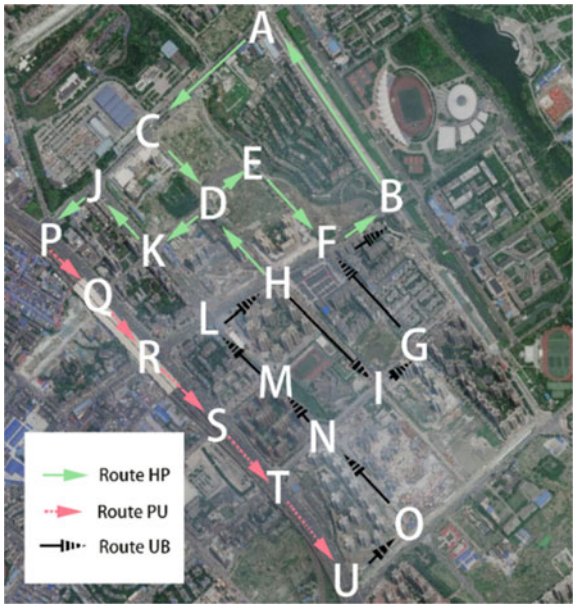


**Fig. 17.1** Mobile monitoring route

**Fig. 17.2** Portable air pollution sensor

PM2.5, PM10, and GPS along roads were collected every 2 s on a bicycle equipped with portable sensor (Fig. 17.2) designed and manufactured in our lab. The transmission service was based on the node.js platform and InfluxDB timing database.

### *17.3.1 Data Description*

The variation of traffic pollutants with mobile monitoring process is shown in Fig. 17.3. The abscissa represents the ordinal points along the monitoring route while the ordinate indicates the concentration of the pollutants. Since the PM2.5 and PM10 concentration trends are almost the same ( $R^2 = 0.997$), we only analyze PM2.5 in the subsequent.

The traffic pollution curve is divided into three main sections according to the geographical characteristics and the overall trends: HP (H → D → E → F → B → A → C → D → K → J → P), PU (P → Q → R → S → T → U), and UF (U → O → N → M → L → H → I → G → F).

In HP, the overall change of air pollutants in green spaces and residential areas with less traffic near roads is moderate, except for the intersections of H and F. Some peaks are noted, but the related concentrations progressively along reasonable gradients instead of abrupt changes. The curves appear steep due to the short abscissa and a large amount of data. The related scenario is the monitoring bicycle stopped

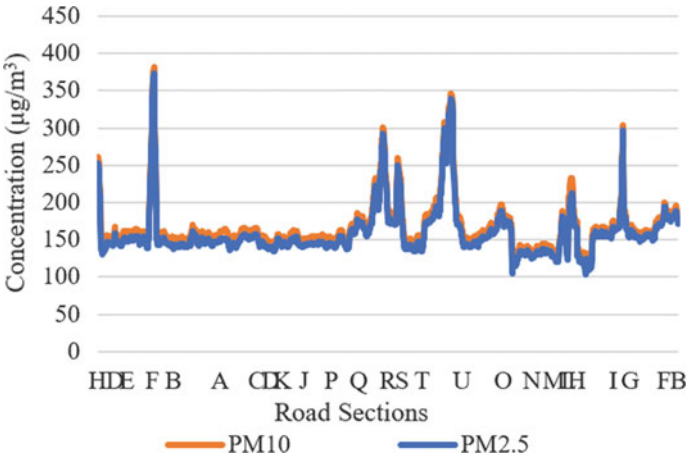


**Fig. 17.3** Spatial variability of PM2.5 and PM10 in mobile monitoring

next to vehicles waiting for the signal at intersections H and F and directly collected emission plumes.

In arterial road PU, there are three periodic peaks of air pollutants lagging slightly behind the intersections of R, S, and U. A possible interpretation is those excessive cars decelerating and idling before the intersections emitted a large amount of pollution. After the intersection, there was no vehicle, and air pollutants dropped rapidly until the end of the queue at the next intersection.

UB contained construction area, residential area, school, and parking lot. But there were no obvious pollution hot spots except for the concentration steep slope generated by the parking lot IG.

The box plot (Fig. 17.4) illustrates the maximum (upper limit), minimum (lower limit), average (×), median (horizontal line), and IQR (interquartile range, the difference between the 75th and 25th percentiles) of the near road pollutants in different road sections. Local concentration peaks deviated from the majority of data are flagged as anomalies since the excessive emissions of vehicles queueing. This phenomenon is an extreme manifestation of the inherent spatial variation.

The impact of vehicle emissions on air pollutant distribution is obvious. For example, the HP section, where around green land and with less traffic, has the narrowest IQR, highly similar median and mean values, and concentrated data distribution. As for arterial road PU, the fluctuation degree of pollutant concentration and the average increase.

The concentration of traffic pollutants in the construction area (OL section) without vehicle passing is the lowest (104 $\mu g/m^3$) in the whole measurements and is regarded as the background concentration. The sections or intersections, where the maximum pollution concentrations are more than twice the background concentration, are regarded as hot spots. In this case, the hot spots include intersections H and F, the parking lot (IG section), and the main road (QS and TU section), which are

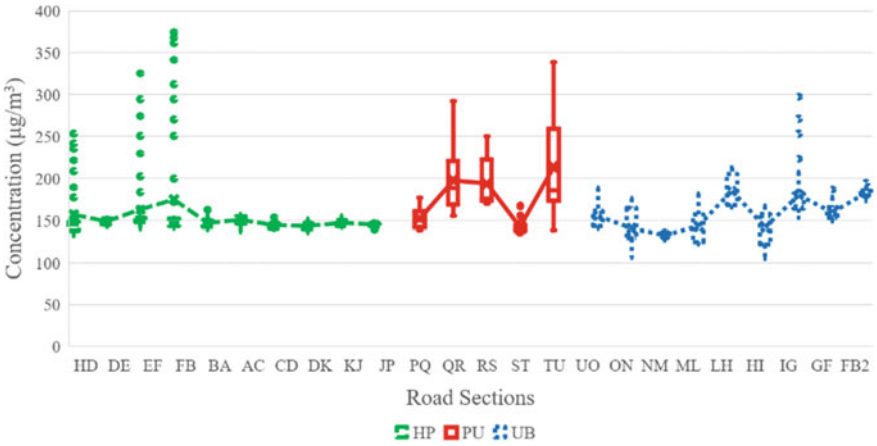


**Fig. 17.4** Boxplots of the PM2.5 concentrations in the different road sections

affected by vehicle emissions heavily. The observed peak concentrations are 2.16, 3.60, 2.86, 2.81, and 3.26 times the background concentrations, respectively.

### *17.3.2 Comparison of Spatial Interpolation*

After analyzing the variation of traffic pollutants with mobile monitoring process, we then utilized these field data and arcGIS to compared the performance of spatial interpolation in fine-grained urban traffic pollution estimation and visualization. The urban traffic pollution distribution images generated by Kriging, NNT, and IDW are shown in Fig. 17.5.

Pollution spread vertically along congested streets in a ribbon pattern while the parallel direction did not affect a large area. According to the data analysis results above, the hot spots are mainly concentrated at intersections and parking lots. The performance of revealing hot spots in three interpolations is similar. Compare with others, the image generated by NNT is transitional smooth and shows the characteristics of contamination diffusion.

Based on the field traffic pollution concentration collected by mobile monitoring in Chengdu, China, the accuracy of Kriging, NNT, and IDW applying to fine-grained urban traffic pollution estimation was verified through calculating the goodness of fit ($R^2$) of different size of samples estimating the overall pollution distribution. Numerical results were shown in Table 17.1. We set incremental sampling ratios. The size of samples is equal to the total number of mobile monitoring data times the sampling ratios. The coverage density of the samples means the number of sample per square kilometer. Since the estimates are affected by the spatial relationships

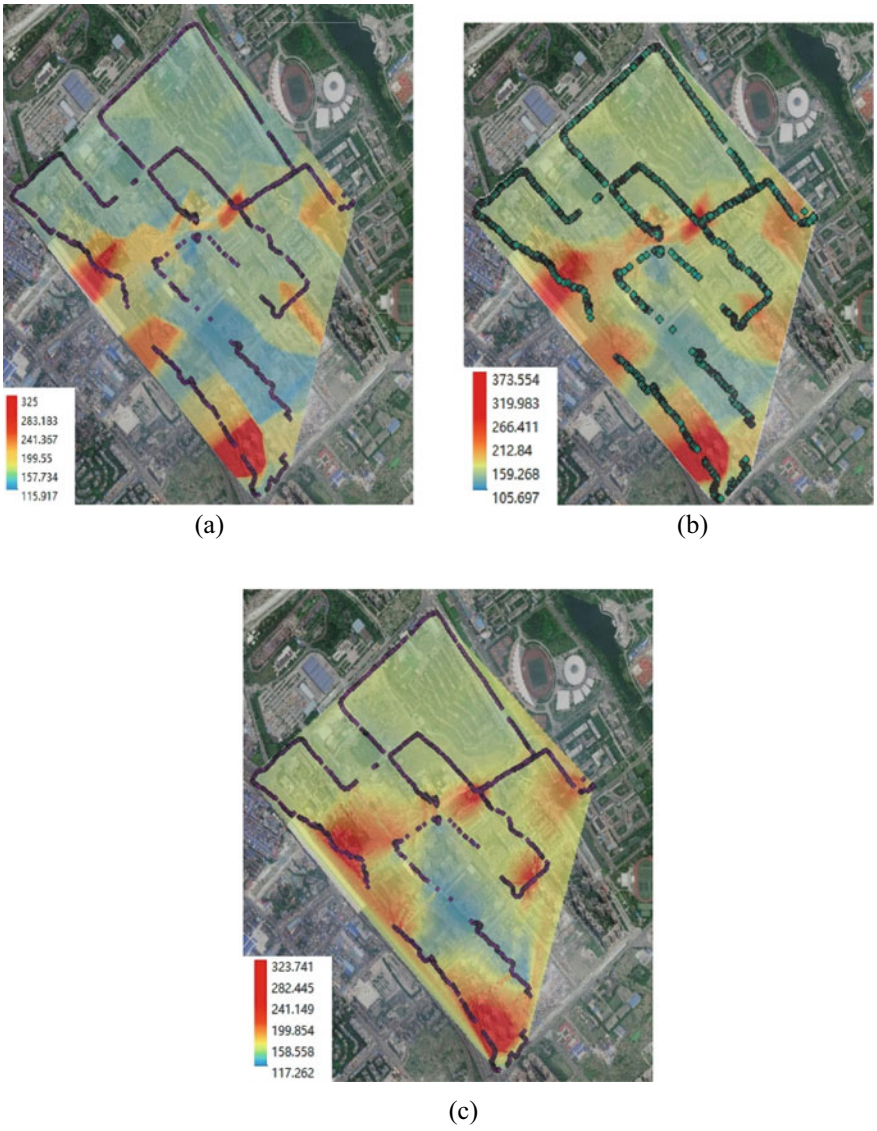


**Fig. 17.5** Fine-grained estimation of air pollutant distribution (**a** Kriging, **b** NNT, **c** IDW)

between known data, even samples of the same size have various estimation results. So the results were taken as the average of the 50 repetitions in Table 17.1.

For all three spatial interpolations, $R^2$ increases with the increasing data. Adding coverage density to 24 samples per $km^2$, IDW obtains better $R^2$ compared to the other two methods, but it is still too low to apply in practice. As the sampling ratio increases to 5%, the NNT starts to dominate. When the sampling ratio increase to

**Table 17.1** Estimation accuracy of the kriging, NNT, and IDW methods with the different proportion of the training subset to the general datasets

| Sampling ratio (%) | The size of samples | Coverage density of the samples (per square kilometer) | $R^2$ | | |
|---|---|---|---|---|---|
| | | | Kriging | NNT | IDW |
| 1 | 18 | 8 | 0.00 | 0.00 | 0.03 |
| 3 | 54 | 24 | 0.00 | 0.18 | 0.25 |
| 5 | 90 | 40 | 0.00 | 0.39 | 0.29 |
| 7 | 126 | 56 | 0.00 | 0.57 | 0.39 |
| 10 | 180 | 80 | 0.00 | 0.65 | 0.46 |
| 20 | 360 | 160 | 0.54 | 0.81 | 0.52 |
| 30 | 540 | 240 | 0.69 | 0.87 | 0.61 |
| 40 | 720 | 320 | 0.69 | 0.91 | 0.68 |
| 50 | 900 | 400 | 0.71 | 0.94 | 0.72 |
| 60 | 1080 | 480 | 0.72 | 0.94 | 0.79 |
| 70 | 1260 | 560 | 0.73 | 0.95 | 0.84 |
| 80 | 1440 | 640 | 0.73 | 0.96 | 0.91 |
| 90 | 1620 | 720 | 0.73 | 0.96 | 0.95 |

20%, NNT reaches a superior performance ($R^2 = 0.81$) among three methods while IDW requires more samples to achieve the same $R^2$.

Since the high precision and ability to estimate appropriate pollutant distribution especially in sparse samples, NNT is the most suitable geographical method for estimating fine-grained traffic pollution. Kriging does not accomplish satisfying results ($R^2 = 0.00$) when the sampling ratio is less than 20%, while NNT ($R^2 = 0.65$) and IDW ($R^2 = 0.46$) have a better effect. The poor performance of Kriging may be caused by abnormal distribution of data collected along roads, which are affected by temporary traffic emissions. IDW, however, does not perform well in complex situation since it seldom reproduces the local shape determined by data and produces local extrema at data points (Burrough 1986).

## 17.4 Conclusion

Aiming to explore the fine-grained urban traffic pollution distribution that is difficult to observe, analyze and effectively monitor, we first collected fine-grained data through mobile monitoring. The pollution data were divided into three main sections according to the geographical characteristics and the overall trends: HP, PU, and UB. The narrowest IQR, highly similar median and mean values occurs in the area with less traffic and nearing green space (HP section). Entering the arterial road PU, the

fluctuation degree and the average of pollutant concentrations increase. The air pollutants in the integrating area UB have comparatively variability. The lowest concentration (104 $\mu g/m^3$) occurs on roads without vehicle passing. The peak concentrations observed at the intersections H and F, parking lot (IG section), and main roads (QS and TU section) are 2.16, 3.60, 2.86, 2.81, and 3.26 times of the minimum concentration respectively. The impact of vehicle emissions on adjacent road pollution is significant, resulting in nearing twice the concentration difference.

In order to find a suitable method for estimating fine-grained urban traffic pollution, the adaptabilities of the spatial interpolation techniques including Kriging, NNT, and IDW were validated. NNT outperforms Kriging and IDW. The overall regional air pollution maps are also generated to illustrate the impact of traffic flow on the distribution of pollutants.

**Acknowledgements** The work is supported by the National Natural Science Foundation of China (NSFC) via grant No. 71701173 and the Science and Technology Project of Chengdu via grant No. 2020-RK00-00208-ZF. Any conclusions, opinions, findings, and recommendations expressed in this paper are those of the authors and do not necessarily reflect the views of the sponsors.

## References

Adam-Poupart A et al (2014) Spatiotemporal modelling of ozone levels in Quebec (Canada): a comparison of kriging, land-use regression (LUR), and combined Bayesian maximum entropy–LUR approaches. Environ Health Perspect 122(9):970–976

Alas HD et al (2018) Spatial characterization of black carbon mass concentration in the atmosphere of a southeast Asian megacity: an air quality case study for metro manila, Philippines. Aerosol Air Qual Res 18(9):2301–2317

Burrough PA (1986) Principles of geographical information systems for land resources assessment. Geocarto Int 1(3):54–54

Chen Y et al (2022) A new mobile monitoring approach to characterize community-scale air pollution patterns and identify local high pollution zones. Atmos Environ 272:118936

Chen J et al (2017) Forecasting smog-related health hazard based on social media and physical sensor. Inf Syst 64:281–291

Deshmukh P et al (2020) Identifying air pollution source impacts in urban communities using mobile monitoring. Sci Total Environ 715:136979

Eslami A, Ghasemi SM (2018) Determination of the best interpolation method in estimating the concentration of environmental air pollutants in Tehran city in 2015. J Air Pollut Health 3(4):187–198

Gao Y et al (2016) Mosaic: a low-cost mobile sensing system for urban air quality monitoring. In: IEEE INFOCOM 2016-the 35th annual IEEE international conference on computer communications, pp 1–9

Hagen H, Roller D (1991) Geometric modelling: methods and applications. Springer, Heidelberg

Haofei Y et al (2018) Cross-comparison and evaluation of air pollution field estimation methods. Atmos Environ 179:49–60

Karner AA et al (2010) Near-roadway air quality: synthesizing the findings from real-world data. Environ Sci Technol 44(14):5334–5344

Lim CC et al (2019) Mapping urban air quality using mobile sampling with low-cost sensors and machine learning in Seoul, South Korea. Environ Int 131:105022

Longley PA (1999) Geographical information systems: principles, techniques, management, and applications. Wiley, New York
Marshall JD et al (2008) Within-urban variability in ambient air pollution: comparison of estimation methods. Atmos Environ 42(6):1359–1369
Oliver M, Webster R (1990) Kriging: a method of interpolation for geographical information systems
Ritter M et al (2013) Air pollution modelling over very complex terrain: an evaluation of WRF-Chem over Switzerland for two 1-year periods. Atmos Res 132–133:209–222
Rodríguez-Amigo MC et al (2017) Mathematical interpolation methods for spatial estimation of global horizontal irradiation in Castilla-León, Spain: a case study. Solar Energy 151:14–21
Sabin LD et al (2005) Analysis of real-time variables affecting children's exposure to diesel-related pollutants during school bus commutes in Los Angeles. Atmos Environ 39(29):5243–5254
Shimadera H et al (2016) Evaluation of air quality model performance for simulating long-range transport and local pollution of PM2.5 in Japan. Adv Meteorol 2016
Wang S et al (2021) Mobile monitoring of urban air quality at high spatial resolution by low-cost sensors: impacts of COVID-19 pandemic lockdown. Atmos Chem Phys 21(9):7199–7215
Yifang Z et al (2002) Study of ultrafine particles near a major highway with heavy-duty diesel traffic. Atmos Environ 36(27):4323–4335
Zhang K et al (2020) Toward understanding the differences of PM2.5 characteristics among five China urban cities. Asia-Pac J Atmos Sci 56(4):493–502

# Chapter 18
# Characteristics of Soil HMs of Different Residential Areas in Qingdao and Their Health Risk Assessment to Human


**Chunrong Zhang, Dezhi Bai, Qiuhui Yao, Shaoyong Li, and Huiming Zheng**

**Abstract** In order to study the characteristics of soil heavy metals (HMs) in residential areas around different types of industries and their health risk assessment to human, 56 soil samples were collected in Qingdao. The contents of 8 HMs were analyzed in these soil samples. Then the characteristics of them and their risk assessment to human health were analyzed by the methods of statistical analysis, geo-accumulation index and USEPA health risk assessment, etc. Analysis showed that the average content of soil HMs in urban of Qingdao is the highest, following is Huangdao, the suburb of Qingdao is the lowest. Except Cd, Cu, Hg, Pb, Zn in urban of Qingdao, Cd, Pb, Hg in suburb of Qingdao and Pb, Zn in Huangdao are unpolluted to moderately polluted, and Zn in suburb of Qingdao are unpolluted to moderately polluted, the other heavy metals are not polluted. The average cumulative health risk of soil HMs will not do harm to human. However, the maximum cumulative health risk of HMs in Huangdao will be harmful to children's. These results of this study will prevent and control of soil HMs pollution of different residential areas in Qingdao and other residential areas of the same industrial type.

**Keywords** Soil HMs · Health risk · Residential area · Qingdao

C. Zhang (✉) · D. Bai
College of Earth Sciences and Engineering, Shandong University of Science and Technology, Qingdao 266590, China
e-mail: Zcrsdust@126.com

Q. Yao
The Third Prospecting Team of Shandong Bureau of Coal Geology, Taian 271000, China

S. Li
The Second Prospecting Team of Shandong Bureau of Coal Geology, Jining 272100, China

H. Zheng
Shandong Lunan Geological Engineering Survey Institute, Jining 272100, China



Z. Yang (ed.), *Environmental Science and Technology: Sustainable Development*, Environmental Science and Engineering, https://doi.org/10.1007/978-3-031-27431-2_18

## 18.1 Introduction

Soil is an important medium of atmosphere, water and biological system. With the rapid development of economy, a large number of pollutants enter urban soil through various ways, such as metal processing and smelting, chemical production, electronic manufacturing, vehicle emission and so on (Bo et al. 2018; Jamal et al. 2019; Li et al. 2003), and they will cause soil pollution. Especially HMs, which are difficult to degrade and highly toxic (Mohammad et al. 2012). And they can reduce the quality and worsen the ecological environment of soil. In addition, they can absorbed by human through hand and mouth intake, skin absorption, respiration and inhalation, and they will harmful to human health when exceeding the human body's tolerance (Mohammad et al. 2012).

Soil HMs pollution in residential area has attracted the attention of a large number of scholars, and it was studied in Beijing, Xi'an and other cities. Cu, Cd, Pb and Zn are enriched of residential areas in Beijing (Xie et al. 2019). Pb and Zn of residential areas in Xi'an are mainly from fossil fuels (Chen and Lu 2017). Cu, Pb and Zn in highly urbanized residential areas of Baltimore are higher than their background values, which will be harmful to human health and so on (Pouyat et al. 2015). However, there are few comprehensive and systematic analysis of the characteristics of soil HMs pollution and their health risk assessment to human in different residential areas, which with developed economy, population and different industrial types. So count the concentration of soil HMs of resident areas in urban, suburb and Huangdao of Qingdao, assess their pollution levels and evaluate their health risks to human can prevent and control of soil HMs pollution in different residential areas of Qingdao and other residential areas of the same industrial type. Firstly, this paper calculates the characteristics of soil HMs of resident areas in urban, suburb and Huangdao of Qingdao. Secondly, the geo-accumulation index is used to assess the pollution level of HMs. Finally, the health risk assessment method of the USEPA was used to evaluate the health risk of HMs to human body.

## 18.2 Methods and Materials

### *18.2.1 Study Areas*

Qingdao is located in the south of Shandong and the west bank of the Pacific. It is adjacent to the Yellow sea. It belongs to the north temperate monsoon climate zone. Qingdao is an important economic center city in the east of Shandong. It is a national historical and cultural city. In recent years, the urban of Qingdao has actively developed cultural tourism, high and new technology, etc., with a permanent population of more than 2.3 million. While the suburb of Qingdao mainly develop steel, building materials, information appliances, etc., with a permanent population of more than 1.2 million. In addition, Huangdao mainly develops petrochemical

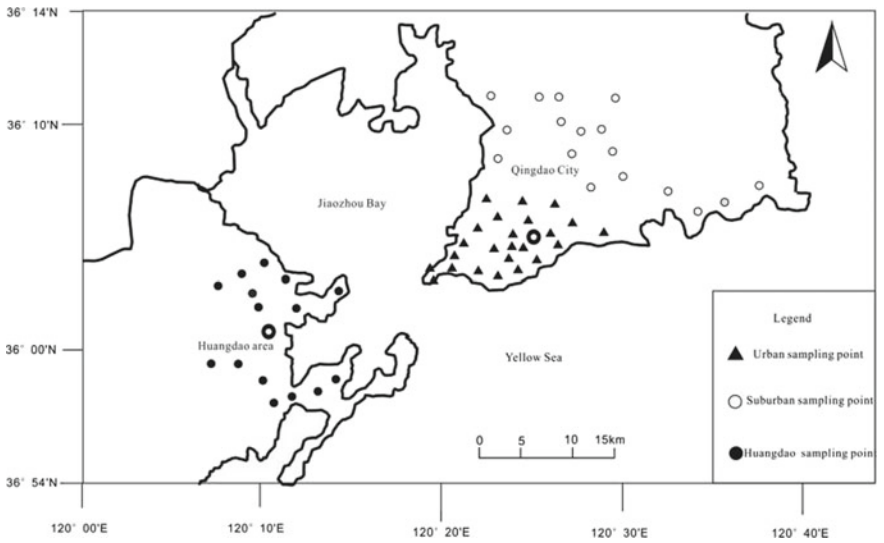


**Fig. 18.1** Schematic of the Soil Samples Sites of Different Residential Areas in Qingdao

industry, information appliances, rubber plastics, etc., with a permanent population of more than 1 million.

### *18.2.2 Sample Collection*

Figure 18.1 lists the location of 56 soil samples. Them included 22 from urban of Qingdao, 19 from suburb of Qingdao, and 15 from Huangdaor. They were collected from lawns, under trees and other open area in residential areas with a long history of soil accumulation, avoiding obvious point like pollution area, garbage bins and newly accumulated soil. At 3–5 points within 100 m around the sampling point, use a bamboo spoon to scrape off the topsoil first, then collect a 20 cm deep soil column and remove the sundries. Finally, the weight of the mixed soil sample is approximately 1 kg.

### *18.2.3 Sample Analysis*

The 56 soil samples were first air-dried, and then grind and contract, 8 HMs of them were analyzed. Among them, As and Hg are measured by Atomic Fluorescence Photometer.

Cd, Cu, Cr, Ni, Pb and Zn are measured by inductively coupled plasma mass spectrometer. In this paper, the soil samples from different residential areas in Qingdao were analyzed by repeated analysis and spot check to ensure the quality of them.

### 18.2.4 Geo-accumulation Index

Müller proposed the geological accumulation index ($I_{geo}$) in 1969. Its calculation formula is Eq. (18.1) (Jamal et al. 2019; Li et al. 2003):

$$I_{geo} = \log_2(C_i/1.5B_i) \tag{18.1}$$

where $C_i$ is the concentration of i, $B_i$ is the corresponding geochemical background value of i in Qingdao, and the 1.5 is a constant value to account for possible variations in background values.

### 18.2.5 Health Risk Assessment

**Exposure Assessment**. HMs can absorbed by human through hand and mouth intake, skin absorption, respiration and inhalation, and they will harmful to human health when exceeding the human body's tolerance (Mohammad et al. 2012). According to the EPA human exposure risk assessment method, the health risk calculation formula is Eqs. (18.2)–(18.4) (USEPA 2001)

$$ADD_{ing} = \frac{C_i \times \mathrm{EF} \times \mathrm{IngR} \times \mathrm{ED}}{\mathrm{AT} \times \mathrm{BW}} \times 10^{-6} \tag{18.2}$$

$$ADD_{inh} = \frac{C_i \times \mathrm{EF} \times \mathrm{InhR} \times \mathrm{ED}}{\mathrm{PEF} \times \mathrm{AT} \times \mathrm{BW}} \tag{18.3}$$

$$ADD_{derm} = \frac{C_i \times \mathrm{SL} \times \mathrm{ABS} \times \mathrm{EF} \times \mathrm{SA} \times \mathrm{ED}}{\mathrm{AT} \times \mathrm{BW}} \times 10^{-6} \tag{18.4}$$

where $C_i$ is the concentration of *i*. EF is exposure frequency, which is 365 $d \cdot a^{-1}$. IngR is the frequency of soil intake by hand and mouth, and children and adults are 200, 100 $mg \cdot d^{-1}$ respectively (USEPA 2001). ED is the age of exposure, and which is 18 a for childhood and 53 a for adulthood. AT is exposure time, which is 71 a * 365 $d \cdot a^{-1}$ (Wang et al. 2009). BW is body weight, and children and adults are 32, 59 kg respectively (Wang et al. 2009). InhR is the frequency of breathing, and children and adults are 8.61, 13.77 $m^3 \cdot d^{-1}$ respectively (Wang et al. 2009). PEF is $1.36 \times 10^9$ $m^3 \cdot kg^{-1}$ (USEPA 2001). SL is the adhesion of skin, which is 2

000 mg · $m^{-2}$ · $d^{-1}$ (USEPA 1993). ABS is 0.001 (USEPA 2002). SA is 0.28 $m^2$ for children and 0.57 $m^2$ for adults (USDOE 2011).

**Risk Characterization**. The calculation formula of the health risk of HMs and the accumulation of them to human health is Eqs. (18.5) and (18.6) (USEPA 2001).

$$H_i = \frac{\sum ADD_{i,j}}{RFD_i} \tag{18.5}$$

$$H = \sum H_i \tag{18.6}$$

where $H_i$ is the health risk of i. $ADD_{ij}$ is the health risk of i through j pathway. $RFD_i$ is the reference dose of daily exposure health risk of i to human health. HMs reference dose of EPA to human health: $RFD_{As} = 0.3$ ug · $kg^{-1}$ · $d^{-1}$, $RFD_{Cd} = 1$ ug · $kg^{-1}$ · $d^{-1}$, $RFD_{Cr} = 3$ ug · $kg^{-1}$ · $d^{-1}$, $RFD_{Cu} = 40$ ug · $kg^{-1}$ · $d^{-1}$, $RFD_{Hg} = 0.1$ ug · $kg^{-1}$ · $d^{-1}$, $RFD_{Ni} = 20$ ug · $kg^{-1}$ · $d^{-1}$, $RFD_{Pb} = 3.57$ ug · $kg^{-1}$ · $d^{-1}$, $RFD_{Zn} = 300$ ug · $kg^{-1}$ · $d^{-1}$ (USEPA 2001). H is the health risk accumulated for HMs.

## 18.3 Results and Discussion

### *18.3.1 Characteristics of HMs*

The soil HMs of different residential areas in Qingdao and other cities in Table 18.1.

According to Table 18.1, the mean of Cd, Cu, Hg, Ni, Pb and Zn in urban of Qingdao are the highest, but Cr is the lowest. The mean of as and Cr in Huangdao are the highest, but Cd, Hg and Pb are the lowest. However, the mean of As, Cu, Ni, Zn in suburb of Qingdao are the lowest. As a whole, the mean of HMs of different residential areas is significantly different. Among them, urban of Qingdao which has actively developed cultural tourism, high and new technology is the highest, following is Huangdao which mainly develops petrochemical industry, information appliances, rubber plastics, etc., suburb of Qingdao is the lowest. The mean of As, Cr and Ni in different residential areas of Qingdao are not exceed the corresponding natural background levels and them may be come from natural origin (Pang et al. 2019). In addition, the other 5 HMs are exceed the corresponding natural background levels, which should be affected by human factors. Therefore, the other 5 HMs are primary pollutants of different residential areas in Qingdao.

The meanof HMs in different residential areas of Qingdao are lower than the selected corresponding standard of HMs in residential areas according to the soil pollution risk control standard for construction land of soil environmental quality in China (Trial) (GB36600-2018). And compared with the mean of HMs of residential areas in Xi'an and Xiamen, the Cd, Cr, Cu, Pb and Zn in Xiamen and As and Ni

**Table 18.1** Soil HMs ($\mu g\ g^{-1}$) of different residential areas in Qingdao

| Area | Eigenvalues | As | Cd | Cr | Cu | Hg | Ni | Pb | Zn |
|---|---|---|---|---|---|---|---|---|---|
| Urban of Qingdao | Mean | 5.56 | 0.283 | 46.5 | 44.3 | 0.105 | 20.7 | 67.7 | 131.4 |
| | Max | 18.59 | 1.524 | 77.1 | 171.3 | 0.440 | 40.2 | 166.1 | 316.5 |
| | Min | 2.29 | 0.088 | 23.7 | 12.3 | 0.022 | 10.3 | 37.7 | 48.6 |
| | Sd | 7.87 | 0.69 | 17.68 | 75.79 | 0.20 | 11.23 | 55.37 | 99.52 |
| Suban of Qingdao | Mean | 5.26 | 0.236 | 47.0 | 19.5 | 0.060 | 19.2 | 64.0 | 86.0 |
| | Max | 8.14 | 0.464 | 72.3 | 30.1 | 0.414 | 32.9 | 102.5 | 155.8 |
| | Min | 1.8 | 0.099 | 24.7 | 9.5 | 0.024 | 9.8 | 41.5 | 50.3 |
| | Sd | 1.77 | 0.1 | 13.20 | 5.56 | 0.09 | 6.05 | 17.07 | 31.29 |
| Huangdao | Mean | 5.65 | 0.183 | 50.1 | 38.9 | 0.032 | 19.7 | 48.7 | 119.8 |
| | Max | 20.73 | 0.674 | 112.7 | 323 | 0.074 | 33.1 | 143.1 | 719.7 |
| | Min | 2.77 | 0.061 | 32.2 | 7.9 | 0.013 | 11.1 | 23.2 | 41.1 |
| | Sd | 4.22 | 0.16 | 19.45 | 76.79 | 0.02 | 5.88 | 28.69 | 165.97 |
| Qingdao (Pang et al. 2019) | Background value | 7.0 | 0.098 | 52.4 | 17.3 | 0.028 | 22.5 | 24.2 | 48.0 |
| Residential Areas of GB36600-2018 | Selected value | 20 | 20 | | 2000 | 8 | 150 | 400 | |
| Beijing (Xie et al. 2019) | Mean | | 0.139 | 48.3 | 23.5 | | 16.1 | | |
| Xi'an (Chen and Lu 2017) | Mean | 11.55 | | | 34.65 | | 32.3 | 37.14 | 92.64 |
| Xiamen (Li et al. 2017) | Mean | | 0.69 | 88.0 | 84.6 | | | 106.5 | 329.9 |

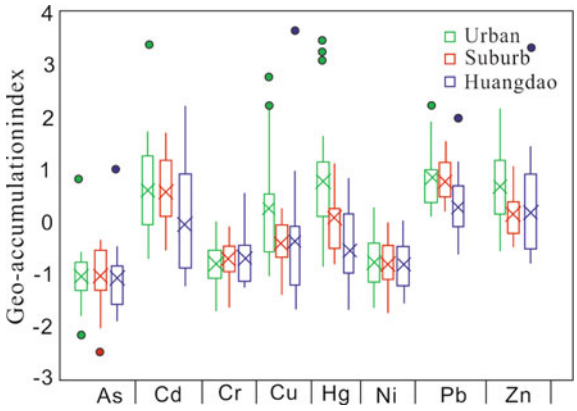


**Fig. 18.2** $I_{geo}$ for soil HMs of different residential areas in Qingdao

in Xi'an are the highest (Chen and Lu 2017; Li et al. 2017). However, except for the Cd in Beijing, the other five HMs are the lowest in Qingdao (Xie et al. 2019). In conclusion, HMs pollution of residential areas in Xiamen is the most serious, following is Xi'an, Beijing, Qingdao are the lowest.

### *18.3.2 Contamination Assessment*

Igeo of soil HMs of different residential areas in Qingdao were calculated in Fig. 18.2.

According to Fig. 18.2, the mean $I_{geo}$ of HMs of different residential areas in Qingdao are significantly different, the decreasing order of them in urban of Qingdao is: Pb > Hg > Zn > Cd > Cu > Ni > Cr > As, the decreasing order of them in suburb of Qingdao is: Pb > Cd > Zn > Hg > Cu > Cr > Ni > As, and the decreasing order of them in Huangdao is: Pb > Zn > Cd > Cu > Hg > Cr > Ni > As. Among them, the mean $I_{geo}$ of some HMs are more than 0 less than 1, such as Cd, Cu, Hg, Pb, Zn in urban of Qingdao, Cd, Hg, Pb, Zn in suburb of Qingdao and Pb, Zn in Huangdao. Based on the $I_{geo}$ value (Jamal et al. 2019; Li et al. 2003), it indicating that they are unpolluted to moderately polluted. In the other hand, the other $I_{geo}$ of HMs are lower than 0, it indicating that they are not polluted. Compared with the mean $I_{geo}$ of HMs of residential areas in Shanghai, Cd, Cu and Zn in urban of Qingdao and Cd in suburb of Qingdao are higher, but all HMs are lower than them in Huangdao (Jaffar et al. 2017).

### *18.3.3 Health Risk Assessment*

Table 18.2 list the health risks soil HMs of different residential areas in Qingdao for adults and children.

**Table 18.2** Health risk of soil HMs of Qingdao residential areas

| Category | Area | | As | Cd | Cr | Cu | Hg | Ni | Pb | Zn | Hi |
|---|---|---|---|---|---|---|---|---|---|---|---|
| Adults | Urban of Qingdao | Range | 0.02–0.18 | 0 | 0.02–0.07 | 0–0.01 | 0–0.02 | 0–0.01 | 0.03–0.13 | 0 | 0.08–0.37 |
| | | Mean | 0.05 | 0 | 0.04 | 0 | 0 | 0 | 0.05 | 0 | 0.16 |
| | Suban of Qingdao | Range | 0.02–0.09 | 0 | 0.02–0.07 | 0 | 0–0.01 | 0 | 0.03–0.08 | 0 | 0.10–0.20 |
| | | Mean | 0.05 | 0 | 0.05 | 0 | 0 | 0 | 0.05 | 0 | 0.16 |
| | Huangdao | Range | 0.03–0.2 | 0 | 0.03–0.11 | 0–0.02 | 0 | 0 | 0.02–0.11 | 0–0.01 | 0.09–0.46 |
| | | Mean | 0.05 | 0 | 0.05 | 0 | 0 | 0 | 0.04 | 0 | 0.15 |
| Children | Urban of Qingdao | Range | 0.05–0.39 | 0–0.01 | 0.05–0.16 | 0–0.03 | 0–0.03 | 0–0.01 | 0.07–0.29 | 0–0.01 | 0.18–0.83 |
| | | Mean | 0.11 | 0 | 0.1 | 0.01 | 0.01 | 0.01 | 0.12 | 0 | 0.35 |
| | Suban of Qingdao | Range | 0.04–0.21 | 0 | 0.05–0.15 | 0 | 0–0.03 | 0–0.01 | 0.07–0.11 | 0 | 0.21–0.35 |
| | | Mean | 0.12 | 0 | 0.1 | 0 | 0 | 0.01 | 0.11 | 0 | 0.35 |
| | Huangdao | Min | 0.06–0.43 | 0 | 0.07–0.24 | 0–0.05 | 0 | 0–0.01 | 0.04–0.25 | 0–0.02 | 0.21–1.00 |
| | | Mean | 0.12 | 0 | 0.1 | 0.01 | 0 | 0.01 | 0.09 | 0 | 0.33 |

According to Table 18.2, the average health risk of HMs for adults is 0.05 of As, 0.04–0.05 of Cr and 0.04– 0.05 of Pb in soil of different residential areas in Qingdao, and the other five HMs is 0. Therefore As, Cr and Pb are harmful to the health of adults. However, the average health risk of HMs for children is 0.11–0.12 of As, 0.1 of Cr, 0–0.01 of Cu, 0–0.01 of Hg, 0.01 of Ni and 0.09–0.12 of Pb of different residential areas in Qingdao, and the other two HMs is 0. Therefore As, Cr, Cu, Hg, Ni and Pb are harmful to the health of children, and the risk of children's health is higher than that of adults' health.

The average cumulative health risk of HMs of residential areas in urban of Qingdao is 0.15–0.16 for adults and 0.33–0.35 for children. Therefore, the children's health risk is higher than adult's. On the whole, the average cumulative health risk of HMs of Qingdao are lower than the safe level ($H < 1$), that HMs of different residential areas in Qingdao will not be harmful to the health of human. However, the maximum cumulative health risk of HMs of residential areas in Huangdao to children's is 1.00, which indicated that it will be harmful to children's health. Therefore, it should strengthen find out the sources of HMs of residential areas in Huangdao to prevent endangering children's health.

## 18.4 Conclusion

The mean of HMs of residential areas in urban of Qingdao is the highest, following is Huangdao, the suburb of Qingdao is the lowest. The mean of $I_{geo}$ of HMs of different residential areas in Qingdao are significantly different, Cd, Cu, Hg, Pb, Zn in urban of Qingdao, Cd, Hg, Pb, Zn in suburb of Qingdao and Pb, Zn in Huangdao are unpolluted to moderately polluted, and the other HMs are not polluted.

The average health risk of soil HMs of different residential areas in Qingdao is 0–0.05 for adults, and 0–0.12 for children. The average cumulative health risk of soil HMs of different residential areas in Qingdao is 0.15–0.16 for adults and 0.33–0.35 for children. On the whole, HMs of different residential areas in Qingdao will not be harmful to the health of human. However, the maximum cumulative health risk of HMs of residential areas in Huangdao to children's health is 1.00, which indicated that it will be harmful to children's health. Therefore, it should strengthen identify the sources of HMs of residential areas in Huangdao to prevent the adverse effects of children's health.

**Acknowledgements** This work was supported by 2019 special funding for scientific research of Shandong coal geology bureau (Lu coal geological character (2019) No. 11) and the Chinese Natural Science Foundation (71303140).

## References

Bo S, Guanghui G, Mei L et al (2018) Assessments of contamination and human health risks of heavy metals in the road dust from a mining county in Guangxi, China. Hum Ecol Risk Assess 24(6):1606–1622

Chen XD, Lu XW (2017) Source apportionment of soil heavy metals in city residential areas based on the receptor model and geostatistics. Environ Sci 38(6):2513–2521

Jaffar S, Luo F, Ye R et al (2017) The extent of heavy metal pollution and their potential health risk in Topsoils of the massively urbanized district of Shanghai. Arch Environ Contam Toxicol 73(3):362–376

Jamal A, Delavar MA, Naderi A et al (2019) Distribution and health risk assessment of heavy metals in soil surrounding a lead and zinc smelting plant in Zanjan, Iran. Hum Ecol Risk Assess 25(4):1018–1033

Li XD, Lee SI, Wong SC et al (2003) The study of metal contamination in urban soils of Hong Kong using a GIS-based approach. Environ Pollut 129(1):113–124

Li FZ, Zhang Z, Zhang ZT et al (2017) Analysis and evaluation of the soil and dust contamination by heavy metals in different functional zones on Xiamen. J Saf Environ 17(2):719–724

Mohammad O, Mohammad SK, Almas Z et al (2012) Soil contamination, nutritive value, and human health risk assessment of heavy metals: an overview. Toxicity of heavy metals to legumes and bioremediation, pp 1–27

Pang X G, Dai J R, Chen L et al (2019) Soil geochemical background value of 17 cities in Shandong province. Shandong Land Resour 35(1):46–56. (in Chinese)

Pouyat RV, Szlavecz K, Yesilonis ID et al (2015) Multi-scale assessment of metal contamination in residential soil and soil fauna: a case study in the Baltimore-Washington metropolitan region, USA. Landsc Urban Plan 142:7–17

USDOE (2011) The risk assessment information system (RAIS). US Department of Energy's Oak Ridge Operations Office (ORO), Argonne, IL

USEPA (1993) Reference Dose (RfD): description and use in health risk assessments. Background document 1A. https://www.epa.gov/iris/reference-dose-rfd-description-and-use-health-risk-assessments

USEPA (2001) Baseline human health risk assessment. Office of Solid Waste and Emergency Response, Washington, DC

USEPA (2002) Supplemental guidance for developing soil screening levels for superfund site. Office of Emergency and Remedial Response, Washington, DC

Wang ZS, Duan XL, Liu P et al (2009) Human exposure factors of Chinese People in environmental health risk assessment. Res Environ Sci 22(10):1164–1170

Xie T, Wang M, Chen WP et al (2019) Impacts of urbanization and landscape patterns on the accumulation of heavy metals in soils in residential areas in Beijing. J Soils Sediments 19(1):148–158

# Chapter 19
# Analysis of Factors Affecting Chinese Enterprises' Carbon Emission Policy


**Jing Zhao, Guan Wei Jang, and Shuping Li**

**Abstract** Reducing carbon emissions is a significant component of superior development for a national economy and the essential basis of enterprises. Considering the conception of "carbon peak and carbon neutrality", studying the influencing factors of carbon emissions by focusing on the targeted measures is a requisite commencement to realize the low-carbon transformation and the superior development of an industry. Addressing the issues of the devastating disasters that are directly influenced by global warming with respect to reducing carbon emissions has become an indispensable goal and mission in relating to global environmental sustainability. This paper investigates energy consumption with a focus on Chinese companies along with carbon emissions in respect of the duration of the four consecutive years, considering from 2018 to 2021. We conducted a multiple regression analysis to determine the five influencing factors of carbon emissions. This research provides the policy recommendations regarding the regulation and planning of carbon emission reduction are presented to facilitate the realization of the goal of reaching the peak of carbon emissions and achieving a sustainable economy and an ecological development.

**Keywords** Carbon emission · Multiple regression analysis · Influencing factor

## 19.1 Introduction

The greenhouse effect can lead to a series of natural environmental issues such as global warming, glacier melting, sea-level rise, and a large amount of carbon

J. Zhao (✉) · S. Li
Guangdong University of Science and Technology, Dongguan, Guangdong, China
e-mail: zhaojing@gdust.edu.cn

S. Li
e-mail: lishuping@gdust.edu.cn

G. W. Jang
Shaoguan University, Shaoguan, Guangdong, China
e-mail: steve.jang@sgu.edu.cn



Z. Yang (ed.), *Environmental Science and Technology: Sustainable Development*,
Environmental Science and Engineering, https://doi.org/10.1007/978-3-031-27431-2_19

dioxide emissions. Global greenhouse gas emissions can generate an increase in global temperature. In light of the negative impacts, actions should be taken to control the emissions.

The international community has been actively taking the corresponding measures to control greenhouse gas emissions. To promote international cooperation and reduce greenhouse gas emissions, countries jointly agreed on the United Nations Framework Convention on Climate Change in June 1992 and the respective Kyoto Protocol, which aims to limit the greenhouse gas emissions in developed countries, was signed in 1997. The Cancun Accord was adopted in 2010 on top of The Copenhagen Accord, which was adopted in 2009. On 22 April 2015, leaders of more than 170 countries signed the Paris Agreement on climate change at the United Nations Headquarters.

As the world's largest energy consumer and carbon emitter, China is increasingly gaining pressure on emissions reduction. At this point, the government pledged to peak carbon emissions by around 2030. According to this target, the State Council of China has placed the remedial emission reduction targets on the respective provincial governments. In this case, each province introduced a series of corresponding emission reduction policies to solve the negative ecological and economic consequences. Nevertheless, the future economic development, technological progress, and policy trends of regions possess unpredictable uncertainties, which could be an impediment to the goal achievements.

## 19.2 Literature Review

### *19.2.1 The Theoretical Basis of Carbon Emission*

**Climate Change and Local Low-Carbon Economic Theory**. Climate change will pose a severe threat to humanity, and measures must be taken to mitigate it. Among them, developing a low-carbon economy is one of the essential measures. Low carbon economic theory is based on demography, resources and environment, economics, and so on, which requires us to improve in many aspects. For example, low carbon production in agriculture and industry; Chen et al. 2021 thought that the government should vigorously develop low-carbon cities, residents should consume low carbon, reduce energy-intensive products, and avoid excessive consumption.

Sun et al. (2021) said greenhouse gases and environmental pollutants have the same root and homology. In the combustion process of coal and other fossil fuels, carbon dioxide isothermal chamber gas and particulate matter, carbon monoxide, sulfur dioxide, and other air pollutants. China's pollution prevention and control process began in the 1970s. Since the eighteenth congress, comprehensively strengthened the party central committee with comrade xi for the core of ecological civilization construction and ecological environment protection of leadership, has launched a

series of fundamental, pioneering, a long-term work, obviously improved the ecological environment, the people a sense show the enhancement, strengthen to build a well-off society in an all-round way of the green background color and quality (Sun et al. 2021).

Menegaki et al. (2022) applied a pooled mean group (PMG) model to identify climate parameters that affected tourism demand. Then, it continued with an input–output table analysis to show the transmission effect of CC on each component of the tourism sector. The PMG model imposed homogeneity on the long-run coefficients and while less restrictive, it was more efficient than other methods of the same family. The estimated gravity equation enabled comparisons of the baseline scenario with various scenarios of CC and found how tourist arrivals could be affected up to 2080. Their results suggested that there was mostly a positive relationship between the squared difference of temperature and precipitation between Greece and tourist origin countries. Their findings also suggested that CC could lead to a fall in Greek GDP between 1.79 and 2.61% (Menegaki et al. 2022).

**Sustainable Development Theory**. The word "sustainable development" first appeared in the International Union for Conservation of Nature's World Natural Resources Conservation Program in 1980. Then, in 1987, the United Nations World Environment Assembly emphasized the concept of sustainable development and put environmental issues and social equity issues on the international political agenda, which made sustainable development widely popular.

In the 15th National Congress of the Communist Party of China in 1997, a sustainable development strategy was identified as a "must be implemented in China's modernization drive." In 2002, the 16th National Congress of the Communist Party of China set "continuously enhancing the capacity for sustainable development" as one of the goals of building a moderately prosperous society in an all-around way.

Sustainable development believes that economic growth and environmental protection are inseparable. It emphasizes the balance between economy, environment, and society and requires us to provide sufficient development space for future generations. To ensure sustainable economic growth and meet the development needs of future generations, environmental protection is imperative.

Wei et al. (2022) thought the Sustainable Development Goals (SDGs) provided a broad spectrum of economic, social, and environmental goals to be achieved by 2030. The Yangtze River Economic Zone (YREZ) is an important national regional development strategy in China. They presented an assessment method for measuring the progress of SDGs at the local level and took the case of the YREZ in China. The local SDGs indicator framework was developed based on the availability of good data and alignment with the global indicator framework (SGIF), including 60 indicators covering 17 goals. The local SDGs index and three target indexes were aggregated based on the entropy-weighting method. The SDGs progress of each province (municipality) in the YREZ was assessed based on the proposed method (Wei et al. 2022).

### *19.2.2 Research Progress of Peak Carbon Emissions*

The Central Economic Work Conference held in December 2020 put carbon peak as one of the eight major work priorities in 2021, and "carbon peak" is also listed as an important content in the 14th Five-year Plan. China's goal of peaking carbon emissions by 2030 is feasible. It is not only an inherent requirement for High-quality development in China but also an enormous effort China has made as a major responsible country in addressing global climate change. By constructing China's energy prediction model, Liu et al. (2018) believed that China's carbon emissions could peak before 2030 under two environmental governance constraint scenarios (Liu et al. 2018). Marcotullio et al. (2013) believe that China's carbon emissions will peak in 2026, but China needs to reduce the annual GDP growth rate to below 4.5% before 2030. Using the energy system optimization model, taking the realization of carbon peak in 2030 as the assumption, analyzing the realization path and possible level of carbon peak, and making some suggestions on energy conservation and emission reduction (Marcotullio et al. 2013). Cao et al. (2016) applied Meta-regression analysis to study the path of carbon peak realization in China. The samples analyzed were consistent with the development of carbon peak realization in 2030 in China (Cao et al. 2016). Michel et al. (2016) studied the case of reaching a carbon peak by calculating the coupling coefficient between carbon dioxide emissions and economic growth. Wu (2021) used the Monte Carlo method and K-means clustering method to predict and describe the state of carbon emission peak in China and concluded that whether China can reach the carbon emission peak mainly depends on cities with low carbon potential and towns in the transition of traditional industries (Wu 2021). Xue et al. (2022) supported that the improvement of carbon emission efficiency (CEE) would promote the development of the green and low-carbon economy in the Beijing-Tianjin-Hebei (BTH) region, China. They used the EBM model of unexpected output to measure the city-level CEE of the BTH region from 2007 to 2016. The spatial distribution characteristics and evolution law of CEE were analyzed concerning overall and local aspects, and the spatial quantile regression model was used to verify the influencing factors of CEE (Xue et al. 2022). The main findings were as follows: (1) The carbon emission in the BTH region was considered to be of medium efficiency, and there were eight cities within the region at middle- and high-efficiency levels. The overall efficiency values showed a downward trend. Beijing, Cangzhou, and Baoding have high-CEE values, whereas Handan, Tangshan, and Zhangjiakou had low-CEE values. (2) The CEE valued for BTH show significant spatial agglomeration characteristics at both the global and local levels. The "H-H" agglomeration areas were primarily distributed in the central region, and the "L-L" agglomeration areas were chiefly distributed in the southern and northern regions. The spatial pattern change was generally stable. (3) The selected factors, URB, PGDP, DS, ISG, FDI, and TEL, had different regression coefficients on CEE at different quantiles.

### 19.2.3 Carbon Emissions and Economic Development

The rapid increase in China's carbon emissions has become essential for economic development. Dunnan and Bowen (2018) building a carbon emission model and using LMDI to decompose China's carbon emissions from 1995 to 2007 concluded that economic factors highly correlated with carbon emissions (Dunnan and Bowen 2018). Xiao and Zhang (2015) analyze the driving factors of carbon emissions in the Yangtze River Delta region. These studies show a high correlation between carbon emissions and economic development factors (Xiao and Zhang 2015). Liu et al. (2022) selected nine provinces and cities in China with an average GDP of more than USD 10,000 as the research object, and the results showed that the relationship between the economic growth of these provinces and cities and their carbon emissions had decoupled, and the decoupling gradually strengthened (Liu et al. 2022). Liu and Deng (2021) used the EKC model to verify that economic development and environmental quality conform to the "inverted N-shaped" curve. Then the decoupling theory is used to analyze the decoupling state of China's carbon emissions in the past 20 years and observe the law of carbon emissions in economic development (Liu and Deng 2021). Tang et al. (2021) analyzed the relationship between urban carbon emission and its carbon peak in China and conducted a regression analysis to explain the relationship between urban carbon emission and high-quality economic development in China (Tang et al. 2021).

### 19.2.4 Summary of Literature Review

From the existing research results, Tan and Wang (2022) mainly focused on the impact of limiting carbon dioxide emissions and energy consumption on economic growth, and discussed how to achieve low carbon transition (Tan and Wang 2022). At the same time, most scholars focus on carbon emissions, energy consumption and economic growth, the relationship between the factor decomposition of carbon emissions, though empirical analysis on the existing literature of carbon inner driving factors and the influence factors of carbon emissions, highlighted the economic growth, industrial structure, energy efficiency and consumption structure is major influential factors of carbon emissions, but the lack of in-depth study of carbon emissions of convergence. It can not effectively meet the needs of decision makers, and lack of comprehensive consideration of the factors affecting carbon emissions. Since carbon emissions and low-carbon economy have different tasks at each stage, it is necessary to consider the influencing factors of carbon emissions from a systematic perspective and analyze the impact of these factors on the future growth path of the country's low-carbon economy.

## 19.3 Research Content

This paper mainly includes three aspects: This paper investigates Chinese enterprises' energy consumption and carbon emissions for four consecutive years from 2018 to 2021. Considering 2020 as the boundary, we group the carbon emission data before and after eliminating backward production capacity, set carbon emission targets and tasks, and use multiple regression analysis to determine five influencing factors of carbon emissions. Based on the above research, policy suggestions on carbon emission reduction planning and regulation are put forward to promote the carbon peak goal and achieve sustainable economic and ecological development. It is mainly divided into three parts.

First, current situation analysis of Energy consumption and carbon emission in China. This paper mainly summarizes the current situation of energy consumption and carbon dioxide emissions in China and provinces from 2018 to 2021 and makes an in-depth analysis of the two data.

Second, through SPSS statistical analysis, analyze the degree of impact of different industries on emission reduction, and determine the main factors affecting carbon emissions.

Last, put forward corresponding measures to reduce carbon emissions and continuously reduce carbon emissions to achieve sustainable development.

## 19.4 Data and Analysis

### *19.4.1 Basic Data*

The carbon emission survey in this paper covers cities at the prefecture level and above in China, and the data involved are mainly from the statistical data from 2018 to 2021. In this paper, a selection of variables including annual information, enterprise energy type, area, number of filing announcements, actual enterprise examination, super target complete number of businesses, according to the target enterprise quantity, number of companies that did not meet the target, carbon emissions after close down backward production facilities, the percentage of carbon emissions after 2020. To better understand the impact of carbon emissions on high-quality social and economic development, we used SPSS statistical software to conduct multiple regression analyses on carbon emission data. The analysis results draw the corresponding conclusions on carbon emission reduction.

### 19.4.2 Data Analysis

Bartlett spherical degree test and KMO measurement were carried out, and the KMO test and Bartlett spherical test were calculated using SPSS. The results were shown in Fig. 19.1. The KMO test value is 0.830, greater than 0.8, and passes the significance test, so it meets the applicable requirements of factor analysis. At the same time, the observed value of the Bartlett sphericity test was 3875.546, Sig = 0.000, indicating that the correlation coefficient was significant at P = 0.001 and the sample data were suitable for factor analysis.

Next, the eigenvalues, contribution rate and cumulative contribution rate of the correlation matrix R were calculated. The size of the eigenvalue represented the amount of information that reflects the description of the corresponding component. The eigenvalue of each principal component was shown in Fig. 19.2. According to the principle that the cumulative contribution rate is greater than 80–85% and only the first eigenvalue is greater than 1, the cumulative contribution rate of this sample is 87.572%, which indicates that the first to fifth principal components can reduce the dimension and explain most of the information. Therefore, only the first to fifth principal components are extracted here.

**KMO and Bartlett's Test**

| | | |
|---|---|---|
| Kaiser-Meyer-Olkin Measure of Sampling Adequacy. | | .830 |
| Bartlett's Test of Sphericity | Approx. Chi-Square | 3875.546 |
| | df | 561 |
| | Sig. | .000 |

**Fig. 19.1** KMO and Bartlett's test

**Total Variance Explained**

| Component | Initial Eigenvalues | | | Extraction Sums of Squared Loadings | | | Rotation Sums of Squared Loadings | | |
|---|---|---|---|---|---|---|---|---|---|
| | Total | % of Variance | Cumulative % | Total | % of Variance | Cumulative % | Total | % of Variance | Cumulative % |
| 1 | 8.534 | 44.918 | 44.918 | 8.534 | 44.918 | 44.918 | 7.191 | 37.847 | 37.847 |
| 2 | 4.131 | 21.740 | 66.658 | 4.131 | 21.740 | 66.658 | 4.040 | 21.264 | 59.111 |
| 3 | 1.727 | 9.089 | 75.746 | 1.727 | 9.089 | 75.746 | 2.410 | 12.684 | 71.794 |
| 4 | 1.201 | 6.322 | 82.068 | 1.201 | 6.322 | 82.068 | 1.927 | 10.144 | 81.938 |
| 5 | 1.046 | 5.504 | 87.572 | 1.046 | 5.504 | 87.572 | 1.071 | 5.634 | 87.572 |
| 6 | .897 | 4.719 | 92.291 | | | | | | |
| 7 | .589 | 3.099 | 95.390 | | | | | | |
| 8 | .485 | 2.554 | 97.944 | | | | | | |
| 9 | .150 | .792 | 98.736 | | | | | | |
| 10 | .097 | .510 | 99.246 | | | | | | |
| 11 | .061 | .319 | 99.565 | | | | | | |
| 12 | .037 | .194 | 99.759 | | | | | | |
| 13 | .019 | .099 | 99.858 | | | | | | |
| 14 | .015 | .079 | 99.937 | | | | | | |
| 15 | .008 | .043 | 99.980 | | | | | | |
| 16 | .004 | .020 | 100.000 | | | | | | |
| 17 | 2.615E-16 | 1.377E-15 | 100.000 | | | | | | |

Extraction Method: Principal Component Analysis.

**Fig. 19.2** Interpretation of total variance of carbon emissions

Among all variable factors, the variable with the highest factor load and the influencing factor of carbon emission are determined according to the rotation component matrix. According to the results of Fig. 19.3, the extraction method was principal component analysis, and the rotation was Kaiser normalized maximum variance method, a represents the rotation convergence of 5 iterations. Among the evaluation factors affecting the enterprise's carbon emissions, the main positive correlation factor of principal component 1 are the number of 10,000 enterprises announced by the state, actual assessment of the number of enterprises, the number of enterprises over-fulfilled, number of completed enterprises, emissions and control the number of emissions. So factor 1 is the carbon emission control amount. The main positive correlation factor of principal component 2 is ID, year, and types of energy, and China eliminated outdated production capacity types. So factor 2 is the enterprise's elimination of outdated capacity. Using the same method for cluster analysis of other factors, factor 3 is the change of the impact of emission reduction targets in different regions on carbon emissions, factor 4 is the carbon emission after 2020, and factor 5 is the number of enterprises' carbon emission standards.

**Rotated Component Matrix[a]**

| | Component | | | | |
|---|---|---|---|---|---|
| | 1 | 2 | 3 | 4 | 5 |
| ID | -.042 | .977 | .126 | -.002 | .000 |
| year | -.009 | -.996 | -.030 | -.040 | -.001 |
| Types of energy | .009 | .996 | .030 | .040 | .001 |
| region | -.104 | -.041 | .809 | -.049 | -.018 |
| The number of 10,000 enterprises announced by the state | .916 | -.015 | -.130 | .199 | .162 |
| Actual assessment of the number of enterprises | .927 | -.015 | -.132 | .164 | .185 |
| The number of enterprises overfulfilled | .751 | -.014 | -.015 | .089 | .358 |
| Number of completed enterprises | .899 | -.014 | -.123 | .147 | .148 |
| Basically complete the number of enterprises | .530 | -.010 | -.205 | .169 | -.502 |
| Number of uncompleted enterprises | .182 | .001 | -.128 | .110 | .745 |
| emissions | .922 | -.005 | -.174 | .183 | -.100 |
| Control the amount of emissions | .894 | .005 | -.183 | .231 | -.078 |
| China eliminated outdated production capacity types | .009 | .996 | .030 | .040 | .001 |
| "Emissions in 2019
(ten thousand tons)" | .388 | .055 | -.095 | .907 | .042 |
| "Emissions in 2020
(ten thousand tons)" | .399 | .071 | -.096 | .899 | .061 |
| "Year-over-year up or down
(%)" | -.229 | .046 | .901 | -.093 | -.039 |
| "2020 emission reduction target
(%)" | -.332 | .308 | .807 | -.047 | -.038 |

**Fig. 19.3** Rotated matrix of carbon emissions

## 19.5 Data and Discussion

According to the carbon emission data of the prefecture-level cities in China over the past two years, this paper indicates five distinct influencing factors of carbon emission. To reduce the carbon emissions, the following countermeasures are proposed.

### *19.5.1 Establish and Improve the Energy Management System and Carbon Emission Management System*

Through analysis of the above results, the amount of carbon emission control is one of the factors, in order to better control carbon emissions, carbon shall establish a unified, standardized management system, for the most part because our country enterprise has yet to establish an effective system, authority is not forced, causing most of the enterprise the current basic in "provide corresponding data according to the requirement of the inspection institution" of "one-time offer" state. If the relevant person in charge is forgotten or replaced, it will lead to the absence of the enterprise management system, and then appear in the same data to provide different data sources, causing great hidden dangers to data consistency. Therefore, it is necessary for China to establish a unified and standardized carbon management system, require key emitters to establish a controllable carbon management system, and formulate relevant data monitoring plans to ensure the consistency of data quality in the future and prepare for international cohesion (Lu and Zhang 2022). The operation of carbon emission energy management system and circular management PDCA (Plan-do-check-act) are important methods and elements to reduce carbon emissions (Hai et al. 2020). Establishing a management system that covers the whole process of energy use and carbon emissions is of great significance to building a long-term mechanism for energy conservation and emission reduction.

### *19.5.2 Accelerate the Elimination of Backward and Inefficient Coal Chemical Production Capacity*

Among the influencing factors of carbon emissions, the elimination of outdated production capacity is also one of the influencing factors. The Implementation Guide for Energy Conservation and carbon Reduction Transformation and Upgrading of Modern coal Chemical Industry issued by the National Development and Reform Commission proposes that the backward and inefficient coal chemical industry production capacity should be eliminated under strict policy constraints, and the coal chemical industry production capacity whose energy efficiency level is below the benchmark value and cannot be reached above the benchmark value through energy

conservation transformation should be eliminated and closed faster. At the same time, according to the "Elimination of Energy-Intensive and Backward Mechanical and Electrical Equipment (Products) Catalogue" proposed by the Ministry of Industry and Information Technology and other departments, the existing leading energy-consuming equipment will be sorted out. We accelerated the phasing out of energy-intensive and outdated mechanical and electrical equipment (products), and improved the energy efficiency of key energy-consuming equipment.

### *19.5.3 Complementary Advantages, Developed Cities in the East to Towns in the Midwest*

Among the influencing factors, the change of the impact of emission reduction targets in different regions on carbon emissions is also the main influencing factor. Cities are classified and studied according to their population and regional location. For large and super-large towns and cities in the eastern region, it is easy to reach peak carbon emissions due to the developed industrial situation. Smaller towns in the Midwest, by contrast, do not. At the same time, different enterprise nature will also affect carbon emissions. Carbon emissions of state-owned enterprises and enterprises in the western region are greater than those of non-state-owned enterprises and enterprises in the eastern region (Guo et al. 2022). Therefore, the government re-examines the overall environmental effects of low-carbon policies, and needs to pay more attention to small and medium-sized towns and important cities in western China, as well as state-owned enterprises in western China when making carbon policies. Caused by a lack of economic development power, carbon management technology is relatively backward, needs through regional coordinated development for carbon peak, better make full use of its advantages in technology, capital of the developed cities and Midwestern city ecological benefits, through technical and financial support, the support of the developed cities and major cities in western China's industrial upgrading, energy conservation and emissions reduction.

### *19.5.4 Establish an Energy Monitoring Center*

According to the above data results, with the national control of carbon emissions, the carbon emissions after 2020 decreased significantly, indicating that national policies have a great impact on carbon emissions. Therefore, in order to control carbon emissions more effectively, relevant data monitoring plans should be developed and energy monitoring centers should be established. Regulatory authorities can explore the use of big data technology to evaluate the quality of carbon emission data, identify the problems existing in the carbon emission accounting of enterprises, improve the level of supervision, and maintain the order of the carbon market. Local governments

can mine the value of enterprise carbon emission data and use enterprise carbon emission data as a tool for classified management of industrial enterprises. Enterprises can reduce contract performance costs and realize asset preservation and appreciation through carbon asset management (Li et al. 2022). Finally, by participating in the carbon trading market, the government can control the carbon emission quota of high-carbon enterprises (Sun et al. 2018) and improve the monitoring impact on energy.

### *19.5.5 Upgrade Energy-Saving Technologies to Achieve Carbon Neutrality*

Among the influencing factors, the number of carbon emission standards of enterprises is also the main influencing factor. Therefore, to ensure that China achieves carbon neutrality before 2060, it is necessary to actively adopt market, administrative, legal and other countermeasures and means to promote the progress and application of clean energy technology while maintaining high-quality economic and social development. To achieve the preset technical goals of SSP1 or SSP4. At the same time, it is necessary to take strong policy measures to actively promote the transformation of non-electric energy into electric energy and vigorously develop wind power and photovoltaic industries (Liu et al. 2022). Through the carbon emission data review energy utilization, tap energy saving potential, use new technologies to improve heating, air conditioning, ventilation, lighting, power distribution, water supply and drainage and other major energy utilization systems.

## 19.6 Conclusions and Future Research

### *19.6.1 Conclusions*

This paper investigated the data of energy consumption and carbon emissions of Chinese enterprises from 2018 to 2021, took 2020 as the boundary, grouped the carbon emission data of obsolete production capacity, seted carbon emission targets and tasks, and used multiple regression analysis to determine the five factors affecting carbon emissions. The policy suggestions of carbon emission reduction planning and regulation were put forward to promote the realization of the carbon peak goal and realize the sustainable development of economy and ecology. The main contributions were as follows.

The current situation of energy consumption and carbon dioxide emissions of provinces and cities in China from 2018 to 2021 was summarized, and the data were analyzed with 2020 as the boundary. The SPSS statistical software was used to determine five factors affecting carbon emissions. Among them, factor 1 is the

carbon emission control amount, factor 2 is the obsolete production capacity of the enterprise, factor 3 is the change of the impact of emission reduction targets in different regions on carbon emissions, factor 4 is the control factor of carbon emissions after 2020, and factor 5 is the standard amount of carbon emissions of the enterprise.

According to the five factors of carbon emissions, carbon reduction measures were put forward respectively, such as to establish and perfect the system of energy management system and carbon management, speed up eliminating backward coal chemical inefficient capacity, complementary advantages, the developed eastern cities to develop towns across the Midwest, building energy monitoring center, through the new technology of energy saving and carbon neutral to upgrade, to continue to reduce carbon emissions, Achieve sustainable development.

### *19.6.2 Future Research*

In this paper, data sources were the provinces of carbon emissions and energy consumption situation, different regions were not considered due to the economic development level of carbon emissions caused by different problems, therefore, the next will be around the area of carbon emissions to continue in-depth study, research different region and different carbon emissions intensity difference change trend.

The research data of the influencing factors of carbon emissions considered in this paper adopts cross-sectional data research, which cannot consider the mutual influence degree of carbon emissions as a whole. Therefore, the following research will continue to verify the spatial effect of carbon emissions (Tong and Li 2017).

As countries around the world pay more attention to ecological environment protection and carbon emissions, the issue of carbon emissions hidden behind international trade has gradually become a hot issue in the intersection of ecological environment and foreign trade. “Embodied carbon emissions” has also become an indispensable research field (Hu et al. 2022). Therefore, the following research can focus on the new situation of international trade and study the hidden carbon emissions.

## References

Cao Z, Wei J, Chen HB (2016) $CO_2$ emissions and urbanization correlation in China based on threshold analysis. Ecol Indic: Integr Monit Assess Manag 61(2):193–201

Chen ST, Zhang KH, Zhang YW (2021) Measurement and decoupling effect of agricultural carbon emission performance. Stat Decis 22:85–88

Michel DE, Hanna F, Niklas H (2016) Greenhouse gas emissions from current and enhanced policies of China until 2030: can produce emissions peak before 2030. Energy Policy 89:224–236

Dunnan L, Bowen X (2018) Can China achieve its carbon emission peaking? A scenario analysis based on STIRPAT and system dynamics model. Ecol Ind 93:647–657

Guo P, Li J, Kuang J, Zhu Y, Xiao R, Duan D, Huang B (2022) Low-carbon governance, fiscal decentralization and sulfur dioxide emissions: evidence from a quasi-experiment with Chinese heavy pollution enterprises. Sustainability 14(6):3220

Hai W, Fu WD, Wang KY (2011) Establishing an enterprise energy management system to promote carbon emission reduction. In: Proceedings of the 13th annual conference of China association for science and technology—ways to reduce carbon dioxide emission intensity per unit GDP by 40–45% in 2020, pp 133–137

Hu JB, Wang KW, Zhang ZY (2022) Bibliometric analysis of China's trade and carbon emissions based on CiteSpace. J Hangzhou Norm Univ (Soc Sci) (01):91–102

Li GY, Zhou CB, Li NN et al (2022) Suggestions on the construction and improvement of the national carbon emission trading market. Environ Prot (08):45–49

Liu YX, Deng XR (2021) An empirical study on influencing factors of carbon emissions in China: based on fixed-effect panel quantile regression model. J Shanxi Univ (philos Soc Sci Ed) 06:86–96

Liu FF, Huang QP, Liu WP (2018) The relationship between regional economic growth and regional carbon emissions—based on the environmental Kuznets model. J Cent South Univ For Technol (Soc Sci Ed) 12(4):20–26+35

Liu ZM, Huang XJ, Lu XH et al (2022) China's carbon neutral path prediction under the shared socio-economic path. J Geogr (09):2189–2201

Lu HY, Zhang XY (2022) Experience of international carbon verification system construction and its enlightenment to China. Ecol Econ 09:1–14

Marcotullio PJ, Rothenberg S, Nakahara M (2013) Globalization and urban environmental transitions. Comparison of New York's and Tokyo's experiences. Ann Reg Sci 37(3):369–390

Menegaki AN, Tsounis N, Agiomirgianakis GM (2022) The economic impact of climate change (CC) on the Greek economy. Environ Dev Sustain Multidiscip Approach Theory Pract Sustain Dev 24(6):8145–8161

Sun ZL, Bian C, Chu ZP, Wang H (2021) Evolution simulation of carbon emission regulation and enterprise low-carbon technology innovation from the perspective of government regulation. Ind Tech Econ 12:103–112

Sun H, Tariq G, Chen H, Zhu J, Liu Y, Wu C (2018) Allocation of carbon emission quotas to Chinese power enterprises. Energy Procedia 152:115–124

Tan YF, Wang L (2022) China's low-carbon economic growth path: a literature review. Econ Spec Zones (01):157–160

Tang SI, Fu JW, Wu JL (2021) Analysis of influencing factors of carbon emissions in typical cities of China. Stat Dec 23:59–63

Tong X, Li XS (2017) Literature review on regional carbon emissions and emission reduction paths. Explor Econ Probl(01):169–176

Wei D, Liu B, Duan Z et al (2022) Measuring local progress of the 2030 Agenda for SDGs in the Yangtze River Economic Zone, China. Environ Dev Sustain Multidiscip Approach Theory Pract Sustain Dev 24(5):7178–7194

Wu HY (2021) Development path selection of China's low-carbon economy under high-quality development. Sci Technol Econ Mark (01):64–66

Xiao J, Zhang XH (2015) Study on driving carbon emission factors in eastern China under spatial effect. J Harbin Univ Commer (soc Sci Ed) 6:110–116

Xue LM, Zheng ZX, Meng S et al (2022) Carbon emission efficiency and spatio-temporal dynamic evolution of the cities in Beijing-Tianjin-Hebei region, China. Environ Dev Sustain Multidiscip Approach Theory Pract Sustain Dev 24(6):7640–7664

# Chapter 20
# Remediation Strategies of Cd Contaminated Soil in Mining Areas


**Zhi-cheng Dong, Yi-hong Li, Yan-qin Sun, Li-na Zhang, and Bing-xin Dong**

**Abstract** As a global problem, soil Cd pollution in mining areas seriously endangers the natural environment, ecosystem and human health. How to repair Cd contaminated soil in mining areas with low cost, high efficiency and fast speed is still a hot and difficult problem to be studied and solved. Hence, the latest physical, chemical, biological and combined strategies and technologies are summarized for Cd contaminated soil remediation in mining areas. It will aid to provide useful references and theoretical basis for remediation of heavy metal contaminated soils.

**Keywords** Remediation of contaminated soil · Cd · Strategies · Methods

## 20.1 Introduction

According to the National Soil Pollution Survey Bulletin published by Ministry of Environmental Protection & Ministry of Land and Resources of China in 2014, 33.4% of the sample sites in seventy surveyed mining areas exceeded the national standard. Moreover, pollution of Cd, As and Pb etc. in the soil around the nonferrous metal mining areas was relatively serious. This leads to serious soil environmental problems in industrial and mining wastelands. Indeed, heavy metals in "three wastes" of mining industry have serious impacts and harms on the environment. Under the dual influence of natural action and human activities, they will migrate, transform and enrich in soils around the mining area (Peipei et al. 2022). This makes the soil around the mining area an important "sink" of heavy metals. Meanwhile, these

Z. Dong · Y. Li · L. Zhang (✉) · B. Dong
School of Geographic Sciences and Tourism, Jiaying University, Meizhou 514015, Guangdong, China
e-mail: zhanglina_2005@126.com

Z. Dong · L. Zhang
Guangdong Provincial Key Laboratory of Conservation and Precision Utilization of Characteristic Agricultural Resources in Mountainous Areas, Jiaying University, Meizhou 514015, Guangdong, China

Y. Sun
Hebei Vocational College of Resources and Environment, Shijiazhuang 050085, Hebei, China



Z. Yang (ed.), *Environmental Science and Technology: Sustainable Development*, Environmental Science and Engineering, https://doi.org/10.1007/978-3-031-27431-2_20

soil heavy metals around the mining area will enter the biological chain under the action of supergene geochemistry and biology, and affect the ecosystem and human health through biomagnification (Yumei et al. 2017). Among these heavy metals, Cd is one of the key food pollutants listed and studied by the World Health Organization. The International Agency for Research on Cancer (IARC) also classified it as a human carcinogen. The Agency for Toxic Substances and Disease Registry (ATSDR) listed it as the 7th hazardous substance to human health. Therefore, remediation of Cd-contaminated soil around mining areas has extremely important practical significance.

Like other pollutants, there are two main remediation principles for Cd contaminated soil around mining areas (Dermont et al. 2008). The first is to remove Cd from polluted soil for soil remediation and cleaning. The second is to change its mobility and bioavailability to make it less toxic or non-toxic, so as to reduce the ecological hazards and environmental risks. Based on these two principles, the current commonly used remediation strategies or technologies mainly include: physical, chemical, biological remediation and combined methods of them (Juan et al. 2022). These remediation strategies or technologies have been well studied and developed in recent decades (Beatrice and Olusola 2020; Marques et al. 2009; Pilon-Smits 2005; Huifen et al. 2020). The latest progresses and achievements are summarized as follows.

## 20.2 Physical Remediation

Physical remediation refers to remove heavy metal pollutants by physical strategies or technologies such as soil removal, soil replacement, deep tillage, isolation and embedding, verification, etc. It is the earliest method used in the field of heavy metal contaminated soil remediation (Peipei et al. 2022). Physical remediation has advantages of simplicity and rapidity, but it also has disadvantages of high cost, large quantities and damages to soil structure (Juan et al. 2022). Compared to other physical remediation strategies or technologies, deep tillage is simpler and less cost. It is mainly applied to those slightly contaminated soils (Juan et al. 2022). However, replacement of some or all soil is still suitable for heavily contaminated soils (Peipei et al. 2022). It is an efficient physical strategy or technology by cleaning up or diluting soil Cd with advantages of mature technology and complete remediation, and disadvantages such as the large investment, the huge works, and easily causing of soil fertility damage (Peipei et al. 2022). As shown in Table 20.1 by Jiang et al. (Jiang et al. 2021), when the contaminated soil was mixed with replacement soil, contents of chlorophyll increased with the mix dosages (0, 20, 35 and 50% (w/w), namely S0, S20, S35 and S50), by the times from 1.75 to 1.81. However, contents of MDA, total and available Cd decreased with the mix dosages, by the times from 0.91 to 0.76, from 0.88 to 0.73 and from 0.95 to 0.86, respectively. Thus, as one of the physical remediation, soil replacement aids to plants growth and soil Cd cleaning.

**Table 20.1** Contents of chlorophyll (Chl a and Chl b), MDA, total and available Cd changing with soil replacement (S0, S20, S35 and S50, stand for contaminated soil mixed with the replacement soil of different dosages, such as 0, 20, 35 and 50% (w/w)). R, S and A stand for radish, soybean and amaranth, respectively

| Groups | Chl a mg/g FW | | | Chl b mg/g FW | | | MDA μmol/L FW | | | Soil Cd mg/kg | |
|---|---|---|---|---|---|---|---|---|---|---|---|
| | R | S | A | R | S | A | R | S | A | Total | Available |
| S0 | 2.78 | 3.25 | 6.46 | 1.52 | 1.86 | 2.18 | 1.76 | 2.34 | 1.38 | 0.52 | 0.22 |
| S20 | 6.96 | 8.34 | 9.59 | 2.46 | 2.17 | 2.58 | 1.44 | 2.03 | 1.46 | 0.46 | 0.21 |
| S35 | 7.05 | 8.64 | 9.65 | 2.42 | 2.22 | 2.45 | 1.17 | 1.97 | 1.21 | 0.42 | 0.19 |
| S50 | 6.87 | 8.56 | 10.50 | 2.38 | 2.57 | 2.57 | 1.13 | 1.56 | 1.33 | 0.38 | 0.19 |

## 20.3 Chemical Remediation

Chemical remediation mainly includes chemical leaching and chemical fixation. The former is an effective, rapid remediation strategy suitable for large contaminated sites. It mainly weakens the chemical activity, mobility or biological toxicity of soil Cd by changing the chemical species. As known, Cd is just temporarily fixed in soils, but is not fundamentally eliminated from soils. The latter is to eliminate Cd and clean soils by using inorganic cleaning agents, chelating agents or surfactants to transfer Cd from the solid phase to the liquid phase. Undoubtedly, chemical remediation has advantages of high efficiency and short time. However, there are also some disadvantages such as high cost, non-permanent remediation, causing possible damage to soil properties and secondary pollution (Adamo et al. 2014).

### *20.3.1 Chemical Leaching*

Chemical leaching remediation of Cd contaminated soil is to remove soil Cd by applying eluents to wash soils and to make Cd flows out with the eluents. At present, there are three categories of commonly used eluents.

The first type is inorganic eluent, such as water (Andrés and Francisco 2010), inorganic acid (Moutsatsou et al. 2006; Tomoyuki et al. 2006), inorganic salts (Tomoyuki et al. 2006) and ferric chloride (Tomoyuki et al. 2006; Xiaofang et al. 2016)), such as hydrochloric acid, sulfuric acid, nitric acid, phosphoric acid, calcium chloride, etc. It is revealed that the possible mechanisms of inorganic acids leaching soil Cd could include ion exchange and dissolution etc., while those of inorganic salts are complexation etc. Moutsatsou et al. found that 1 M HCl was more effective to eliminate 47% of total metals after 4 h mixing than other inorganic acids and $Na_2EDTA$ (Moutsatsou et al. 2006). Tomoyuki et al. found that 0.1 mol/L $CaCl_2$ could extract about 30% (As shown in Fig. 20.1) of total soil Cd when the soil-solution ratio was 1:1.2 (Tomoyuki et al. 2006). This was attributed to the successive formation of

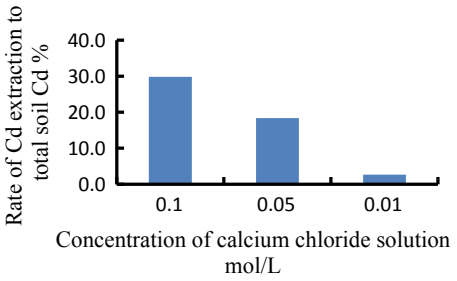


**Fig. 20.1** Percentage of extracted Cd by calcium chloride solutions of different concentrations under the soil/solution ratio (w/v) of 1:1.2. According to Tomoyuki et al. (2006)

Cd-Cl complexes in the extracts of $CaCl_2$ and the decrease of the exchangeable and acid-soluble Cd fractions by these complexes.

The second type is organic chelating agents (Dermont et al. 2008), such as citric acid (Xin et al. 2020), acetic acid (Haiyin et al. 2021), EDTA (Qiang et al. 2020), EGTA (Apostolos et al. 2009), DTPA (Apostolos et al. 2009), GLDA (Lirong et al. 2022), etc. The main mechanism of these chelating agents efficiently removing soil Cd is to change Cd from insoluble states to soluble ones by forming stable chelates with Cd ions in soil solution (Fig. 20.2). Unfortunately, some chelating agents may affect the ecological function of soil owing to their poor biodegradability. It was found that Cd removal efficiency of batch leaching reached a maximum value of 89.1% by using citric acid at a concentration of 0.1 M and a pH of 5 (Xin et al. 2020). Haiyin et al. found that acetic acid allowed 91.8% Cd removal (Haiyin et al. 2021). It was revealed that the extraction efficiency for Cd decreased in order of NTA > EGTA > DTPA (Apostolos et al. 2009). It was found that in spite of removing Cd and lowering the human and environmental hazards of the remediated soil, EDTA could extract the trace elements those were essential for soil biota and decrease soil enzyme activity significantly (Masa and Domen 2014). Hence, when selecting chelating agents for soil leaching, their potential impacts on soil properties and structures, together with the subsequent application for contaminated sites should be evaluated.

The third type is surfactants, such as Brij-35, Tween 80 (Luis et al. 2012), dodecyl sulfate (SDS) (Jinhui et al. 2018), sodium dodecyl benzene sulfonate (SDBS) (Ge et al. 2022), saponin (Zygmunt and Ewa 2012), rhamnolipid (Ruijie et al. 2020), Triton X-100 (TX-100) (Jinhui et al. 2018), and other macromolecular organics with

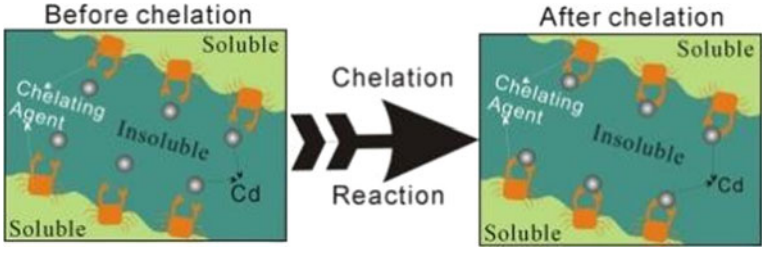


**Fig. 20.2** Reaction mechanism of chelating agent and Cd

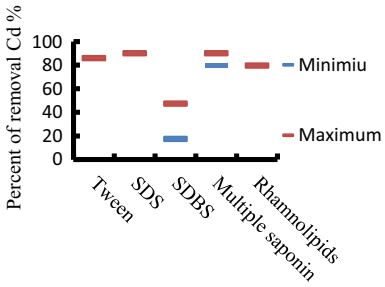


**Fig. 20.3** Percent of removal Cd by different surfactants such as Tween 80 (Luis et al. 2012), SDS (Jinhui et al. 2018), SDBS (Ge et al. 2022), multiple saponin (Zygmunt and Ewa 2012) and rhamnolipids (Ruijie et al. 2020)

both hydrophilic and lipophilic groups. It was found that Cd removal by Tween 80 could reach 85.9% (Luis et al. 2012). And almost 90% of Cd was removed when SDS concentration was merely 4 mmol/L (Jinhui et al. 2018). Ge et al. suggested that modified SDBS could be used as a promising effective passivation agent for Cd remediation, since its maximum adsorption capacity of $Cd^{2+}$ could be 241.39 mg/g and DTPA extracted Cd content could decrease by 17.41–47.33% (Ge et al. 2022). Result revealed 80–90% of soil Cd could be eliminated by single washing with multiple saponin (Zygmunt and Ewa 2012). Result demonstrated that rhamnolipids could desorb Cd(II) from the minerals with a maximum desorption of 79.6%, hence, they were applicable for enhancing the release of cationic metals associated with minerals in the bioremediation process via washing (Ruijie et al. 2020). It was illustrated that the main mechanism of leaching heavy metal contaminated soil with rhamnolipid solution was the formation of rhamnolipid-heavy metal complex (Mulligan et al. 1999). Although surfactants have good performances in dealing with Cd pollution (Fig. 20.3), there are still some problems to be solved (Wenjun and Lizhong 2004). For example, compared with biosurfactants, chemical surfactant residues could cause secondary pollution to soil and endanger soil health. And sometimes, the treatment effect of single surfactant is not good enough.

### *20.3.2 Chemical Fixation*

As one of Cd contaminated soil remediation strategies, chemical fixation is to change the physical and chemical properties or chemical species of soil Cd by using solidified materials, so as to minimize the toxicity, bioavailability and mobility. At present, the widely used materials include phosphate compounds (Rong et al. 2022), biochar (Yumei et al. 2017; Meili et al. 2022), clay mineral (Beatrice and Olusola 2020), silicate wastes (Huifen et al. 2020), sewage sludge (Muhammad et al. 2022) and composts (Song et al. 2020), etc. Results showed that using phosphate compounds such as calcium magnesium phosphate (CMP), calcium superphosphate (SSP), triple superphosphate (TSP), diammonium phosphate (DAP), and phosphate rock (PR) etc. during soil remediation, could significantly decrease the bioavailability of soil Cd (Rong et al. 2022; Usarat and Chongrak 2009; Carne et al. 2021). This should be

attributed to their effects on soil bacterial community, soil available Cd content, and Cd accumulation in plants (Rong et al. 2022; Lei et al. 2019). It was also found that biochar (BC) could significantly reduce the acid-soluble Cd contents in soils of three different contaminated levels, with the maximum reduction ratio of more than 20%. This should be related to the significant increases of soil pH, soil organic matter, cation exchange capacity, and the activities of catalase, but decrease of the richness and diversity of bacterial communities (Meili et al. 2022). As shown in Fig. 20.4, Lijuan et al. found that application of 5% sulfur modified chicken manure biochar (SCMB) decreased bioavailable Cd in soil and Cd accumulation of *brassica chinensis* shoots by 33.01% and 20.78%, since its maximum $Cd^{2+}$ adsorption capacity was 188.20 mg/kg. The mechanism should include ion exchange, complexation, precipitation and $C_{\pi}$-Cd (Lijuan et al. 2022). Junhao et al. suggested that the sintering red mud-biochar composite had generally better effects on immobilizing the soil-borne trace elements compared to the Bayer red mud-biochar composite (Junhao et al. 2022). Results showed that use of sepiolite could be an adequate strategy to immobilization remediation of Cd contaminated soils, since treatments of sepiolite decreased availability of soil Cd by 15.2–47.8% (Penggang et al. 2021). It was found that modified sepiolite also had a more excellent passivation effect on available Cd in soil with the passivation rate of 36.83–48.46%, and it could be employed as an effective agent for immobilization remediation of Cd contaminated soil (Sha et al. 2020). Huifen et al. supposed that four typical silicate wastes such as straw ash (SA), coal fly ash (CFA), ferronickel slag (FNS) and blast-furnace slag (BFS) decreased the content of available Cd in soil (Huifen et al. 2020). Song et al. found that the decrease of Cd availability by compost addition led to a reduction of Cd content in roots and leaves, decrease of Cd content in pakchoi cabbage and the BCF of leaves (Song et al. 2020). Muhammad et al. concluded that using sewage sludge (SS-2%) could reduce the potential mobility of heavy metals while increasing the residual fraction in polluted soils (Muhammad et al. 2022).

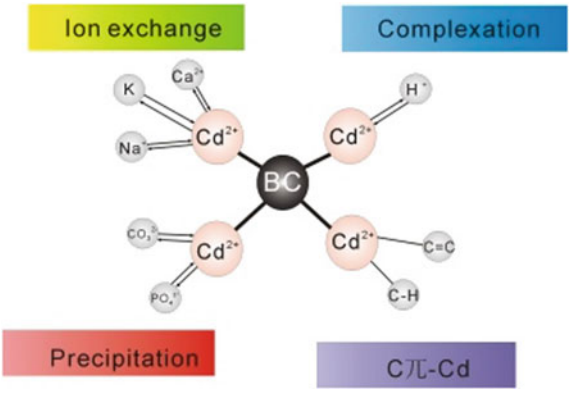


**Fig. 20.4** Mechanism of SCMB decreasing bioavailable Cd in soil: modified according to Lijuan et al. (2022)

## 20.4 Bioremediation

Compared with other remediation technologies, bioremediation has advantages of cost saving, no secondary pollution and small environmental disturbance. Therefore, bioremediation of heavy metal contaminated soil has broad application prospects (Li et al. 2022). At present, bioremediation technologies mainly include phytoremediation, microbial remediation and animal remediation. Among them, phytoremediation and microbial remediation are mainly studied and used. In particular, phytoremediation has become a potential bioremediation technology due to its low cost, easy implementation and environmental friendliness (Mahdi et al. 2022). Phytoremediation of Cd contaminated soil is a remediation technology that uses specific plants to absorb, transfer and enrich Cd to reduce soil Cd concentration (Marques et al. 2009). This remediation technology includes plant extraction, plant fixation and rhizosphere filtration (Purakayastha and Chhonkar 2009). Plant extraction, as the main technology, is to use Cd-hyperaccumulator to absorb soil Cd and transport it to shoots, so as to completely remove Cd from soil. Nevertheless, it is undeniable that phytoremediation also has some limitations, such as slow plant growth, long remediation cycle and low efficiency (Li et al. 2022; Qixing and Yufang 2018), together with difficulty in remediation plants selection and in large scale application (Pilon-Smits 2005), etc.

In recent decades, great progress has been gained in phytoremediation studying. For example, many Cd-hyperaccumulators have been selected and breed, such as *Brassica napus* (Zhongwei et al. 2022), *Solanum nigrum L.* (Marie-Laure et al. 2021), *sedum alfredii* (Yuankun et al. 2022), *Thlaspi caerulescens* (Lotfollah et al. 2012), *Lantana camara L.* (Shiliang et al. 2019), *Arabidopsis halleri* (Maximilian et al. 2022), *Arabidopsis arenosa* (Żaneta et al. 2021), *Sphagneticola calendulacea* (Ruirui et al. 2022), *Arabidopsis halleri ssp. Gemmifera* (Christine et al. 2022), *Microsorum pteropus* (Xinyu et al. 2020), *Solanum melongena* (Jiakang et al. 2020), *Arabidopsis halleri* (Filis and Hendrik 2020), *B. juncea* (Zhongwei et al. 2022), *Bidens pilosa L.* (Yuebing et al. 2009), *Solanum photeinocarpum* (Xingfeng et al. 2011), *Arabis paniculata* (Xiaowen et al. 2011), *hytolacca americana* (Le et al. 2011), *Arthrocnemum macrostachyum* (Susana et al. 2010), etc. Although these Cd-hyperaccumulators can significantly accumulate soil Cd, most of them have disadvantages such as small biomass, slow growth and easy to be restricted by regional climate (Wei and Chen 2001). Hence, some non-hyperaccumulators of fast growing, well developed roots, good adaptability and strong resistance, are usually applied for Cd contaminated soil phytoremediation. For instance, the phytoremediation ability and efficiency of ryegrass in Cd contaminated soil were discussed and demonstrated by Hui et al. (Hui et al. 2021). It is found that ryegrass could effectively decrease soil Cd contents by accumulating Cd in the roots (27.82 mg/kg) and stems (10.25 mg/kg) with the biological accumulating coefficient (BAC) and biological transfer coefficient (BTC) of 2.16 and 0.37, respectively (Hui et al. 2021). Guirong et al. found that ryegrass (*Lolium perenne L.*) growing in soils with Cd content of 16.8 mg/kg represented higher germination rate and biomasss than tall fescue (*Festuca arundinacea*

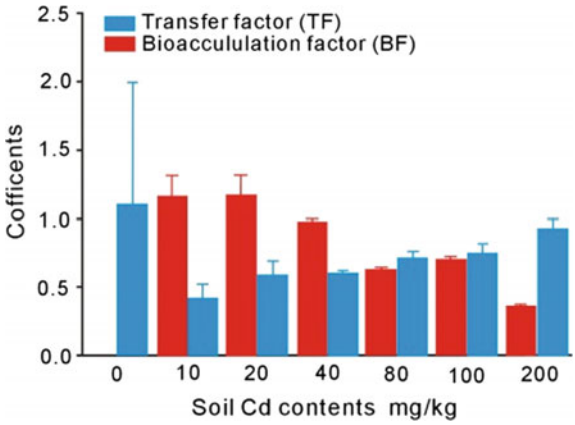


**Fig. 20.5** Transfer factor (TF) and bioaccumulation factor (BF) of Cd by *H. annuus* grown on Cd contaminated soils: according to Qin et al. (2019)

*Schreb.*), alfalfa (*Medicago sativa L.*) and white clover (*Trifllium repens L.*) (Guirong et al. 2021). As shown in Fig. 20.5, Qin et al. found that Cd contents of the guttation fluids that the tall fescue (*Festuca arundinacea*) excreted were 0.4–0.8 mg/L from the emerging leaves and 0.88–1.07 mg/L from the mature leaves (Qin et al. 2019). It was attributed that leaf hydathodes were the pathway of Cd excretion in tall fescue (Qin et al. 2019). Based on leaf hydathodes excreting 5.122 mg Cd onto the leaf surface per plant in 75 days, the calculated annual soil Cd removal amount could be 14.4% (Qin et al. 2019). Khalid et al. suggested that *H. annuus* could be able for Cd uptake and for the remediation of Cd contaminated soils, since its TF was higher than 1 when the soil Cd content was lower than 20 mg/kg (Khalid et al. 2018).

## 20.5 Combined Remediation

Conventional physical, chemical or biological remediation has more or less defects, such as the high cost, poor effect and low efficiency (Qixing and Yufang 2018), etc. Therefore, the combined remediation of Cd contaminated soil in mining areas is very popular at present (Andrew et al. 2007). The combined remediation is usually dominated by bioremediation, supplemented by chemical and physical methods, such as gene technology-assisted phytoremediation, microorganism-assisted phytoremediation, chemical-assisted phytoremediation, etc. It should be noted that the combined remediation is not a simple superposition of various technologies, but have a synergistic effect on the remediation efficiency (Li et al. 2022; Andrew et al. 2007).

In the field of gene technology-assisted phytoremediation, scholars have focused on exploring and studying the key genes and proteins that absorb, transport and accumulate heavy metals in plants at the molecular level, and using them to improve the phytoremediation ability. On the one hand, studies in this field mainly focus on the editing of metal transporter genes. For instance, result showed that the natural resistance-associated macrophage protein (Nramp) in *Solanum nigrum L.* could help

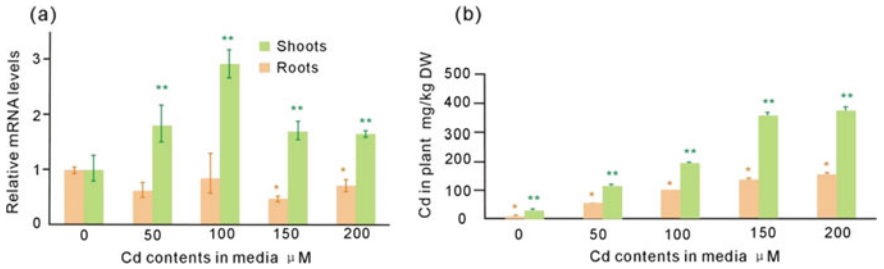


**Fig. 20.6** NRAMP mRNA expression (**a**) and Cd contents (**b**) in *Solanum nigrum L.* exposed to Cd. Error bars stands for the standard deviation of the data. Results represent three replicate samples for each of three independent experiments. Significant difference between treat and untreated is marked by a single asterisk (*) and significant difference between treatment is marked by double asterisks (**). Modified and according to Song et al. (2014)

Cd cross the plasma membrane, i.e. high expression of Nramp gene could increase Cd absorption and transportation of *Solanum nigrum L.*, and the Nramp gene expression in shoots was closely related to the Cd accumulation in that part (as demonstrated in Fig. 20.6) when Cd contents in media was lower than 100 mg/kg (Song et al. 2014). Therefore, changing the expression amount or expression mode by editing the genes of Nramp and other protein families, the heavy metal (such as Cd etc.) absorption and tolerance of plants can be affected (Yang et al. 2019). On the other hand, studies in this field also focus on improving the remediation ability by implanting genes responsible for regulating phytochelatin synthases (PCSs) and metal ligands into plants (Basharat et al. 2018). For example, research showed that inserting the PCS gene (IpPCS1) from Ipomoea pes-caprae into Arabidopsis thaliana, could improve its cadmium (Cd) tolerance (Su et al. 2020). Hence, it is potential in improving the Cd phytoremediation capacity of plants.

As to microorganism-assisted phytoremediation, the phytoremediation efficiency can be improved mainly in two ways. First, rhizosphere microorganisms promote plant growth to improve phytoremediation efficiency by enhancing plant absorption of nutrients and plant resistance to pathogens, together with synthesizing growth factors (Walton and Anderson 1990). For instance, Wan et al. found that when seeds were inoculated with endophyte *serratia nematodiphila* LRE07, the antioxidative enzymes activities of *Solanum nigrum L.* were improved, and the uptake of essential mineral nutrition were enhanced (Wan et al. 2012). This made the *Solanum nigrum L.* grew more vigorously (as shown in Fig. 20.7), and improved the Cd enrichment ability of *Solanum nigrum L.* Tan et al. revealed that PGPR addition significantly could increase the shoot and root biomasses of ryegrass by 43.53–90.29% in soil Cd content of 30 mg/kg (Tan et al. 2021). Second, except for affecting the chemical species of heavy metals (such as Cd etc.) by changing the physical and chemical properties of soil, rhizosphere microorganisms can also activate (chelate, acidolysis, oxidation, reduction, complexation, adsorption, desorption etc.) heavy metals by secreting and releasing chelating agents, organic acids, surfactants and other substances, and enhance their migration and transformation ability as well as

bioavailability by changing their chemical species to make them more easily absorbed by plants, and to improve the phytoremediation efficiency (Nadeem et al. 2017). For example, result revealed that inoculating the endophytic *Pseudomonas fluorescens* in the root soil of *Sedum alfredii H* could promote the growth and Cd absorption, and could improve the phytoremediation efficiency. This is mainly due to the activation of soil CdO by a variety of low molecular weight organic acids such as malic acid, citric acid, oxalic acid and acetic acid produced by the endophytic bacterium *Pseudomonas fluorescens* during its growth and metabolism (Deng et al. 2016).

There are two main ways of chemical-assisted phytoremediation. On the one hand, using chemical modifiers, growth regulators or acid–base regulators, such as red mud, urban sludge, hydrated lime, sepiolite, bone charcoal, phosphate rock powder, zeolite, biochar etc., can not only adsorb heavy metals and reduce their harm to plants (Saqib et al. 2020), but also regulate the physical and chemical properties and nutritional conditions of soil and improve the soil environment (Heeraman et al. 2001). This will aid to promote plant growth (Fangdong et al. 2019) and to improve the phytoremediation efficiency (Heeraman et al. 2001; Yasir et al. 2019; Xu et al. 2019). For instance, result demonstrated that cornstalk biochar reduced the DTPA-extractable Cd concentration and stimulated the dry root weight of *Beta vulgaris var. cicla L.* increased by more than 1.5 folds, together with the Cd accumulation in *Beta vulgaris* increased by more than one fold (Gu et al. 2020). Other result showed that extra biochar additions increased the biomass of *Medicago sativa L.*

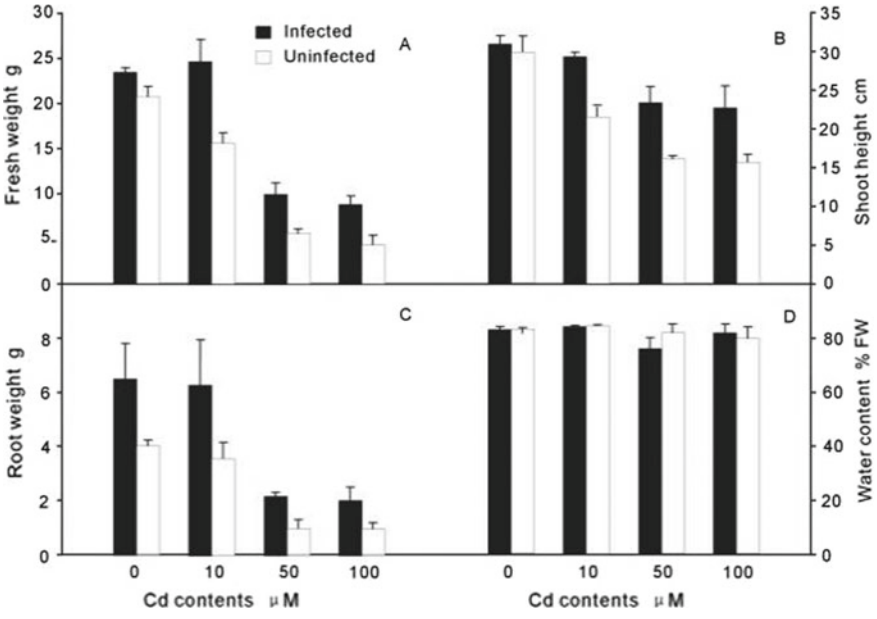


**Fig. 20.7** Effects of *S. nematodiphila* LRE07 on plant growth of *Solanum nigrum L.* According to Wan et al. (2012)

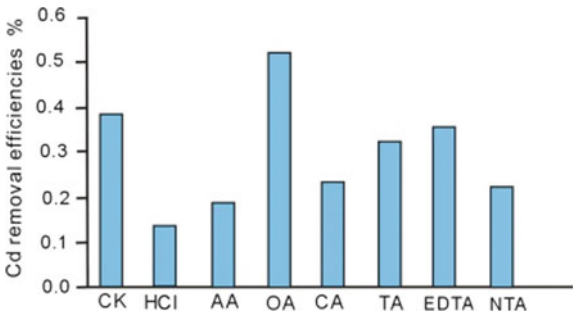


**Fig. 20.8** Cd removal efficiencies by chemical-assisted phytoremediation. According to Xiao et al. (2019)

(alfalfa) and the phytoextraction of Cd (Zhang et al. 2019). On the other hand, using chelating agents or surfactants such as ethylene diamine tetraacetic acid (EDTA), tetrasodium *glutamate diacetate (GLDA*), ethylene glycol tetraacetic acid (EGTA), ethylene diamine disuccinic acid (EDDS), nitrilotriacetic Acid (NTA), citric acid (CA), oxalic acid (OA), tartaric acid (TA), Tween 80, saponin, etc. (Song et al. 2008), could activate heavy metals such as Cd etc. by changing the surface charge and absorbed potential energy of soil, or by ion exchange, complexation, chelation and other actions, and could make them enter the soil solution to enhance their mobility and bioavailability (Tao et al. 2020), so as to improve the phytoremediation efficiency (Hu et al. 2017, 2020; Xiao et al. 2019). For instance, it was found that EDTA could increase Cd accumulation of Italian ryegrass (*Lolium perenne L.*) by 24% (Li et al. 2020). And as shown in Fig. 20.8, it was also shown that the efficiency of chemical-assisted phytoremediation of Cd followed the order of OA > EDTA > HCl > TA > CA > NTA > AA > HCl (Xiao et al. 2019).

## 20.6 Conclusions and Perspective

The global situation of soil Cd pollution is severe. So it is urgent to eliminate its impact and harm. Especially, the remediation of Cd contaminated soil in mining areas has been a hot and difficult issue to be solved. Although, various remediation strategies and technologies have been studied and amazing progress and development were gained in recent decades. Among these strategies and technologies, there are still more or less defectives in terms of cost, environmental protection, simplicity and large-scale application, etc. Hence, some problems still need to be solved in the remediation strategies and technologies of Cd contaminated soil in mining areas. Such as:

(1) Research and development of cheap, environment-friendly and simple green remediation agent.
(2) Research and development of synergistic combined remediation technologies with multiple methods and means.

(3) Research and development of combined remediation technology that could improve soil while remediation.
(4) Research and development of remediation strategies that take into account the safety of water, soil, atmosphere, biology and other media and supergene environment.
(5) Research on safe disposal strategies and method of remediation wastes.

**Acknowledgements** This study was supported by Guangdong Basic and Applied Basic Research Foundation (2020A1515011077, 2022A1515012010), Scientific Research Projects of Jiaying University (2020KJY05, 2019KJY05), Yantai Key Research and Development Plan (2019XDHZ103), the Key Research Foundation of Education Department of Guangdong Province of China (2021ZDZX4046).

## References

Adamo P, Mingo A, Coppola I, Motti R, Stinca A, Agrelli D (2014) Plant colonization of brownfield soil and post-washing sludge: effect of organic amendment and environmental conditions. Int J Environ Sci Technol 12(6):1811–1824

Andrés N, Francisco M (2010) The use of soil-flushing to remediate metal contamination in a smelting slag dumping area: column and pilot-scale experiments. Eng Geol 115(1–2):16–27

Andrew CS, Thomas B, Chloe AH, Smithc JAC, Ian PT (2007) Phytoremediation of mixed-contaminated soil using the hyperaccumulator plant Alyssum lesbiacum: evidence of histidine as a measure of phytoextractable nickel. Environ Pollut 147(1):74–82

Apostolos G, Arism N, Despina P, Evangelos G (2009) Chelating agent-assisted electrokinetic removal of cadmium, lead and copper from contaminated soils. Environ Pollut 157(12):3379–3386

Basharat Z, Novo L, Yasmin A (2018) Genome editing weds CRISPR: what is in it for phytoremediation? Plants 7(3):51

Beatrice OO, Olusola OO (2020) A review on the application of clay minerals as heavy metal adsorbents for remediation purposes. Environ Technol Innov 18:100692

Carne G, Leconte S, Sirot V, Breysse N, Badot PM, Bispo A, Deportes IZ, Dumat C, Rivière G, Crépet A (2021) Mass balance approach to assess the impact of cadmium decrease in mineral phosphate fertilizers on health risk: the case-study of French agricultural soils. Sci Total Environ 760:143374

Christine DAPW, Chihiro I, Mei-Fang C (2022) HMA4 and IRT3 as indicators accounting for different responses to Cd and Zn by hyperaccumulator Arabidopsis halleri ssp. Gemmifera. Plant Stress 2:100042

Deng P, Zhang X, Long X (2016) Effects of acid producing endophytic bacteria pseudomonas fluorescens R1 on the growth responses, Zn and Cd accumulation in *sedum alfredii*. Chin J Environ Eng 10(9):5245–5254 (In Chinese with English abstract)

Dermont G, Bergeron M, Mercier G, Richer-Laflèche M (2008) Soil washing for metal removal: a review of physical/chemical technologies and field applications. J Hazard Mater 152(1):1–31

Fangdong Z, Wenzeng Z, Xingchao Y, Bo L, Tianguo L, Yanqun Z, Ming J, Yuan L (2019) Field experiment on the effects of sepiolite and biochar on the remediation of cd- and pb-polluted farmlands around a pb-zn mine in yunnan province, china. Environ Sci Pollut Res Int 26(8):7743–7751

Filis M, Hendrik K (2020) Direct inhibition of photosynthesis by Cd dominates over inhibition caused by micronutrient deficiency in the Cd/Zn hyperaccumulator Arabidopsis halleri. Plant Physiol Biochem 155:252–261

Ge G, Sha X, Shunan Z, Yingming X, Yuebing S (2022) Two-step modification (sodium dodecylbenzene sulfonate composites acid-base) of sepiolite (SDBS/ABsep) and its performance for remediation of Cd contaminated water and soil. J Hazard Mater 433:128760

Gu P, Zhang Y, Xie H, Wei J, Lou X (2020) Effect of cornstalk biochar on phytoremediation of cd-contaminated soil by *Beta vulgaris* var. Cicla L. Ecotoxicol Environ Saf 205:111144

Guirong L, Zongshuo W, Yujing L, Shengyong J, Fukai C, Yinbo L, Long H (2021) Effect of culturing ryegrass (Lolium perenne L.) on Cd and pyrene removal and bacteria variations in co-contaminated soil. Environ Technol Innov 24:101963

Haiyin X, Peiling Z, Qiyang R, Wenjuan L, Ping W, Yuanling L, Chao H, Xiong Y, Jingxuan Y, Ruiqi Z (2021) Enhanced electrokinetic remediation for Cd-contaminated clay soil by addition of nitric acid, acetic acid, and EDTA: effects on soil micro-ecology. Sci Total Environ 772:145029

Heeraman DA, Claassen VP, Zasoski RJ (2001) Interaction of lime, organic matter and fertilizer on growth and uptake of arsenic and mercury by zorro fescue (vulpia myuros l.). Plant Soil 234(2):215–231

Hu X, Liu X, Zhang X, Cao L, Chen J, Yu H (2017) Increased accumulation of Pb and Cd from contaminated soil with *Scirpus triqueter* by the combined application of NTA and APG. Chemosphere 188:397–402

Hu N, Chen S, Lang T, Zhang H, Ding D (2020) A novel method for determining the adequate dose of a chelating agent for phytoremediation of radionulides contaminated soils by *M. Cordata.* J Environ Radioact 227(10):106468

Hui X, Yuhan M, Yuying W, Fengxia S, Ruiyuan L, Xin L, Yuxin X (2021) Biological response and phytoremediation of perennial ryegrass to halogenated flame retardants and Cd in contaminated soils. J Environ Chem Eng 9(6):106526

Huifen Y, Ge Z, Peng F, Zhen L, Wenkai M (2020) The evaluation of in-site remediation feasibility of Cd-contaminated soils with the addition of typical silicate wastes. Environ Pollut 265(Part B):114865

Jiakang R, Wen Z, Hongbin W, Haijuan W, Qinchun L (2020) Indole-3-acetic acid promotes cadmium (Cd) accumulation in a Cd hyperaccumulator and a non-hyperaccumulator by different physiological responses. Ecotoxicol Environ Saf 191:110213

Jiang S, Dai G, Zhou J, Zhong J, Liu J, Shu Y (2021) An assessment of integrated amendments of biochar and soil replacement on the phytotoxicity of metal(loid)s in rotated radish-soya bean-amaranth in a mining acidy soil. Chemosphere 287:132082

Jinhui H, Hua L, Guangming Z, Lixiu S, Yanling G, Yahui S, Bi T, Xuemei L (2018) Removal of Cd (II) by MEUF-FF with anionic-nonionic mixture at low concentration. Sep Purif Technol 207:199–205

Juan DA, Enzo ER, Juliana MS, Stefanie BC, Analía Á, Claudia SB, Marta AP (2022) The current approach to soil remediation: a review of physicochemical and biological technologies, and the potential of their strategic combination. J Environ Chem Eng 10(2):107141

Junhao Q, Xi W, Mujuan D, Huashou L, Chuxia L (2022) Red mud-biochar composites (co-pyrolyzed red mud-plant materials): characteristics and improved efficacy on the treatment of acidic mine water and trace element-contaminated soils. Sci Total Environ 844:157062

Khalid AA, Berhan A, Graham B (2018) Phytoremediation of Pb and Cd contaminated soils by using sunflower (*Helianthus annuus*) plant. Ann Agric Sci 63(1):123–127

Le Z, Yongle S, Suxia C, Mei C, Haomeng Y, Huimin L, Tuanyao C, Fang H (2011) Cd-induced changes in leaf proteome of the hyperaccumulator plant *Phytolacca americana.* Chemosphere 85(1):56–66

Lei S, Zhaohui G, Chi P, Xiyuan X, Wenli F, Bo H, Hongzhen R (2019) Immobilization of cadmium and improvement of bacterial community in contaminated soil following a continuous amendment with lime mixed with fertilizers: a four-season field experiment. Ecotoxicol Environ Saf 171:425–434

Li W, Dongguang Y, Rongjian C, Fang M, Gen W (2022) How a functional soil animal-earthworm affect arbuscular mycorrhizae-assisted phytoremediation in metals contaminated soil? J Hazard Mater 435:128991

Li FL, Qiu YH, Xu XY, Yang F, Wang J (2020) EDTA-enhanced phytoremediation of heavy metals from sludge soil by Italian ryegrass (*Lolium perenne L.*). Ecotoxicol Environ Saf 191:110185

Lijuan S, Peiyun G, Yafei S, Qin Q, Ke S, Jing Y, Hong Z, Bin Z, Yong X (2022) Modified chicken manure biochar enhanced the adsorption for $Cd^{2+}$ in aqueous and immobilization of Cd in contaminated agricultural soil. Sci Total Environ 851(Part 2):158252

Lirong L, Dinggui L, Yayin L, Xuexia H, Yu L, Lezhang W, Tangfu X, Qihang W, Guowei L (2022) Risk assessment of groundwater pollution during GLDA-assisted phytoremediation of Cd- and Pb-contaminated soil. Ecol Ind 139:108913

Lotfollah K, Hermann H, Broder JM (2012) Effect of microbial siderophore DFO-B on Cd accumulation by *Thlaspi caerulescens* hyperaccumulator in the presence of zeolite. Chemosphere 88(6):683–687

Luis GT, Rosario BL, Margarita B (2012) Removal of As, Cd, Cu, Ni, Pb, and Zn from a highly contaminated industrial soil using surfactant enhanced soil washing. Phys Chem Earth Parts a/b/c 37–39:30–36

Mahdi P, Mohammad A, Pegah F, Paridokht A, Matin M (2022) Recent progress on sustainable phytoremediation of heavy metals from soil. J Environ Chem Eng 10(5):108482

Marie-Laure P, Blanche C, Emmanuel D, Perrine C, Till F, Clément L, Catherine K, Jérôme R (2021) X-ray absorption spectroscopy evidence of sulfur-bound cadmium in the Cd-hyperaccumulator *Solanum nigrum* and the non-accumulator *Solanum melongena.* Environ Pollut 279:116897

Marques APGC, António OSSR, Paula MLC (2009) Remediation of heavy metal contaminated soils: phytoremediation as a potentially promising clean-up technology. Crit Rev Environ Sci Technol 39(8):622–654

Masa J, Domen L (2014) Effect of EDTA washing of metal polluted garden soils. Part I: toxicity hazards and impact on soil properties. Sci Total Environ 475:132–141

Maximilian VBK, Hassan A, Michael S, Ute K, Uwe K (2022) Elemental bioimaging of Zn and Cd in leaves of hyperaccumulator Arabidopsis halleri using laser ablation-inductively coupled plasma-mass spectrometry and referencing strategies. Chemosphere 305:135267

Meili X, Weijie D, Zilin Z, Jiatong Z, Fei H, Chuang M, Shuting H, Chufan L, Peng W, Rongbo X (2022) Effect of rice straw biochar on three different levels of Cd-contaminated soils: Cd availability, soil properties, and microbial communities. Chemosphere 301:134551

Moutsatsou A, Gregou M, Matsas D, Protonotarios V (2006) Washing as a remediation technology applicable in soils heavily polluted by mining–metallurgical activities. Chemosphere 63(10):1632–1640

Muhammad SR, Guijian L, Balal Y, Yasir H, Abdul R, Mehr AMM, Muhammad A, Rafay A, Yu S (2022) Assessing the influence of sewage sludge and derived-biochar in immobilization and transformation of heavy metals in polluted soil: Impact on intracellular free radical formation in maize. Environ Pollut 309:119768

Mulligan CN, Yong RN, Gibbs BF, James S, Bennett H (1999) Metal removal from contaminated soil and sediments by the biosurfactant surfactin. Environ Sci Technol 33(21):3812–3820

Nadeem S, Muhammad I, Muhammad RS, Wajid I, Muhammad AK, Amar M, Abdur R, Saddam H (2017) Phytoremediation strategies for soils contaminated with heavy metals: modifications and future perspectives. Chemosphere 171:710–721

Peipei S, Dan X, Jingyuan Y, Yuanchen M, Shujun D, Jing F (2022) Recent advances in soil remediation technology for heavy metal contaminated sites: a critical review. Sci Total Environ 838(Part3):156417

Penggang P, Yuebing S, Lin W, Xuefeng L, Yingming X (2021) In-situ stabilization of Cd by sepiolite co–applied with organic amendments in contaminated soils. Ecotoxicol Environ Saf 208:111600

Pilon-Smits E (2005) Phytoremediation. Annu Rev Plant Biol 56:15–39

Purakayastha TJ, Chhonkar PK (2009) Phytoremediation of heavy metal contaminated soils. Soil Heavy Metals 16:389–429

Qiang M, Wanfu Z, Dong-Xing G, Henry HT, Junfeng J, Lena QM (2020) Comparing $CaCl_2$, EDTA and DGT methods to predict Cd and Ni accumulation in rice grains from contaminated soils. Environ Pollut 260:14042

Qin D, Ling F, Cheng W, Shuai H, Zhaolong W (2019) Cadmium excretion via leaf hydathodes in tall fescue and its phytoremediation potential. Environ Pollut 252(Part B):1406–1411

Qixing Z, Yufang S (2018) Principles and methods of contaminated soil remediation. Science Press, Beijing (in Chinese)

Rong H, Yanqiong L, Feng L, Xiuling Y, Ran L, Zhimin W, Xuefeng L, Zhian L (2022) Phosphate fertilizers facilitated the Cd contaminated soil remediation by sepiolite: Cd mobilization, plant toxicity, and soil microbial community. Ecotoxicol Environ Saf 234:113388

Ruijie Y, Haibing W, Meimei S, Yongguang J, Yiran D, Liang S (2020) Biosurfactant rhamnolipid affacts the desorption of sorbed As(III), As(V), Cr(VI), Cd(II) and Pb(II) on iron (oxyhydr)oxides and clay minerals. Int Biodeterior Biodegradation 153:105019

Ruirui L, Zunhe H, Qilei Z, Yuqi L, Min L, Xianling W, Xueni W, Jieting Y, Liqin Z, Yuanxiao J, Changlian P (2022) The effect of Funneliformis mosseae on the plant growth, Cd translocation and accumulation in the new Cd-hyperaccumulator Sphagneticola calendulacea. Ecotoxicol Environ Saf 203:110988

Saqib B, Umeed A, Muhammad S, Allah BG, Javaid I, Shahbaz K, Arif H, Niaz A, Sajid M, Muhammad K, Hongqing H (2020) Role of sepiolite for cadmium (Cd) polluted soil restoration and spinach growth in wastewater irrigated agricultural soil. J Environ Manag 258:110020

Sha X, Lin W, Yingming X, Dasong L, Yuebing S, Shunan Z (2020) Performance and mechanisms of immobilization remediation for Cd contaminated water and soil by hydroxy ferric combined acid-base modified sepiolite (HyFe/ABsep). Sci Total Environ 740:140009

Shiliang L, Shafaqat A, Rongjie Y, Jianjun T, Bo R (2019) A newly discovered Cd-hyperaccumulator *Lantana camara L.* J Hazard Mater 371:233–242

Song SS, Zhu LZ, Zhou WJ (2008) Simultaneous removal of phenanthrene and cadmium from contaminated soils by saponin, a plant-derived biosurfactant. Environ Pollut 156(3):1368–1370

Song L, Xiangyang S, Yuanxin L, Suyan L, Jiali Z (2020) Remediation of Cd-contaminated soils by gwc application, evaluated in terms of cd immobilization, enzyme activities, and pakchoi cabbage uptake. Environ Sci Pollut Res 27(9):76–83

Song Y, Hudek L, Freestone D, Puhui J, Michalczyk AA, Senlin Z, Ackland ML (2014) Comparative analyses of cadmium and zinc uptake correlated with changes in natural resistance-associated macrophage protein (NRAMP) expression in *Solanum nigrum L.* and *Brassica rapa.* Environ Chem 11(6):653–660

Su H, Zou T, Lin R, Zheng J, Jian S, Zhang M (2020) Characterization of a phytochelatin synthase gene from Ipomoea pes-caprae involved in cadmium tolerance and accumulation in yeast and plants. Plant Physiol Biochem 155:743–755

Susana RG, Enrique MN, Luis AM (2010) Accumulation and tolerance characteristics of cadmium in a halophytic Cd-hyperaccumulator, *Arthrocnemum macrostachyum.* J Hazard Mater 184(1–3):299–307

Tan K, Guangyu G, Junrong L, Chao Z, Yue T, Panpan W, Yanhong X, Lanzhou C (2021) Improvement of the Cu and Cd phytostabilization efficiency of perennial ryegrass through the inoculation of three metal-resistant PGPR strains. Environ Pollut 271:116314

Tao Q, Li J, Liu Y, Luo J, Xu Q, Li B, Li Q, Li T, Wang C (2020) *Ochrobactrum intermedium* and saponin assisted phytoremediation of Cd and B[a]P co-contaminated soil by Cd-hyperaccumulator *Sedum alfredii*. Chemosphere 245:125547

Tomoyuki M, Kazuo S, Yasuhiro S, Hiroyuki T, Takashi K, Kouta S, Tadashi I, Naoki S (2006) Remediation of cadmium contamination in paddy soils by washing with chemicals: selection of washing chemicals. Environ Pollut 144(1):2–10

Usarat T, Chongrak P (2009) Evaluation of phosphate fertilizers for the stabilization of cadmium in highly contaminated soils. J Hazard Mater 165(1–3):1109–1113

Walton BT, Anderson TA (1990) Microbial degradation of trichloroethylene in the rhizosphere: potential application to biological remediation of waste sites. Appl Environ Microbiol 56(4):1012
Wan Y, Luo S, Chen J, Xiao X, Chen L, Zeng G, Liu C, He Y (2012) Effect of endophyte- infection on growth parameters and Cd- induced phytotoxicity of Cdhyperaccumulator Solanum nigrum L. Chemosphere 89(6):743–750
Wei CY, Chen TB (2001) Research progress on heavy metal hyperaccumulator plants and phytoremediation technology. Acta Ecol Sin 21(7):1196–1203 (in Chinese)
Wenjun Z, Lizhong Z (2004) Solubilization of pyrene by anionic–nonionic mixed surfactants. J Hazard Mater 109(1–3):213–220
Xiao R, Ali A, Wang P, Li R, Tian X, Zhang Z (2019) Comparison of the feasibility of different washing solutions for combined soil washing and phytoremediation for the detoxification of cadmium (Cd) and zinc (Zn) in contaminated soil. Chemosphere 230:510–518
Xiaofang G, Zebin W, Qitang W, Chunping L, Tianwei Q, Wei Z (2016) Effect of soil washing with only chelators or combining with ferric chloride on soil heavy metal removal and phytoavailability: field experiments. Chemosphere 147:412–419
Xiaowen Z, Rongliang Q, Rongrong Y, Yetao T, Lu T, Xiaohang F (2011) The differentially-expressed proteome in Zn/Cd hyperaccumulator *Arabis paniculata* Franch. in response to Zn and Cd. Chemosphere 82(3):321–328
Xin K, Feijie Z, Yan Z, Haijun Z, Guanlin G, Yu T (2020) Removal of Cd, Pb, Zn, Cu in smelter soil by citric acid leaching. Chemosphere 255:126690
Xingfeng Z, Hanping X, Zhian L, Ping Z, Bo G (2011) Identification of a new potential Cd-hyperaccumulator Solanum photeinocarpum by soil seed bank-metal concentration gradient method. J Hazard Mater 189(1–2):414–419
Xinyu L, Qishuang H, Bin Y, Yunyun Y, Xinyuan L, Fuliu X (2020) Influence of Cd exposure on $H^+$ and $Cd^{2+}$ fluxes in the leaf, stem and root of a novel aquatic hyperaccumulator—*Microsorum pteropus*. Chemosphere 249:126552
Xu M, Gao P, Yang Z, Su L, Wu J, Yang G, Xiaohongk Z, Jing M, Hong P, Yinlong X (2019) Biochar impacts on phosphorus cycling in rice ecosystem. Chemosphere 225:311–319
Yang CH, Zhang Y, Huang CF (2019) Reduction in cadmium accumulation in *japonica* rice grains by CRISPR/Cas9-mediated editing of *OsNRAMP5*. J Integr Agric 18:688–697
Yasir H, Lin T, Muhammad IS, Xuerui C, Bilal H, Muhammad ZA, Muhammad U, Zhen-li H, Xiaoe Y (2019) An explanation of soil amendments to reduce cadmium phytoavailability and transfer to food chain. Sci Total Environ 660:80–96
Yuankun L, Min L, Daniel PP, Jipeng L, Yongchao L, Tingqiang L (2022) The involvement of nitric oxide and ethylene on the formation of endodermal barriers in response to Cd in hyperaccumulator *Sedum alfredii*. Environ Pollut 307:119530
Yuebing S, Qixing Z, Lin W, Weitao L (2009) Cadmium tolerance and accumulation characteristics of *Bidens pilosa L.* as a potential Cd-hyperaccumulator. J Hazard Mater 161(2–3):808–814
Yumei H, Kate VH, Wolfgang FH (2017) The use of red mud as an immobilizer for metal/metalloid-contaminated soil: a review. J Hazard Mater 325:17–30
Żaneta G, Krzysztof S, Paulina ZR, Michał S, Magdalena RJ, Adam R, Małgorzata R, Eugeniusz M (2021) Ecophysiology of *Arabidopsis arenosa*, a new hyperaccumulator of Cd and Zn. J Hazard Mater 412:125052
Zhang M, Wang J, Bai SH, Zhang Y, Teng Y, Xu Z (2019) Assisted phytoremediation of a co-contaminated soil with biochar amendment: contaminant removals and bacterial community properties. Geoderma 348:115–123
Zhongwei Z, Zong-Lin D, Qi T, Hong-Qian P, Fan W, Yu-Fan F, Xin-Yue Y, Pei-Zhou X, Yun L, Chang-Quan W, Yang-Er C, Ming Y, Ting L, Xiao-Yan T, Guang-Deng C, Jian Z, Shu Y (2022) Salicylate and glutamate mediate different Cd accumulation and tolerance between *Brassica napus* and *B. juncea.* Chemosphere 292:133466
Zygmunt MG, Ewa K (2012) Metal (Cu, Cd and Zn) removal and stabilization during multiple soil washing by saponin. Chemosphere 86(4):383–391

# Part V
# Wastewater Treatment and Utilization

# Chapter 21
# Utilization of Three Typical Urban Solid Wastes


**Chaoyi Gan, Yihan Jiang, Zirou Zhang, and Renrui Liu**

**Abstract** This chapter focuses on the resource utilization of solid waste and provides an effective method for the utilization of the three typical urban solid wastes. This method integrates various processes for treating sludge, plastics and kitchen waste, and performs different treatments on three kinds of solid wastes and generates value. The maximum total profit generated under different treatment processes is calculated by establishing a mathematical model. This method is applied to a case study of New York City, and a method of using New York City water treatment to generate solid waste is designed. Since carbon emission, an important environmental problem, needs to be considered when using solid wastes, and the profit maximization and carbon emission minimization are also sought, this paper analyzes three scenarios: Scenario 1: trade-off will be made between the total economic profit and carbon emission using multiple objective function. Scenario 2: Carbon tax policy in New York is taken into account. Scenario 3: Regulations from RGGI is taken into account. The research on the three scenarios shows that when the profit is high, the carbon emissions are often high. The carbon tax proposal can effectively promote carbon reduction, but it greatly reduces the total profit; The RGGI carbon market model does not reduce the total profit but has no effect in controlling carbon emissions. The secondary market of RGGI is not considered in this paper and needs further research.

**Keywords** Urban solid wastes · Water treatment · Carbon emission · Economy circular

C. Gan
College of Natural Resources and Environment, South China Agricultural University, Guangzhou 510642, China

Y. Jiang (✉)
Department of International, Changjun High School, Changsha 410013, China
e-mail: hunter789654@gmail.com

Z. Zhang
Experimental High School Attached to Beijing Normal University, Beijing 100032, China

R. Liu
College of Environmental Engineering, University of Nottingham Ningbo China, Ningbo 315199, China



Z. Yang (ed.), *Environmental Science and Technology: Sustainable Development*, Environmental Science and Engineering, https://doi.org/10.1007/978-3-031-27431-2_21

## 21.1 Introduction

Nowadays, there are plenty of solid wastes in cities. For example, urban residents discharge large amounts of wastes into the environment in their daily life, which are mainly kitchen waste and plastics (Hongying and Bo 2019). Besides, most water treatment processes use activated sludge process, an effective water treatment method, but this method will produce a large amount of waste sludge after sewage treatment (Wei and Dajiang 2013). How to deal with the above-mentioned solid waste and properly utilize it as a resource is indeed a thought-provoking problem. If these solid waste resources are effectively utilized, not only can solid waste pollution get reduced, but additional benefits can also be obtained. Without a proper utilization plan, solid wastes will cause serious environmental pollution and resource loss.

The above three solid wastes have a wide range of treatment processes and uses. Sludge can be composted to produce fertilizer, calcined into building materials such as ceramsite, and pyrolyzed into pyrolysis fuel (Li et al. 2022); Plastic can be incinerated and pyrolyzed (Xingcai et al. 2022), it can also be recycled to make a new plastic; kitchen waste can also be composted to produce fertilizer, be incinerated and pyrolyzed (Liu et al. 2021), and can be anaerobically digested (Pollution Control Department, Ministry of Natural Resources and Environment 2004).

The research topic of this paper is similar to the design of *urban biorefinery* for waste processing to integrate the recycling process of plastic and paper, focusing on the three typical solid wastes generated in cities: kitchen waste, plastic and sludge. Combined with the environmental background and public policy of New York City, this paper proposes a method to use these solid wastes, with integrating processes, and conduct different treatment of the three kinds of solid wastes and generate value. The research method of this paper also refers to the superstructure optimization approach in *urban biorefinery* for waste processing, by establishing the mathematical model to calculate and the total profit of the three solid wastes under different processes, then the maximum total profit of each treatment process can be obtained. In addition, in the process of using solid waste, by fully considering the problem of energy conservation and emission reduction, our model should produce as much profit as possible and at the same time effectively reduce carbon emissions. Reducing carbon emissions will become an important constraint for the use of solid waste technology, and the establishment of a carbon trading market or carbon tax can conduct more in-depth and specific research on carbon emissions.

## 21.2 Optimized Methods for Using the Three Typical Urban Solid Wastes

### *21.2.1 Problem Statement*

Since the types of solid waste produced in cities vary and the treatment processes of each solid waste are different, the model designed must be able to process all the waste. Therefore, the utilization of solid waste in urban water treatment can be expressed as following: given a variety of waste flows in a particular city, find the optimal combination of processes that properly treat the resources contained in each part of streams, and finally obtain useful energy and material products under certain constraints.

The design of treatment model can not only minimize and control the pollution of solid waste in cities, but also reuse it as resources. However, this method is limited by the constraints of environmental background and public policies in specific cities. How to maximize the output value of waste under the constraints is another important problem that we need to explore in this method. This question will be explored in detail in the case study. Besides, carbon emissions will be specifically studied in the case study section, exploring how policies like carbon trading market and carbon tax can have impact on the model.

Sets:

S: process.
W: waste stream.
P: product.
R: utility.

Parameter:

$Cheat$ heat cost.
$Cel$ electric cost.
$Cr$ utility cost.
$Es$ annualized capital cost of process S.
$Irs$ utility requirement of process S.
$Vel$ electricity selling price.
$Vh$ heat selling price.
$Vp$ price of product p.
$T$ total waste.
$Xw$ fraction of waste stream w.
$Yps$ product p's yield of process S.

Variables:

$Fs$ Total amount of waste flowing into process s.
$Fps$ Flow rate of product p from process s.
$FELss'$ flow rate of electricity supplied internally from process s to process s'.

$FHEss'$ flow rate of heat supplied internally from process s to process s'.
$Mws$ flow rate of waste fraction w to the process s.
$Xs's$ exchange flow rate from process s' to process s.

### *21.2.2 Methodology*

The methodology comprises three steps:

1. Waste streams to be treated are all identified and the processes for each are selected.
2. Through the technical and economic analysis of each processing technology, the processing technology was characterized.
3. Information will be added to the mathematical model. Different scenarios will have different location-specific data.

**Waste and Process Selected**. So far, three types of solid waste have been identified, namely kitchen waste, plastic and sludge. Then the treatment of each waste needs to be studied. The nature of each waste can be determined, the processing efficiency and technical and economic assessment information of the relevant process can be found, the existing plant operation mode can be investigated, and a preliminary summary can be made to select an effective process and technical solution.

The first waste stream to be considered is kitchen waste, which consists mainly of organic waste. According to its nature, it has been decided to use four different technologies (anaerobic digestion, short for AD in the text below, pyrolysis, incineration and composting) to treat this waste stream.

The second waste stream is sludge. Sludge was treated by composting, calcination and pyrolysis. The digestate produced by AD can be applied as fertilizer. The main product of composting is fertilizer. Power and heat resources can be recovered through incineration. The product of calcination is ceramsite, which can be sold. Pyrolysis oil can be obtained by pyrolysis.

The treatment of plastic should also be considered. Here are some ways to deal with plastic solid waste: 1. Recycled by mechanical means for reuse of plastic products. 2. Pyrolysis is a widely used recycling method. In this process, plastics are thermally cracked in an inert atmosphere to produce pyrolytic. 3. Incineration is an effective treatment. Plastic has a high calorific value, so it can generate a lot of heat and electricity that can be utilized.

**Description**. After determining the process, the next step is to describe the technical and economic characteristics. It is necessary to collect data on capital cost, namely the cost for machines used, raw material consumption, product price and so on for economic analysis.

For data in the tables, they come from a variety of different sources (PCDMNRE 2004; Ringer et al. 2006; World Bank 1999; Metropolitan Electricity Authority 2015; Electricity Generating Authority of Thailand 2015; Ruangrong 2012; Selder 1998; Metropolitan Waterworks Authority 2015; Valin 2001; Kramer et al. 2009; University

of Southern Indiana (USI) 2015; Van Oel and Hoekstra 2012; Natural Resources Canada (NRC) 2006; Planyc 2011). The operational costs and material consumption of the selected processes are shown in Table 21.1. The products and their prices are shown in Table 21.2. The capital costs are shown in Table 21.3. All data in the table are average value.

**Building the Superstructure**. With the choices in the previous sections, then put them all together in the superstructure in Fig. 21.1. Different proportions of waste are represented by index w and process is represented by s. The connection between the two is $Mws$, represents the flow rate of waste proportion w to process s, and

**Table 21.1** Utility requirement, other operating costs

| Utility and other operating costs for the processes selected | | | | | | | |
|---|---|---|---|---|---|---|---|
| Utility requirement | AD | Compost | Incineration | Calcination | Recycling | Pyrolysis | Price |
| 1. Eletricity (kW h/t) | 0 | 35 | 36.1 | 0 | 536 | 0 | 0.12$/kW h |
| 2. Water ($m^3$/t) | 12.4 | 0 | 0 | 0 | 1 | 14.43 | 1.3$/$m^3$ |
| 3. Heat (kW h/t) | 0 | 0 | 0 | 493.6 | 0 | 277.7 | 0.025$/kW h |
| 4. Diesel (L/t) | 0 | 2 | 0 | 0 | 0 | 0 | 0.51$/L |
| 5. Other operating cost ($/t) | 14.68 | 21.43 | 51.02 | 51.68 | 1.59 | 12.97 | / |

**Table 21.2** Products and prices

| Product yields obtained from 1 t of waste treated in each process technology and product prices | | | | | | | |
|---|---|---|---|---|---|---|---|
| Utility requirement | AD | Compost | Incineration | Calcination | Recycling | Pyrolysis | Price |
| 1. Eletricity (kW h) | 270 | 0 | 847 | 0 | 0 | 36.54 | 0.12$/kW h |
| 2. Heat (kW h) | 0 | 0 | 1784 | 0 | 0 | 0 | 0.025$/kW h |
| 3. Ceramic particles (t) | 0 | 0 | 0 | 0.5 | 0 | 0 | 300$/t |
| 4. Compost (t) | 0.27 | 0.415 | 0 | 0 | 0 | 0 | 150$/t |
| 5. Pyrolysis oil (t) | 0 | 0 | 0 | 0 | 0 | 0.392 | 411$/t |
| 6. Recycling plastic (t) | 0 | 0 | 0 | 0 | 0.676 | 0 | 371$/t |

**Table 21.3** Capital cost for one ton of waste treated in each process

| Capital cost for per ton of waste treated in each process | | | | | | |
|---|---|---|---|---|---|---|
| | AD | Compost | Incineration | Calcination | Recycling | Pyrolysis |
| Capital cost ($/ton) | 364.08 | 15.17 | 388.36 | 388 | 267 | 97.07 |

each process s can produce one or more products p. By the exchange of streams, it is possible to integrate between different processes.

**Mathematical Model**. Based on the design problem of solid waste treatment, the corresponding formula can be obtained by considering the system objective. For a given total waste ($T$), waste fraction ($Xw$), product price ($Vp$), utility costs ($Cr$), yield of product ($Yps$), utility requirements ($Irs$), the optimization problem can be formulated as:

Objective function.

Maximized Total Profit

$$\begin{aligned}&\sum\nolimits_{p\in P}\sum\nolimits_{s\in S} FsYps\ Vp + (Cel - Vel) \times \sum\nolimits_{s\in S'}\sum\nolimits_{s\in S} FELss' \\ &+(Cheat - Vh) \times \sum\nolimits_{s\in S'}\sum\nolimits_{s\in S} FHEss' - \sum\nolimits_{r\in R}\sum\nolimits_{s\in S} FsIrsCr \\ &-\sum\nolimits_{s\in S} FsEs\end{aligned} \tag{21.1}$$

$F_s$ is total amount of waste flowing into process s. $FEL_{ss'}$ and $FHE_{ss'}$ are flow rate of electricity and heat supplied internally from process s to process s', respectively. $C_{heat}$ and $C_{el}$ are heat cost and electric cost, respectively. $V_{el}$ and $V_h$ are electricity selling price and heat selling price, respectively. $E_s$ is annualized capital cost of process of s.

The optimization is influenced by the constraint equations below.

Waste stream balance

$$\sum\nolimits_{s\in S} Mws = Txw \tag{21.2}$$

where $M_{ws}$ is flow rate of waste fraction w to the process s. Streams of a certain type of waste into all processes are equal to total amount of waste of that type.

The balance for the electricity and heat produced and internally supplied are given in Eqs. (21.3) and (21.4), respectively.

$$\sum\nolimits_{s'\in S} FELss' \le FsYpw \tag{21.3}$$

Internal supply of electricity should be smaller than the electricity produced

$$\sum\nolimits_{s'\in S} FHEss' \le FsYpw \tag{21.4}$$

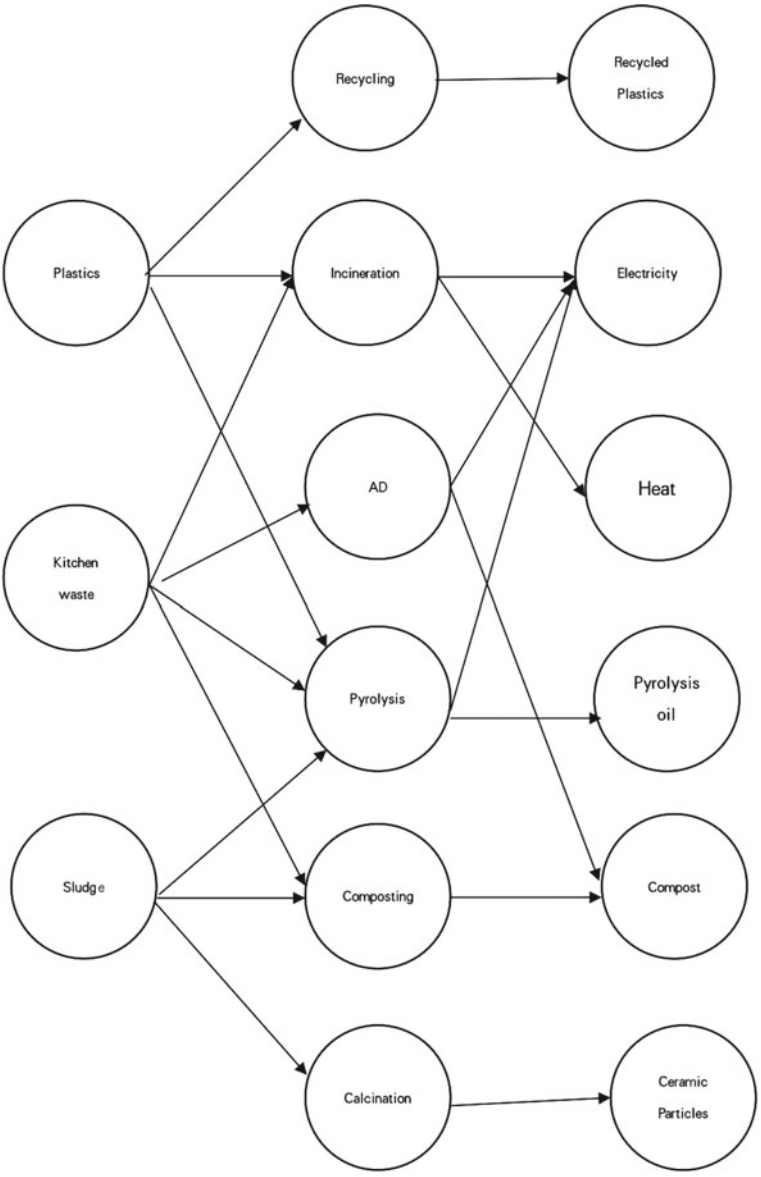


**Fig. 21.1** Superstructure

Internal supply of heat should be smaller than the heat produced.

The constraints for internally satisfying the electricity and heat demands are given in Eqs. (21.5) and (21.6), respectively.

$$\sum\nolimits_{s' \in S} FELss' = Fs'Irs' \tag{21.5}$$

Internal supply of electricity must meet the demand of all utility of electricity required by all processes

$$\sum\nolimits_{s' \in S} FHEss' = Fs'Irs' \tag{21.6}$$

Internal supply of electricity must meet the demand of all utility of heat required by all processes.

The following Fig. 21.2 shows the result of the model without policy.

All of sludge, 5,000,000 ton all flows to composting. All of the plastics, 18,000 ton all flows to incineration 1,037,620 ton of kitchen waste flows to composting, 1,298,286 tons of it flows to pyrolysis and 184,093 ton of it flows to incineration 171,172.900 MWh of electricity is yielded from incineration 360,534.2 MWh of heat is yielded from incineration 47,439.39 MWh of electricity is yield from pyrolysis 508,928 tons pyrolysis oil is yield from pyrolysis 2,505,612 ton of compost is yielded from composting.

## 21.3 Case Study: New York

New York, one of the most population-dense cities in the world, is a giant waste producer. The prosperous economy and culture of the city comes at a cost of huge amount of waste produced. In New York City alone the waste generated in a year reaches about 14 million tons. A good waste processing system can not only keep the huge amount of waste well disposed of but also gain a considerable amount of profit from selling the products of waste treatment.

See below for the Table 21.4 of carbon emitted by processing one ton of waste in each process:

Noticeably, as a State who has always been engaged in RGGI, Regional Greenhouse Gas Initiative, a cooperative and market-based program that aims to cap and reduce carbon emission, New York never stopped thinking about achieving carbon neutralization. Undoubtedly, it is important for New York to both live up to the economic potential of well treating the tremendous amount of waste and at the same time minimize the carbon emission, therefore achieving a sustainable way of development.

In this essay, three different scenarios in New York will be assessed for its effect in both achieving the economic potential and reducing the carbon emission.

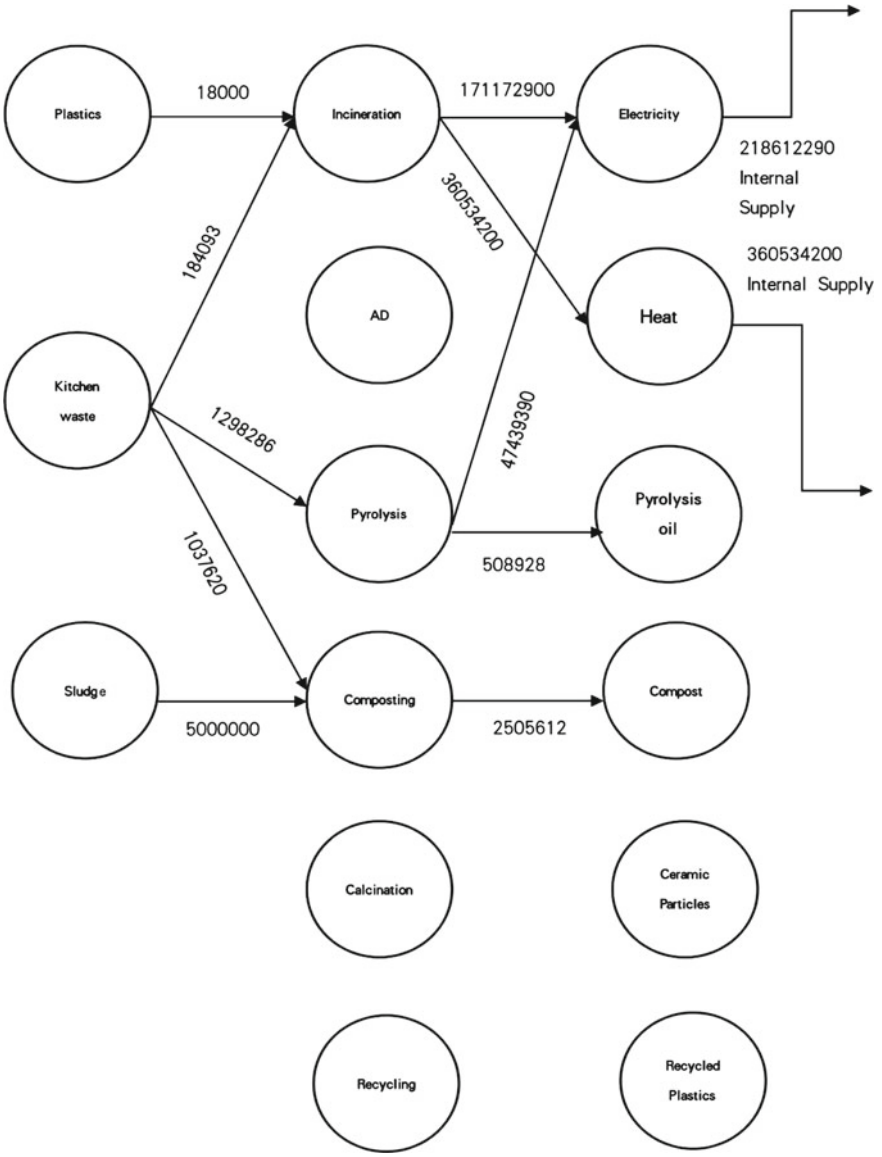


**Fig. 21.2** Result

**Table 21.4** Carbon emission for the processes selected

| | AD | Compost | Incineration | Calcination | Recycling | Pyrolysis |
|---|---|---|---|---|---|---|
| Carbon emission(t) | 1.3 | 0.057 | 1.2 | 1.2 | 1.973 | 2.1 |

Scenario 1: Trade-off will be made between the total economic profit and carbon emission using multiple objective function.

Scenario 2: Carbon tax policy in New York is taken into account.

Scenario 3: Regulations from RGGI is taken into account.

### 21.3.1 Scenario One: Making a Trade-Off Between Total Profit and Carbon Emission

It's hard to both satisfy high profit and low carbon emission at the same time, so there has to be a trade-off made between profit and carbon. In this scenario, a compromise will be made between profit and carbon emission by applying double objective function that can generate a Pareto Front.

In this scenario, there will be two different objective functions:

Objective function one:

$$\begin{aligned}&\text{Obj1: Total Profit} = \sum\nolimits_{p\in P}\sum\nolimits_{s\in S} FsYpsVp\\&+(Cel - Vel)\times\sum\nolimits_{s\in S'}\sum\nolimits_{s\in S} FELss' + (Cheat - Vh)\\&\times\sum\nolimits_{s\in S'}\sum\nolimits_{s\in S} FHEss' - \sum\nolimits_{r\in R}\sum\nolimits_{s\in S} F_sIrsCr - \sum\nolimits_{s\in S} FsEs\end{aligned} \tag{21.7}$$

Objective function two:

$$\text{Obj2: Carbon Emission } Ce = \sum\nolimits_{s\in S} FsTe \tag{21.8}$$

The real objective function that needs to be optimized in this scenario can be expressed as:

$$Obj3 = Obj1 \times w + (-Obj2 \times (1 - w)) \tag{21.9}$$

where w stands for weight, whose value ranges from 0 to 1, with increment of 0.1 each time (w = [0, 0.1, 0.2, …0.9, 1], a vector that contains 11 elements). Different weight means different priority on carbon emission and total profit. When the w = 0, minimizing carbon emission is given all the priority, while when w = 1, the total profit is given all the priority and profit is maximized. By changing the weight of each objective, a Pareto Front can be constructed where each dot represents a possible decision, reflecting different priority assigned to the two objectives.

The following Fig. 21.3 shows the result of Pareto Front of Total profit against (-Carbon emission).

As long as the weight is not 0, the carbon emission remains 3,313,055.745 ton and total profit remains 101,836,500$. When weight reaches 0, as minimizing carbon emission is given all the priority, the carbon emission becomes 786,159.309 ton and

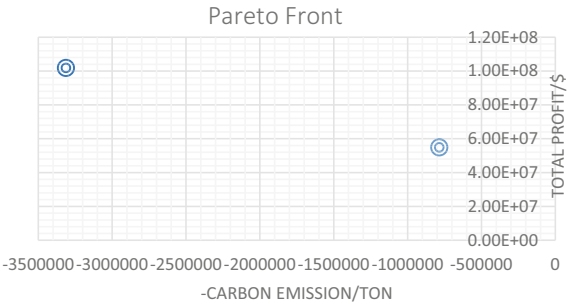


**Fig. 21.3** Pareto front

the total profit becomes 54,850,040 $. The Pareto Front suggests that without stimulus of policies, there are only two possible combinations, either the profit is maximized or the carbon emission is minimized.

### *21.3.2 Scenario Two: Carbon Tax*

**Introduction to Carbon Tax**. Fighting greenhouse gas emission is an effort that requires huge fund support. To solve potential problem of financial shortage, the idea of carbon tax starts to gain attention. A proposed $55 surcharge for one short ton of carbon dioxide emitted will be charged. The revenue from the tax is said to be directly funding environmental efforts.

In this scenario, the idea of carbon tax in the proposal will be taken into account. It is still unknown what difference the bill will make in reality. Therefore, through modelling a prediction can be made to see how waste treatment planning will be influenced by the proposed carbon tax.

**Modification of the Model and Result**. With carbon tax imposed, the total profit becomes:

$$\text{Carbon Emission } Ce = \sum\nolimits_{s\in S} FsTe \tag{21.10}$$

where $T_e$ stands for carbon emission of each process.

Total Profit

$$\begin{aligned} &\sum\nolimits_{p\in P}\sum\nolimits_{s\in S} FsYpsVp + (Cel - Vel) \\ &\times \sum\nolimits_{s\in S'}\sum\nolimits_{s\in S} FELss' + (Cheat - Vh) \times \sum\nolimits_{s\in S'}\sum\nolimits_{s\in S} \text{FHEss}, \\ &- \sum\nolimits_{r\in R}\sum\nolimits_{s\in S} FsIrsCr - FsEs - Ce \times Tc \end{aligned} \tag{21.11}$$

where $T_c$ stands for carbon tax for every one ton of carbon dioxide emitted, which is 60.4 $/t.

The following shows result of modelling:

The carbon tax is set to be 55 $ for one short ton (60.4 $/ton) of $CO_2e$ emitted. The total profit is 7.4 million $ and the $CO_2e$ emitted in this scenario is 786159 ton. All of sludge, 5,000,000 ton all flows to composting. All of the plastics, 18,000 ton all flows to incineration 2,226,107.341 ton of kitchen waste flows to composting and 293,892.659 ton of it flows to incineration 264,173,100 kWh of electricity is yielded from incineration 556,416,500 kWh of heat is yielded from incineration 2,998,834.547 ton of compost is yielded from composting. Internally, 163,877,300 kwh of electricity from incineration is used in composting, and 7,295,562.257 kWh is used back in incineration 47,439,390 kWh of electricity from pyrolysis is internally used in composting 360,534,200 kWh of heat from incineration is used internally in pyrolysis.

The following Fig. 21.4 shows the result of scenario 2, with carbon tax:

### *21.3.3 Scenario 3: Carbon Market*

**Introduction to Carbon Market**. To stimulate emission reductions, economists and policy makers have designed programs that aims at making reductions profitable. One of these programs is the carbon market, also known as the "cap-and-trade" program. Generally, the government sets the limit ("the cap") to the volume of carbon dioxide that can be emitted within a period of time, divides this volume into small units, assigns allowances, or credits, without which companies cannot emit carbon dioxide, to these units, and distributes or auctions these allowances to emitters (often companies). Emitters can trade the allowances in a secondary market. It's assumed that emitters would be encouraged to cut emissions, save allowances, and trade them in this market for profit.

Currently, many countries and confederations, such as the European Union and China, have adopted the carbon market scheme. New York is a member of the Regional Green House Gas Initiative (RGGI), an organization that enforces a regional cap-and-trade program on its member states. (Facts about RGGI) RGGI rules that all fossil fuel-fired power plants with a capacity of 25 MW or higher can only emit carbon dioxide if they have purchased the allowances in the primary auction or secondary trading market. Although the incineration, anaerobic digestion, and pyrolysis facilities in our model cannot be strictly regarded as "fossil fuel-fired power plants", and the other facilities cannot generate electricity, determining the potential effects of the carbon market on the results of the optimization model has the merit of producing a guideline on whether the RGGI should be imposed on waste treatment facilities.

**Modification of the Model and Results**. When the RGGI regulations are taken into account, the objective function of total profit is modified as follows, where $C_a$ stands for amount of carbon that the primary purchase of allowances at the auction allows the industry to emit, $P_a$ stands for the clearing price of the allowances in the auction, and $P_t$ stands for the price of the allowances in the secondary market:

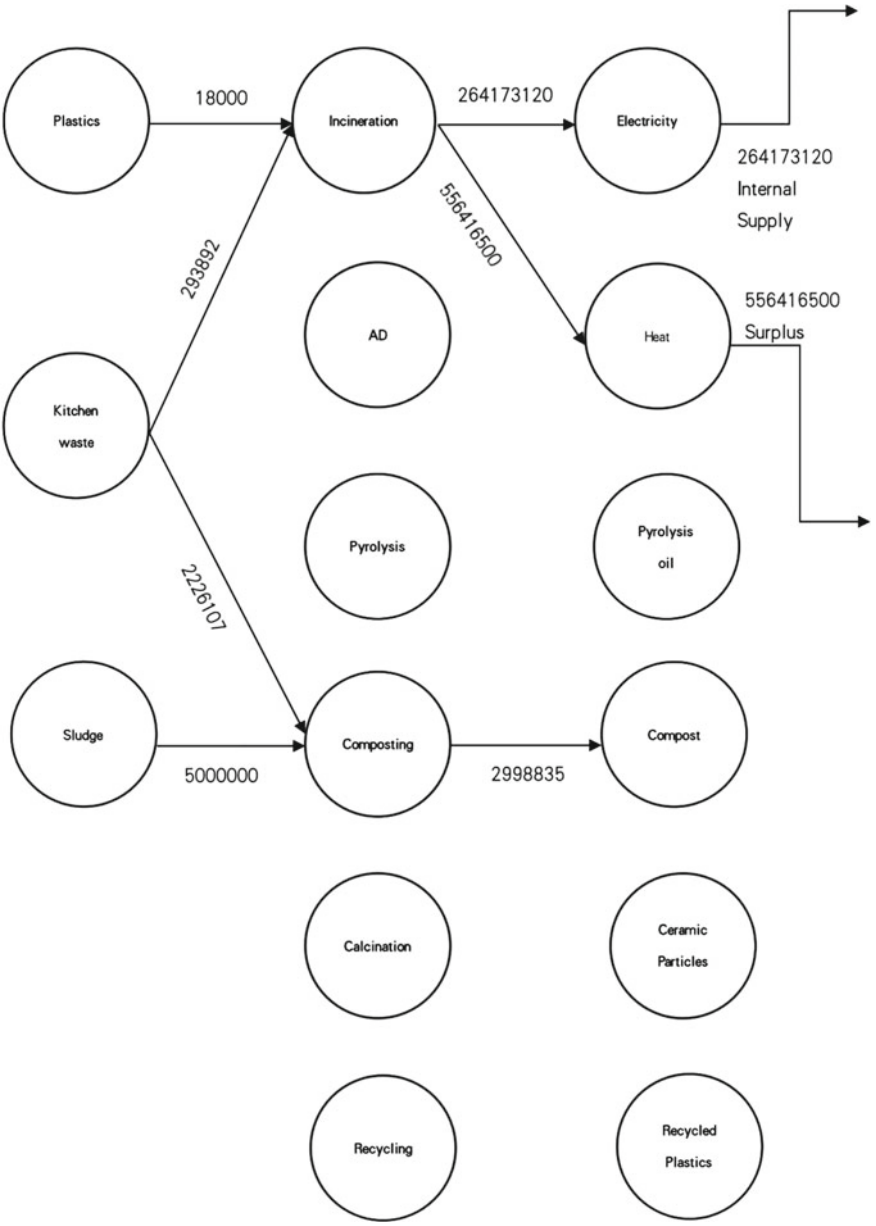


**Fig. 21.4** Scenario 2 result

$$\sum_{p\in P}\sum_{s\in S} FsYpsVp + (Cel - Vel) \times \sum_{s\in S'}\sum_{s\in S} \mathrm{FELss}' + (Cheat - Vh) \times \sum_{s\in S'}\sum_{s\in S} FHEss' - \sum_{r\in R}\sum_{s\in S} F_s IrsCr - \sum_{s\in S} \mathrm{Fs}Es - Ca \times Pa - (Ce - Ca) \times Pt \tag{21.12}$$

In the secondary market, the selling price of allowance cannot be determined unless the whole market is known. Therefore, this paper only considers the primary auction and its effects on the results of the optimization model. It assumes that the number of carbon allowances purchased in the auction is exactly the same as the number needed to emit all the carbon dioxide generated in the processes. The objective function is simplified as:

$$\sum_{p\in P}\sum_{s\in S} FsYpsVp + (Cel - Vel) \times \sum_{s\in S'}\sum_{s\in S} FELss' + (Cheat - Vh) \times \sum_{s\in S'}\sum_{s\in S} FHEss' - \sum_{r\in R}\sum_{s\in S} FsIrsCr - \sum_{s\in S} FsEs - Ce \times Pa \tag{21.13}$$

The clearing price of one allowance is found to be 13.00 $, when each allowance is assigned to one short ton of carbon emission. (eia. gov) The data is inputted, and the optimum solution yields an annual profit of 43,925,515.9570 $ and an annual carbon emission of 3,313,057.7453 tons, with 3,701,713.515 tons of sludge flowing into composting, 1,298,286.485 tons into pyrolysis; 18,000.000 tons of plastics into incineration; 2,335,906.863 tons of kitchen waste into composting, and 184,093.137 tons into incineration.

The following Fig. 21.5 shows the result of scenario 3, with carbon market.

### *21.3.4 Comparison*

Our model reveals that the carbon tax proposal will drastically lower both the profit (by approximately 93%) and carbon emission (by approximately 73%) if enacted, whereas the primary auction of RGGI has no effect on the amount of carbon dioxide emitted (both the basic scenario with no constraints and the scenario under the RGGI program have an annual carbon emission of 3,313,057.75 tons) but reduces the profit of the waste treatment industry significantly (by about 57%). The carbon tax proposal can be deemed unreasonable and impracticable, for although it cuts down a gigantic volume of carbon dioxide emissions, it diminishes the profit to its 7%. In contrast, the auction part of the RGGI program is ineffective in isolation, its overall consequence detrimental: the aggregate revenue of the companies and the government, earned from auctioning allowances, is lower than that of the scenario where the companies are not restrained by regulations. However, it's possible that the program as whole is useful in curbing emissions, since the secondary market, the more essential component, is not examined.

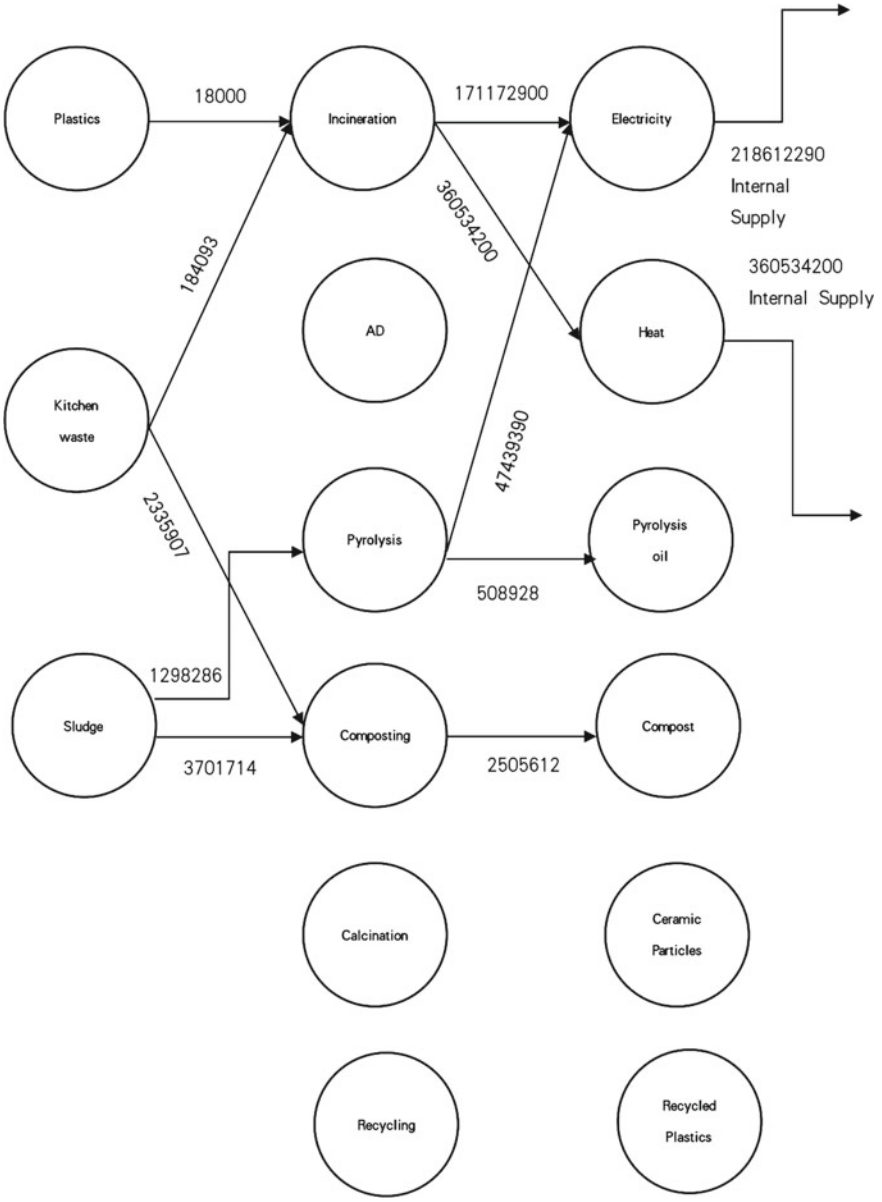


**Fig. 21.5** Scenario 3 result

## 21.4 Conclusions

In this paper, the feasibility of integrating the treatment of plastics, kitchen waste, and sludge is studied and proven. A model that can compare the different routes of their treatment and recommend the option that optimizes the profit is constructed and coded into GAMS. The model is applied to the state of New York. Since carbon dioxide emissions contribute significantly to climate warming, and waste treatment facilities are productive of carbon dioxide, the model is converted into a double objective model with the objectives of maximizing profit and minimizing carbon emissions. A Pareto front is constructed, which shows the trade-off between economic gain and emission control. Without regulations, the costs of cutting emissions are incompatible with companies' pursuit of profit. To determine and compare the effects of carbon emissions regulations, a proposal of carbon tax and the auction part of the RGGI carbon market are applied to the model respectively. When imposed, the two programs both lower the maximum total profit; however, while the carbon tax constraints dramatically curb emissions, the imposition of the carbon market program has no effects on the carbon emission of the optimum option (i e. the option with the maximum total profit). The carbon tax proposal is therefore effective in reducing emission, but as it lowers emission at too much expense of the companies, the proposal is considered unreasonable and impracticable. It's thus recommended that further research should focus on the pricing of the carbon tax, designing more feasible regulations. In contrast, although the primary auction of allowances of the RGGI scheme does not reduce the profit of companies as much, it is ineffective in curbing emissions and detrimental to the economy. Nevertheless, since the secondary market of RGGI, the more essential part of the program, is not considered, it might be possible that the RGGI market as a whole is effective. Hence, it's advised that further studies should analyze the impacts of the secondary market or assess the program as a whole. It's worth noting that the distribution scheme of allowances, which currently takes the form of auction that we studied, should be reconsidered, as other forms of distribution might be more beneficial and reasonable.

**Acknowledgements** Chaoyi Gan, Yihan Jiang, Zirou Zhang, and Renrui Liu contributed equally to this work and should be considered co-first authors.

## References

Electricity Generating Authority of Thailand (2015) Energy sales. http://www.egat.co.th/en/index.php?option=comcontent&view=article&id=90&Itemid=116. Accessed 10 June 2015

Hongying G, Bo Z (2019) Improvement design of urban sewage pretreatment scheme. Technol Innov (23):24–25 + 29

Kramer KJ, Masanet E, Xu T, Worrell E (2009) Energy effificiency improvement and cost saving opportunities for the pulp and paper industry. Ernest Orlando Lawrence Berkeley National Laboratory, Berkley, USA. http://ietd.iipnetwork.org/content/increased-use-recycled664pulp. Accessed 10 June 2015

Li Y, Yang J, Wei J, Liu J, Hou Y, Song X, Lu Q (2022) Research progress of urban sludge recycling technology [J/OL]. Ind Water Treat 1–10

Metropolitan Electricity Authority (2015) A statistics for electricity demand. http://www.mea.or.th/profifile/index.php?tid=5&mid=125&pid=122. Accessed 01 April 2015

Metropolitan Waterworks Authority (2015) Operation highlights. http://www.mwa.co.th/main.php?fifilename=stat. Accessed 01 April 2015

Natural Resources Canada (NRC) (2006) Benchmarking energy use in Canadian pulp and paper mills [Online]. https://www.carbontrust.com/media/206496/ctg059-paper-industrial-energy-efficiency.pdf. Accessed 6 Sept 2015

Planyc (2011) Solid waste. https://media.nyc.gov/agencies/planyc2030/pdf/planyc_2011_solid_waste.pdf. Accessed 28 Sept 2022

Pollution Control Department, Ministry of Natural Resources and Environment (2004) Municipal solid waste character observation and analysis in all municipalities project. http://infofifile.pcd.go.th/waste/Reportwaste.pdf?CFID=8235539&CFTOKEN=60317797

Ringer M, Putsche V, Scahill J (2006) Large-scale pyrolysis oil production: a technology assessment and economic analysis. In: Technical report. Midwest Research Institute

Ruangrong P (2012) Power tariff structure in Thailand. http://www.eria.org/events/Power%20Tariff%20Structure%20in%20Thailand.pdf

Selder H (1998) New process technology for high quality deinked pulp. Twogether Paper Technol J (6):5–15

University of Southern Indiana (USI) (2015) Paper recycling facts. http://www.usi.edu/recycle/paper-recycling-facts. Accessed 6 Sept 2015

Valin M (2001) Bangkok, municipal solid waste management: from public-operated to shared management and fifinancing. In: Report. SOGREAH Consulting and National University of Singapore

Van Oel PR, Hoekstra AY (2012) Towards quantifification of the water footprint of paper: a fifirst estimate of its consumptive component. Water Resour Manage 26:733–749. https://doi.org/10.1007/s11269-011-9942-7(2011)

Wei L, Dajiang T (2013) Research progress of sludge reduction technology. National sludge treatment and disposal and resource utilization of new technology and new equipment exchange seminar

World Bank (1999) Municipal solid waste incineration. In: Technical report. The World Bank, Washington, DC

Xingcai X, Shilu W, Crane G (2022) Review of plastic waste resource treatment. Qinghai Sci Technol 29(01):113–118

Xu L, Kaiwen Z, Lei Z, Sheng W, Xu Y (2021) Study on incineration and pyrolysis behavior of MSW components. J Liaoning Petrochem Univ 41(05):9–16

# Chapter 22
# Greywater Treatment Coupled with Electricity Generation in a Constructed Wetland Microbial Fuel Cell

**Palmer Oston A. Estole, Sean Paolo L. Isidro, and Kristopher Ray S. Pamintuan**

**Abstract** One of the most reliable forms of technology that have been brought by the demand for clean water and sustainable energy is the Constructed Wetland Microbial Fuel Cells (CWMFC). This technology utilizes both microbial activity and natural processes that result into catalytic reactions that have the capacity to generate bioenergy and treat wastewater. In this study, the potential of *Paspalum conjugatum* to treat greywater was scrutinized through a series of CWMFCs. In a 2-week analysis for bioelectricity generation and wastewater treatment, it was found out that the CWMFC generated a maximum power density of 1976.4 $\mu W/m^2$ and was able to attain a 95.5% BOD removal, 96.5% COD removal, 15% Phosphate removal and through polarization, the maximum power output that was given off was determined to be 6.2 mW. From the garnered power density and removal efficiencies, results have shown that the specific design of this study's CWMFC outperformed other conventional forms. It was proven that *Paspalum conjugatum* (carabao grass) is a viable plant for a CWMFC and this study proven its worth for further review for a larger scale design.

**Keywords** Bioelectricity · Constructed wetland-microbial fuel cell · Greywater treatment

## 22.1 Introduction

The increase in water pollution and energy demand has been a significant problem worldwide. Water which is an essential resource needed by all living organisms to survive and produce energy. On the other hand, power such as electricity is required to

P. O. A. Estole · S. P. L. Isidro · K. R. S. Pamintuan (✉)
School of Chemical, Biological, and Materials Engineering and Sciences, Mapua University, Manila, Philippines
e-mail: krspamintuan@mapua.edu.ph

K. R. S. Pamintuan
Center for Renewable Bioenergy Research, Mapua University, Manila, Philippines



Z. Yang (ed.), *Environmental Science and Technology: Sustainable Development*, Environmental Science and Engineering, https://doi.org/10.1007/978-3-031-27431-2_22

operate different infrastructures and industries like manufacturing plants, wastewater treatment plants, textile plants, and distilleries. The current rise in energy demand has led to the accelerated consumption of our non-renewable resources of energy such as fossil fuels. Furthermore, the increased consumption has also led to increased wastewater production. The rise in the demand for water resources has paved the way to introducing greywater reuse. Greywater is a composition of domestic water that may be drawn from households such as from bathing, sinks, and kitchen. Systems for the treatment of greywater can be performed onsite that would maximize the exploitation to reduce the demands of the population (Benami et al. 2016) significantly. An emerging technology that has drawn the attention of scientists is microbial fuel cells (MFC). Its potential to generate electricity by using natural processes and microorganisms has paved the way for a possible renewable energy source. The MFC produces electricity by converting organic matter into bioelectricity through microbial activities (Teoh et al. 2020). Similarly, constructed wetlands are also seen as a potential answer to the increasing water pollution problem. Constructed wetlands (CW) are a wastewater treatment process that uses natural processes to treat and purify wastewater. The fusion between MFCs and constructed wetlands is a possible answer to water pollution and energy demand. The likeness between these two drove researchers to merge these two technologies.

Constructed wetland microbial fuel cells (CW-MFC) are a recently emerging technology dealing with wastewater treatment while producing bioelectricity through natural processes. The CW-MFC is an open-loop biological system that is subdivided into two main structures, one for bioprocessing and the other for biocontrol (Cardiel et al. 2000). The two main structures involved are the aerobic cathode and anaerobic anode chamber which is separated by fibrous materials, soils, or membranes. These two structures are needed for the operation of the MFC. Moreover, these structures can be obtained naturally in constructed wetlands based on the flow direction and depth of the wetland (Yadav et al. 2012). The depth and flow are not the only factors taken into consideration in the operation of CW-MFCs. The plants, microorganisms, substrates, and electrodes also have a key role in the effectiveness of the technology. The merging of these two systems could improve individual weaknesses of the CW and MFC. In terms of sustainability, CW-MFCs tend to produce a lower carbon footprint compared to the standalone systems of CWs and MFCs (Ebrahimi et al. 2020). However, CW-MFCs are considered to be higher in operating and construction costs than the individual CW, but they are more economically viable than the MFC alone. Alternatively, the additional output provided by the CW-MFC gives an economic balance between the cost. The capital costs of CW-MFCs would be less compared to MFCs (Ebrahimi et al. 2020). Greywater is low-strength wastewater that has a very high potential to be reused and applied in different areas due to its significant amounts of organic materials and basic constituents. On average, the greywater produced by a person in poor areas can range from as low as 15 L to several hundred per day (Oteng-Peprah et al. 2018). These constituents present within the greywater may be used for the CW-MFC system since it contains necessary microbes that are needed for electricity generation.

Research regarding the effectiveness of CW-MFCs in treating greywater using tropical plants was limited from previous literature. It is crucial for studies to be done since this type of wastewater is commonly present in our households.

This study aims to determine the performance of a Constructed Wetland Microbial Fuel Cell (CWMFC) with *Paspalum conjugatum* in treating greywater. It also involves the CWMFC's efficiency in terms of wastewater treatment and bioelectricity generation. Percent removal in COD and phosphate concentrations was determined to determine its wastewater treatment efficiency. In addition, this study shows the process of building the system using resources found within every household. The low-cost and low-technology backyard approach wherein greywater will be treated to reduce the volume of wastes would significantly impact the community. In terms of environmental factors, this study aims to promote sustainable bioelectricity generation. It would also lessen the carbon footprint that may be drawn from the existing forms of electricity generators or sources of energy. This study would significantly contribute to future research due to the variations used to construct CWMFCs since it does not consume much space and provides two functions simultaneously, bioelectricity generation and wastewater treatment. The results of this study may contribute to future research involving small-scale productions that may eventually come up to large-scale productions.

## 22.2 Methodology

### *22.2.1 Materials and Equipment*

The Constructed Wetland Microbial Fuel Cell (CW-MFC) was a gravity surface flow system that utilized three plastic containers with nominal dimensions of 24.5 in. × 13 in. × 10 in. (L × W × H) connected in series provided an approximate usable volume of 99 L. The 3D model of the CW-MFC is found in Fig. 22.1a, b. The substrate used for the system was comprised of coarse river sand with a particle diameter ranging from 2 to 3 mm. Six carbon fiber electrodes that were 30 cm × 30 cm were used for the setup, the sides of the cathode and the anode were sewn to keep it intact. One of the electrodes acted as a cathode that was then buried 1 in. from the top, while the other electrode acted as an anode placed 1 in. above the bottom surface in aerobic conditions. These carbon fiber electrodes were an open circuit. The voltage produced was monitored with the use of a digital multimeter.

A 1-in. deep standing water surface was utilized in the setup. As for the greywater, the researchers produced a synthetic recipe by placing a set of dirty clothes into a 33 L tub with 150 g of Ariel powdered laundry detergent and washing and rinsing it four times. The clothing placed into the tub was a pair of jeans, four colored shirts, and four plain white shirts. The wastewater produced was then placed into the sump tank. Since the setup could utilize surface flow, the flow at the top and bottom of the cell became stagnant. To compensate for the evaporation losses, distilled water was

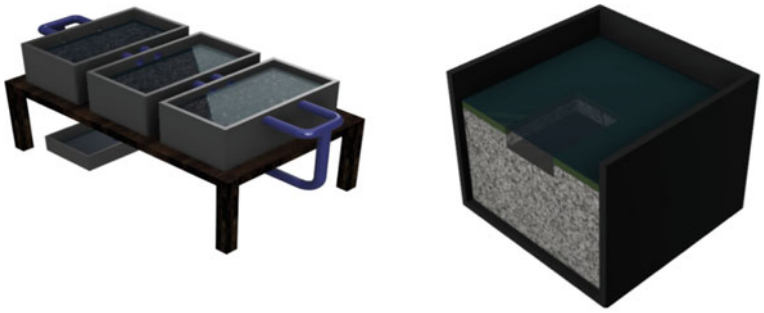


**Fig. 22.1** Three-dimensional model of the whole system (**a**) and **b** the inside of the CW-MFC

refilled up to the 2 in. mark daily. *Paspalum conjugatum* served as the constructed wetland plant to supply the microbial community present in the whole system and for bioelectricity generation. For the setup, ten young *Paspalum conjugatum* were planted 3 in. apart in each container. For the operation of the CW-MFC, a recirculating batch setup was utilized. The process began with the storage of the greywater in a sump tank (24.5 in. × 13 in. × 10 in., H × W × L). A 9 W flow adjustable submersible pump and a 1/2 in. PVC pipe were used to bring the greywater from the sump into the first CW-MFC. The effluents from the CW-MFC setup recirculated into the sump by using tubes. The average flow rate of the system was estimated to be 230 L/h, while its hydraulic retention time (HRT) was 26 min.

### *22.2.2 Measurement and Monitoring*

An initial and final sample was gathered from the system for the water analysis. The system ran for two weeks. The parameters analysed from the samples were its BOD, COD, nitrate, and phosphate content. The BOD content of the samples was analysed through a five-day BOD (BOD5) test, while its COD content was analysed through an open reflux method. The BOD5 test involves placing the sample in dark and incubated conditions over five days. After five days, the initial and final dissolved oxygen (DO) concentration was gathered from the sample. As for the open reflux method, it was utilized due to it being suitable for a wide range of wastes, and oxidation of most organic compounds was up to 95–100% of the theoretical value. The ion-selective electrode method and stannous chloride method were utilized for the phosphate and nitrate content. The ion-selective electrode is an analytical method that involves measuring electrical potential to determine the ions' activity in an aqueous solution. As for the voltage output measurement, a digital multimeter was used. The voltages were measured and recorded every afternoon for two weeks.

For the polarized analysis, voltage readings against a 1000-Ω resistor were recorded using a multimeter. Current ($I = V/R$), power ($P = V^2/R$), current density ($I_D = I/A$), as well as power density ($P_D = P/A$) were determined from the raw data. Polarization studies were performed through a gradual increase of external resistance (from 5 to 5000 Ω) and voltage recording. A polarization curve was produced from the data gathered wherein a plot of the current density and power density was shown.

## 22.3 Results and Discussion

### *22.3.1 Bioelectricity Generation*

The average power density that was measured after one week for CMWFC 1 was 206.065 $\mu W/cm^2$; for CWMFC 2, it was 653.8 $\mu W/cm^2$, and 1341.5 $\mu W/cm^2$ for CWMFC 3. Figure 22.2 represents the relationship between the average power density and average voltage against time. From Fig. 22.2, a decrease in terms of power density was observed with respect to time which mainly suggests that the CWMFC system could generate large amounts of energy output during days at which the nutrients in the substrate are rich and the microbial activity is high. Comparing the output of the CWMFC in terms of the power generation capacity from typical MFCs, the latter outperforms the study due to the proneness to ohmic and potential losses (Bolton and Randall 2019). In comparing the maximum power density that has been drawn from this study, a study of Microbial Fuel Cells in treating household water, particularly kitchen sink water, a maximum power density of 3.91 $mW/m^2$ was measured (You et al. 2021). In an integrated wetland microbial fuel cell and sand filtration system for greywater treatment, the power density that was measured was 4.33 $mW/m^2$ (Fajardo and Naoe 2020). From these values, it may be proven that the design of the study shows its performance that outweighs other forms of CWMFCs. In other existing systems and designs of CWMFCs, the maximum power density output of the study, 1976.4 $\mu W/m^2$, is significantly lower. Given that there were variations in the wastewater inlet in these systems, the total nitrates present in the utilized wastewater may be considered a factor in bioelectricity generation as it acts as an electron acceptor during the redox reaction and electricity production in turn (Fang et al. 2013). Along with these factors and by considering the fluctuations that can be seen from the data, the factor that was also observed in terms of power generation was hydraulic retention time (HRT). This factor involves the instabilities and inconsistencies in terms of the inlet flow rate. A study was able to show that when the HRT of the inlet is short, therefore the electricity generation becomes lower. This is due to the inverse relationship between flow rate and HRT. In addition, as the HRT becomes shorter and shorter, the rate of organic matter load increases which rapidly depletes the substrate present within the CWMFC (Fang et al. 2013).

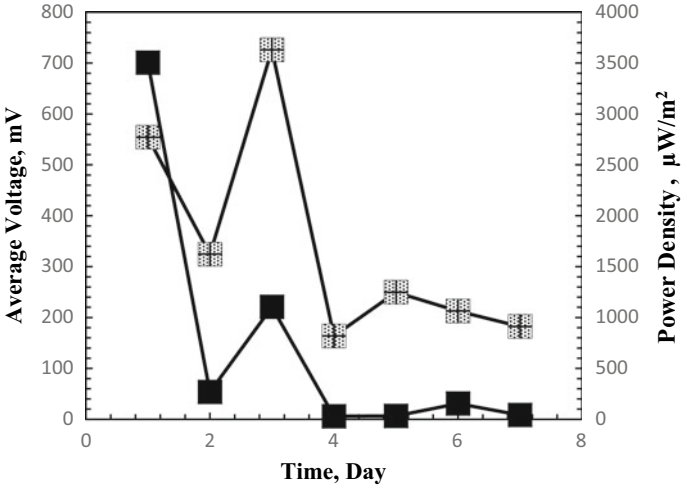


**Fig. 22.2** Average power density and average voltage output of the CW-MFC where in ▮ is for the average voltage and ▒ is for the average power density

From Fig. 22.2, the highest average voltage recorded from the system was from day 3, which was 726 mV. The CW-MFC that averaged the highest voltage was from CW-MFC 3, wherein it averaged 460 mV while CW-MFC 1 and 2 only averaged 239 mV and 337 mV, respectively. The oscillations in the graph were consistent with previous studies (Bolton and Randall 2019; Fang et al. 2013). The oscillations were the result of the photosynthetic activity of the plants (Bolton and Randall 2019). Photosynthetic activities are expected to increase the electrical output of the CW-MFC during sunlight hours due to the increased level of substrate available (Corbella et al. 2015). The weather conditions caused the fluctuations in the voltage output during the time of recording. It was observed that fluctuations occurred when the conditions were rainy and gloomy. The study conducted by Bolton and Randall observed that the light/dark cycle had a direct influence on the voltage output (Bolton and Randall 2019).

Figure 22.3, which is the system's polarization curves, serves as the plot representing the voltage as the function of current as per the resistances involved (from 5 to 5000 Ω). The internal resistances for each CW-MFC were obtained from the polarization curve by calculating the inverse slope of the linear region of the polarization curves. The internal resistances estimated were valued at 5.19 Ω for CW-MFC 1, 5.46 Ω for CW-MFC 2, and 10.01 Ω for CW-MFC 3. Comparing these values to the resistances obtained by similar CW-MFC studies, it was found that our system's output had a significantly lower resistance (Bolton and Randall 2019; Fang et al. 2013). The lower resistance may be attributed to the system's configuration since the system utilizes a surface flow system, lesser restrictions occur, thus resulting in higher power output.

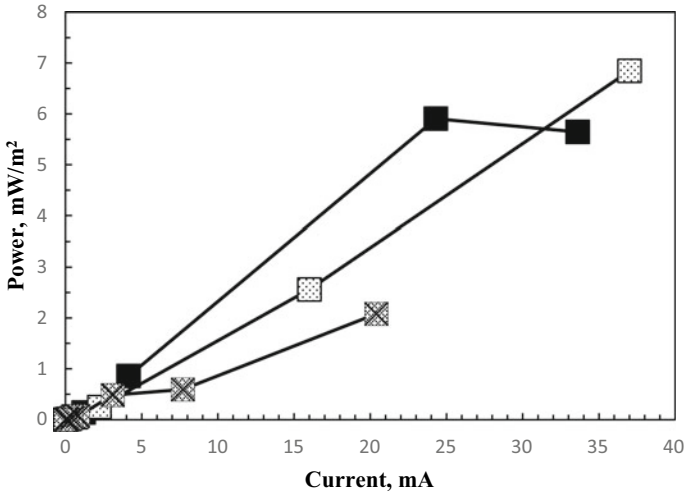


**Fig. 22.3** Polarization curve for the CW-MFC where in ▉ is for the 1st CWMFC, ▒ is for the 2nd CWMFC and ▒ is for the 3rd CWMFC

### *22.3.2 Removal Efficiency*

Through a variety of test methods in a laboratory setup, different parameters of the test sample, which is artificial greywater, were determined. Percent removals of different water quality parameters are given in Table 22.1. The total nitrate content of the sample increased from 0.45 mg/L up to 30.4, which was an undesired result for a wastewater treatment system. From this value, the probable causes that were considered for this spike in total nitrate were environmental factors and the utilization of a natural aerobic process. In addition, rainy weather conditions affected the effluent significantly since nitric oxides were present within the rain reacted that accumulated within the CWMFC. Another probable cause was nitrification that would naturally be occurring as the nitrogen content oxidizes, increasing the total nitrates in the CWMFC. In the case of phosphate removal, a slightly desirable result was shown as the phosphate content decreased from 3 to 2.53 mg/L. This may be due to an inefficient system in a biological processing unit such as a CWMFC wherein the biosolids at which phosphates accumulate were not removed as the system does not have an activated sludge removal system installed along with the system.

With regards to the oxygen demand, a more promising result was given off. The chemical oxygen demand (COD) decreased significantly from 1,231 to 43 mg/L, while the biochemical oxygen demand also decreased from 427 to 10 mg/L. From this, a 0.23 BOD/COD ratio may be obtained. Given these data, it can be proved that the wastewater treating capacity of the CWMFC in treating greywater is highly effective. In this case, A low BOD suggests that the rate of consumption of dissolved oxygen is generally low, wherein the water is purer (Fajardo and Naoe

**Table 22.1** Percent removal of BOD, COD, nitrates, and phosphates

| Parameter | Raw graywater | Treated graywater | Percent removal (%) |
|---|---|---|---|
| BOD (mg/L) | 427 | 19 | 95.55 |
| COD (mg $O_2$/L) | 1231 | 43 | 96.51 |
| Nitrates (mg/L) | 0.45 | 30.4 | −6655.55 |
| Phosphate (mg/L) | 3.00 | 2.53 | 15.67 |

2020). The same thing applies to COD; therefore, once the treated wastewater is disposed of in large bodies of water, the aquatic life would then be safer since the dissolved oxygen would not be consumed by organic matter, which was present in the untreated wastewater (Fang et al. 2013). Generalizing the results that have been recorded and by comparing them to the guidelines that have been set based on DAO 2016-08, the treated greywater would then be categorized as class D wastewater as the water analysis was able to comply with the set parameters for the said class (Corbella et al. 2015).

## 22.4 Conclusion

This study determined the potential of CWMFC that utilizes *Paspalum conjugatum* (carabao grass) as the plant for a constructed wetland in the treatment of greywater and bioelectricity generation. It has been proven that this design could generate a significant amount of maximum power density, which was 6.845 mW/m$^2$. In this study, the percent removal for parameters such as COD, BOD, Total Nitrates, and Total Phosphates were measured. A very promising water treatment efficiency of 95.5 and 96.5% in terms of BOD and COD, respectively. However, due to environmental impacts and other natural factors such as weather conditions, the results of the experiment from the obtained water effluent and current were significantly affected. The total phosphate content only decreased by 15%, while the total nitrate increased by 29.95 mg/L.

Despite the undesired results that have been mostly caused by natural factors and the uncontrolled environment, it has been proven that the greywater treatment coupled with electricity generation in a constructed wetland microbial fuel cell may be considered for the need and demand for a sustainable energy source and wastewater treatment technology, this CWMFC design has proven its worth for future and further studies and investigation towards a larger scale of design.

## References

Benami M, Gillor O, Gross A (2016) Potential microbial hazards from graywater reuse and associated matrices: a review. Water Res 106:183–195. https://doi.org/10.1016/j.watres.2016.09.058

Bolton CR, Randall DG (2019) Development of an integrated wetland microbial fuel cell and sand filtration system for greywater treatment. J Environ Chem Eng 7(4):103249. https://doi.org/10.1016/J.JECE.2019.10324

Cardiel GG, Caparanga AR, Doma BT Jr, Salvacion JL, Yang ST (2000) Preliminary engineering geological-geotechnical and instability risk assessment of slopes at Peace Village, Barangay San Luis, Antipolo, Rizal. Mapua Res J 1(2):79–84

Corbella C, Guivernau M, Viñas M, Puigagut J (2015) Operational, design and microbial aspects related to power production with microbial fuel cells implemented in constructed wetlands. Water Res 84:232–242

Ebrahimi A, Sivakumar M, McLauchlan C, Ansari A, Vishwanathan AS (2020) A critical review of the symbiotic relationship between constructed wetland and microbial fuel cell for enhancing pollutant removal and energy generation. J Environ Chem Eng 105011. https://doi.org/10.1016/j.jece.2020.105011

Fajardo RR, Naoe RC (2020) Effects of thermally-treated stainless steel electrodes on the performance of constructed wetland-microbial fuel cells growing cogon grass (Imperata cylindrica)

Fang Z, Song HL, Cang N, Li XN (2013) Performance of microbial fuel cell coupled constructed wetland system for decolorization of azo dye and bioelectricity generation. Biores Technol 144:165–171

Oteng-Peprah M, Acheampong MA, deVries NK (2018) Greywater characteristics, treatment systems, reuse strategies and user perception—a review. Water Air Soil Pollut 229(8). https://doi.org/10.1007/S11270-018-3909-8

Teoh TP, Ong SA, Ho LN, Wong YS, Oon YL, Oon YS, Tan SM, Thung WE (2020) Up-flow constructed wetland-microbial fuel cell: influence of floating plant, aeration and circuit connection on wastewater treatment performance and bioelectricity generation. J Water Process Eng 36:101371

Yadav AK, Dash P, Mohanty A, Abbassi R, Mishra BK (2012) Performance assessment of innovative constructed wetland-microbial fuel cell for electricity production and dye removal. Ecol Eng 47:126–131. https://doi.org/10.1016/j.ecoleng.2012.06.029

You J, Greenman J, Ieropoulos IA (2021) Microbial fuel cells in the house: a study on real household wastewater samples for treatment and power. Sustainable Energy Technol Assess 48:101618. https://doi.org/10.1016/J.SETA.2021.101618

# Chapter 23
# Removal of Heavy Metals from Wastewater: A Review


**Wei Liao, Chuan Yang, Yan Xue, and Xiaowen Yu**

**Abstract** With the rapid development of the economy and the accelerated process of industrialization, numerous of industrial pollutants are discharged into the environment, resulting in a growing issue of environmental pollution. Heavy metal pollution is attracting increasingly attention from the public due to its widely existence and severity of hazard. Owing to this fact, the removal of heavy metal ions from water is of great significance to the protection of public health and the environment. For decades, various strategies have been developed for easy, efficient, and economic removal of heavy metal ions from various wastewater sources. These strategies could be classified into chemical precipitation, ion exchange, adsorption, membrane separation, etc. By summarizing relevant researches, we have comprehensively reviewed and discussed these treatments in terms of removal efficiency, economy, advantage and disadvantage, and application potentiality, providing research directions and methods for the treatment of heavy metals polluted wastewater in the future.

**Keywords** Removal of heavy metals · Chemical precipitation · Ion exchange · Adsorption · Biologic method · Membrane filtration

W. Liao · C. Yang (✉) · X. Yu
Chongqing CEPREI Industrial Technology Research Institute Co. LTD, Chongqing, China
e-mail: lwei0314@163.com

W. Liao
Chongqing Institute of Green and Intelligent Technology, Chinese Academy of Sciences, Chongqing, China

Y. Xue
Chongqing University School of Law, Chongqing, China

X. Yu
Chongqing Key Laboratory of Reliability Technologies for Smart Electronics, Chongqing, China



Z. Yang (ed.), *Environmental Science and Technology: Sustainable Development*, Environmental Science and Engineering, https://doi.org/10.1007/978-3-031-27431-2_23

## 23.1 Introduction

Heavy metals are generally categorized with a density exceeding 5 g/cm$^3$, including Gold (Au), Silver (Ag), Copper (Cu), Cadmium (Cd), Zinc (Zn), Lead (Pb), Mercury (Hg), and Chromium (Cr), etc. (Shrestha et al. 2021). In terms of environmental pollution, heavy metals mainly refer to Hg, Cd, Pb, Cr, Ni, and other heavy metals with biological toxicity. With the process of industrialization, a large number of toxic heavy metals and its compounds are directly or indirectly discharged into the environment, resulting in a growing issue of heavy metal pollution. The sources of heavy metals in wastewater include natural and anthropogenic sources. Anthropogenic activities, particularly, industries (mining, metallurgy, battery, textile dyes, tannery, etc.) are the main sources of heavy metal pollutants. The presence of heavy metals in aqueous systems can cause adverse effects to both human health and environment, because they are highly toxic, non-degradable and have the characteristics of bioaccumulation and biomagnification in result of food chain (Malik et al. 2019).

Owning to these facts, remediation of heavy metal polluted aqueous systems is one of the most urgent environmental topics need to be studied. At present, the main treatments employed to remove heavy metals from wastewater including chemical precipitation, ion exchange, adsorption, membrane separation, etc., all of these methods have their inherent advantages and limitations. To choose the appropriate methods, cost, efficiency, feasibility, environmental impact, practicability and operation conditions should be considered. The scope of this study is to summarize the methods for removing heavy metals from aqueous systems, comparing their traits, effectiveness, and applications.

## 23.2 Methods for the Removal of Heavy Metals

### *23.2.1 Chemical Precipitation*

Chemical precipitation is regarded as one of the effective methods for removal of heavy metals from wastewater. In this process, heavy metals are separated and removed by reacting with specific chemical reagents and converting the soluble heavy metal ions into insoluble precipitates. Majority of metals could be precipitated by hydroxide precipitation, other methods such as sulphide precipitation, chelating precipitation, and ferrite method are also commonly used. Some chemical precipitation studies for the removal of heavy metals are summarized in Table 23.1. Hydroxide precipitation is a pH-dependent process, its removal efficiency is greatly affected by the pH value. Alkaline condition with pH value of 9–11 is conducive to the removal of heavy metals (Qasem et al. 2021). The chemical precipitation is especially effective in treating wastewater containing high concentration of heavy metals, but it shows poor removal efficiency for wastewater containing low concentration of heavy metals. As

**Table 23.1** Removal of heavy metals by chemical precipitation

| Heavy metals | Initial concentration (mg/L) | Precipitants | pH | Removal efficiencies (%) | References |
|---|---|---|---|---|---|
| $Pb^{2+}$ | 100 | NaOH and microbial flocculant | 6.2 | 98 | Huang et al. (2019) |
| $Cr^{3+}$ | 5363 | CaO or MgO | 8 | >99.0 | Guo et al. (2006) |
| $Cr^{3+}$ and $Cu^{2+}$ | 100 | AT-HBP | | >98 | Mohseni, et al. (2019) |
| $Fe^{2+}$ | 194 | BDET | 4.5 | >99 | Matlock et al. (2002) |
| $Zn^{2+}$ | 100 | $Ca(OH)_2$, $Na_2S$, and $Na_2CO_3$, respectively | 11.2, 10.6, and 9.3, respectively | >99 | Chen et al. (2018) |
| $Cu^{2+}$ | 100 | $Ca(OH)_2$, $Na_2S$, and $Na_2CO_3$, respectively | 9.4, 10.4, and 9.3, respectively | >99 | Chen et al. (2018) |
| $Pb^{2+}$ | 100 | $Ca(OH)_2$, $Na_2S$, and $Na_2CO_3$, respectively | 10.9, 10.0, and 7.9, respectively | 76.14, 99.75, and 97.78, respectively | Chen et al. (2018) |
| $Cu^{2+}$ | 5000 | FeS | 9.8 | >96 | Zhang et al. (2020) |
| $Cu^{2+}$ | 300 | $CaCO_3$ | 7.4 | >99.9 | Zhang et al. (2018) |
| $Mn^{2+}$ | 100,000 | $Na_2CO_3$ | 8.0–10.0 | >99 | Liu et al. (2018) |

a traditional technology for heavy metals removal from wastewater, chemical precipitation is the most widely used process in industry which has the advantages of mature process, stable operation, good treatment effect, low cost, and high automation (Pohl 2020). However, this method has some drawbacks in engineering application, such as large volumes of sludge, easy to cause secondary pollution, and greatly affected by water quality conditions.

### 23.2.2 Ion Exchange

Ion exchange is another classical method for heavy metals removal from wastewater. In this process, heavy metals are removed by ion-exchange reaction between functional groups on ion exchanger and heavy metal ions in aqueous systems. There are two most commonly used cation exchanger, strong acidic resins with sulfonic acid group (–$SO_3H$) and weak acidic resins with carboxyl group (–COOH), where $H^+$ ions in sulfonic group or carboxyl group play a main role in exchanging with heavy metal ions (Malik et al. 2019). Factors like pH, temperature, initial concentration of heavy metal ions, contact time, and selection of ion exchanger have a great influence on the removal efficiency of ion exchange resins (Pathania et al. 2014). The ion exchange method has a wide application in the soften of drinking water and the recovery of precious metals due to its advantages of high treatment efficiency, good effluent quality, less sludge volume, high selectivity, recycling of heavy metals, and recyclable, etc. (Cegłowski and Schroeder 2015). However, the operating and raw material cost is high and the regenerated liquid need further treatment, which limit the applications in the treatment of large-scale industrial wastewater.

Cegłowski and Schroeder (2015) have successfully synthesized a new porous resin with Schiff base chelating groups, and used to remove heavy metal ions of $Cu^{2+}$, $Cd^{2+}$, $Cr^{3+}$, $Ni^{2+}$ and $Co^{2+}$ from wastewater samples. Zhang et al. (2019) used a low-cost exchange resin to remove $Cr^{3+}$ and $Ni^{2+}$ and the ion exchange process was investigated. The schematics of ion exchange for removal of heavy metal ions by SR-16 are shown in Fig. 23.1.

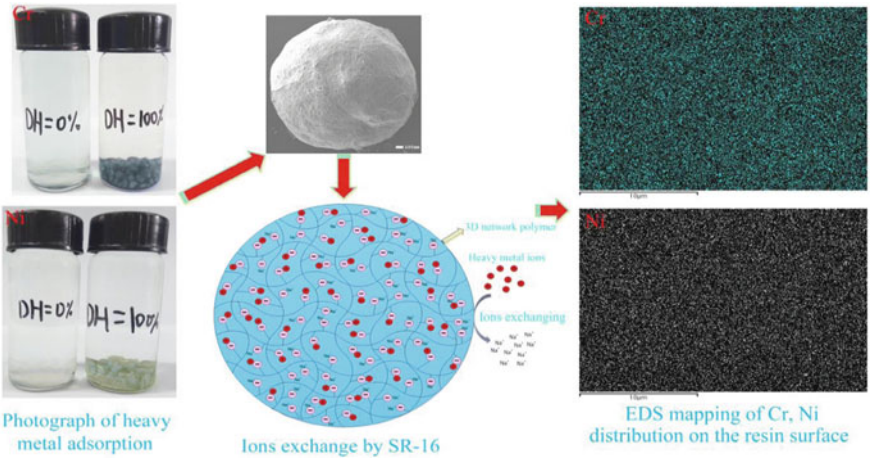


**Fig. 23.1** The schematics of ion exchange for removal of heavy metal ions using synthesized SR-16

### 23.2.3 Adsorption

Adsorption is based on the interaction between adsorbent and heavy metal ions by physical forces or chemical bonds to achieve the purpose of remediating polluted wastewater. Porous adsorbents with large surface areas and functional groups generally have high adsorption capacity. Many functional groups like amino, thiol, carboxyl, and hydroxyl groups have great affinity to heavy metals (Ge and Ma 2015; Zhao et al. 2018). The adsorption capacities can be improved by grafting these functional groups onto the surface of adsorbents (Liao 2021). The most advantages of adsorption are that the process is reversible and the adsorbents can be regenerated by desorption (Burakov et al. 2018). The other important advantage is that this method can effectively remove heavy metal ions even at low levels. The most significant factor affecting the performance of adsorption is the selection of adsorbents (Długosz and Banach 2018). The adsorption capacities of some reported adsorbents have been summarized in Table 23.2. Recently, various nano-materials like graphene, g-$C_3N_4$, MXenes, and Metal–organic frameworks (MOFs) have attracted growing attention in remediation of polluted wastewater. In particular, some novel modified nano-materials exhibit excellent attributes and enhanced adsorption performance, which endow these nano-materials great potential to replace traditional adsorbents. However, these novel materials also have some limitations of cost and efficiency. Therefore, it is still the main research goal to look for low-cost, efficient and environment-friendly adsorbents.

### 23.2.4 Biologic Method

Biologic method is an environment friendly method, it utilizes the metabolic activities and physiological characteristics of organisms (plants, animals, microorganisms or algae) to reduce the concentration of heavy metals in aqueous systems (Ayangbenro and Babalola 2017). This method is cost effective, simple to maintenance, and eco-friendly. Additionally, phytoremediation also can beautify the environment. In recent years, lots of studies have found that microalgae has considerable advantages in the degradation of toxic heavy metals. Microalgae can effectively remove heavy metal ions Pb (75–100%), Zn (15.6–99.7%), Cr (52.54–96%), Hg (77–97%), Cu (45–98%) and Cd (2–93.06%) from polluted aquatic systems (Singh et al. 2021). Meanwhile, the biomass produced by microalgae can be used as an efficient source of by-products such as bio-fuels, carbohydrates, lipids and proteins, which makes the process more economical and sustainable. However, the application of biologic method has certain limitations. In general, the operation period for biologic method is long, and the removal performance is susceptible to external conditions (such as heavy metal toxicity, wastewater composition, etc.). Furthermore, biosafety regulations must be strictly obeyed to ensure environmental safety. So far, remediation

**Table 23.2** Adsorption capacities for heavy metals by reported adsorbents

| Heavy metals | Adsorbent | Reaction conditions | Adsorption capacities (mg/g) | References |
|---|---|---|---|---|
| $Pb^{2+}$ | $Fe_3O_4$@$SiO_2$-HO-S | pH: 6.0, temperature: 25 °C, time: 12 h | 178.13 | Zhao et al. (2018) |
| $Pb^{2+}$ | β-CD | pH: 4.7, temperature: 25 °C, time: 12 h, $C_0$: 3000 mg/L | 130.6 | Zhao et al. (2019) |
| $Cu^{2+}$ | PS/$Fe_3O_4$/CS-PEI | pH: 6, temperature: 30 °C, time: 6 h, $C_0$: 1000 mg/L | 212.3 | Xiao et al. (2017) |
| $Cu^{2+}$ | F-MWCNTs | pH: 3, time: 60 min, $C_0$: 20 mg/L | 118.41 | Gupta et al. (2017) |
| $Cd^{2+}$ and $Cu^{2+}$ | LDH@GO-SH | pH: 5, temperature: 35 °C, time: 24 h, $C_0$: 100 mg/L | 102.77 and 234.80, respectively | Liao (2021) |
| $Cd^{2+}$ | MCFN | pH: 6, temperature: 35 °C, time: 180 min, $C_0$: 500 mg/L | 97.09 | (Xue, et al. 2019) |
| $Hg^{2+}$ and $Ni^{2+}$ | LDH/MOF NC | Temperature: 22 °C, time: 120 min, $C_0$: 250 mg/L | 530 and 439, respectively | (Soltani et al. 2021) |

of heavy metals polluted wastewater by biologic method is still in the experimental stage and has not been widely applied in practical engineering.

### *23.2.5 Membrane Filtration*

Membrane filtration method use specially manufactured films with selective transmission for separation, purification, and concentration by external pressure or concentration difference. It includes reverse osmosis (RO), ultrafiltration (UF), microfiltration (MF), and nanofiltration (NF). The main processes are basically the same, but different in pore structure (pore size distribution and porosity), membrane permeability and application pressure (Zioui et al. 2015). Membrane filtration technology has an extensive application prospect in the field of refined water and seawater desalination, due to its advantage of low energy consuming, no phases change, good selectivity, easy operation, and no need to add other chemicals. Table 23.3 summarizes the application of membrane processes in heavy metal removal. Mondal et al. (2020) prepared polymeric composite ultrafiltration membranes with different ratios

**Table 23.3** Membrane used in membrane processes for heavy metals removal

| Heavy metals | Membrane | Initial concentration (mg/L) | Pressure (bar) | Removal efficiencies (%) | References |
|---|---|---|---|---|---|
| $Pb^{2+}$ | AFC 80 membrane | 250 | 25 | >98 | Gherasim and Mikulášek (2014) |
| $Cd^{2+}$ and $Ni^{2+}$ | NF-300 membrane | 5 | 20 | 97.26 and 98.90 | Chaudhari and Murthy (2010) |
| Al, Ni, and Cr | RO (SW30) membrane | 5, 1.3, and 134.6, respectively | 10 | 99, 99, and 97, respectively | Ates and Uzal (2018) |
| $Ni^{2+}$ and $Cu^{2+}$ | PVC-TNT/SH-1.5 electrospun nanofiber membrane | 60 | 1 | 90 and 86.7, respectively | Hezarjaribi et al. (2021) |
| $Pb^{2+}$ and $Cd^{2+}$ | Polyacrylonitrile/polyanilie-nylon core–shell nanofiber membrane modified by diethylenetriamine | 50 | 4 | 96.77 and 95.11, respectively | Almasian et al. (2018) |
| $Cr^{6+}$ and $Pb^{2+}$ | Chitosan/PVA/PES-aminated-$Fe_3O_4$ electrospun nanofiber membrane | 20 | 1 | >80 | Koushkbaghi et al. (2018) |
| As, Cd and Pb | Polysulfone-$AlTi_2O_6$ composite membrane | 10 | 2 | 96, 98, and 99, respectively | Sunil et al. (2018) |

for the removal of heavy metals. The results showed that the lower feed concentration and the lower flux were favorable for the long-time operation of membranes, and high efficiency could be obtained without regeneration. The application of membrane separation in engineering is restricted by several aspects: (i) Membrane modules are too expensive, which greatly increase treatment cost; (ii) The membranes are easily contaminated during the process of using, resulting in poor treatment performance; (iii) Membrane materials are the foundation and core of membrane separation method, and their properties need to be further improved.

## 23.3 Conclusion and Recommendations

In summary, each technology has its own advantages and disadvantage, and range of application. The selection of the most appreciate methods for the purification of heavy metals polluted should obey the principles of environmental protection, high efficiency, safety, less consumables and low cost. To meet the enhanced treatment effect, combination or upgradation of treatment processes should be took into consideration.

## References

Almasian A et al (2018) Removal of heavy metal ions by modified PAN/PANI-nylon core-shell nanofibers membrane: filtration performance, antifouling and regeneration behavior. Chem Eng J 351:1166–1178

Ates N, Uzal N (2018) Removal of heavy metals from aluminum anodic oxidation wastewaters by membrane filtration. Environ Sci Pollut Res 25(22):22259–22272

Ayangbenro AS, Babalola OO (2017) A new strategy for heavy metal polluted environments: a review of microbial biosorbents. 14(1)

Burakov AE et al (2018) Adsorption of heavy metals on conventional and nanostructured materials for wastewater treatment purposes: a review. Ecotoxicol Environ Saf 148:702–712

Cegłowski M, Schroeder G (2015) Preparation of porous resin with Schiff base chelating groups for removal of heavy metal ions from aqueous solutions. Chem Eng J 263:402–411

Chaudhari LB, Murthy ZVP (2010) Separation of Cd and Ni from multicomponent aqueous solutions by nanofiltration and characterization of membrane using IT model. J Hazard Mater 180(1):309–315

Chen Q et al (2018) Comparison of heavy metal removals from aqueous solutions by chemical precipitation and characteristics of precipitates. J Water Process Eng 26:289–300

Długosz O, Banach M (2018) Kinetic, isotherm and thermodynamic investigations of the adsorption of $Ag^{+}$ and $Cu^{2+}$ on vermiculite. J Mol Liq 258:295–309

Ge H, Ma Z (2015) Microwave preparation of triethylenetetramine modified graphene oxide/chitosan composite for adsorption of Cr(VI). Carbohyd Polym 131:280–287

Gherasim C-V, Mikulášek P (2014) Influence of operating variables on the removal of heavy metal ions from aqueous solutions by nanofiltration. Desalination 343:67–74

Guo Z-R et al (2006) Enhanced chromium recovery from tanning wastewater. J Clean Prod 14(1):75–79

Gupta VK et al (2017) Adsorption mechanism of functionalized multi-walled carbon nanotubes for advanced Cu (II) removal. J Mol Liq 230:667–673
Hezarjaribi M et al (2021) Novel adsorptive PVC nanofibrous/thiol-functionalized TNT composite UF membranes for effective dynamic removal of heavy metal ions. J Environ Manag 284:111996
Huang J et al (2019) Enhancement of heavy metals removal by microbial flocculant produced by Paenibacillus polymyxa combined with an insufficient hydroxide precipitation. Chem Eng J 374:880–894
Koushkbaghi S et al (2018) Aminated-$Fe_3O_4$ nanoparticles filled chitosan/PVA/PES dual layers nanofibrous membrane for the removal of Cr(VI) and Pb(II) ions from aqueous solutions in adsorption and membrane processes. Chem Eng J 337:169–182
Liao W et al (2021) Cu(II) and Cd(II) removal from aqueous solution with LDH@GO-NH2 and LDH@GO-SH: kinetics and probable mechanism. Environ Sci Pollut Res
Liu W et al (2018) Effect of pH on the selective separation of metals from acidic wastewater by controlling potential. Sep Purif Technol 205:223–230
Malik LA et al (2019) Detection and removal of heavy metal ions: a review. Environ Chem Lett 17(4):1495–1521
Matlock MM, Howerton BS, Atwood DA (2002) Chemical precipitation of heavy metals from acid mine drainage. Water Res 36(19):4757–4764
Mohseni M et al (2019) Amine-terminated dendritic polymers as a multifunctional chelating agent for heavy metal ion removals
Mondal S, Kumar Majumder S (2020) Fabrication of the polysulfone-based composite ultrafiltration membranes for the adsorptive removal of heavy metal ions from their contaminated aqueous solutions. Chem Eng J 401:126036
Pathania D et al (2014) Synthesis and characterization of a new nanocomposite cation exchanger polyacrylamide Ce(IV) silicophosphate: photocatalytic and antimicrobial applications. J Ind Eng Chem 20(5):3596–3603
Pohl A (2020) Removal of heavy metal ions from water and wastewaters by sulfur-containing precipitation agents. Water Air Soil Pollut 231(10)
Qasem NAA, Mohammed RH, Lawal DU (2021) Removal of heavy metal ions from wastewater: a comprehensive and critical review. npj Clean Water 4(1)
Shrestha R et al (2021) Technological trends in heavy metals removal from industrial wastewater: a review. J Environ Chem Eng 9(4)
Singh DV et al (2021) Microalgae in aquatic environs: a sustainable approach for remediation of heavy metals and emerging contaminants. Environ Technol Innov 21:101340
Soltani R et al (2021) A water-stable functionalized NiCo-LDH/MOF nanocomposite: green synthesis, characterization, and its environmental application for heavy metals adsorption. Arab J Chem 14(4):103052
Sunil K et al (2018) Al-$Ti_2O_6$ a mixed metal oxide based composite membrane: a unique membrane for removal of heavy metals. Chem Eng J 348:678–684
Xiao C et al (2017) Sub-micron-sized polyethylenimine-modified polystyrene/$Fe_3O_4$/chitosan magnetic composites for the efficient and recyclable adsorption of Cu(II) ions. Appl Surf Sci 394:378–385
Xue Z et al (2019) Adsorption of Cd(II) in water by mesoporous ceramic functional nanomaterials. 6(4)
Zhang T et al (2018) Antibacterial activity of the sediment of copper removal from wastewater by using mechanically activated calcium carbonate. J Clean Prod 203:1019–1027
Zhang M et al (2019) Preparation of ion exchange resin using soluble starch and acrylamide by graft polymerization and hydrolysis. Environ Sci Pollut Res 26(4):3803–3813
Zhang X et al (2020) Selective sulfide precipitation of copper ions from arsenic wastewater using monoclinic pyrrhotite. Sci Total Environ 705:135816
Zhao J et al (2018) Synthesis of Schiff base functionalized superparamagnetic $Fe_3O_4$ composites for effective removal of Pb(II) and Cd(II) from aqueous solution. Chem Eng J 347:574–584

Zhao H-T et al (2019) β–cyclodextrin functionalized biochars as novel sorbents for high-performance of $Pb^{2+}$ removal. J Hazard Mater 362:206–213
Zioui D et al (2015) Membrane technology for water treatment applications. Int J Chem Environ Eng (IJCEE) 6

# Chapter 24
# Effects of Chronic Exposure to Microcystin-LR on Leaf Growth and Non-structural Carbohydrates of *Oenanthe Javanica* (Blume) DC

**Zhaorui Yuan, Guoyuan Chen, Teng Ma, Ziqing Yu, and Jiping Wang**

**Abstract** The leaf growth and non-structural carbohydrates content of *Oenanthe javanica* (Blume) DC were studied by irrigating an aqueous solution containing microcystin-LR (MC-LR) at environmentally relevant concentrations (1–30 $\mu g\ L^{-1}$), which can provide theoretical guidance for the use of eutrophic water to irrigate *Oenanthe javanica* (Blume) DC. The results showed that the photosynthesis of *O. javanica* leaves was enhanced, the glucose content increased, and the leaf growth state was good after 40 days of irrigation with 1 $\mu g\ L^{-1}$ MC-LR aqueous solution. After irrigation of 10 $\mu g\ L^{-1}$ MC-LR aqueous solution for 40 d, *O. javanica* leaves coped with MC-LR stress by moderately increasing the soluble sugar (fructose and glucose) content and protected their photosynthetic physiological properties. After irrigation of 30 $\mu g\ L^{-1}$ MC-LR aqueous solution for 40 days, *O. javanica* was severely stressed, and non-structural carbohydrates in the leaves were mainly in the form of soluble sugars (fructose, glucose and sucrose), and leaf growth was adversely affected. Therefore, the stress effect of MC-LR on aquatic vegetables should not be ignored when the eutrophic water which contained MC-LR exceeding 30 $\mu g\ L^{-1}$ is used for irrigation.

**Keywords** Microcystin-LR · *Oenanthe javanica* (Blume) DC · Leaf growth · Non-structural carbohydrates

## 24.1 Introduction

In recent decades, with the rapid development of economic globalization and the acceleration of the urbanization process, a large number of domestic sewage and industrial wastewater discharge have led to an increasing degree of eutrophication of

Z. Yuan · G. Chen (✉) · T. Ma · Z. Yu · J. Wang
School of Environmental Science and Engineering, Xiamen University of Technology, Xiamen 361024, China
e-mail: chengy@xmut.edu.cn

G. Chen · J. Wang
Xiamen Key Laboratory of Water Resources Utilization and Protection, Xiamen 361024, China



Z. Yang (ed.), *Environmental Science and Technology: Sustainable Development*, Environmental Science and Engineering, https://doi.org/10.1007/978-3-031-27431-2_24

water bodies (Gurbuz et al. 2009; Dorr et al. 2010). According to the "2020 Bulletin on the State of China's Ecological Environment", among the 110 important lakes (reservoirs) in China, lakes with poor trophic status (reservoirs) account for 9.1%, and lakes with medium trophic status (reservoirs) account for 61.8%, lakes with mild eutrophic status (reservoirs) account for 23.6%, lakes with moderate eutrophic status (reservoirs) account for 4.5% and lakes with severe eutrophication status (reservoirs) account for 0.9% (http://www.mee.gov.cn/hjzl/sthjzk/zghjzkgb/202105/P020210526572756184785).

The increasing eutrophication of water bodies has led to frequent outbreaks of cyanobacterial blooms. Studies have shown that about 25–70% of the world's cyanobacterial blooms produce phycotoxins (Duy et al. 2000). Microcystins (MCs) are one the most widely distributed, most toxic and most harmful species (Kenefick et al. 1993). When people or animals eat food or water containing MCs, they will have shortness of breath, vomiting, fatigue, diarrhea, etc., which can be caused when severe death by suffocation (Su and Deng 2013). China is one of the countries with the most frequent cyanobacterial bloom outbreaks, the widest distribution range and the largest number of phycotoxin species (Song et al. 2007). In the natural environment, the reported mass concentrations of water MCs are typically less than 30 $\mu g\ L^{-1}$ (Wan et al. 2017; Wejnerowski, et al. 2018). Mass concentrations of MCs can be as high as 1800 $\mu g\ L^{-1}$ when algae die in large quantities in a short period of time (Corbel et al. 2014).

Currently, surface freshwater irrigation is the most common agricultural irrigation measure. However, there is currently no effective removal method for MCs in irrigation water, so the direct use of surface water contaminated with MCs as irrigation water will inevitably make MCs contaminate farmland soils. Studies have shown that MCs accumulate in the soil after irrigating crops with water containing MCs, which will affect crops grown in the environment (Bibo et al. 2008; Chen et al. 2006). Codd et al. (1999) studies found after irrigation with water containing *Microcystis aeruginosa*, MCs were detected on *Lactuca sativa* L. leaves and could not be washed away. Peuthert et al. (2007) irrigated 11 crops with MC-LR contaminated water and found that their seedlings could absorb MC-LR through the roots and then migrate to the aboveground part. The MCs that enter the plant will have a certain impact on plant growth. MacKintosh et al. (1990) studies have found that MC-LR can significantly inhibit the activity of serine/threonine protein phosphatase l and 2A (PPI and PP2A) in plants. Kós et al. (1995) have found that the use of cyanobacteria crude extract to stress white mustard (*Sinapis alba* L.) inhibits its seedlings of growth. Zhan et al. (2013) studies have shown that the germination rate of cabbage seeds under MCs pollution conditions has not changed significantly, but the growth of its roots and shoots has been significantly inhibited, and its biomass has also been significantly reduced. In addition, after treating *Brassica rapa var. chinensis* (Linnaeus) Kitamura with MC-LR and MC-RR, as the the concentration of algal toxins increased, its aboveground partial mass and plant height gradually declines, and the leaves exhibit a withered yellowing phenomenon (Jin et al. 2013). The above results show that after irrigating farmland with water bodies containing MCs, MCs accumulate in crops and have different degrees of influence on their growth characteristics. Therefore, it is

necessary to understand the effects of MCs on the growth of aquatic vegetables in order to rationally use eutrophic water for irrigation.

*Oenanthe javanica* (Blume) DC is a perennial herb of cress in the Umbellifera family, with a well-developed root system, strong adaptability, a wide range of cultivation in the country, and its stems and leaves have high medicinal and economic value. In this study, *O. javanica* was used as a test material to regularly water an aqueous solution containing environment-related concentrations of MC-LR (1–30 $\mu g\ L^{-1}$) for 40 days, revealing the effects of chronic exposure of MC-LR on leaf growth and non-structural carbohydrates content of *O. javanica*, and then providing theoretical guidance for the cultivation of *O. javanica* irrigated with eutrophication water.

## 24.2 Materials and Methods

### *24.2.1 Test Materials*

The old root seed stems of *O. javanica* were purchased from Hunan Jiahe Special Vegetables Fruit and Vegetable Co., Ltd. Nutrient soil was purchased from Beijing Liqing Biotechnology Co., Ltd. Pure MC-LR (Calbiochem, Germany), purity ≥95%, purchased from Shanghai Hengyuan Biotechnology Co., Ltd.

### *24.2.2 Test Methods*

Preparation of MC-LR irrigation solution: 1 mL of methanol was first added to the reagent bottle containing 500 μg MC-LR dry powder standard, fully dissolved, and then treated with ultrapure water to 500 mL to obtain 1 $\mu g\ mL^{-1}$ MC-LR mother liquor, and stored at −4 °C for later use. Subsequently, irrigation solutions containing different concentrations of MC-LR (0, 1, 10, 30 $\mu g\ L^{-1}$) were prepared according to the mother liquor.

Experimental design: Firstly, a soil layer thickness of about 22 cm was laid in an incubator of 46.5 cm × 32.5 cm × 25.5 cm according to the growth requirements. Then select the old root seed stems with consistent height (about 10 cm) and good growth, gently rinse it with tap water, and then wash them with ultrapure water, plant 3 old root seed stems in each incubator, 3 parallels per treatment, and then were cultivated under outdoor natural conditions. The temperature was 20–30 °C, the air humidity was 70–90%, and it was covered by a canopy on rainy days. Germination was obtained after 1 week of preculture, and then 600 mL of irrigation solution containing different concentrations of MC-LR was irrigated regularly at 5 p.m. daily. After 40 days of culture, photosynthetic indexes, chlorophyll SPAD value and the number of stem-growing leaves were measured in situ. The area of stem-growing

leaves and the contents of soluble sugars (sucrose, fructose and glucose) and starch in leaves were measured by sampling.

### *24.2.3 Determination Methods*

Three *O. javanica* seedlings were randomly selected per group to obtain the top fully unfolded leaves, and the leaf area was determined using the checkered counting method (Liu et al. 2020a). Net photosynthetic rate (A), transpiration rate (E) and water use efficiency (WUE) were determined using the TARGAS-1 portable photosynthetic analyzer (Lufthansa Scientific Instruments Inc.). Chlorophyll SPAD value measured using SPAD-502 chlorophyll meter (Konica Minolta Corporation, Japan). The extract of soluble sugars (sucrose, fructose and glucose) in the leaves was operated according to the method of Shanghai Institute of Plant Physiology of the Chinese Academy of Sciences (1999), and the starch was operated with the extract included in the enzyme-linked immunoassay kit (Shanghai Hengyuan Biotechnology Co., Ltd.). Finally, the contents of soluble sugars (sucrose, fructose and glucose) and starch were determined on the SpectraMax M2 multifunctional microplate reader.

### *24.2.4 Data Processing*

Origin 2018 software was used to map the data. ANOVA was used to compare significant differences between the means of data from different treatment groups by Sigmaplot 10.0 software ($P < 0.05$).

## 24.3 Results and Analysis

### *24.3.1 Effects of MC-LR Aqueous Solution Irrigation on Chlorophyll SPAD, A, E and WUE Values of* O. Javanica *Leaves*

According to Fig. 24.1, chlorophyll SPAD values of *O. javanica* leaves in the MC-LR treatment groups of 1 and 10 $\mu g\ L^{-1}$ were increased to varying degrees, but the difference was not significant ($P > 0.05$). The chlorophyll SPAD values of leaves in the 30 $\mu g\ L^{-1}$ MC-LR treatment group decreased significantly compared with the control group ($P < 0.05$).

The A and E values of *O. javanica* leaves in the 1 $\mu g\ L^{-1}$ MC-LR treatment group increased significantly ($P < 0.05$), and the E values of *O. javanica* leaves in the 10 $\mu g\ L^{-1}$ MC-LR treatment group increased significantly ($P < 0.05$), while

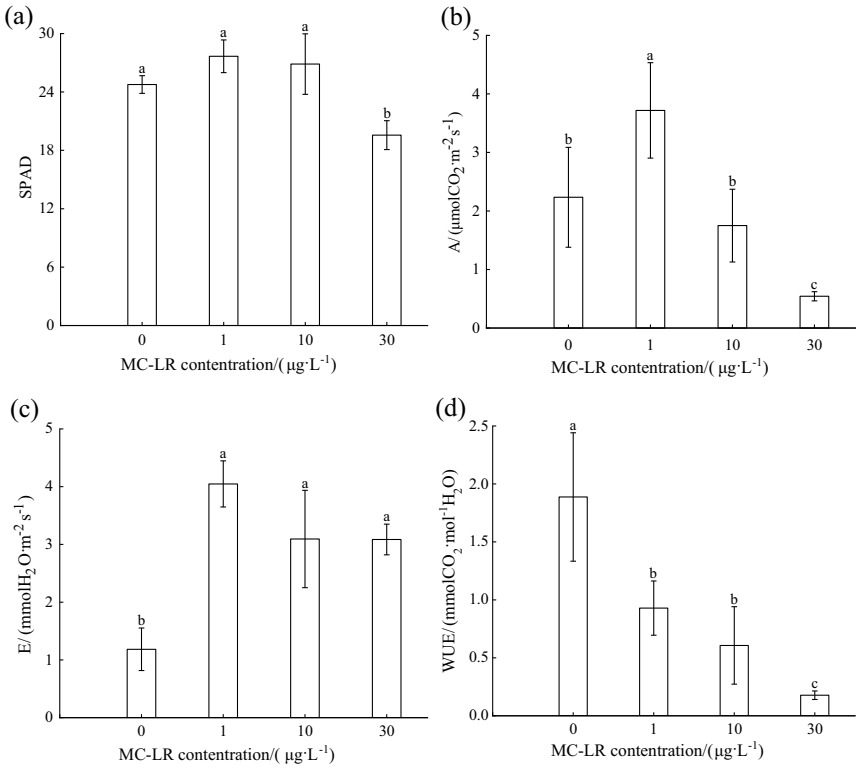


**Fig. 24.1** Different lowercase letters indicate significant differences between different treatments ($P < 0.05$), and the sample size is $n = 3$. The same applies below. Effects of MC-LR aqueous solution irrigation on chlorophyll SPAD (**a**), A (**b**), E (**c**) and WUE (**d**) values in leaves of *Oenanthe javanica* (Blume) DC

there was no significant difference in A values ($P > 0.05$). The E values of leaves in the 30 μg $L^{-1}$ MC-LR treatment group increased significantly ($P < 0.05$) and A values decreased significantly ($P < 0.05$). The WUE values of *O. javanica* leaves in all MC-LR treatment groups were reduced to varying degrees ($P < 0.05$).

### *24.3.2 Effects of MC-LR Aqueous Solution Irrigation on Non-structural Carbohydrates of* O. Javanica *Leaves*

According to Fig. 24.2, the sucrose, fructose and starch content of *O. javanica* leaves in the 1 μg $L^{-1}$ MC-LR treatment group were not significant different compared with the control group ($P > 0.05$), while the glucose content increased significantly

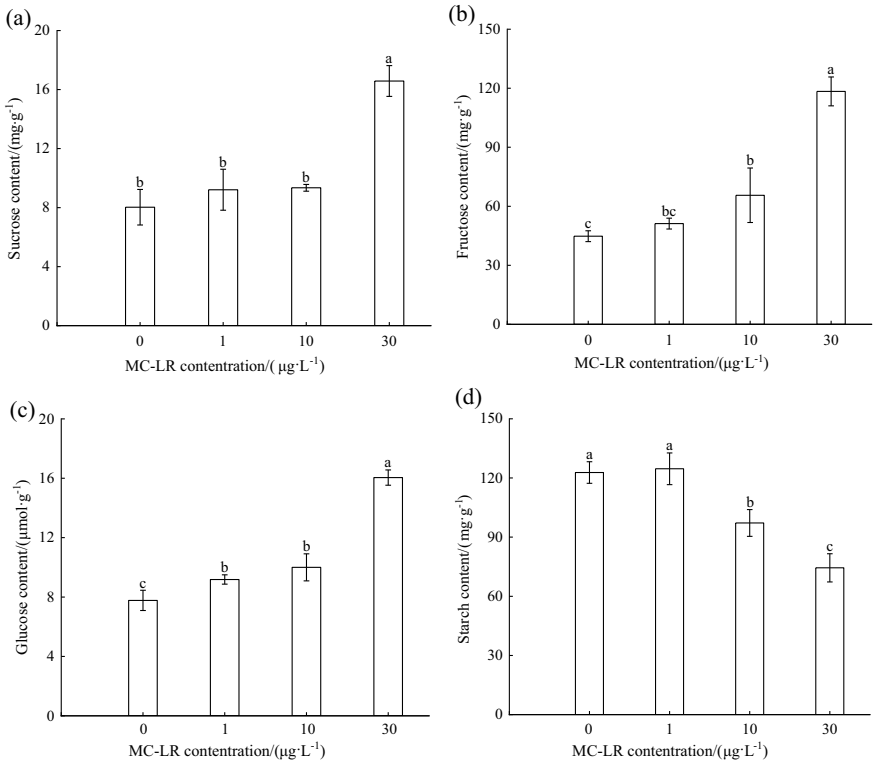


**Fig. 24.2** Effects of MC-LR aqueous solution irrigation on sucrose (**a**), fructose (**b**), glucose (**c**) and starch content (**d**) in leaves of *Oenanthe javanica* (Blume) DC

compared with the control group ($P < 0.05$). Fructose and glucose content of *O. javanica* leaves in the 10 μg $L^{-1}$ MC-LR treatment group increased significantly compared with the control group ($P < 0.05$), sucrose content did not differ significantly from the control group ($P > 0.05$), while starch content decreased significantly compared with the control group ($P < 0.05$). The sucrose, fructose and glucose content of leaves in the 30 μg $L^{-1}$ MC-LR treatment group increased significantly compared with the control group ($P < 0.05$), while the starch content decreased significantly compared with the control group ($P < 0.05$).

### *24.3.3 Effects of MC-LR Aqueous Solution Irrigation on Leaf Area and Number of* O. Javanica

According to Fig. 24.3, the leaf area of *O. javanica* in the treatment group of 1 μg $L^{-1}$ MC-LR was significantly increased compared with that of the control

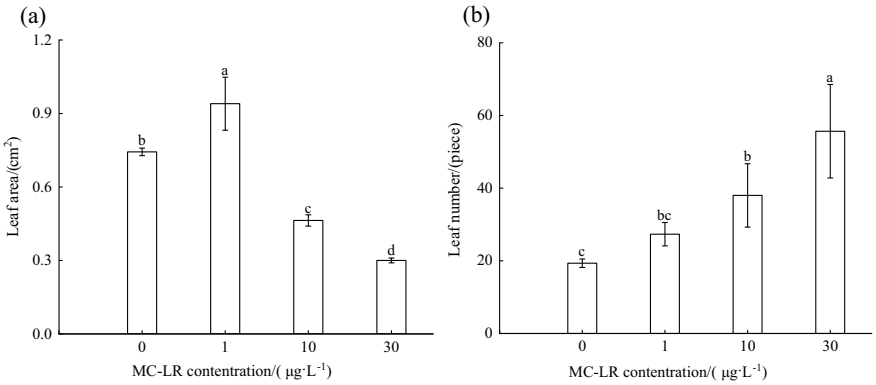


**Fig. 24.3** Effects of MC-LR aqueous solution irrigation on leaf area (**a**) and leaf number (**b**) in leaves of *Oenanthe javanica* (Blume) DC

group ($P < 0.05$), while, there was no significant difference in the number of leaves ($P > 0.05$). The leaf areas in the 10 and 30 μg $L^{-1}$ MC-LR treatment groups were significantly reduced compared to the control group ($P < 0.05$), while, the number of leaves increased significantly ($P < 0.05$). The higher the concentrations of MC-LR in the irrigation solution were, the greater the decrease in leaf area and the increase in leaf number of *O. javanica* was.

## 24.4 Discussion

### *24.4.1 Effects of MC-LR Aqueous Solution Irrigation on Leaf Area and Number of* O. Javanica

Leaves are one of the most important organs of plants, and their growth state is closely related to the photosynthesis of plant (Wang 2017). The leaf area of *O. javanica* in the 1 μg $L^{-1}$ MC-LR treatment group was significantly larger than the control group ($P < 0.05$), while the leaf area of *O. javanica* in the 10 and 30 μg $L^{-1}$ MC-LR treatment groups ware significantly smaller than the control group ($P < 0.05$). The results show that 1 μg $L^{-1}$ MC-LR aqueous solution irrigation has a promoting effect on the increase of *O. javanica* leaf area, while 10 and 30 μg $L^{-1}$ MC-LR aqueous solution irrigation significantly inhibits the increase of *O. javanica* leaf area. There was no significant difference in the number of *O. javanica* leaves in the 1 μg $L^{-1}$ MC-LR treatment group compared with the control group ($P > 0.05$), while the number of *O. javanica* leaves in the 10 and 30 μg $L^{-1}$ MC-LR treatment group was significantly higher than the control group ($P < 0.05$). This shows that irrigation with an aqueous solution containing higher concentrations (10–30 μg $L^{-1}$) MC-LR contributed to the increase in the number of *O. javanica* leaves. This may be because

MCs accumulate in the soil after irrigation with water containing MCs (Bibo et al. 2008; Chen et al. 2006), while plants absorb MCs from the soil through the roots and migrate to aboveground parts (Peuthert et al. 2007), which has an impact on plant leaf growth. Yin et al. (2004) found that the use of MC-RR to *Vallisneria natans* (Lour.) Hara can inhibit its growth and development, and at concentration of 0.1–10,000 $\mu g\ L^{-1}$, the germination of its seeds, leaves and roots were significantly inhibited with the increase of MC-RR concentrations. In summary, as the concentration of MC-LR in the irrigation solution increases, *O. javanica* may regulate MC-LR stress by reducing the leaf area and increasing the number of leaves.

### 24.4.2 *Effect of MC-LR Aqueous Solution Irrigation on Photosynthetic Characteristics of* O. Javanica

The photosynthesis of leaves is closely related to the growth and development of plants, and the photosynthetic process is more sensitive under adverse conditions (Abe et al. 1996; Pflugmacher et al. 2007a, b). Chlorophyll is the main pigment of photosynthesis, and its content is not only an important indicator of leaf photosynthetic ability, but also can be used as a measure of plant stress resistance (Xue and Liu 2008). The results of the study showed that the chlorophyll SPAD value of *O. javanica* in the 1 and 10 $\mu g\ L^{-1}$ MC-LR treatment groups were higher than the control group, but there was no significant difference ($P > 0.05$), while the chlorophyll SPAD value of *O. javanica* in the 30 $\mu g\ L^{-1}$ MC-LR treatment group was significantly lower than the control group ($P < 0.05$). This shows that 30 $\mu g\ L^{-1}$ MC-LR aqueous solution irrigation for 40 days could significantly reduce the chlorophyll content of *O. javanica*, thereby seriously affecting its photosynthesis. Järvenpää et al. (2007) showed that the chlorophyll content of *Brassica oleracea* var. *botrytis* Linnaeus and *Brassica juncea* (Linnaeus) Czernajew did not change significantly under the exposure conditions of l and 10 $\mu g\ L^{-1}$ MCs. Wang et al. (2014) have shown that under exposure conditions of 1–100 $\mu g\ L^{-1}$ MCs, the chlorophyll content of *Oryza sativa* L. showed a tendency to increase first and then decrease with the increase of MC-LR concentration. Chlorophyll content in plant leaves is in a dynamic balance of chlorophyll synthesis and degradation (Jacob-Wilk et al. 1999), and chlorophyll content changes are a response of plants to environmental stress (Chen et al. 2021a). Studies have shown that adverse environmental factors may inhibit the transformation of chlorophyll intermediates, thereby affecting chlorophyll synthesis (Dalal and Tripathy 2012; Xiang et al. 2020; Zhang et al. 2015). Chen et al. (2021b) found that 30 $\mu g\ L^{-1}$ MC-LR exposure for 30 days produced severe oxidative stress on *Ipomoea aquatica* Forssk, and the chlorophyll degradation rate was higher than the synthesis rate, resulting in a significant decrease in chlorophyll content in the leaves of *Ipomoea aquatica* Forssk. Thus, the higher concentration of MC-LR accumulated in *O. javanica* in the 30 $\mu g\ L^{-1}$ MC-LR treatment group disrupted the dynamic balance of chlorophyll synthesis

and degradation in *O. javanica* by inhibiting chlorophyll synthesis or promoting the decomposition of chlorophyll, resulting in a decrease in its chlorophyll content.

Net photosynthetic rate (A) is expressed as the total photosynthetic rate minus the respiration rate, which can indicate the organic matter yield accumulated by the plant under photosynthesis. After 1 μg $L^{-1}$ MC-LR aqueous solution irrigation for 40 d, the A value of *O. javanica* leaves increased significantly compared with the control group ($P < 0.05$). After 10 μg $L^{-1}$ MC-LR aqueous solution irrigation for 40 d, the A value of *O. javanica* leaves decreased compared with the control group, but the difference was not significant ($P > 0.05$). After 30 μg $L^{-1}$ MC-LR aqueous solution irrigation 40 d, the A value of *O. javanica* leaves decreased significantly compared with the control group ($P < 0.05$). The results showed that 1 μg $L^{-1}$ MC-LR aqueous solution irrigation promoted photosynthesis of *O. javanica*, while MC-LR (10–30 μg $L^{-1}$) aqueous solution inhibited the photosynthesis of *O. javanica* leaves to varying degrees, and the higher of MC-LR concentration, the stronger the inhibition. Abe et al. (1996) have shown that the chlorophyll content of *Phaseolus vulgaris* L. after MCs exposure was significantly reduced, and its A value was significantly reduced by 50%, and some plants were deformed or even necrotic. Pflugmacher et al. (2007b) used 5 μg $L^{-1}$ MCs to stress 6 species of *Spinacia oleracea* L. for 42 d, and found that the photosynthetic oxygen rate of the leaves was significantly reduced. Transpiration rate (E) and water use efficiency (WUE) were key factors affecting plant photosynthesis. E refers to the amount of water that plants lose through transpiration per unit time and unit leaf area. WUE refers to the ratio of $CO_2$ assimilated to transpiring water by plants, with a value of A/E (Liu et al. 2020b). This study showed that the E value of leaves in the 10 and 30 μg $L^{-1}$ MC-LR treatment groups increased significantly compared with the control group, which is consistent with other studies. For example, Zhang (2015) showed that after 10 μg $L^{-1}$ MC-LR exposure, the E value of rice leaves increased significantly at all stages of stress, after 50 μg $L^{-1}$ MC-LR exposure, the E values of rice leaves also increased significantly in the early and late stress stages. The WUE values of *O. javanica* leaves in the 10 and 30 μg $L^{-1}$ MC-LR treatment groups decreased significantly compared with the control group. The results showed that after the irrigation of MC-LR aqueous solution for 40 d, the transpiration effect of *O. javanica* was enhanced, and the evaporation of water was accelerated, resulting in a decrease in water utilization, which affects photosynthesis.

### 24.4.3 *Effects of MC-LR Aqueous Solution Irrigation on Non-structural Carbohydrates of* O. Javanica

Carbohydrates are the main products of plant photosynthesis, and non-structural carbohydrates (NSC) are important energy substances for plant growth and metabolic activities (He et al. 2007; Sun et al. 2018; Dong and Li 2013). The NSC content in plants has the effect of balancing the supply and demand relationship of carbon, and

it contains soluble sugars (sucrose, fructose, glucose, etc.) and starch which exceed 90% of the total content of NSC (Koch et al. 2004; Hoch et al. 2003). Soluble sugars are small molecule substances that play an important role in regulating penetration, and their content is an important indicator of plant stress resistance (Yu et al. 2003). The results showed that the glucose and fructose content in the leaves of the 1 and 10 $\mu g\ L^{-1}$ MC-LR treatment groups increased significantly compared with the control group ($P < 0.05$), the glucose, fructose and sucrose content in the leaves of the 30 $\mu g\ L^{-1}$ MC-LR treatment group increased significantly compared with the control group ($P < 0.05$). Studies have shown that an increase in soluble sugar content is beneficial to maintaining plant glycolytic metabolism, increasing the concentration of solutes in cells, and regulating the osmosis potential, thereby protecting cell membranes from damage (Li et al. 2020; Kang et al. 2011). Therefore, under the chronic exposure conditions of MC-LR (1–30 $\mu g\ L^{-1}$), the leaves of *O. javanica* adjust the stress of MC-LR by increasing the soluble sugar content, and the higher the MC-LR concentrations were, the more severe the stress was, and the greater the accumulation of soluble sugar was. Starch is an important energy storage substance in plants, and its content is in a state of dynamic equilibrium (Salleo et al. 2009; Zhang et al. 2020). The results showed that the starch content in the leaves of the 1 $\mu g\ L^{-1}$ MC-LR treatment group did not change significantly compared with the control group ($P < 0.05$), while the starch content of *O. javanica* in the 10 and 30 $\mu g\ L^{-1}$ MC-LR treatment group decreased significantly compared with the control group ($P < 0.05$). Studies have shown that the decrease in photosynthetic rate of plants leads to a decrease in photosynthetic products, plant growth will consume stored carbohydrates, while amylase activity increases, promoting starch hydrolysis into soluble sugars, thereby providing substances and energy for plant growth and development (Murata et al. 1968). Yi et al. (2016) have shown that 50 $\mu g\ L^{-1}$ MC-LR treated rice seeds have significantly increased amylase activity compared with the control group, thereby affecting seed germination. Liu (2019) showed that the starch content of 100 $\mu g\ L^{-1}$ MC-LR treated rice was significantly reduced compared with the control group at the seedling stage, pregnant ear stage and mature stage, which affected the nutritional quality of rice. The results of this study showed that chronic exposure of 10 and 30 $\mu g\ L^{-1}$ MC-LR exerted some degree of stress on *O. javanica*, and the starch in the leaves tended to hydrolyze into sucrose, fructose and glucose, thereby increasing the accumulation of soluble sugars and helping *O. javanica* cope with the adverse effects of MC-LR.

## 24.5 Conclusion

Within the concentration range of this experimental study, MC-LR aqueous solution showed obvious dose effect on leaf growth and non-structural carbohydrates content of *O. javanic* after irrigation for 40 days. The specific manifestations are:

(1) The irrigation of 1 μg $L^{-1}$ MC-LR aqueous solution for 40 d promoted the growth of *O. javanica* leaves. The leaf area, glucose content, A and E values were significantly increased.
(2) After irrigation of 10 μg $L^{-1}$ MC-LR aqueous solution for 40 d, the number of leaves began to increase, while the area of leaves decreased. *O. javanica* could regulate MC-LR stress by moderately increasing the content of soluble sugars (fructose and glucose) to protect its photosynthetic physiological characteristics.
(3) After irrigation of 30 μg $L^{-1}$ MC-LR aqueous solution for 40 d, *O. javanica* was severely stressed, and the non-structural carbohydrates in the leaves were mainly in the form of soluble sugars (fructose, glucose and sucrose), and the leaves growth were severely suppressed.

**Acknowledgements** The paper was funded by the Natural Science Foundation of Fujian Province, China (2019J01849; 2020J01256); Grant for Items in "Climbing" Program from Xiamen University of Technology (XPDKT19026) and Xiamen University of Technology Graduate Student Science and Technology Innovation Plan Fund Project (YKJCX2021161).

## References

Abe T, Lawson et al (1996) Microcystin-LR inhibits photosynthesis of phaseolus vulgaris primary leaves: implications for current spray irrigation practice. New Phytologist 133(4):651–658
Bibo L, Yan G, Bang X et al (2008) A laboratory study on risk assessment of microcystin-RR in cropland. J Environ Manage 86(3):566–574
Chen W, Song L, Gan N et al (2006) Sorption, degradation and mobility of microcystins in Chinese agriculture soils: risk assessment for groundwater protection. Environ Pollut 144(3):752–758
Chen LY, Xu H, Xu G et al (2021a) Effects of different habitats on the growth, chlorophyll content and chlorophyll fluorescence characteristics of medicinal and edible plants Sambucus chinensis Lind. Ecol Sci 40(5):69–77
Chen GY, Liao TF, Li QS (2021b) Effects of chronic exposure to microcystin-LR on photosynthetic physiology of Ipomoea aquatica. J Northwest A & F Univ (Natural Science Edition) 9:129–136+143
Codd GA, Metcalf JS, Beattie KA (1999) Retention of Microcystis aeruginosa and microcystin by salad lettuce (Lactuca sativa) after spray irrigation with water containing cyanobacteria. Toxicon 37(8):1181–1185
Corbel S, Mougin C, Bouaicha N (2014) Cyanobacterial toxins: Modes of actions, fate in aquatic and soil ecosystems, phytotoxicity and bioaccumulation in agricultural crops. Chemosphere 96(2):1–15
Dalal VK, Tripathy BC (2012) Modulation of chlorophyll biosynthesis by water stress in rice seedlings during chloroplast biogenesis. Plant Cell Environ 35(9):1685–1703
Dong L, Li JY (2013) Relationship among drought, hydraulic metabolic, carbon starvation and vegetation mortality. Acta Ecol Sin 33(18):5477–5483
Dorr FA, Pinto E, Soares RM et al (2010) Microcystins in South American aquatic ecosystems: occurrence, toxicity and toxicological assays. Toxicon 56:1247–1256
Duy TN, Paul KS, Shaw GR et al (2000) Toxicology and risk assessment of fresh water cyanobacterial (blue-green algae) toxins in water. Rev Environ Contam Toxicol 163:113–185
Gurbuz F, Metcalf JS, Karahan AG et al (2009) Analysis of dissolved microcystins in surface water samples from Kovada Lake, Turkey. Sci Total Environ 407:4038–4046

He YJ, Zhong ZC, Liu JM et al (2007) The effects of VA mycorrhizal fungus inoculation on material metabolism of Broussonetia papyrifera seedlings. Acta Ecol Sin 12:5455–5462
Hoch G, Richter A, Krner C (2003) Non-structural carbon compounds in temperate forest trees. Plant, Cell Environ 26(7):1067–1081
Shanghai Institute of Plant Physiology, Chinese Academy of Sciences (1999) Experimental guide of modern plant physiology. Science Press, Beijing, pp 113–115
Jacob-Wilk D, Holland D, Goldschmidt EE et al (1999) Chlorophyll breakdown by chlorophyllase: isolation and functional expression of the Chlase1 gene from ethylene-treated Citrus fruit and its regulation during development. Plant J 20(6):653–661
Järvenpää S, Lundberg-Niinistö C, Spoof L et al (2007) Effects of microcystins on broccoli and mustard, and analysis of accumulated toxin by liquid chromatography-mass spectrometry. Toxicon 49(6):865–874
Jin HM, Jiang J, Chang ZZ (2013) Effect of microcystins on growth of Brassica Chinensis and its accumulation in vivo. Asian J Ecotoxicol 8(4):529–536
Kang YY, Yang X, Guo SR et al (2011) Effects of 24-Epibrassinolide on carbohydrate metabolism and enhancement of tolerance to root-zone hypoxia in cucumber(*Cucumis sativus L.*). Scientia Agricultura Sinica 44(12):2495–2503
Kenefick S, Hrudey S, Peterson H et al (1993) Toxin release from Microcystis aeruginosa after chemical treatment. Water Sci Technol 27:433–440
Koch G, Sillett S, Jennings G et al (2004) The limits to tree height. Nature 428:851–854
Kós P, Gorzó G, Suranyi G et al (1995) Simple and efficient method for isolation and measurement of cyanobacterial hepatotoxins by plant tests (*Sinapis alba* L.). Anal Biochem 225(1):49–53
Li X, Ma XD, Cheng YH et al (2020) Effects of phenanthrene on the physiological and biochemical characteristics of salix viminalis. J Nucl Agric Sci 34(08):1855–1861
Liu HY (2019) Effects of microcystins on growth, hormone level and mineral nutrient absorption of rice (*Oryza sativa*). Jiangnan University, Su Zhou
Liu XR, Huang CD, Zhu HW (2020a) Studies on measuring methods of leaf area in lettuce. China Vegetables 1(12):78–81
Liu F, Liu P, Cao M et al (2020b) Review on the applications of stable isotope technique in the study of plant and water relation. Ecol Sci 39(06):224–232
MacKintosh C, Beattie KA, Klumpp S et al (1990) Cyanobacterial microcystin-LR is a potent and specific inhibitor of protein phosphatases 1 and 2A from both mammals and higher plants. FEBS Lett 264(2):187–192
Ministry of Ecology and Environment of the People's Republic of 2020 Bulletin on the State of China's Ecological Environment. http://www.mee.gov.cn/hjzl/sthjzk/zghjzkgb/202105/P020210526572756184785 (2020-5-26)
Murata T, Akazawa T, Fukuchi S (1968) Enzymic mechanism of starch breakdown in germinating Rice seeds I. An analytical study. Plant Physiol 43(12):1899–1905
Peuthert A, Chakrabarti S, Pflugmacher S (2007) Uptake of microcystins-LR and -LF (cyanobacterial toxins) in seedlings of several important agricultural plant species and the correlation with cellular damage (lipid peroxidation). Environ Toxicol 22(4):436–442
Pflugmacher S, Hofmann J, Hübner B (2007a) Effects on growth and physiological parameters in wheat(*Triticum aestivum L.*) grown in soil and irrigated with cyanobacterial toxin contaminated water. Environ Toxicol Chem 26(12):2710–2716
Pflugmacher S, Aulhorn M, Grimm B (2007b) Influence of a cyanobacterial crude extract containing microcystin-LR on the physiology and antioxidative defence systems of different spinach variants. New Phytol 175(3):482–489
Salleo S, Trifilò P, Esposito S et al (2009) Starch-to-sugar conversion in wood parenchyma of field-growing Laurus nobilis plants: a component of the signal pathway for embolism repair? Funct Plant Biol 36(9):815
Song L, Chen W, Peng L et al (2007) Distribution and bioaccumulation of microcystins in water columns: a systematic investigation into the environmental fate and the risks associated with microcystins in Meiliang Bay, Lake Taihu. Water Res 41(13):2853–2864

Su YL, Deng YR (2013) Microcystins in eutrophic lakes and their controlling and removing methods. Environ Sci Technol 36(6):62–66
Sun S, Zhang XJ, Liu JP et al (2018) Synergistic effects of shade and drought on the physiological metabolism and resistance system of Arthraxon hispidus. Acta Ecol Sin 38(5):1770–1779
Wan X, Tai YP, Wang R et al (2017) Distribution patterns of microcystins-producing microcystis and microcystis-LR during blooms in drinking water source areas of Lake Erhai. Acta Sci Circum 37(6):2040–2047
Wang WM (2014) Effects of microcystins on growth and photosynthesis of rice at different stages. Jiangnan University, Wuxi
Wang NY (2017) Research of effects of microcystins on aquatic plant Iris pseudacorus L. and its degradation characteristics. Tianjin University, Tianjin
Wejnerowski, Rzymski L, Kokociński P et al (2018) The structure and toxicity of winter cyanobacterial bloom in a eutrophic lake of the temperate zone. Ecotoxicology 27:752–760
Xiang LX, Hu LP, Meng S et al (2020) Effect of Foliar-spraying spermidine on chlorophyll synthesis metabolism of tomato seedlings under heat stress. Acta Botan Boreali-Occiden Sin 40(5):846–851
Xue YF, Liu ZP (2008) Effects of NaCl and $Na_2CO_3$ stresses on photosynthesis and parameters of chlorophyll fluorescence in Helianthus tuberosus seedings. Chin J Plant Ecol 32(1):161–167
Yi N, Xue YF, Shi ZQ et al (2016) Inhibitory effect of microcystins on seed germination and seedling growth of rice. Jiangsu J Agric Sci 32(04):729–735
Yin LY, Huang JQ, Li DH (2004) The Effect of microcystin on the growth and development of submergent macrophyte vallisneria natans hara. Acta Hydrobiol Sin 28(2):147–150
Yu FY, Xu XZ, Guy RD (2003) Effects of water and heat stress on the needle sugar content of four coniferous tree seedlings. J Nanjing Forestry Univ (natural Sciences Edition) 28(5):1–5
Zhan XJ, Xiang L, Li YW et al (2013) Influences of microcystin-LR and chromium on seed germination of Chinese cabbage. J Agro-Environ Sci 32(1):203–204
Zhang MM (2015) Study on ecophysiological effects and toxicant mechanism of microcystins-LR on Oryza sativa L. Nanjing University of Information Science and Technology, Nanjing
Zhang L, Xu ZR, Hu XH et al (2015) Effect of Foliar-spraying spermidine on seedlings growth contents of chlorophyll biosynthesis precursors in leaves of tomato under saline-alkaline stress. Acta Botan Boreali-Occiden Sin 35(1):125–130
Zhang WL, Zhang LG, Yang HJ et al (2020) Effects of sigma broad on photosynthesis characteristics and soluble substances content in leaves of foxtail millet. J Nuclear Agric Sci 34(06):1294–1301

# Chapter 25
# Cultivation of Energy Crops in Constructed Wetlands for Wastewater Treatment: An Overview


**Henrique J. O. Pinho and Dina M. R. Mateus**

**Abstract** The need for sustainable, clean, and secure energy sources is a current issue for all nations. All kinds of vegetal biomass can be used as energy-source or as raw material for biofuel production, but some species are commonly classified as energy crops. This work evaluates the energy potential of 35 species of energy crops when produced in constructed wetlands (CW). Producing energy crops in CW is a route to link wastewater treatment to energy production, avoiding the abstraction of freshwater for crop irrigation, and simultaneously avoiding the use of arable land. However, for most of the energy crops, there are no data available in the literature about biomass productivity in CWs. Although 20 of the 35 crops have been tested as CW vegetation, the biomass productivity in CWs was only found for 13 species. Reported biomass productivity in CW is similar to or even higher than the productivity reported for conventional production, but most reported data is for pilot-scale CW, which points to the need for future work in full-scale systems. From the combination of biomass productivity and the biomass calorific value, *Arundo donax*, *Miscanthus x giganteus*, *Cynodon dactylon*, *Phragmites australis*, and *Typha latifolia* show higher ranges up to 3064 MJ/ha year for *Arundo donax*. Future works on CW design can be focused on the potential of using energy crops as vegetation.

**Keywords** Bioenergy · Energy crops · Constructed wetlands

## 25.1 Introduction

Sustainable, clean, and market-secure energy is a current hot topic for all nations. Although thermal and photovoltaic direct capture of solar energy and indirect solar-driven sources of renewable electricity such as wind and dams are attaining market

H. J. O. Pinho (✉)
Smart Cities Research Center (Ci2), BIOTEC, Instituto Politécnico de Tomar, Tomar, Portugal
e-mail: hpinho@ipt.pt

D. M. R. Mateus
Technology, Restoration and Arts Enhancement Center (Techn&Art), BIOTEC, Instituto Politécnico de Tomar, Tomar, Portugal



Z. Yang (ed.), *Environmental Science and Technology: Sustainable Development*, Environmental Science and Engineering, https://doi.org/10.1007/978-3-031-27431-2_25

share, biomass-derived biofuels consist in a solution for many applications where electrification may be difficult or expensive (Li et al. 2022).

Biomass is usually referred to as plants or other photosynthetic organisms such as algae (Ahmed et al. 2022; Siddiki et al. 2022). Almost all kinds of plant biomass can be used directly as a heat source by combustion or converted to a range of biofuels such as bioethanol, biodiesel, and biogas (Liu et al. 2022). Energy crops are species in which energy valorization is traditional or easier such as maize (*Zea mays*), sorghum (*Sorghum* spp.), sugarcane (*Saccharum officinarum*), switchgrass (*Panicum virgatum*), and willow (*Salix viminalis*), among others (Laurent et al. 2015; Margaritopoulou et al. 2016; Oleszek et al. 2019). Although energy crops represent a relevant alternative to non-renewable fuels, their cultivation requires land, fresh water, and fertilizers, competes with the food and feed chains, and can cause negative impacts on greenhouse gas emissions and biodiversity (Fritsche et al. 2010; Paschalidou et al. 2018; Knápek et al. 2021).

Plants are an essential component of constructed wetlands (CW). CW are engineered systems that use the treatment mechanisms of natural wetlands to eco-efficiently treat wastewater (Vymazal 2022; Mader et al. 2022). CW vegetation is usually named macrophytes and can be rooted or floating species depending on the type of wetland design. The plants contribute directly to the uptake of nutrients and other water pollutants, and indirectly through the fixation of biofilms, transfer of oxygen and pH regulation, providing conditions for pollutants assimilation and conversion by microorganisms, and conferring thermal isolation, preventing clogging, allowing wildlife habitat, and contributing to aesthetics of CW (Jesus et al. 2018; Sandoval et al. 2019; Kulshreshtha et al. 2022). To avoid the back release of nutrients into the system at the end of the plant's growing season the wetlands vegetation must be harvested, which can provide biomass for bioenergy and other uses (Avellan et al. 2017; Avellán and Gremillion 2019). This approach can be a contribution of CW to the water-energy nexus: using CW to produce vegetal biomass for bioenergy applications avoids simultaneously the need for arable land, fertilizers, and freshwater.

Although the literature on bioenergy is vast the potential of using CWs as a source of biomass for biofuels production is scarcely explored. Therefore, the purpose of this work consists in evaluating the energy potential of producing crops in CWs. To attain that goal, the review work of Laurent et al. (2015) on the productivity of energy crops under conventional cultivation was used as the basis for the identification of the main plant species cultivated for energy purposes. Then, the energy potential was computed from available data in the literature on crop productivity in CWs and on its energy production by combustion.

## 25.2 Methods

The present work was conducted in four steps:

- A first survey of the literature to obtain references to productivity in CWs of the species identified in the work of Laurent et al. (2015);
- Selection of species whose productivity in CWs is reported;
- A second survey of the literature to gather data of calorific value expressed as Higher Heating Value (HHV, MJ/kg) for the selected species;
- Computation of the energy potential of each specie, consisting of the product of the productivity (ton/ha year) by the HHV to obtain the calorific potential of cultivation in CWs (MJ/ha year).

The lower and higher reported figures of biomass productivity and calorific value were used to obtain a low–high range of calorific potential of crops cultivation in CWs.

## 25.3 Results and Discussion

The work of Laurent et al. (2015) reports 35 species of energy crops, giving data on biomass productivity in land conventional production. The *Saccharum* spp. was not considered in the present work because the cited work also reports values of *S. arundinaceum* e *S. officinarum*.

Figure 25.1 shows the relative use of the 35 species in CWs, from the first survey. The common reed (*Phragmites australis*) and cattail (*Typha latifolia*) are the most common wetland plants. *Arundo donax*, *Phalaris arundinacia*, and *Pennisetum purpureum* are less common wetland plants. Those results are in line with several review works on CW's plants (Vymazal 2011, 2013; Bhatia and Goyal 2014; Kataki et al. 2021; Varma et al. 2021). The remaining energy crops are rarely tested as CW vegetation. Moreover, any work on CWs was identified for 15 of the reported energy crops. Those first results point to future perspectives for research on the evaluation of non-conventional CWs vegetation focusing on its valorization as energy raw material.

Although 20 of the 35 crops have been tested as CW vegetation, the biomass productivity in CWs was only found for 13 species (Table 25.1). Figure 25.2 presents the minimum and maximum plant biomass productivity in CW retrieved from the surveyed literature. The figure also shows the range of biomass productivity reported by Laurent et al. (2015).

Although several species have been evaluated in full-scale CWs, most reported productivity data reports to pilot-scale and even lab-scale experiments. From Fig. 25.2 it can be observed that the productivity in CWs is higher than the production in soil, but the lack of results obtained in full-scale CWs, and from a long-time operation, prevents concluding that CW's productivity in real operation can be so high. However,

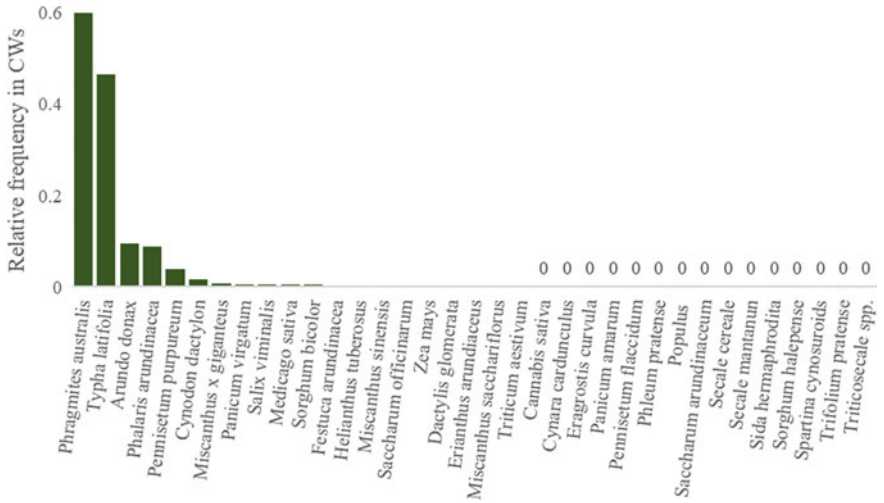


**Fig. 25.1** Relative frequency of the surveyed works that refer to the use of energy crops as constructed wetland vegetation. The *Phragmites australis* frequency corresponds to the unit but the y-axis range is reduced to show the lower frequency results. The zeros identify the species for which no records of use in CWs were found

there can be concluded that the productivity in CWs is not below the productivity in soil, which is a positive result.

Figure 25.3 presents the estimated energy potential for the 13 energy crops when produced in CWs. Although the results may be affected by the uncertainty and scarcity of biomass productivity data in CWs, *Arundo donax*, *Miscanthus x giganteus*, *Cynodon dactylon*, *Phragmites australis*, and *Typha latifolia* show the higher energy potential by hectare and year. All these species are very common or common vegetation of CWs. The energy potential of *Saccharum officinarum* and *Sorghum bicolor*, two uncommon CW's vegetation, is lower than the 4 most energy-productive species but is similar to some common CWs plants, such as *Pennisetum purpureum*, *Phalaris arundinacea*, and *Salix viminalis.*

The energy productivity of energy crops as CW's vegetation was estimated on a simple calorific value basis. However, crop biomass can be converted into different types of biofuels by biochemical or thermochemical processes, such as bioethanol, biodiesel, and biohydrogen, among others. As an example, the most common CW plant (*Phragmites australis*) has already been studied as a raw material to produce bioethanol by aerobic fermentation after hydrolysis (Liu et al. 2012; He et al. 2015; Lin et al. 2020), biogas by anaerobic digestion (Gizińska-Górna et al. 2016; Odhiambo et al. 2009), biohydrogen by dark fermentation (Tran et al. 2021), syngas by gasification (Köbbing et al. 2014), and bio-oils by pyrolysis (Aysu 2014). This evidence represents an opportunity to develop a framework for the future use of constructed wetlands as a source for a broad matrix of biofuels.

**Table 25.1** Biomass productivity in CWs and reported higher heating value[a]

| Specie | CW scale | Biomass productivity (ton/ha year) | HHV (MJ/kg) |
|---|---|---|---|
| *Arundo donax* | Pilot, Full | 6.7–159.6 (Maucieri et al. 2019; Ruan et al. 2021) | 17.68–19.2 (Cano-Ruiz et al. 2020) |
| *Cynodon dactylon* | Pilot | 7.5–86.3 (Matos et al. 2010a, b) | 17.96–19.18 (Mishra et al. 2020; Cantrell et al. 2009) |
| *Helianthus tuberosus* | Pilot | 5.9 (Gizińska-Górna et al. 2016) | 14.93–17.6 (Szostek et al. 2018; Godin et al. 2013) |
| *Miscanthus x giganteus* | Pilot | 110.4 (Maucieri et al. 2019) | 17–19.5 (Godin et al. 2013; Cossel et al. 2021) |
| *Panicum virgatum* | Lab | 0.1 (Recsetar et al. 2021) | 16.5–19.2 (Godin et al. 2013; Cossel et al. 2021) |
| *Pennisetum purpureum* | Pilot | 8.1–25.0 (Matos et al. 2010a; Klomjek 2016) | 18.11–18.55 (Rocha et al. 2017; Reza et al. 2020) |
| *Phalaris arundinacea* | Full | 3.4–22.3 (Vymazal and Krőpfelová 2005; Vymazal et al. 2010) | 16.6–18.7 (Usťak et al. 2019) |
| *Phragmites australis* | Pilot, Full | 13.6–83.1 (Maucieri et al. 2019; Gizińska-Górna et al. 2016) | 18.49–18.72 (Bernal et al. 2021; Demko et al. 2017) |
| *Saccharum officinarum* | Pilot | 8.4–27.2 (Mateus et al. 2016, 2017) | 17.83–18.77 (Charusiri and Vitidsant 2017; Muigai et al. 2021) |
| *Salix viminales* | Pilot, Full | 4.8–16.4 (Listosz et al. 2018) | 16.13–19.26 (Listosz et al. 2018) |
| *Sorghum bicolor* | Lab, Pilot | 1.3–23.6 (Recsetar et al. 2021; Zhu et al. 2017) | 15.58–18.4 (Zhu et al. 2017; Cabrera-Ariza et al. 2018) |
| *Typha latifolia* | Pilot | 20.2–41.8 (Andries et al. 2018; Parlakidis et al. 2022) | 17.02–20.5 (Petrovič et al. 2021) |
| *Zea mays* | Pilot | 10 (García-Pérez et al. 2010) | 17.68–19.02 (Kopecký et al. 2021; Povilaitis et al. 2016) |

[a] Minimum and maximum values reported inthe surveyed literature are presented

Although the main goal of constructed wetlands is the treatment of wastewater, the sustainability of this green technology can be improved through the bioenergy valorization of the plant biomass produced. However, more research efforts should be made to select operational conditions that allow using energy crops as vegetation without compromising the phytoremediation objective of CW's plants. At this point, the five species with the greatest potential are common CW vegetation, but other energy crops may also have effective phytoremediation capabilities. In the present overview, the productivity or even the capability as a phytoremediation plant was not found for several energy crops. Thus, further work can be carried out to assess the potential of energy crops as the vegetation of constructed wetlands, assessing their

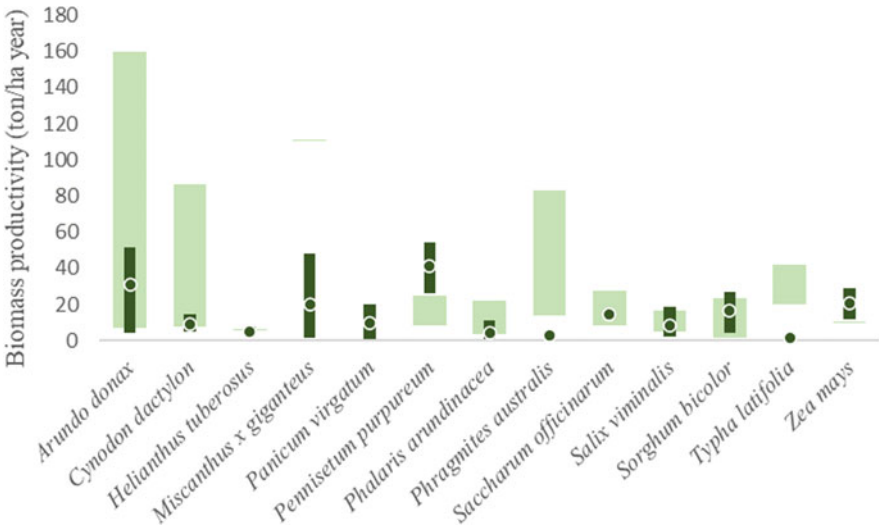


**Fig. 25.2** Biomass productivity. The light and large bars present the range of productivity in CWs. The dark and narrow bars present the range of productivity in soil, as reported by Laurent et al. (2015). The dots represent the average value in soil

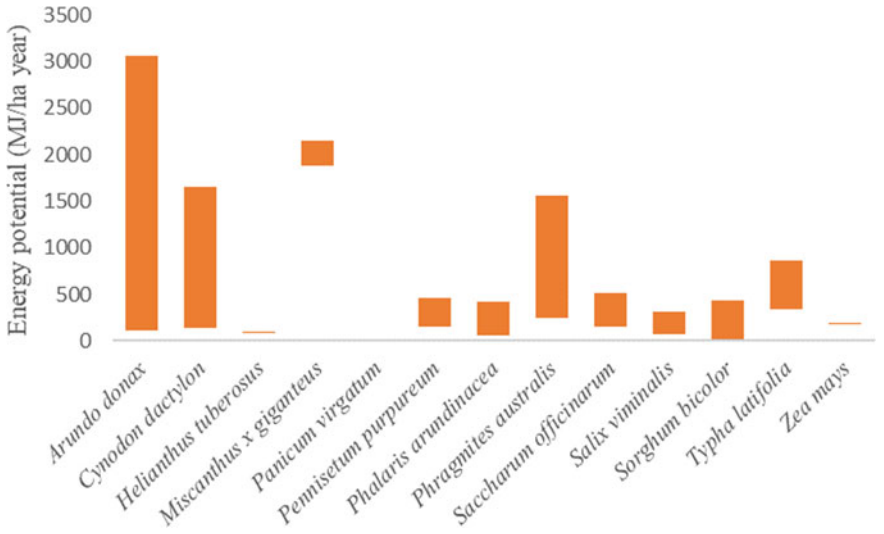


**Fig. 25.3** Estimated energy productivity of energy crops cultivated in CWs treating wastewater

ability to remove pollutants from wastewater and to grow in the aquatic environment of constructed wetlands.

## 25.4 Conclusions

The use of CW vegetation for energy production makes this wastewater treatment technology more sustainable because it avoids the use of arable land and freshwater for irrigation. Thus, avoiding the main disadvantages of producing energy crops.

In this overview work, the energy potential of cultivating energy crops in CWs was evaluated through available data on biomass productivity and the calorific values of energy crops. A total of 35 species of energy crops were considered, but data on biomass productivity in CWs was found for only 13 species.

Although the results may be affected by the uncertainty and scarcity of biomass productivity data in CWs, *Arundo donax*, *Miscanthus x giganteus*, *Cynodon dactylon*, *Phragmites australis*, and *Typha latifolia* show a higher energy potential by hectare and year, from 118 to 3064 MJ/ha year for *Arundo donax*, a less common CW's vegetation. For comparison, the evaluated energy-productivity of *Phragmites australis*, the most common CW vegetation, ranged from 251 to 1556 MJ/ha year.

Future work on the evaluation of energy crops as CW's vegetation could be a way to increase the sustainability of CWs and develop a framework to connect wastewater treatment and recovery with bioenergy production, alleviating the pressure on freshwater extraction and land usage for energy purposes. The perspective of valorizing the vegetation of CWs can be intensified as a research goal but also making part of CW's set of design criteria.

**Acknowledgements** This research was funded by FCT, The Portuguese Foundation for Science and Technology, grant number UIDB/05567/2020.

## References

Ahmed S, Mofijur M, Chowdhury S, Nahrin M, Rafa N, Chowdhury A, Nuzhat S, Ong H (2022) Pathways of lignocellulosic biomass deconstruction for biofuel and value-added products production. Fuel 318:123618

Andries R, Matos A, Freitas W (2018) Estimation of plant productivity and nutrient extraction capacity along the length of horizontal subsurface flow constructed wetland treating swine wastewater. Ambiente e Agua—an Interdiscip J Appl Sci 13(3):1–11

Avellan C, Ardakanian R, Gremillion P (2017) The role of constructed wetlands for biomass production within the water-soil-waste nexus. Water Sci Technol 75(10):2237–2245

Avellán T, Gremillion P (2019) Constructed wetlands for resource recovery in developing countries. Renew Sustain Energy Rev 99:42–57

Aysu T (2014) The effect of Boron minerals on pyrolysis of common reed (Phragmites australis) for producing bio-oils. Energy Sour Part A Recovery Utilization Environ Effects 36(22):2511–2518

Bernal M, Grippi D, Clemente R (2021) Potential of the biomass of plants grown in trace element-contaminated soils under Mediterranean climatic conditions for bioenergy production. Agronomy 11(9):1750

Bhatia M, Goyal D (2014) Analyzing remediation potential of wastewater through wetland plants: a review. Environ Prog Sustain Energy 33(1):9–27

Cabrera-Ariza A, Tozzini C, Espinoza-Meza S, Santelices-Moya R, Magni-Díaz C, Alonso-Valdés M (2018) Effect of crop management intensity on energy and carbon dioxide balance of two bioenergy Sorghum bicolor hybrids. Ital J Agron 14(1):26–33

Cano-Ruiz J, Sanz M, Curt M, Plaza A, Lobo M, Mauri P (2020) Fertigation of Arundo donax L. with different nitrogen rates for biomass production. Biomass Bioenergy 133:105451

Cantrell K, Stone K, Hunt P, Ro K, Vanotti M, Burns J (2009) Bioenergy from Coastal bermudagrass receiving subsurface drip irrigation with advance-treated swine wastewater. Bioresour Technol 100(13):3285–3292

Charusiri W, Vitidsant T (2017) Upgrading bio-oil produced from the catalytic pyrolysis of sugarcane (Saccharum officinarum L) straw using calcined dolomite. Sustain Chem Pharm 6:114–123

Demko J, Machava J, Saniga M (2017) Energy production analysis of Common Reed—Phragmites australis (Cav.) Trin Folia Oecologica 44(2):107–113

Fritsche U, Sims R, Monti A (2010) Direct and indirect land-use competition issues for energy crops and their sustainable production—an overview. Biofuels Bioprod Biorefin 4(6):692–704

García-Pérez A, Harrison M, Grant B (2010) Engineered green technology to grow fuel corn (Zea mays L.): recirculating vertical flow constructed wetland treating sewage on-site. In: American Water Works Association annual conference and exposition 2010

Gizińska-Górna M, Czekała W, Jóźwiakowski K, Lewicki A, Dach J, Marzec M, Pytka A, Janczak D, Kowalczyk-Juśko A, Listoz A (2016) The possibility of using plants from hybrid constructed wetland wastewater treatment plant for energy purposes. Ecol Eng 95:534–541

Godin B, Lamaudière S, Agneessens R, Schmit T, Goffart J-P, Stilmant D, Gerin P, Delcarte J (2013) Chemical characteristics and biofuel potential of several vegetal biomasses grown under a wide range of environmental conditions. Ind Crops Prod 48:1–12

He M, Hu Q, Zhu Q, Pan K, Li Q (2015) The feasibility of using constructed wetlands plants to produce bioethanol. Environ Prog Sustain Energy 34:276–281

Jesus J, Danko A, Fiúza A, Borges M (2018) Effect of plants in constructed wetlands for organic carbon and nutrient removal: a review of experimental factors contributing to higher impact and suggestions for future guidelines. Environ Sci Pollut Res 25(5):4149–4164

Kataki S, Chatterjee S, Vairale M, Dwivedi S, Gupta D (2021) Constructed wetland, an eco-technology for wastewater treatment: a review on types of wastewater treated and components of the technology (macrophyte, biolfilm and substrate). J Environ Manage 283:111986

Klomjek P (2016) Swine wastewater treatment using vertical subsurface flow constructed wetland planted with Napier grass. Sustain Environ Res 26(5):217–223

Knápek J, Králík T, Vávrová K, Valentová M, Horák M, Outrata D (2021) Policy implications of competition between conventional and energy crops. Renew Sustain Energy Rev 151:111618

Köbbing J, Patuzzi F, Baratieri M, Beckmann V, Thevs N, Zerbe S (2014) Economic evaluation of common reed potential for energy production: a case study in Wuliangsuhai Lake (Inner Mongolia, China). Biomass Bioenerg 70:315–329

Kopecký M, Mráz P, Kolář L, Váchalová R, Bernas J, Konvalina P, Perná K, Murindangabo Y (2021) Effect of fertilization on the energy profit of tall wheatgrass and reed canary grass. Agronomy 11(3):445

Kulshreshtha N, Verma V, Soti A, Brighu U, Gupta A (2022) Exploring the contribution of plant species in the performance of constructed wetlands for domestic wastewater treatment. Bioresour Technol Rep 18:101038

Laurent A, Pelzer E, Loyce C, Makowski D (2015) Ranking yields of energy crops: a meta-analysis using direct and indirect comparisons. Renew Sustain Energy Rev 46:41–50

Li L, Lin J, Wu N, Xie S, Meng C, Zheng Y, Wang X, Zhao Y (2022) Review and outlook on the international renewable energy development. Energy Built Environ 3(2):139–157
Lin Y, Zhao Y, Ruan X, Barzee T, Zhang Z, Kong H, Zhang X (2020) The potential of constructed wetland plants for bioethanol production. Bioenergy Res 13(1):43–49
Listosz A, Kowalczyk-Juśko A, Jóźwiakowski K, Marzec M, Urban D, Tokarz E, Ligęza S (2018) Productivity and chemical properties of Salix viminalis in a horizontal subsurface flow constructed wetland during long-term operation. Ecol Eng 122:76–83
Liu D, Wu X, Chang J, Gu B, Min Y, Ge Y, Shi Y, Xue H, Peng C, Wu J (2012) Constructed wetlands as biofuel production systems. Nat Clim Chang 2:190–194
Liu T, Miao P, Shi Y, Tang K, Yap P-S (2022) Recent advances, current issues and future prospects of bioenergy production: a review. Sci Total Environ 810:152181
Mader A, Holtman G, Welz P (2022) Treatment wetlands and phyto-technologies for remediation of winery effluent: challenges and opportunities. Sci Total Environ 807:150544
Margaritopoulou T, Roka L, Alexopoulou E, Christou M, Rigas S, Haralampidis K, Dimitra M (2016) Biotechnology towards energy crops. Mol Biotechnol 58(3):149–158
Mateus D, Vaz M, Capela I, Pinho H (2016) The potential growth of sugarcane in constructed wetlands designed for tertiary treatment of wastewater. Water (Switzerland) 8(3):93
Mateus D, Vaz M, Pinho H (2017) Valorisation of phosphorus-saturated constructed wetlands for the production of sugarcane. J Technol Innov Renew Energy 6:1–6
Matos A, Abrahão S, Monaco P, Sarmento A, Matos M (2010a) Capacidade extratora de plantas em sistemas alagados utilizados no tratamento de águas residuárias de laticínios. Rev Bras Eng Agrícola e Ambient 14(12):1311–1317
Matos A, Freitas W, Martinez M, Tótola M, Azevedo A (2010b) Tifton grass yield on constructed wetland used for swine wastewater treatment. Rev Bras Eng Agrícola e Ambient 14(5):510–516
Maucieri C, Borin M, Milani M, Cirelli G, Barbera A (2019) Plant species effect on $CO_2$ and $CH_4$ emissions from pilot constructed wetlands in Mediterranean area. Ecol Eng 134:112–117
Mishra R, Lu Q, Mohanty K (2020) Thermal behaviour, kinetics and fast pyrolysis of Cynodon dactylon grass using Py-GC/MS and Py-FTIR analyser. J Anal Appl Pyrolysis 150:104887
Muigai H, Choudhury B, Kalita P, Moholkar V (2021) Physico–chemical characterization and pyrolysis kinetics of Eichhornia Crassipes, Thevetia Peruviana, and Saccharum Officinarum. Fuel 289:119949
Odhiambo J, Martinsson E, Soren S, Mboya P, Onyango J (2009) Integration water, energy and sanitation solution for stand-alone settlements. Desalination 248(1–3):570–577
Oleszek M, Kowalska I, Oleszek W (2019) Phytochemicals in bioenergy crops. Phytochem Rev 18(3):893–927
Parlakidis P, Mavropoulos T, Vryzas Z, Gikas G (2022) Fluopyram removal from agricultural equipment rinsing water using HSF pilot-scale constructed wetlands. Environ Sci Pollut Res 29(20):29584–29596
Paschalidou A, Tsatiris M, Kitikidou K, Papadopoulou C (2018) Using energy crops for biofuels or food: the choice. Springer, Cham
Petrovič A, Vohl S, Predikaka T, Bedoić R, Simonič M, Ban I, Čuček L (2021) Pyrolysis of solid digestate from sewage sludge and lignocellulosic biomass: kinetic and thermodynamic analysis, characterization of biochar. Sustainability 13(17):9642
Povilaitis V, Šlepetienė A, Šlepetys J, Lazauskas S, Tilvikienė V, Amalevičiūtė K, Feizienė D. Feiza V, Liaudanskienė I, Cesevičienė J, Kadžiulienė Ž, Kukujevas A (2016) The productivity and energy potential of alfalfa, fodder galega and maize plants under the conditions of the nemoral zone. Acta Agric Scand Sect B—Soil Plant Sci 66(3):259–266
Recsetar M, Fitzsimmons K, Cuello J, Hoppe-Jones C, Snyder S (2021) Evaluation of a recirculating hydroponic bed bioreactor for removal of contaminants of emerging concern from tertiary-treated wastewater effluent. Chemosphere 262:128121
Reza M, Islam S, Afroze S, Bakar M, Sukri R, Rahman S, Azad A (2020) Evaluation of the bioenergy potential of invasive Pennisetum purpureum through pyrolysis and thermogravimetric analysis. Energy Ecol Environ 5(2):118–133

Rocha J, Machado J, Carneiro P, Carneiro J, Resende M, Pereira A, Carneiro J (2017) Elephant grass ecotypes for bioenergy production via direct combustion of biomass. Ind Crops Prod 95:27–32
Ruan W, Cai H, Xu X, Man Y, Wang R, Tai Y, Chen Z, Vymazal J, Chen J, Yang Y, Zhang X (2021) Efficiency and plant indication of nitrogen and phosphorus removal in constructed wetlands: a field-scale study in a frost-free area. Sci Total Environ 799:149301
Sandoval L, Zamora-Castro S, Vidal-Álvarez M, Marín-Muñiz J (2019) Role of wetland plants and use of ornamental flowering plants in constructed wetlands for wastewater treatment: a review. Appl Sci 9(4):685
Siddiki S, Mofijur M, Kumar P, Ahmed S, Inayat A, Kusumo F, Badruddin I, Khan T, Nghiem L, Ong H, Mahlia T (2022) Microalgae biomass as a sustainable source for biofuel, biochemical and biobased value-added products: an integrated biorefinery concept. Fuel 307:121782
Szostek M, Kaniuczak J, Hadjuk E, Stanek-Tarkowska J, Jasiński T, Niemiec W, Smusz R (2018) Effect of sewage sludge on the yield and energy value of the aboveground biomass of Jerusalem artichoke (Helianthus tuberosus L.). Arch Environ Prot 44(3):42–50
Tran V, Chu C-Y, Unpaprom Y, Ramaraj R, Chen T-H (2021) Effects of substrate concentration and hydraulic retention time on hydrogen production from common reed by enriched mixed culture in continuous anaerobic bioreactor. Int J Hydrogen Energy 46(27):14036–14044
Usťak S, Šinko J, Muňoz J (2019) Reed canary grass (Phalaris arundinacea L.) as a promising energy crop. J Cent Eur Agric 20(4):1143–1168
Varma M, Gupta A, Ghosal P, Majumder A (2021) A review on performance of constructed wetlands in tropical and cold climate: Insights of mechanism, role of influencing factors, and system modification in low temperature. Sci Total Environ 755:142540
Von Cossel M, Lebendig F, Müller M, Hieber C, Iqbal Y, Cohnen J, Jablonowski N (2021) Comparison of thermochemical conversion and anaerobic digestion of perennial flower-rich herbaceous wild plant species for bioenergy production. Bioresour Technol 340:125724
Vymazal J (2011) Plants used in constructed wetlands with horizontal subsurface flow: a review. Hydrobiologia 674(1):133–156
Vymazal J (2013) Emergent plants used in free water surface constructed wetlands: a review. Ecol Eng 61:582–592
Vymazal J (2022) The historical development of constructed wetlands for wastewater treatment. Land 11(2):174
Vymazal J, Krőpfelová L (2005) Growth of Phragmites australis and Phalaris arundinacea in constructed wetlands for wastewater treatment in the Czech Republic. Ecol Eng 25(5):606–621
Vymazal J, Kröpfelová L, Švehla J, Štíchová J (2010) Can multiple harvest of aboveground biomass enhance removal of trace elements in constructed wetlands receiving municipal sewage? Ecol Eng 36(7):939–945
Zhu F-M, Zhu H-G, Shen W-Y, Chen T-H (2017) Integrating a tidal flow wetland with sweet sorghum for the treatment of swine wastewater and biomass production. Ecol Eng 101:145–154